frontiers | Research Topics

# Interactions between land surface and climate

**Edited by**
Bo Huang, Yan Li and Merja H. Tölle

**Published in**
Frontiers in Environmental Science
Frontiers in Earth Science
Frontiers in Ecology and Evolution

ISSN 1664-8714
ISBN 978-2-83251-943-1
DOI 10.3389/978-2-83251-943-1

## About Frontiers

Frontiers is more than just an open access publisher of scholarly articles: it is a pioneering approach to the world of academia, radically improving the way scholarly research is managed. The grand vision of Frontiers is a world where all people have an equal opportunity to seek, share and generate knowledge. Frontiers provides immediate and permanent online open access to all its publications, but this alone is not enough to realize our grand goals.

## Frontiers journal series

The Frontiers journal series is a multi-tier and interdisciplinary set of open-access, online journals, promising a paradigm shift from the current review, selection and dissemination processes in academic publishing. All Frontiers journals are driven by researchers for researchers; therefore, they constitute a service to the scholarly community. At the same time, the *Frontiers journal series* operates on a revolutionary invention, the tiered publishing system, initially addressing specific communities of scholars, and gradually climbing up to broader public understanding, thus serving the interests of the lay society, too.

## Dedication to quality

Each Frontiers article is a landmark of the highest quality, thanks to genuinely collaborative interactions between authors and review editors, who include some of the world's best academicians. Research must be certified by peers before entering a stream of knowledge that may eventually reach the public - and shape society; therefore, Frontiers only applies the most rigorous and unbiased reviews. Frontiers revolutionizes research publishing by freely delivering the most outstanding research, evaluated with no bias from both the academic and social point of view. By applying the most advanced information technologies, Frontiers is catapulting scholarly publishing into a new generation.

## What are Frontiers Research Topics?

Frontiers Research Topics are very popular trademarks of the *Frontiers journals series*: they are collections of at least ten articles, all centered on a particular subject. With their unique mix of varied contributions from Original Research to Review Articles, Frontiers Research Topics unify the most influential researchers, the latest key findings and historical advances in a hot research area.

Find out more on how to host your own Frontiers Research Topic or contribute to one as an author by contacting the Frontiers editorial office: frontiersin.org/about/contact

# Interactions between land surface and climate

**Topic editors**

Bo Huang — Norwegian University of Science and Technology, Norway

Yan Li — Beijing Normal University, China

Merja H. Tölle — University of Kassel, Germany

**Citation**

Huang, B., Li, Y., Tölle, M. H., eds. (2023). *Interactions between land surface and climate*. Lausanne: Frontiers Media SA. doi: 10.3389/978-2-83251-943-1

# Table of contents

frontiers | Frontiers in Environmental Science

TYPE Editorial
PUBLISHED 03 March 2023
DOI 10.3389/fenvs.2023.1169298



OPEN ACCESS

EDITED AND REVIEWED BY
Riccardo Buccolieri,
University of Salento, Italy

*CORRESPONDENCE
Bo Huang,
bo.huang@ntnu.no

SPECIALTY SECTION
This article was submitted to Land Use Dynamics, a section of the journal Frontiers in Environmental Science

RECEIVED 19 February 2023
ACCEPTED 27 February 2023
PUBLISHED 03 March 2023

CITATION
Huang B, Li Y and Tölle MH (2023), Editorial: Interactions between land surface and climate.
*Front. Environ. Sci.* 11:1169298.
doi: 10.3389/fenvs.2023.1169298



# Editorial: Interactions between land surface and climate

Bo Huang[1]*, Yan Li[2,3] and Merja H. Tölle[4]

[1]Department of Energy and Process Engineering, Industrial Ecology Programme, Norwegian University of Science and Technology (NTNU), Trondheim, Norway, [2]State Key Laboratory of Earth Surface Processes and Resources Ecology, Beijing Normal University, Beijing, China, [3]Institute of Land Surface System and Sustainable Development, Faculty of Geographical Science, Beijing Normal University, Beijing, China, [4]Center of Environmental Systems Research (CESR), University of Kassel, Kassel, Germany

KEYWORDS

**land cover, land use (LCLU), land surface process, climate response, biogeophysical effects, climate modelling**

Editorial on the Research Topic
Interactions between land surface and climate

The rate of climate change intensification will increase with growing emissions of greenhouse gases in the future. Regional terrestrial temperature increases differ in magnitude from global warming due to feedback processes. This has far-reaching consequences to our society especially for our ecosystems, agricultural food production, water availability, living habitat and electric power generation.

Anthropogenic changes in land use/cover can influence the lower atmosphere by modifying land surface properties that control the exchange of energy, water, and momentum, and thus affect the regional or local climate. Teleconnections are possible depending on the magnitude of land surface transformations. The strength of the land-atmosphere coupling is linked to the morphological characteristics of the land surface including vegetation and urban areas. Here, the species composition and distribution play a crucial role with their transpiration and photosynthesis, reflection ability of radiation, and roughness. The scale and nature of land surface modifications affect those processes, but the quantification of these interactions is not resolved, and the strength of the impact is still debated. This fact limits decision-makers to modulate land management strategies at different scales in light of climate change mitigation and adaptation. Thanks to the development of monitoring, satellite remote sensing and climate modelling, this Research Topic brings together novel observational and numerical modelling studies regarding the interaction between land surface and climate change at global and regional or local scales, from bed-rock to the upper atmosphere, in the past, present, and future. Eight papers contribute to this Research Topic.

Recent climate change significantly impacts on the phenology of vegetation. The growing season average NDVI of grassland vegetation significantly increase around 0.023/10a over the Mongolian Plateau Li et al.. Land use/cover management is a key sector to meet climate change mitigation and adaptation strategies. Land cover management will change the surface vegetation structure, and then affect land surface processes. For example, forest canopy closure determines the local snow depth and snowfall intensity, higher forest canopy closure leads to a lower snow depth (Gao et al.). Land cover changes also impact on the large general circulation (Zhang et al.) and surface solar radiation (Jin et al.).

Climate model is an important tool to investigate the interaction between land surface and climate. Vegetation structure and physiology in the model determines the model

performance in capturing land surface processes. Jones et al. found that implementing the Newton-Raphson stomatal optimisation method in the model can better predict gross primary productivity, stomatal transpiration and leaf water potential, with a much higher computational efficiency. Using a regional climate model (i.e., RegCM), Li et al. investigated the effect of forest change on convective rainfall, and Li et al. studied the temperature extremes response to present-day irrigation over China. Reforestation in southern China significantly enhanced local convective afternoon rainfall during the post-flood season (Li et al.). Present-day irrigation led to significant reductions (slightly changes) in the extreme indices associated with the warm (cold) tails of the maximum and minimum temperatures distributions, e.g., hot days, tropical nights (cold nights, frost days), particularly in the regions with intense irrigation (e.g., the North China Plain) (Li et al.).

Dirmeyer et al. employed multi-model simulations to explore the evolution of land surface feedbacks on extreme heat. The climatological land-heat coupling mirrors other metrics of land–atmosphere interaction, peaking in transition regions between arid and humid climates. Changes from preindustrial to recent historical conditions are dominated by decreased land surface controls on extreme heat, mainly over the broad areas that have experienced expanded or intensified agriculture over the last 150 years. Future projections for increased atmospheric $CO_2$ concentrations show a waning of areas of weakened land-heat feedbacks, while areas of increasing feedbacks expand over monsoon regions and much of the midlatitudes.

This Research Topic of papers provides valuable insights into how changes in land surface affect regional climate. However, there is still large uncertainty about how land cover changes affect regional extreme climate and its transition of teleconnection effect. To better understand the impacts of land cover management strategies on climate change mitigation and adaptation, more studies are needed to consider both the regional and global biogeophysical and biogeochemical effects.

## Author contributions

BH, YL, and MT devised the concept for the editorial. BH drafted the manuscript. YL and MT provided editorial comments and revisions. BH finalized the manuscript and submitted.

## Conflict of interest

The authors declare that the research was conducted in the absence of any commercial or financial relationships that could be construed as a potential conflict of interest.

## Publisher's note

frontiers in Earth Science

ORIGINAL RESEARCH
published: 02 March 2022
doi: 10.3389/feart.2022.855634

# Characteristics of Transient Eddies During Ural Blocking Events With Different Lifetime in Winter

*Jinyu Zhang*[1], *Yan Li*[2,3]*, *Zhilan Wang*[1], *Yu Zhang*[1] *and Yao Lu*[2]

[1]Institute of Arid Meterology, China Meteorological Administration, Lanzhou, China, [2]College of Atmospheric Sciences, Lanzhou University, Lanzhou, China, [3]Key Laboratory of Semi-Arid Climate Change, Ministry of Education, Lanzhou University, Lanzhou, China

Ural blocking high (hereafter UB) is one of the most important weather systems influencing the weather and climate of China, with its onset and development closely connected with transient eddies. Herein, we classified the wintertime UB events during 1979–2015 into three types according to their lifetime, i.e., short, medium, and long lifetime UB events and further analyzed the characteristics of momentum and heat fluxes transported by transient eddies during the three types of UB events. The results show that the eddy momentum and heat transport by transient eddies over the Ural regions is strong, while the westerly is weak, favorable for the establishment and maintenance of the UB. Before the onset of all the UB events there are enhanced lower-level temperature disturbances, decelerated westerly and convergence of transient momentum and heat fluxes. After the onset of the UB, the upper-level jet stream is accelerated and eddy flux convergence is enhanced. Furthermore, it is found that the duration and position of convergence could be one of important factors determining the lifetime of UB event. The long-time strong convergence of transient eddies favors the maintenance of UB. During long UB events, the polar jet and the convergence of eddy momentum fluxes have the strongest intensity and northward shifted position. The convergence is further strengthened until Day +2 and weakened since Day +7, favorable for the long-time maintenance of UB. There is convergence on Day -3 of both short and medium UB events, which disappears on Day +4 during short events, while strengthened after the onset of medium events, leading to a long-time maintenance of UB. Furthermore, among the three types of UB events, the upward propagation of wave activity and E-P flux divergence are the strongest and most long-lasting during long UB events, while the weakest and shortest during short UB events, which can also verify strong atmospheric baroclinicity and long-lasting strong convergence of transient eddies are favorable for long duration of the UB.

**Keywords: Ural blocking, transient eddy, transport of momentum and heat, E-P flux, lifetime of blocking high**



***Edited by:***
*Bo Huang,*
*Norwegian University of Science and Technology, Norway*

***Reviewed by:***
*Yaocun Zhang,*
*Nanjing University, China*
*Yipeng Guo,*
*Nanjing University, China*

***Correspondence:**
*Yan Li*
*liyanlz@lzu.edu.cn*

***Specialty section:***
*This article was submitted to Interdisciplinary Climate Studies, a section of the journal Frontiers in Earth Science*

***Received:*** *15 January 2022*
***Accepted:*** *04 February 2022*
***Published:*** *02 March 2022*

***Citation:***
*Zhang J, Li Y, Wang Z, Zhang Y and Lu Y (2022) Characteristics of Transient Eddies During Ural Blocking Events With Different Lifetime in Winter. Front. Earth Sci. 10:855634. doi: 10.3389/feart.2022.855634*

## 1 INTRODUCTION

Blocking high is one of the weather systems with anomalous meridional development of mid-high latitude atmospheric circulations, the onset and collapse of which can lead to meridional exchange of large-scale air parcel and heat (e.g., Charney and Devore 1979; Mokhov et al., 2013). This can induce drastic changes in the large-scale, or even hemispheric, atmospheric circulation and further lead to

weather and climate extremes, or even severe weather disasters. Ural region is one of the regions with the largest blocking frequency over Northern Hemisphere in winter (e.g., Lupo and Smith 1995; Masato et al., 2013). The Ural blocking (hereafter UB) is important for the weather and climate in China. The onset, development and collapse of UB are closely linked to the Meiyu rainfall over the Jianghuai region in China and the establishment of UB is also an important precursor for the outbreak of cold spells over East Asia (Ding and Johnny 2005; Takaya and Nakamura 2005; Bueh et al., 2011; Luo et al., 2016a). Therefore, it is necessary to investigate the main factors influencing the establishment of wintertime UB and the dynamic and thermodynamic characteristics during the onset of UB events, which can not only provide theoretic basis for understanding the mechanism of the UB development, but also help improve our understanding of the causes of the weather and climate extremes associated with UB events.

Many previous studies have investigated the underlying mechanism responsible for the development of blocking high: Yeh (2010) studied the onset and decay of blocking high from a perspective of energy dispersion. Huang and Zou (1989) found that basic mean flow provides energy for eddies during the establishment of blocking high, leading to a rapid strengthening of eddies. Luo 2003; Luo et al., 2016b) and Shi and Nakamura 2020 revealed the close connection between the development and maintenance of UB and the propagation of Rossby waves. Luo and Zhang (2020a) considered that the local wave activity fluxes are favorable for the establishment of blocking high during its growth phase. Many studies found that the energy for the establishment and maintenance of blocking high mainly comes from baroclinic energy conversion of effective potential energy from basic zonal flow and non-linear interaction between waves, with vorticity transport by transient eddies as a manifestation of the latter (Luo et al., 2014; Ma and Liang 2017; Li et al., 2020). Similarly, the convergence and divergence of transient vorticity and heat flux play a major role in the onset and maintenance of the wintertime blocking high (Nakamura et al., 1997; Luo and Chen 2005; Athar and Lupo 2010). Xu and Jin (2011) diagnosed the influence of transient eddy fluxes on anomalous blockings and found that anti-cyclonic flow is strengthened due to wave-mean flow interaction. Shi and Wang (2021) found that high-frequency transient eddies are favorable for the maintenance of wintertime UB through barotropic energy conversion.

As a large-scale weather system, the lifetime of blocking high is 5–7 days on average, with the longest events up to 20 days (Diao et al., 2006; Yao et al., 2017). Blocking highs with different lifetimes have different influences on the weather and climate (Ye et al., 2015). Some previous studies focused on the potential factors influencing blocking lifetime. Kong and Hu (2014) also declared that long-duration UB events could occur more frequently during negative stratospheric northern annular mode (hereafter NAM) events. Ye et al. (2015) found that the stronger the blocking highs over Atlantic and Pacific, the more possibly long UB events could occur. Furthermore, it is found that the meridional gradient of potential vorticity can significantly influence the lifetime and intensity of UB events (Luo et al., 2019; Luo and Zhang 2020b). In addition, Luo (2003) demonstrated that the pre-existing synoptic-scale eddies are a key driver of the spatio-temporal evolution of blocking. The negative phase of North Atlantic Oscillation (NAO) can enhance the planetary-scale split-jetflow prior to blocking onset, through the interaction with upstream synoptic-scale waves, favorable for the establishment and long duration of blocking high (Luo and chen 2005; Wan and Luo 2009) and then the enhanced Eurasian cold extremes (Feng et al., 2019). However, so far, there are few studies on the influence of transient waves on the life cycle of the UB events.

From the above-mentioned previous studies, it can be found that transient eddy, as an important component of atmospheric waves, is important for the maintenance of blocking high. However, the potential influence of transient eddies on the lifetime of UB event still remains unclear. In this study, we attempted to address the following two questions: 1) what is the role of transient eddies in the development of UB events in boreal winter? 2) What are the characteristics and possible impact of transient eddies on UB events with different lifetimes? The rest of the paper is organized as follows: **Section 2** describes the data and methodologies. **Section 3** describes the characteristics of atmospheric circulation evolution during the UB events. **Sections 4** and **5** analyze the characteristics of eddy momentum and heat transported by transient eddies during the UB events with different lifetimes, respectively. The conclusions and discussion are presented in **Section 6**.

# 2 DATA AND METHODOLOGIES

## 2.1 Data

The reanalysis dataset used in this study is provided by Nation Centers for Environmental Prediction (hereafter NCEP) from Nation Centers for Atmospheric Research (NCAR). The daily mean dataset is on a grid with a horizontal resolution of 2.5 × 2.5 and 17 vertical pressure levels (1,000, 925, 850, 700, 600, 500, 400, 300, 250, 200, 150, 100, 70, 50, 30, 20 and 10 hPa). The time period from January 1979 to February 2016 of this dataset is analyzed in this study, including geopotential height, air temperature and horizontal wind.

# 3 METHODOLOGIES

## 3.1 Objective Blocking Detection Method

In this study, an objective analysis method of Zhu et al. (2007) to select UB events and we choose the 5 days as the minimum duration of UB events referring to the definition of Davini et al., 2012. The detailed criteria are shown as follows:

(1) There is a closed high-pressure center on 500 hPa over the mid-high latitudes (north of 50°N);
(2) The warm high-pressure center lasts for at least 5 days and during this period it is commonly quasi-stationary, sometimes moving eastward or westward with a speed less than 7-8 longitude degree/day;

(3) Over the blocking region, the westerly jet is significantly decelerated and splits into two branches west of the high-pressure center. The two branches, i.e., northern and southern branches, merge in the east of it. The zonal distance between split and merge points is larger than 40–50 longitude degrees.

One of the advantages of this detection method is avoiding the mis-interpretation of the relatively high geopotential height anomalies without anti-cyclonic structure as blocking high (Jin et al., 2009). Though less simple than some other methods, such as T&M method (Tibaldi and Molteni 1990), this detection method satisfies our need for recognition of the lifetime of blockings, especially for dates of establishment and collapse.

### 3.1.1 Momentum and Heat Transport of Transient Eddies

In this study, we used a decomposition method for the atmospheric variables. According to the principle of physical decomposition (Qian and Jiang 2014), the temporal anomalous fields, such as $u'$, $v'$ and $T'$, are defined on a calendar date (t) in the year (y) at latitude ($\varphi$). The detailed method is as follows:

An observational daily mean variable field $\mathrm{F}(\lambda,\ \varphi,\ t)_y$, such as u, v or T, is defined on a calendar date (t) in a year (y) at a spatial grid point of longitude ($\lambda$) and latitude ($\varphi$). Then it can be decomposed into a climatological field $\bar{\mathrm{F}}(\lambda,\ \varphi,\ t)_y$ and temporal anomalous field $\mathrm{F}'(\lambda,\ \varphi,\ t)_y$.

$$\mathrm{F}(\lambda,\ \varphi,\ t)_y = \bar{\mathrm{F}}(\lambda,\ \varphi,\ t)_y + \mathrm{F}'(\lambda,\ \varphi,\ t)_y \tag{1}$$

The climatological fields are estimated by averaging 38 years (1979–2016) of data based on the NCEP/NCAR reanalysis data on the calendar date (t).

$$\bar{\mathrm{F}}(\lambda,\ \varphi,\ t)_y = \sum_{1979}^{2016} \mathrm{F}(\lambda,\ \varphi,\ t)_y \Big/ 38 \tag{2}$$

The temporal anomalous fields can be derived after removing the climatological fields from the original observations. One is the zonal-averaged anomalous fields on calendar date (t) in year (y) at latitude ($\varphi$).

$$\left[\mathrm{F}(\lambda,\ \varphi,\ t)\right]_y^{Z'} = \sum_{\lambda=\lambda_1}^{\lambda_2} \left[\mathrm{F}(\lambda,\ \varphi,\ t)_y - \bar{\mathrm{F}}(\lambda,\ \varphi,\ t)_y\right] \Big/ (\lambda_2 - \lambda_1 + 1) \tag{3}$$

This component is referred to as the zonal-averaged (or planetary-scale) anomaly that is used in this paper. The zonal-mean momentum and heat transport of transient eddies are represented by $[u'v']$ and $[v'T']$, respectively. The square brackets indicate zonal mean.

### 3.1.2 The Generalized E-P Flux

The generalized Eliassen-Palm flux defined by Andrews and Mcintyre (1976) is used in this study to investigate the wave activity during UB events. According to the transformed Eulerian mean formulation under the approximation of $\beta$ plane, the E-P flux is defined as follows:

$$\vec{F} \equiv \vec{j}F_y + \vec{k}F_z \tag{4}$$

where $F_y$ and $F_z$ are the meridional and vertical components of EP flux:

$$F_y = -\rho_0 \overline{u'v'} \tag{5}$$

$$F_z = \rho_0 f_0 R\overline{v'T'} \Big/ \left(N^2 H\right) \tag{6}$$

where $\rho_0$ indicates air density, $u'$, $v'$ and $T'$ are the disturbance of $u$, $v$ and $T$, $f_0$ is the Coriolis parameter and R shows the gas constant for dry air. N and H represent buoyancy frequency and scale height, respectively.

Then the divergence of E-P flux is written as:

$$\nabla \bullet \vec{F} = \frac{\partial F_y}{\partial y} + \frac{\partial F_z}{\partial z} \tag{7}$$

## 4 THE CLASSIFICATION OF BLOCKING EVENTS AND THE CHARACTERISTIC ANALYSIS OF THE CIRCULATION EVOLUTION

According to the blocking detection method described in the Method section, 32 winter blocking events over the Ural region are detected during 1979–2015 and the onset and collapse dates of these events are shown in **Table 1**. Firstly, **Figure 1** shows the composited geopotential height and horizontal wind fields on 500 and 850 hPa pressure levels from 5 days prior (Day -5) to 3 days after (Day +3) the onset of UB. On Day -5, the mid-latitudes are dominated by westerly. There are negative geopotential height anomalies west of Ural region, north of Europe, while the Ural region is dominated by weak positive geopotential height anomalies. 2 days after, the negative geopotential height anomalies west of the Ural region are strengthened, forming a weak trough, which is more obvious on 850-hPa pressure level. On Day -1, the positive geopotential height anomalies over the Ural region are significantly strengthened, forming a weak ridge. The trough west of the Ural region is also deepened. In addition, there are negative geopotential height anomalies over the western Siberian Plain, tilting towards northeast-southwest. On Day 0, the Ural positive anomalies are further strengthened, with their center value up to 140 gpm, forming an anti-cyclone anomaly on 850-hPa pressure level. The negative Siberian anomalies are also expanded. On Day +3, the Ural ridge shows a northwest-southeast tilt. The trough west of the Ural region is significantly weakened, indicating the weakening of the upstream energy and the blocking tends to decay.

Generally, the circulation fields from Day −3 to Day +3 show distinct evolution characteristics, but it is hard to reveal the influences of the troughs and ridges on the lifetime of the blocking high based on the above-mentioned composited results. Therefore, in order to investigate the possible impact of the transient eddies on the lifetime of blocking high, according to the lifetime of the blocking high, the following

**TABLE 1 |** Onset and collapse dates of the Ural blocking events during 1979–2015.

| | Onset date | Collapse date | Lasting days (d) | | Onset date | Collapse date | Lasting days (d) |
|---|---|---|---|---|---|---|---|
| 1 | 1979/12/28 | 1980/01/03 | 7 | 17 | 1995/02/15 | 1995/02/20 | 6 |
| 2 | 1980/01/27 | 1980/02/05 | 10 | 18 | 2000/01/09 | 2000/01/15 | 7 |
| 3 | 1981/01/17 | 1981/01/22 | 6 | 19 | 2001/02/03 | 2001/02/07 | 5 |
| 4 | 1981/02/20 | 1981/02/25 | 6 | 20 | 2003/01/19 | 2003/01/25 | 7 |
| 5 | 1982/12/19 | 1982/12/26 | 8 | 21 | 2003/02/06 | 2003/02/11 | 6 |
| 6 | 1984/01/13 | 1984/01/18 | 6 | 22 | 2003/12/27 | 2004/01/04 | 9 |
| 7 | 1984/01/23 | 1984/02/03 | 12 | 23 | 2004/01/31 | 2004/02/04 | 5 |
| 8 | 1984/02/07 | 1984/02/12 | 6 | 24 | 2005/01/23 | 2005/02/09 | 18 |
| 9 | 1984/02/15 | 1984/02/23 | 9 | 25 | 2007/12/08 | 2007/12/12 | 5 |
| 10 | 1984/12/14 | 1984/12/28 | 15 | 26 | 2007/12/26 | 2007/12/31 | 6 |
| 11 | 1985/01/05 | 1985/01/12 | 8 | 27 | 2009/02/15 | 2009/02/23 | 9 |
| 12 | 1985/02/20 | 1985/02/28 | 9 | 28 | 2010/02/02 | 2010/02/06 | 5 |
| 13 | 1986/01/28 | 1986/02/03 | 7 | 29 | 2011/01/07 | 2011/01/11 | 5 |
| 14 | 1988/01/22 | 1988/01/31 | 10 | 30 | 2012/01/17 | 2012/01/29 | 13 |
| 15 | 1990/02/15 | 1990/02/21 | 7 | 31 | 2012/12/10 | 2012/12/19 | 10 |
| 16 | 1995/01/17 | 1995/01/22 | 6 | 32 | 2016/02/10 | 2016/02/14 | 5 |

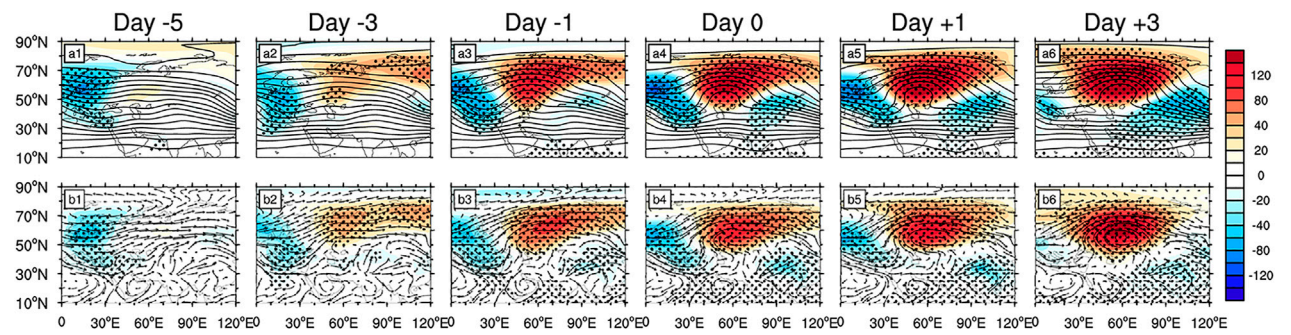


**FIGURE 1 |** Composited geopotential height (contours; units: gpm), its anomalies (shading; units: gpm) and horizontal wind (vectors; reference vector is 5 m $s^{-1}$) on **(A1-A6)** 500-hPa and **(B1-B6)** 850-hPa pressure levels. The values over the dotted regions are statistically significant at the 90% confidence level according to Student's *t*-test.

parts classify these blocking events into three types of events: short (5–6 days), medium (7–9 days) and long (≥10 days) lifetime events. These events are sorted by their onset dates. 3, 4, 6, 8, 16, 17, 19, 21, 23, 25, 26, 28, 29 and 32 are sorted as short events, 1, 5, 9, 11, 12, 13, 15, 18, 20, 22 and 27 as medium events and 2, 7, 10, 14, 24, 30 and 31 as long events. The Ural region in this study is outlined as the region between 40°E-80°E. In the following parts, the characteristics of the transient eddies during different lifetime blocking events are analyzed according to the composited results of transient eddy momentum flux and heat transport.

## 5 CHARACTERISTIC ANALYSIS OF TRANSIENT EDDY MOMENTUM TRANSPORT

The onset of blocking high is often accompanied by the abrupt collapse of westerly. The westerly jet could split into the northern and southern branches. Strong transient transport is associated with strong jet stream (Hoskin and Ambrizzi 1993; Ren et al., 2011). Therefore, the characteristics of upper-level jet stream during the blocking events are also analyzed, with positive $[u'v']$ denoting the northward eddy momentum flux.

Firstly, the westerly jet stream and transient eddy momentum transport from Day -3 to Day +3 of the short UB events are shown in **Figure 2** (a1-a7). From **Figure 2**, it can be found that during the blocking events westerly splits into two branches, i.e., sub-tropic and polar jets, south and north of the Ural blocking, respectively. Before the onset of UB, both the two jet streams are relatively weak, with the positive $[u'v']$ dominating the mid-upper troposphere between 40°N-60°N (**Figures 3**a1,a2), indicating the poleward transport of eddy momentum flux by transient eddies. On Day -3, the positive $[u'v']$, up to 70 $m^2$ $s^{-2}$, centers around 65°N, 300 hPa, while there is weak negative $[u'v']$ north of 80°N, forming the convergence of eddy momentum flux around 80°N. Two days after, the westerly jet stream splits up and the polar jet is shifted northward to 70°N, forming the strong westerly belt between 50°N-70°N. The positive center of $[u'v']$ is strengthened and the convergence center is shifted equatorward to 75°N. The convergence of eddy momentum flux and the decelerated

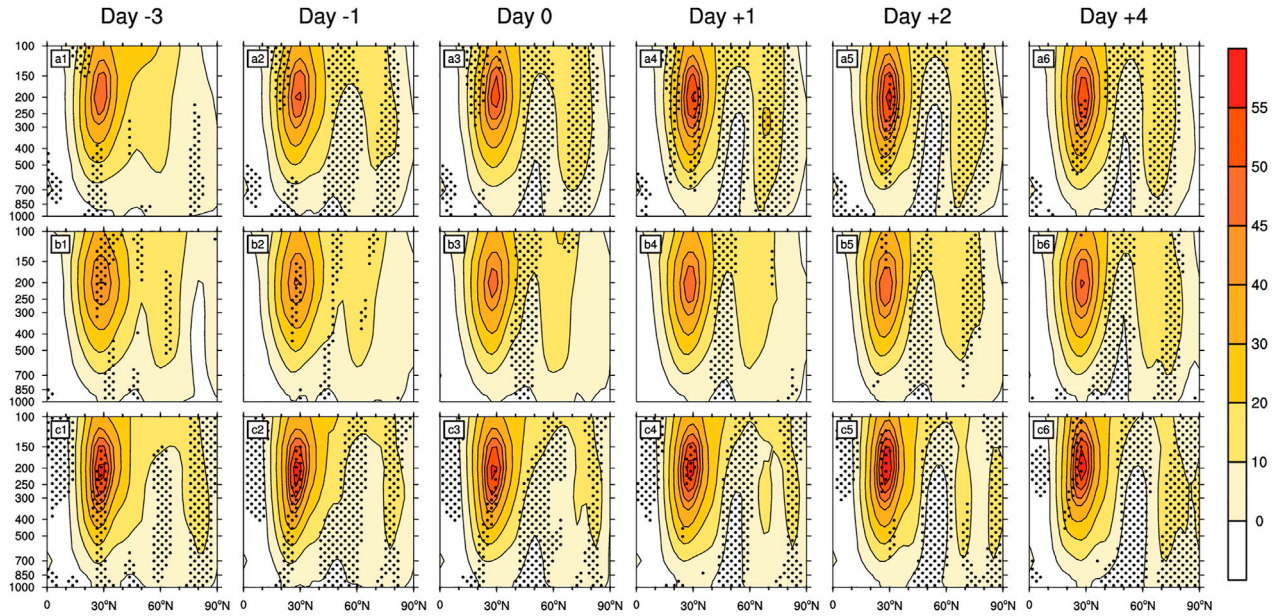


**FIGURE 2 |** Latitude-height cross-section of composited zonal wind (units: m $s^{-1}$) during **(A1-A6)** short **(B1-B6)** medium and **(C1-C6)** long lifetime Ural blocking events. The values over the dotted regions are statistically significant at the 90% confidence level according to Student's *t*-test.

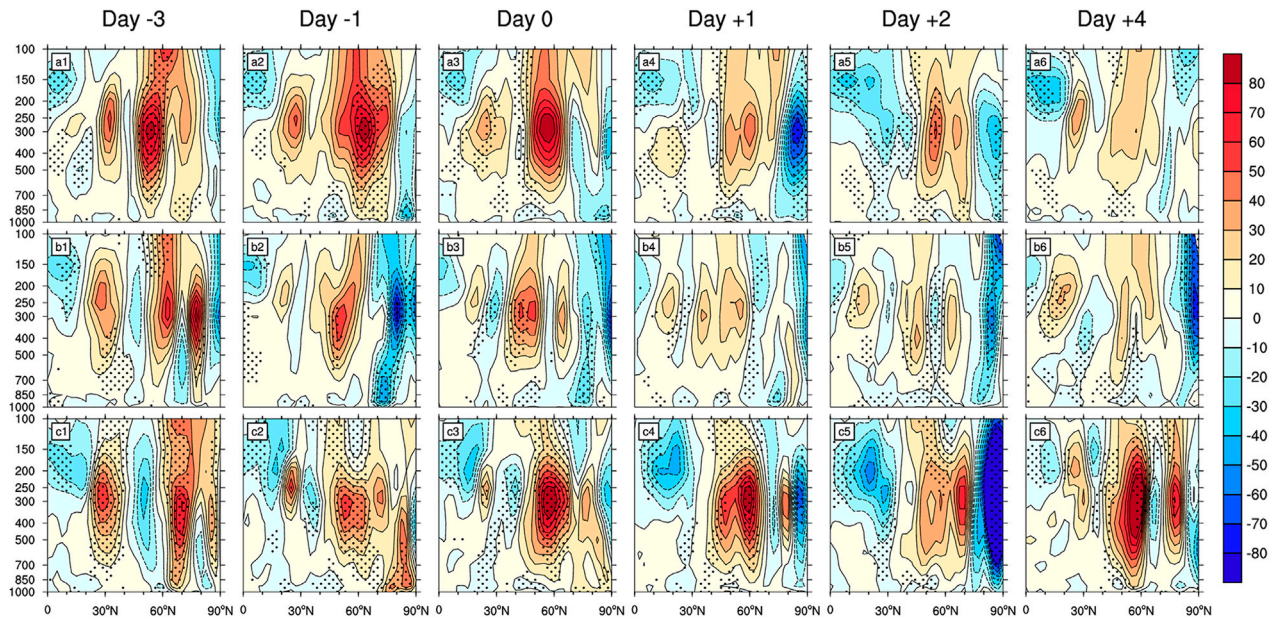


**FIGURE 3 |** Latitude-height cross-section of composited northward eddy momentum flux (units: $m^{-2}{\cdot}s^{-2}$) during **(A1-A6)** short **(B1-B6)** medium and **(C1-C6)** long lifetime Ural blocking events. The values over the dotted regions are statistically significant at the 90% confidence level according to Student's *t*-test.

westerly are favorable for the establishment of the blocking high (Xu and Jin 2011; Li et al., 2019). On Day 0, the sub-tropic jet stream is accelerated, with its maximum up to 55 m $s^{-1}$ around 30°N, 200 hPa. The convergence center of eddy momentum flux is shifted to 70°N, maintaining the UB. One day after, the two jet streams are continuously strengthened, reaching their maximum. The negative $[u'v']$ also reaches its maximum and then $[u'v']$ is weakened, along with the weakening and poleward shift of eddy momentum convergence. On Day +4, both the two jet streams are significantly decelerated. The transport of eddy momentum grows weaker over the blocking region and the blocking high tends to collapse.

Then, the westerly jet stream and transient eddy momentum transport from Day -3 to Day +3 of the medium lifetime UB

events are also shown **Figure 2** (b1-b7). Similar to the short events, the westerly in the medium events also splits into the northern and southern branches. On Day -3, the sub-tropic jet is located around 30°N, 200 hPa, up to 45 m $s^{-1}$, while the polar jet is located between 50°N-70°N. [*u'v'*] is positive (negative) south (north) of 65°N (**Figure 3**b1). Then [*u'v'*] is continuously strengthened. On Day -1, the positive [*u'v'*] centers around 50°N, 400 hPa, up to 70 $m^2$ $s^{-2}$, while the negative [*u'v'*] dominates the whole troposphere over the high latitudes, with the convergence centering around 60°N. On Day 0, both the two jet streams are enhanced, with the polar jet core located over the upper troposphere at 60°N. The transient eddy momentum transport is slightly weakened, but still converges around 60°N, favorable for the maintenance of UB. After that, the sub-tropic jet stream is continuously accelerated, while the polar jet is strengthened and shifted northward. On Day +2 [*u'v'*] over the high latitudes is greatly reduced, with its center descending to 500 hPa. The convergence center of eddy momentum fluxes is also weakened and shifted southward to around 50°N. The northward eddy momentum flux over the middle latitudes is also greatly weakened, with its center descending to 500 hPa. The convergence center at 70°N appears again and is strengthened 2 days after.

The results of the long lifetime UB events are also shown in **Figure 2** (c1-c7). The westerly still splits into two branches and the sub-tropic jet is stronger, which is up to 55 m $s^{-1}$. Polar jet stream is located north of 75°N, indicating the strong development of the Ural ridge. On Day -3, the westerly already splits up. The northward transport of eddy momentum converges in the lower troposphere around 75°N. Then, the negative [*u'v'*] is weakened. On Day -1, the westerly jet between 55°N-75°N is decelerated and the transient eddies around 55°N transport energy for the blocking high. After the onset of the blocking high, the westerly over the blocking region is continuously weakened and the sub-tropic jet is significantly strengthened. On Day +1, the positive [*u'v'*] at 55°N is up to 80 $m^2$ $s^{-2}$. The eddy momentum fluxes converge around 65°N and are strengthened continuously, weakening after Day +7 (not shown), which is favorable for the long-time maintenance of the blocking high.

## 6 CHARACTERISTIC ANALYSIS OF TRANSIENT EDDY HEAT TRANSPORT

The synoptic-scale transient eddies are closely linked to the growth of atmospheric baroclinicity in the lower troposphere. The transient eddies are due to the instability of temporal mean flow, which is mainly produced in the strong baroclinic region and moves towards the weak baroclinic region. The outlet of the jet stream (weak baroclinicity) is where the blocking high happens (Diao et al., 2004). Transient eddies usually propagate along the gradient and play an important role in the development of the mid-latitude baroclinic systems and establishment of blocking high. Similar to the eddy momentum transport, the positive/negative [*v'T'*] denotes the poleward/equatorward transport of eddy heat flux.

**Figure 4** (a1-a7) and **Figure 5** (a1-a7) shows the latitude-height cross-section of the temperature disturbance and [*v'T'*] during the short lifetime UB events. During the short UB events, the temperature disturbance anomalies are mainly distributed over the middle and high latitudes and there is an "upper cold, lower warm" pattern vertically over the high latitudes, with the transition layer around 300 hPa. The low latitudes are dominated by relatively weak warm anomalies. On Day -3, significant negative temperature anomalies, upper to −4 K, appear in the upper troposphere over the high latitudes, while the positive anomalies mainly exist in the lower troposphere between 1,000–700 hPa. There are northward eddy heat fluxes transported by transient eddies in the lower troposphere over the mid-high latitudes, whereas in the upper troposphere between 70°N-80°N exists weak southward transport of eddy heat flux. 2 days after, the near-surface positive temperature anomalies are enhanced and extend upward to 400 hPa. Then, the temperature anomalies in the upper troposphere are reduced drastically, leading to the weakening of the vertical temperature gradient over the blocking region and growth of atmospheric baroclinicity (Hu et al., 2018). Consequently, the transient eddies transport eddy heat flux along the temperature gradient. [*v'T'*] is significantly strengthened and there is weak convergence of eddy heat flux on 300 hPa around 50°N. The transient eddies in the lower troposphere at 50°N transport eddy heat fluxes northward and provide energy for the establishment of the blocking high. On Day 0, there is northward transport of eddy heat flux over the blocking region and the convergence region is located in the upper troposphere around 70°N, transporting heat fluxes to the lower troposphere. The positive temperature anomalies over the high latitudes reach the maximum 1 day after, when the atmospheric baroclinicity also reaches its maximum. There is northward eddy heat flux transport throughout the whole troposphere and the heat transport in the convergence zone is favorable for the establishment of blocking high. On Day +4 [*T'*] throughout troposphere are weakened a lot and the southward transport of eddy heat flux by the transient eddies is reduced and diminished, leading to the weakening and collapse of blocking high.

The transient eddy heat flux transport during medium lifetime UB events is shown in **Figure 5** (b1-b7). During these events, positive [*T'*] appears in the lower latitudes and shows little changes, which has negligible impact on the blocking events and therefore will not be discussed in the following parts of this study. There still exists an "upper cold, lower warm" vertical pattern over the mid-high latitudes. However, the positive [*T'*] is relatively weak and the negative [*T'*] in the upper troposphere also appears very late. On Day -3, the positive center of [*T'*] is located south of 60°N in the lower troposphere and is also relatively weak. There is large-scale transient eddy heat transport over the mid-high latitudes. There is northward/southward transport of eddy heat flux south/north of 60°N in the mid-lower troposphere, indicating the convergence of eddy heat fluxes. 2 days after, the lower-level positive [*T'*] is strengthened and the atmospheric baroclinicity gradually grows stronger. The convergence center is also shifted northward to 60°N and negative [*T'*] in the lower troposphere

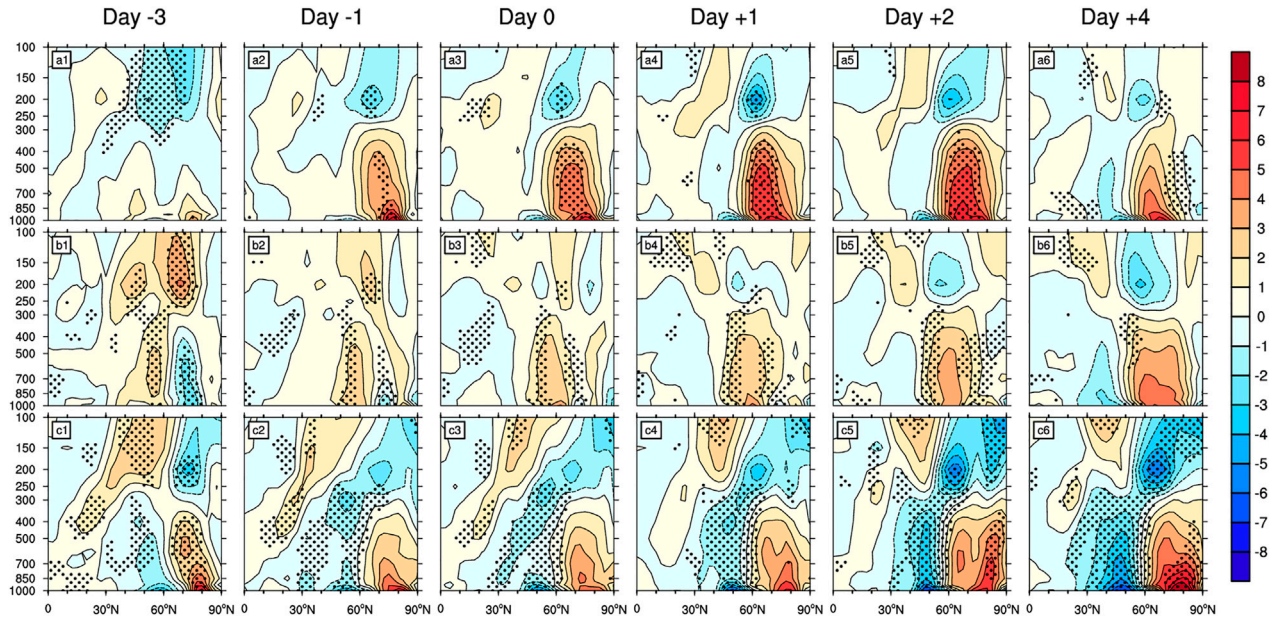


**FIGURE 4 |** Latitude-height cross-section of temperature pertubation (units: K) during **(A1-A6)** short **(B1-B6)** medium and **(C1-C6)** long lifetime Ural blocking events. The values over the dotted regions are statistically significant at the 90% confidence level according to Student's *t*-test.

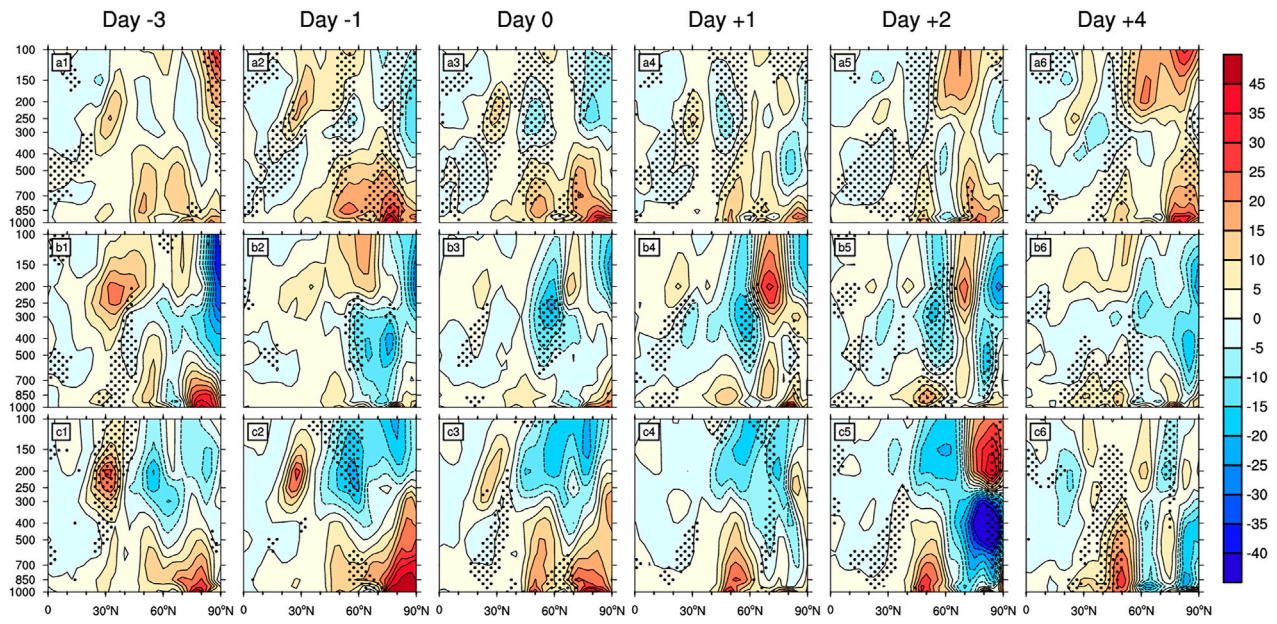


**FIGURE 5 |** Latitude-height cross-section of composited northward eddy heat flux (units: K m·s$^{-2}$) during **(A1-A6)** short **(B1-B6)** medium and **(C1-C6)** long lifetime Ural blocking events. The values over the dotted regions are statistically significant at the 90% confidence level according to Student's *t*-test.

reaches its maximum, with its center descending to 500 hPa. The strong heat transport over the convergence zone provides energy for the establishment of blocking high. After the onset of the blocking events, the "upper cold, lower warm" pattern over the high latitudes is more significant and the extent and intensity of [$T$'] are also strengthened, weakening the temperature gradient in the lower level. According to the thermal wind balance, the thermal wind is weakened and the mid-latitude westerly is decelerated, which is favorable for the enhancement of heat transport and establishment of blocking high. On Day +4 [$v'T'$] in the mid-lower troposphere is weakened, leading to the decay and collapse of the blocking high.

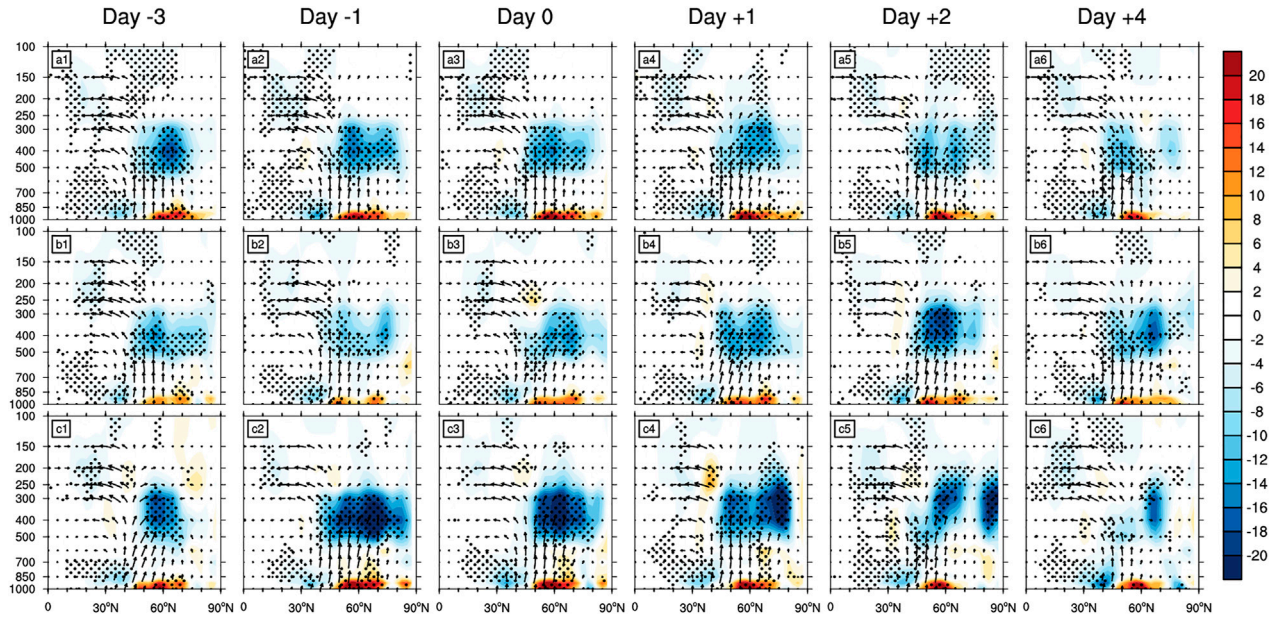


**FIGURE 6 |** Latitude-height cross-section of composited E-P flux (vectors; scaled by square root of air pressure; the vertical and meridional components are scaled by $10^4$ and $10^6$, respectively; units: m·s$^{-2}$; the reference vector denotes 10 m s$^{-2}$) and its divergence (shading; units: s$^{-2}$) during **(A1-A6)** short **(B1-B6)** medium and **(C1-C6)** long lifetime Ural blocking events. The values over the dotted regions are statistically significant at the 90% confidence level according to Student's t-test.

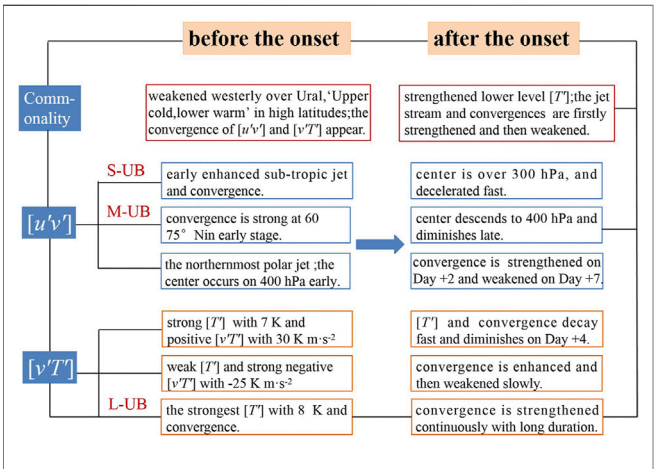


**FIGURE 7 |** Comparison results of transient eddy characteristics among different lifetime UB events. SUB, MUB and LUB denote short, medium and long lifetime UB events.

**Figure 4** (c1-c7) and **Figure 5** (c1-c7) show the latitude-height cross-section of the temperature disturbance and the transient eddy heat flux during the long lifetime UB events. Different from the short and medium blocking events, [$T'$] is significant throughout the whole life cycle of the blocking events. There is an "upper warm, lower cold" pattern over the middle latitudes, contrast to that over the high latitudes. The negative [$T'$] throughout the whole troposphere implies that the high-pressure ridge during the blocking events induces the southward intrusion of polar cold air mass and strengthens the surface cold high pressure center, which is favorable for cold extremes. On Day -3, the eddy heat flux converges around 60°N in the mid-lower troposphere. After that [$T'$] over the high latitudes is further enhanced and the meridional heat transport splits on 400 hPa, with southward transport in the upper troposphere and northward transport in the lower troposphere, favorable for the establishment of blocking high. After the onset of the blocking events, the lower-tropospheric [$T'$] is significantly enhanced. According to the thermal wind balance, the mid-latitude westerly is decelerated. On Day +2, the transient eddy heat transport in the convergence zone around 65°N is further enhanced, with negative [$v'T'$] up to 50 K m·s$^{-2}$, favorable for the long-time maintenance of blocking high.

## 6 CONCLUSION AND DISCUSSION

In this study, the wintertime UB events are selected according to objective analysis method and these events are further classified into three types according to their lifetime, i.e., short, medium and long lifetime UB events. Based on the analysis of the characteristics of transient eddy momentum and heat transport during UB events with different lifetime, we find the convergence of transient eddy flux plays an important role in the lifetime of UB and the transient eddy shows different characteristics during UB events with different lifetimes. As an important diagnostic, the E-P flux, which takes into account thermal and momentum transport by transient eddies together, can be applied in this study to diagnose the wave activities associated with blocking high and verify the above conclusions.

This study further analyzes the E-P flux and its divergence during the UB events, which are shown in **Figure 6**. The E-P flux

divergence has an important influence on the evolution of basic zonal wind in the upper-level jet stream region, namely wave-mean flow interaction. The acceleration and deceleration of basic zonal flow mainly result from the meridional transportation of eddy momentum flux (Zhang and Ni 1991). It can be found from **Figure 6** that there is obvious E-P flux convergence in the middle troposphere between 50°N-70°N during all the three types of UB, consistent with the above-mentioned results. The westerly could be decelerated, or even turn into easterly, where the E-P flux converges. It can be noted from **Figure 2** that the westerly over the blocking region is significantly decelerated, providing favorable background for the establishment of UB. On Day -3, there already exists obvious E-P flux divergence in the middle troposphere over the blocking region during all these blocking events. However, the convergence in the medium UB events is relatively weak, while the convergence in the long UB events is the strongest. Then, the convergence grows stronger gradually and the westerly over the blocking region is decelerated, favorable for the establishment of the blocking high. The convergence of the E-P flux after the onset of the blocking events is gradually weakened during the short UB events, with only $-8\ s^{-2}$ on Day +4, which could be one of the possible causes of its short life cycle. The E-P flux convergence during the medium UB events is significantly strengthened and can still maintain its strength 2 days after, favorable for the maintenance of blocking high. On Day +1 of the long UB events, the E-P flux convergence reaches $-20\ s^{-2}$, with a northward shifted center and larger extent, indicating the strong development of the Ural ridge. Consistent with the results of transient eddy momentum and heat fluxes, the strong E-P flux divergence persists throughout the whole long blocking events, only showing a weakening trend on Day +4, favorable for the long duration of blocking high.

In general, the E-P flux and transient eddy momentum and heat transport show similar characteristics. Before the onset of UB, westerly splits into two branches, and the lower-level [$T'$] is strengthened in the middle and high latitudes, leading to a weakened westerly over Ural. Meanwhile, the strong convergence of transient eddies and E-P fluxes occur over the Ural region. All of these are favorable for the establishment of UB. After the onset of UB, both two jet streams and the convergence of the transient eddy momentum and heat transport are significantly enhanced, leading to the long-term maintenance of UB. Therefore, our results are consistent with some previous studies, i.e., the weakened westerly and the enhanced convergence of transient eddy are favorable for the establishment of UB (e.g., Xu and Jin 2011; Li et al., 2019).

Further we find the transient eddy shows different characteristics during UB events with different lifetimes. The comparison results are shown in **Figure 7**. Some studies found that the strong baroclinicity of the atmosphere and the enhanced split-jet flow are favorable for the establishment and long maintenance of UB (Luo 2005; Luo and Zhang 2020b). Consistent with these studies, we found that the jet stream, the [T'] and the baroclinicity of the atmosphere during long events are the strongest among all the UB events. Also, we found that the convergence of transient eddies is the strongest during the long UB events. The convergence of transient eddy momentum and heat flux appears early with a strong intensity, further strengthened on Day +2 and weakened on Day +7, favorable for the long-time maintenance of UB. The jet stream and [$T'$] during short UB events are strengthened on Day -1, with a strong convergence of eddy momentum flux, which also decay fast, leading to an early collapse of UB. The convergence of eddy momentum and heat flux during medium UB events appears on Day -3 and further strengthens after the onset of UB. Though weaker than those during long events, the transient eddies can still maintain UB for a long time. In addition, consistent with the result of Kong and Hu (2014) that the strong upward propagation of wave fluxes over the Ural region favors the long-time maintenance and development of UB events, the upward propagating wave activity over Ural during long UB events is also the strongest and most long-lasting in this study.

This study investigated the characteristics of transient eddies during the evolution of wintertime UB events, which is consistent with Athar and Lupo (2010) and Xu and Jin (2011). We also find that strong baroclinicity and strong convergence of transient eddies with long duration are closely linked to the long-time maintenance of UB. However, in this study only the characteristics of transient eddies are investigated around the onset of UB, lacking the discussion on the results during the other stages of UB (growth, mature, and decay). In addition, considering that blocking high is a result of interaction between different large-scale waves (Austin 1980), the possible role of stationary momentum and heat fluxes should also be investigated. Therefore, the dynamical mechanism of the momentum and heat exchange between mean and eddy flow during the blocking events will be further investigated in the future study. Also, different blocking regions will be studied and model results will be used to validate the findings from observation.

## DATA AVAILABILITY STATEMENT

Publicly available datasets were analyzed in this study. This data can be found here: https://psl.noaa.gov/data/gridded/data.ncep.reanalysis.html

## AUTHOR CONTRIBUTIONS

JZ contributed to manuscript original draft. YL provided the conceptualization and manuscript review and editing. ZW and YZ provided the formal analysis, validation and funding acquisition. YL provided the data curation

## FUNDING

This research was supported by the National Key Research & Development (R&D) Program of China (2019YFA0606801), the Natural Science Foundation of China (41975111), the Natural Science Foundation of Gansu Province (20JR5RA120) and Research Project of Lanzhou Institute of Arid Meteorology, China Meteorological Administration (KYS2021SSKY01).

## REFERENCES


Andrews, D. G., and Mcintyre, M. F. (1976). Planetary Waves in Horizontal and Vertical Shear: Asymptotic Theory for Equatorial Waves in Weak Shear. *J. Atmos. Sci.* 33, 2049–2053. doi:10.1175/1520-0469(1976)033<2049:pwihav>2.0.co;2

Athar, H., and Lupo, A. R. (2010). Scale Analysis of Blocking Events from 2002 to 2004: a Case Study of an Unusually Persistent Blocking Event Leading to a Heat Wave in the Gulf of Alaska during August 2004. *Adv. Meteorol.* 12, 185–194. doi:10.1155/2010/610263

Austin, J. F. (1980). The Blocking of Middle Latitude westerly Winds by Planetary Waves. *Q.J R. Met. Soc.* 106, 327–350. doi:10.1002/qj.49710644807

Bueh, C., Fu, X., and Xie, Z. W. (2011). Large-scale Circulation Features Typical of Wintertime Extensive and Persistent Low Temperature Events in china. *Atmos. Oceanic Sci. Lett.* 4, 7. doi:10.1080/16742834

Charney, J. G., and Devore, J. G. (1979). Multiple Flow Equilibria in the Atmosphere and Blocking. *J. Atmos. Sci.* 36, 1205–1216. doi:10.1175/1520-0469(1979)036<1205:mfeita>2.0.co;2

Davini, P., Cagnazzo, C., Gualdi, S., and Navarra, A. (2012). Bidimensional Diagnostics, Variability, and Trends of Northern Hemisphere Blocking. *J. Clim.* 25, 6496–6509. doi:10.1175/JCLI-D-12-00032.1

Diao, Y., Li, J., and Luo, D. (2004). A Dynamic Study of the Interaction between Transient Eddies and Blocking. *Chin. J. Atmos. Sci. (in Chinese).* 28, 24.

Diao, Y., Li, J., and Luo, D. (2006). A New Blocking index and its Application: Blocking Action in the Northern Hemisphere. *J. Clim.* 19, 4819–4839. doi:10.1175/jcli3886.1

Ding, Y., and Johnny, C. L. (2005). The East Asian Summer Monsoon: an Overview. Meteorol. *Atmos. Phys.* 89, 117–142. doi:10.1007/s00703-005-0125-z

Feng, J., Li, J., Liao, H., and Zhu, J. (2019). Simulated Coordinated Impacts of the Previous Autumn North Atlantic Oscillation (NAO) and winter El Niño on winter Aerosol Concentrations over Eastern China. *Atmos. Chem. Phys.* 19, 10787–10800. doi:10.5194/acp-19-10787-2019

Hoskins, B. J., and Ambrizzi, T. (1993). Rossby Wave Propagation on a Realistic Longitudinally Varying Flow. *J. Atmos. Sci.* 50, 1661–1671. doi:10.1175/1520-0469(1993)050<1661:rwpoar>2.0.co;2

Hu, S., Cheng, J., Xu, M., and Chou, J. (2018). Three-pattern Decomposition of Global Atmospheric Circulation: Part II-Dynamical Equations of Horizontal, Meridional and Zonal Circulations. *Clim. Dyn.* 50, 2673–2686. doi:10.1007/s00382-017-3763-1

Huang, R. H., and Zou, H. (1989). Interaction between Upward Propagating Planetary Waves and Zonal Mean Flow in a Spherical Baroclinic Atmosphere. *Chin. J. Atmos. Sci. (in Chinese)* 392, 1006–9895. doi:10.3878/j.issn

Jin, R. H., Li, Y., and Wang, S., 2009. Comparison and Analysis Among Four Objective and Quantificational Blocking Indexes. *Plateau Meteorology*.28, 5.

Kong, W., and Hu, Y. (2014). Influence of Stratospheric Nam Anomalies on the Ural Blocking High. *Acta Scientiarum Naturalium Universitatis Pekinensis. (in Chinese)* 50, 445–455. doi:10.13209/j.0479-8023.2014.082

Li, Y., Lu, Y., and Wang, C. (2020). Characteristics of thermal and Momentum Transport during the Lifetime of Ural Blocking Highs. *Int. J. Climatol.* 40, 77–93. doi:10.1002/joc.6195

Li, Y., Zhang, J., Lu, Y., Zhu, J., and Feng, J. (2019). Characteristics of Transient Eddy Fluxes during Blocking Highs Associated with Two Cold Events in China. *Atmosphere* 10, 235. doi:10.3390/atmos10050235

Luo, D. (2003). A Barotropic Envelope Rossby Soliton Model for Block Eddy Interaction. Part I: Effect of Topography. *J. Atmos. Sci.* 62, 3839–3859. doi:10.1175/JAS3573.1

Luo, D. (2005). Why Is the north atlantic Block More Frequent and Long-Lived during the Negative NAO Phase. *Geophys. Res. Lett.* 32, 20804. doi:10.1029/2005GL022927

Luo, D., Cha, J., Zhong, L., and Dai, A. (2014). A Nonlinear Multiscale Interaction Model for Atmospheric Blocking: The Eddy-Blocking Matching Mechanism. *Q.J.R. Meteorol. Soc.* 140, 1785–1808. doi:10.1002/qj.2337

Luo, D., and Chen, Z. (2005). The Role of Land–Sea Topography in Blocking Formation in a Block–Eddy Interaction Model. *J. Atmos. Sci.* 63, 3056–3065. doi:10.1175/JAS3774.1

Luo, D., Xiao, Y., Diao, Y., Dai, A., Franzke, C. L. E., and Simmonds, I. (2016b). Impact of Ural Blocking on winter Warm Arctic-Cold Eurasian Anomalies. Part II: the Link to the north atlantic Oscillation. *J. Clim.* 29, 3949–3971. doi:10.1175/jcli-d-15-0612.1

Luo, D., Xiao, Y., Yao, Y., Dai, A., Simmonds, I., and Franzke, C. L. E. (2016a). Impact of Ural Blocking on winter Warm Arctic-Cold Eurasian Anomalies. Part I: Blocking-Induced Amplification. *J. Clim.* 29, 3925–3947. doi:10.1175/JCLI-D-15-0611.1

Luo, D., and Zhang, W. (2020b). A Nonlinear Multiscale Theory of Atmospheric Blocking: Dynamical and Thermodynamic Effects of Meridional Potential Vorticity Gradient. *J. Atmos. Sci.* 77. doi:10.1175/JAS-D-20-0004.1

Luo, D., and Zhang, W. (2020). A Nonlinear Multiscale Theory of Atmospheric Blocking: Eastward and Upward Propagation and Energy Dispersion of Tropospheric Blocking Wave Packets. *J. Atmos. Sci.* 77, 4025–4049. doi:10.1175/JAS-D-20-0153.1

Luo, D., Zhang, W., Zhong, L., and Dai, A. (2019). A Nonlinear Theory of Atmospheric Blocking: A Potential Vorticity Gradient View. *J. Atmos. Sci.* 76, 2399–2427. doi:10.1175/jas-d-18-0324.1

Lupo, A. R., and Smith, P. J. (1995). Climatological Features of Blocking Anticyclones in the Northern Hemisphere. *Tellus A.* 47, 439–456. doi:10.1034/j.1600-0870.1995.t01-3-00004.x

Ma, J., and San Liang, X. (2017). Multiscale Dynamical Processes Underlying the Wintertime atlantic Blockings. *J. Atmos. Sci.* 74, 3815–3831. doi:10.1175/jas-d-16-0295.1

Masato, G., Hoskins, B. J., and Woollings, T. (2013). Wave-breaking Characteristics of Northern Hemisphere winter Blocking: A Two-Dimensional Approach. *J. Clim.* 26, 4535–4549. doi:10.1175/jcli-d-12-00240.1

Mokhov, I. I., Akperov, M. G., Prokofyeva, M. A., Timazhev, A. V., Lupo, A. R., and Le TreutLe, H. (2013). Blockings in the Northern Hemisphere and Euro-atlantic Region: Estimates of Changes from Reanalysis Data and Model Simulations. *Dokl. Earth Sc.* 449, 430–433. doi:10.1134/s1028334x13040144

Nakamura, H., Nakamura, M., and Anderson, J. L. (1997). The Role of High- and Low-Frequency Dynamics in Blocking Formation. *Mon. Wea. Rev.* 125, 2074–2093. doi:10.1175/1520-0493(1997)125<2074:trohal>2.0.co;2

Qian, W., and Jiang, M. (2014). Early Signals of Synoptic-Scale Atmospheric Anomalies Associated with the Summer Low Temperature Events in Northeast china. *Meteorol. Atmos. Phys.* 124, 33–46. doi:10.1007/s00703-013-0306-0

Ren, X., Yang, X., Zhou, T., and Fang, J. (2011). Diagnostic Comparison of Wintertime East Asian Subtropical Jet and Polar-Front Jet: Large-Scale Characteristics and Transient Eddy Activities. *Acta Meteorol. Sin.* 25, 21–33. doi:10.1007/s13351-011-0002-2

Shi, N., and Nakamura, H. (2020). A New Detection Scheme of Wave-Breaking Events with Blocking Flow Configurations. *J. Clim.* 34, 1–55. doi:10.1175/JCLI-D-20-0037.1

Shi, N., and Wang, Y. (2021). SuolangtajieEnergetics of Boreal Wintertime Blocking Highs Around Ural Mountains. *J. Meteorol. Res.* 36, 1–21. doi:10.1007/s13351-022-1069-7

Takaya, K., and Nakamura, H. (2005). Mechanisms of Intraseasonal Amplification of the Cold Siberian High. *J. Atmos.* 62, 4423–4440. doi:10.1175/jas3629.1

Tibaldi, S., and Molteni, F. (1990). On the Operational Predictability of Blocking. *Tellus A* 42, 343–365. doi:10.1034/j.1600-0870.1990.t01-2-00003.x

Wan, H., and Luo, D. (2009). The Relationship between Wintertime Blockings in the north Hemisphere and north atlantic Oscillation. *J. Trop. Meteorol. (in Chinese)* 25, 61560084–61566204. doi:10.1016/S1003-6326(09)

Xu, H., and Jin, R. H. (2011). Analysis on the Effect of the Transient Eddy on Ural Blocking High in 2008. *Plateau. Meteorol. (in Chinese)* 45, 286–298. doi:10.1111/j.1469-8986.2007.00615.x

Yao, Y., Luo, D., Dai, A., and Simmonds, I. (2017). Increased Quasi Stationarity and Persistence of winter Ural Blocking and Eurasian Extreme Cold Events in Response to Arctic Warming. Part I: Insights from Observational Analyses. *J. Clim.* 30, 3549–3568. doi:10.1175/jcli-d-16-0261.1

Ye, P., Li, Y., Wang, S., Wang, X., and Shang, K. (2015). Variation Characteristics of Different Atmospheric Blocking and its Influence on Temperature over

Northern Hemisphere. *J. Lanzhou Univ. (Natural Sciences) (in Chinese)* 51, 639–645. doi:10.13885/j.issn.0455-2059.2015.05.008

Yeh, C. T. (2010). On Energy Dispersion in the Atmosphere. *J. Atmos. Sci.* 6, 1–16. doi:10.1175/1520-0469(1949)006<0001:OEDITA>2.0.CO;2

Zhang, P., and Ni, Y. Q. (1991). The Effect of Topographic Forcing on the Formation and Maintenance of Blocking. *Adv. Atmos. Sci.* 8, 317–326. doi:10.1007/BF02919614

Zhu, Q., Lin, J., Shou, S., and Tang, D. (2007). Synoptic Principles and Methods. China Meteorological Press (In Chinese). 186–187.

**Conflict of Interest:** The authors declare that the research was conducted in the absence of any commercial or financial relationships that could be construed as a potential conflict of interest.

**Publisher's Note:** All claims expressed in this article are solely those of the authors and do not necessarily represent those of their affiliated organizations, or those of the publisher, the editors, and the reviewers. Any product that may be evaluated in this article, or claim that may be made by its manufacturer, is not guaranteed or endorsed by the publisher.

frontiers | Frontiers in Environmental Science

ORIGINAL RESEARCH
published: 01 July 2022
doi: 10.3389/fenvs.2022.929309

# Impact of Forest Canopy Closure on Snow Processes in the Changbai Mountains, Northeast China

*Yuan Gao[1,2], Lidu Shen[1]*, Rongrong Cai[1], Anzhi Wang[1], Fenghui Yuan[1,3], Jiabing Wu[1], Dexin Guan[1] and Huaxia Yao[4]*

[1]CAS Key Laboratory of Forest Ecology and Management, Institute of Applied Ecology, Chinese Academy of Sciences, Shenyang, China, [2]College of Resources and Environment, University of Chinese Academy of Sciences, Beijing, China, [3]Department of Soil, Water, and Climate, University of Minnesota, Saint Paul, MN, United States, [4]Department of Geography, Nipissing University, North Bay, ON, Canada

Forest canopy closure affects snow processes by changing the redistribution of snowfall, snow interception, accumulation, sublimation, and melt. However, how the forest closure impacts snow processes at different periods has not been well explored. We conducted 3-year measurements of snow density and depth and carried out snow process calculations (i.e., interception, sublimation, and snowmelt) from 2018 to 2021 in four mixed forests with different canopy closures and an open site in the Changbai Mountains, northeast China. We found that the snow density of the five study sites varied greatly (0.14–0.45 g/cm$^3$). The snow depth (*SD*) at four mixed forests sites was smaller than that of the nearby open site. The *SD* decreased as the forest canopy closure increased. Additionally, the forest interception effect increased with the canopy closure and decreased as the snowfall intensity increased. The total interception efficiency of the four mixed forests in normal snow years changed from 34% to 73% and increased with forest canopy closure. The averaged sublimation rate ($S_s$) and snowmelt rate ($S_r$) of the four mixed forests varied during different periods of snow process. The $S_s$ was 0.1–0.4 mm/day during the accumulation period and 0.2–1.0 mm/day during the ablation period, and the $S_r$ was 1.5–10.5 mm/day during the ablation period. There was a good correlation between $S_s$, or $S_r$, and canopy closure, but interannual variation was observed in the correlation. The mean values of the effect of the four mixed forests on understory SWE (snow water equivalent) over the 3 years ranged from –45% to –65%. Moreover, the impact effect was correlated with the forest canopy closure and enhanced with the canopy closure. This study provided more scientific information for studies of snow cover response to forest management.

**Keywords: forest canopy closure, forest snow, interception, sublimation, snowmelt**

OPEN ACCESS

***Edited by:***
*Bo Huang,*
*Norwegian University of Science and Technology, Norway*

***Reviewed by:***
*Weibin Li,*
*Lanzhou University, China*
*Meng Yang,*
*Nanjing University of Information Science and Technology, China*

****Correspondence:***
*Lidu Shen*
*shenlidu@iae.ac.cn*

***Specialty section:***
*This article was submitted to Interdisciplinary Climate Studies, a section of the journal Frontiers in Environmental Science*

***Received:*** *26 April 2022*
***Accepted:*** *20 May 2022*
***Published:*** *01 July 2022*

***Citation:***
*Gao Y, Shen L, Cai R, Wang A, Yuan F, Wu J, Guan D and Yao H (2022) Impact of Forest Canopy Closure on Snow Processes in the Changbai Mountains, Northeast China. Front. Environ. Sci. 10:929309. doi: 10.3389/fenvs.2022.929309*

## 1 INTRODUCTION

Snow cover and its changes are important as they alter the soil temperature and soil water content in forestland (Chang et al., 2014; Maurer and Bowling, 2014; Lyu and Zhuang, 2018), and they also impact the climate feedback in forestland (Henderson et al., 2018; Krinner et al., 2018). Forest cover, annual snowfall, elevation, winter temperature, and snowfall form are the main factors affecting forest snow (Lopez-Moreno and Stahli, 2008; Lundquist et al., 2013; O'Gorman, 2014). A previous

review study of 65 sites by Varhola et al. (2010) showed that forest cover was the most important factor affecting the forest snow process and that forest cover changes could explain 57%–72% of the relevant variation in the forest snow process. This is mainly because the forest canopy changes the amount and spatial distribution of snow on the ground through canopy interception at the local scale. In the meantime, the canopy structure altered the amount of the long-wave and short-wave radiation input to the understory snow surface, which in turn affected the snow surface energy balance and ultimately controlled the forest snow accumulation and ablation process (Ellis et al., 2010; Musselman et al., 2012; Roth and Nolin, 2017). Thus, the snow processes in the understory would be altered synchronously with changes in forest structure. Many studies have reported the effect mechanisms of forest structure changes on snow processes, such as deforestation (Schelker et al., 2013; Revuelto et al., 2016; Krogh et al., 2020), fire disturbance (Maxwell et al., 2019; Schwartz et al., 2020), insect pests (Pugh and Gordon, 2013; Perrot et al., 2014), and avalanche disturbances (Bebi et al., 2009; Casteller et al., 2018). Although the study of the mechanistic processes of forest snow is the key to reveal the relationship between forest structural changes and the response of snow processes, there are still many limitations in the application and extension of the results of previous studies to other regions, such as northeastern China. First, forest snow processes are localized and strongly dependent on forest structure characteristics, and there are obvious regional differences in the two elements affecting forest structure (regional climate and forest disturbance patterns). Second, the multiple forest structure parameters (e.g., LAI, forest cover, and canopy cover) and abundant research methods (e.g., modeling method, remote sensing method, and snow survey method) also make the research results low comparability with each other. Again, due to fewer studied cases in northeastern China, there is a lack of comprehensive understanding of the variation of forest snow sub-processes (interception, sublimation, and ablation) in different periods and years in this region. Thus, these constrained our understanding of snow processes in the widely distributed mixed forests in northeastern China and also limited the follow-up studies on the simulation and prediction of the effects of different climate change scenarios and different forest management methods on snow processes in the future.

The influence of forest structure on snow processes is basically a small-scale interaction process, and the interaction between forest and snow is strongly dependent on the factors such as forest structural characteristics, climate type, altitude factors, and the atmospheric conditions of winter. Some studies have also quantified the effects of forests on snow processes using the open area and forest normalized contrast method (Veatch et al., 2009; Varhola et al., 2010; Broxton et al., 2015). However, most of these studies were conducted in Europe and North America and in other forest regions with large amounts of snowfall (i.e., SnowMIP2 sites). There are few studies on the impact of a mixed forest structure on snow cover in northeast China. In particular, the widespread natural mixed forests in this region have experienced cutting at multiple intensities of 20%, 40%, 80% and 100% since the 1980s, and forest structure elements, such as canopy closure, have changed greatly, which also caused complex changes in the forest snow processes. It is difficult to directly use the findings from previous studies regarding the effects of snow processes on changes under the forest closure gradient to reveal the interaction process and mechanism between forest and snow in northeast China. How the changes in the canopy closure affected forest snow regime in this region is still unclear.

Changes in forest structure and their impacts on snow processes are complicated. A selection of appropriate forest structure indicators to quantify the impact is particularly critical, but the diversity of indicators and methods has instead limited research expansion. A variety of forest structure indicators have been used to reveal the impact of forests on snow processes, such as forest cover (Varhola et al., 2010; Pomeroy et al., 2012; Varhola and Coops, 2013), canopy cover (Pomeroy et al., 2002), leaf area index (Gelfan et al., 2004; Woods et al., 2006; Rutter et al., 2009; Lendzioch et al., 2019), and canopy closure (Broxton et al., 2021). In the meantime, as technology continues to progress, various methods have been applied comprehensively, such as forest snow sampling survey (Watson et al., 2006; Parajuli et al., 2020), snow model simulation (Pomeroy et al., 2007; Rutter et al., 2009; Krinner et al., 2018; Napoly et al., 2020), statistical modeling (López-Moreno and Nogués-Bravo, 2006), snow remote sensing (Zhang et al., 2010; Frei et al., 2012; Hojatimalekshah et al., 2021), LiDAR technology (Harpold et al., 2014; Broxton et al., 2021; Russell et al., 2021), UAV remote sensing (Lendzioch et al., 2019), and delayed photography (Parajka et al., 2012; Dong and Menzel, 2017). When studying forest snow process in specific areas, the most appropriate method needs to be selected and balanced, as each method has certain advantages and limitations. Snow surveys need to take into account a variety of heterogeneous landscapes and survey frequency and strategy (Watson et al., 2006), and these factors can result in higher implementation costs. Snow model method has the problems of a coarse resolution and the simplification of the interaction processes between forest and snow (Broxton et al., 2021), restricting the ability of existing models to quantify effects of the forest canopy structure changes on snow processes. For example, Rutter et al. (2009) and Krinner et al. (2018) only focused on the accurate simulation of snow processes in specific forests and in adjacent open areas when conducting SnowMIP2 and ESM-SnowMIP studies. In addition, snow remote sensing products cannot be widely used to complex forest areas because of their high cost and limited snow capture accuracy (Rutter et al., 2009; Steele et al., 2017; Jacobs et al., 2021). Therefore, previous studies on the interaction between forest and snow have some deficiencies in terms of expanding their application to other regions (i.e., northeast China), due to the diversity of forest structure parameters, the different survey strategies and models selected, and the specific climate and forest types in other regions.

In addition, the impact of forests on snow processes varied over different periods and forest cover. An integrative study of 65 sites in North America and Europe by Varhola et al. (2010) showed that forest cover may have both positive and negative impacts on snow processes. One reason for this is that the impact of forests on the snow process is a result of the continuous or

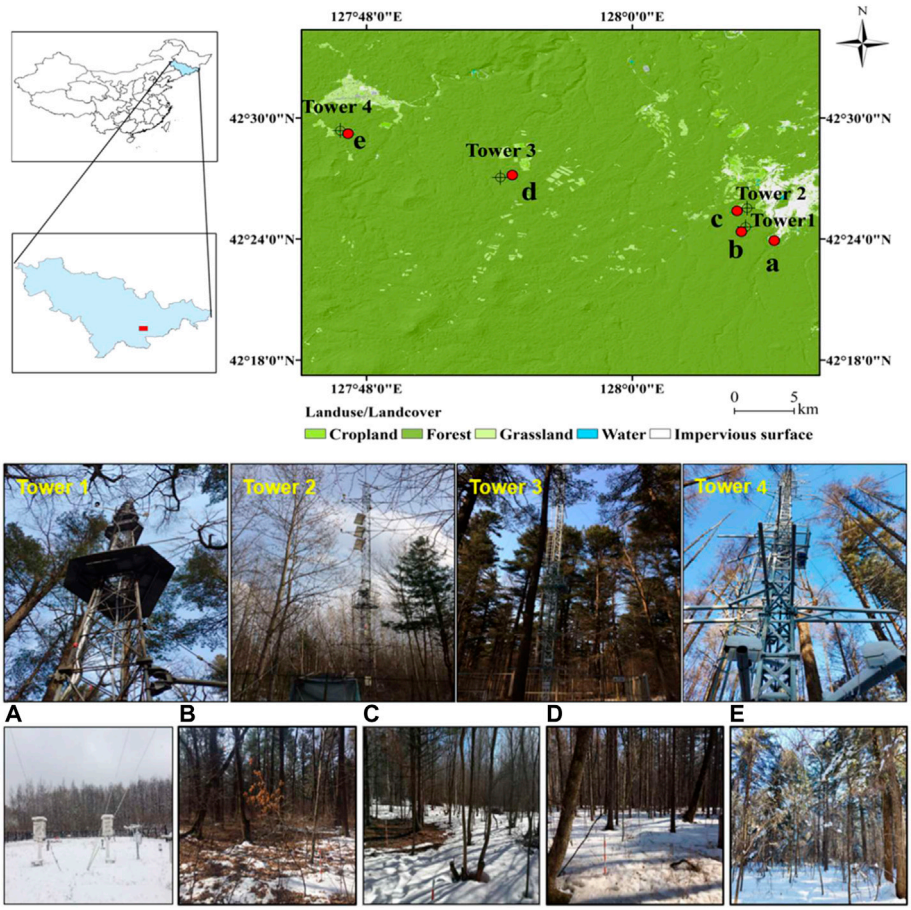


**FIGURE 1 |** The location of the study area (top row), pictures of the open-path eddy covariance (EC) flux system (middle row), and pictures of the plots in the study area in the Changbai Mountains, northeastern China (bottom row). The EC flux system corresponds to the plots one by one: Tower 1-b, Tower 2-c, Tower 3-d, and Tower 4-e. The letters in top and bottom rows correspond to different land types and disturbance intensities: **(A)** the open site (OS); **(B)** the natural mixed forest (NMF); **(C)** the high-intensity cutting mixed forest (HCF); **(D)** the moderate-intensity cutting mixed forest (MCF); and **(E)** the low-intensity cutting mixed forest (LCF).

cumulative impact on multiple sub-processes (snow interception, snow sublimation, snow metamorphism, and snow ablation) after every single snowfall event. Though many previous studies have investigated the sub-processes of forest snow, such as canopy interception (Stähli et al., 2009), snow sublimation (Montesi et al., 2004; Li et al., 2013; Li et al., 2016; Sexstone et al., 2018), and snow ablation (Burles and Boon, 2011), in single forest types, the effects of forest on different sub-processes varied not only in magnitude but also among the periods of the related sub-processes in question, and the total effect was the combined result of continuous multiple snow sub-processes. Few studies have addressed whether there are differences in the effects of forest structure in different periods and years. Likewise, random effects caused by focusing on a single snow sub-process or specific period are inevitable, and it is difficult to reflect the comprehensive impact of forest on the entire snow process. This makes previous studies lack representation on different snow years. Therefore, it is particularly important to comprehensively or quantitatively evaluate the impact of forest structure on snow process throughout the whole snow season. The effects of forest structure or its change on snow process need more in-depth or quantitative investigation.

To reveal this impact effect comprehensively and provide more region-specific information, we conducted a three-year study of the snow processes at four forest sites with different levels of forest canopy closure and at a nearby open site in the Changbai Mountains, northeast China. The snow characteristics (snow density and depth) and snow sub-processes (snow interception, snow sublimation rate, and snowmelt rate) were measured. We selected the forest canopy closure as a forest structure parameter to study the impact of the forest on snow processes and analyzed the relationships of these sub-processes with forest canopy closure. The purpose is to provide the characteristics and distribution regularity of snow properties in the forest area, which is beneficial for developing a forest snow model based on forest closure. The sections of this article are as follows. **Section 2** provides information about the forests in the study area, the investigation methods to determine forest structure and snow cover characteristics, and the calculation methods of snow processes. **Section 3** compares the snow

**TABLE 1** | Detailed information of forest plots.

| Plot type | Elevation (m) | Dominant tree species | Mean forest canopy height (m) | Canopy closure (%) | | |
|---|---|---|---|---|---|---|
| | | | | Mix | Mean | Max |
| OS | 750 | — | — | — | — | — |
| HCF | 755 | *Populus*, *F. mandshurica*, *Ulmus pumila*, *Maackia amurensis* | 15 | 61.3 | 65.3 | 67.7 |
| MCF | 866 | *P. koraiensis*, *F. mandshurica*, *T. amurensis* | 25 | 68.3 | 69.7 | 72.4 |
| NMF | 768 | *P. koraiensis*, *T. amurensis*, *F. mandshurica*, *Q. mongolica* | 27 | 67.1 | 70.2 | 73.6 |
| LCF | 793 | *P. koraiensis*, *T. amurensis*, *F. mandshurica* | 26 | 74 | 77.3 | 78.8 |

forest cover characteristics (i.e., snow density and snow depth) with canopy closure, analyzes the relationship between forest canopy closure and snow sub-processes, and quantifies the impact of each forest on the different snow processes. Finally, a discussion and conclusions are provided in **Sections 4** and **5**, respectively.

# 2 STUDY AREA AND METHODS

## 2.1 Study Area

The study area (42.29°–42.57°N, 127.75°–128.13°W) is located in the Changbai Mountains, northeast China (**Figure 1**). It has a temperate continental climate with an annual average temperature of 3.6°C and annual precipitation of 735 mm (Li et al., 2016). The average temperature for winter is −14°C, and the annual snowfall is about 133 mm, which accounts for 18.2% of the annual precipitation. Forest snow cover generally lasts from November to April. The region has a distribution area of temperate natural coniferous and broad-leaved mixed forest, and this type of mixed forest is typical in northeast China. After decades of different management methods (protection and selective cutting), the natural mixed forests and multi-type forests have been disturbed by human activities. The main tree species in these natural mixed forests are *Pinus koraiensis*, *Tilia amurensis*, *Fraxinus mandshurica*, *Quercus mongolica*, *Acer mono*, and *White birch*. Canopy height varies between 15 and 30 m. The stand density can reach 560 stems/ha (stem diameter > 8 cm), and the maximum leaf area index can be 6.0 (Wu et al., 2012). The soil type is montane dark brown and was developed from volcanic ash (Guan et al., 2006).

Four plots of mixed forests with different cutting intensities were selected (0, 20%, 40%, and 100%), from a similar altitude (750 m), with a low slope and at same slope orientation, and having a forest stand size of 40 m × 40 m. The plots comprised a natural mixed forest (NMF) without cutting, low-intensity cutting mixed forest (LCF, 20%), moderate-intensity cutting mixed forest (MCF, 40%), and high-intensity cutting mixed forest (HCF, 100%) (**Figure 1**). These four forests formed gradually after harvesting the original natural mixed forests using different cutting intensities 30 years ago. A nearby open site (OS) was used as a contrast plot or control to study the effect of forest canopy structure on snow processes. Field conditions and forest information of the five plots are shown in **Figure 1** (bottom row) and **Table 1**.

## 2.2 Field Observations

### 2.2.1 Meteorological Observations

Meteorological data were collected from the open site meteorological station (**Figure 1A**). The main meteorological elements included temperature and humidity (using the HMP45C, Vaisala, Helsinki, Finland), wind speed (A100R, Vector Instruments, Denbighshire, United Kingdom), net radiation (CNR 4, Kipp & Zonen, Delft, the Netherlands), and precipitation (Rain Gauge 52203, Young, Traverse City, MI, United States). Surface snow depth was observed by delayed photography (CC5MPX, Campbell, United States). Each meteorological element was recorded at half-hour intervals. The daily meteorological data were obtained from the conversion of half-hour intervals data.

### 2.2.2 Snow Surveys

Snow surveys were conducted at five study sites (four forested and one open site) from November to April of each year during 2018–2021 (**Figure 2**). Snow survey frequency was once weekly to bi-weekly according to the snowfall in the accumulation period, and the frequency was increased to every 3–5 days depending on the accessibility of mountain roads in the ablation period. The investigation strategy to determine the snow depth at the stand level is shown in **Figure 2A**. Each forest plot (40 m × 40 m) was divided into sub-grids of six rows and six columns, and a snow ruler was placed in each sub-grid (**Figure 2A**), meaning that each plot had a total of 36 snow depth rulers distributed within it. The positions of the snow rulers were further adjusted according to the distribution positions of the tree trunks and forest gaps in each sub-grid so that each ruler could represent the approximate average snow depth value of the sub-grid as accurate as possible. To reduce the disturbance of the forest snow caused by human activities, we used a telescope to observe the snow depth rulers remotely. The snow depth at the five sites was measured by using fixed snow rulers (**Figure 3A**). A red and white alternate ruler was fixed on the ground, and the minimum accuracy was 1 cm, and the maximum value was 80 cm (**Figure 3A**).

The snow density was calculated using the weighing wedge snow density box cutter method (5 cm × 4.54 cm × 4.2 cm, 235.6 g) (**Figure 3B**). This method had been applied in snow surveys and the performance of this device was evaluated by Hao et al. (2021). In the snow field survey, the method was used together with a high rate of accuracy (0.1 g), low-temperature resistance (−40°C to 40°C), and a waterproof electronic scale (**Figure 3C**). Before the snow sample was taken, a vertical snow

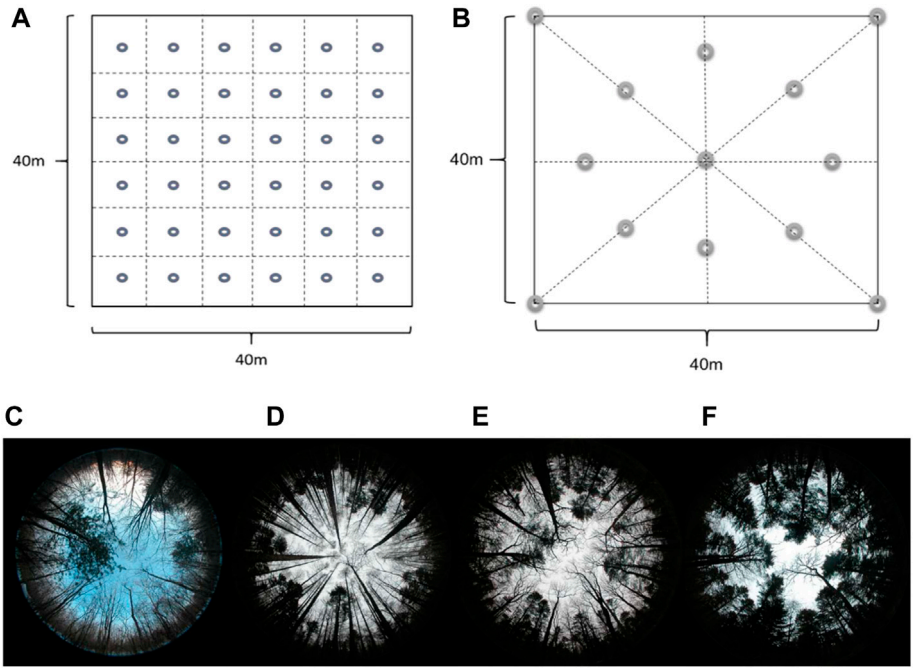


**FIGURE 2 |** Investigation strategy maps of the forest snow depth **(A)**, investigation location of canopy closure at the stand level **(B)**, and forest hemisphere images (bottom row, C, D, E, and F). The circles in **(A)** represent the location of snow rulers, and the circles in **(B)** represent image captures in the forest plot. Four forest hemisphere images (bottom row): **(C)** high-intensity cutting mixed forest (HCF); **(D)** moderate-intensity cutting mixed forest (MCF); **(E)** natural mixed forest (NMF); **(F)** low-intensity cutting mixed forest (LCF).

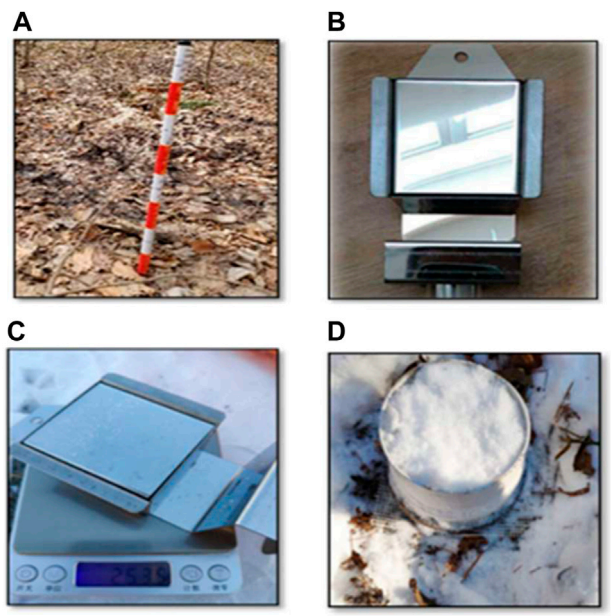


**FIGURE 3 |** Investigation methods to determine snow cover characteristics: **(A)** snow depth ruler, **(B)** rectangular snow box cutter, **(C)** weight to determine the snow mass, and **(D)** snow sublimation rate measurement method.

profile was excavated first, and the profiles were layered at 10 cm intervals. Then, the long end of the density device was inserted into the corresponding layer in the same direction as the vertical snow profile to collect the snow samples. After the snow filled up the inner space of the box, the box was removed, the cover was put on top of it, and it was finally placed on the electronic scale for weighing (**Figure 3C**).

### 2.2.3 Eddy Covariance Measurement of Snow Sublimation

Near each forest plot, there was an open-path eddy covariance (EC) flux system installed on the meteorological tower in each area to take long-term meteorological records (**Figure 1**, Tower 1–4). The EC principle uses the deviation in vertical wind speed and the deviation of water vapor concentration to calculate the water vapor flux (*ET*) as follows:

$$ET = \overline{\rho_d} * \overline{w's'}, \quad (1)$$

where *ET* is the water vapor flux (kg/m$^2$·s), $\rho_d$ is the air density (kg/m$^3$), $w'$ is the vertical wind speed (m/s), and $s'$ is the dry mole fraction of the gas in water (kg/kg). The overbar represents an average value over 30 min.

The water vapor flux was pre-processed using EddPro-7.0.2 software and post-processed using Tovi™ software. A missing threshold of pre-processed raw data was set to 10%, and the

vertical wind speed threshold was set to 3 m/s. After that, we used the double coordinate rotation method proposed by Wilczak et al. (2001) to correct the vertical wind speed and used the Webb-Pearman-Leuning (WPL) correction developed by Webb et al. (1980) to correct the water vapor flux, which was caused by the density effect. Next, we applied the recommended tools from Tovi™ to execute gap-filling (Reichstein et al., 2005), data screening, spectral corrections, and energy balance residual correction (Mauder et al., 2013; Charuchittipan et al., 2014; De Roo et al., 2018). Finally, we converted half-hour data of water flux into day flux.

### 2.2.4 Forest Structure Measurements

The forest structure parameters (i.e., dominant species, tree height, and canopy closure) were measured and collected. We combined the relative height of the tower to obtain the height information of the main forest species and investigated the dominant species in each plot. Detailed information of forest plots was summarized in **Table 1**.

Hemispherical Canopy Photography is an indirect optical technique that has been widely used to determine forest canopy structure. The canopy openness of the forest plots was obtained by hemispherical photography based on the optical imaging principle (device information: EOS 5D + EF, 8–15 mm Fisheye, Canon Inc., Japan). An upward-looking method was used to obtain hemispherical images during the winter period when the canopy structure parameters were stable (**Figure 2**). In each forest plot (40 m × 40 m), a photographing route along the four sides and along the diagonal of the plot was adopted (**Figure 2B**). The photographing positions were placed in this way: four at the four corners of the square forest plot, one at the plot center, and eight around the center stretching out in eight directions, creating a total of 13 images for each plot (**Figure 2B**). The images data were analyzed by using the Gap Light Analyzer (GLA) software and the calculation methods by Frazer et al. (1999). The canopy closure ($\theta$) was calculated using the formula: $\theta$ = 1 - canopy openness.

## 2.3 Calculation Methods

### 2.3.1 Standardizing Snow Depth

The large distance between the four forest plots (25 km) from east to west (**Figure 1**) may lead to spatial variation in snowfall, so we standardized the snow depth. After multiple snow surveys, we found that the snowfall near plots MCF and LCF had slightly higher snow depth than that in the reference site OS. We synchronously observed the snow depth of the open space near the LCF and found that the ratio between them remained approximately stable over a long period of time. Here, we assumed that the temporal changes in the snow cover caused by wind blowing and snow sublimation in two open areas (OS and the open space near LCF) with similar surface environments were mostly equal. Therefore, the ratio coefficient ($\alpha$) for the annual snowfall in the two areas was equal to the snow depth ratio in two open areas.

Snowfall was the most important factor in controlling the forest snow depth. To compare the influence of the forest on snow depth under the conditions of unified snowfall, this coefficient was further used to uniformly adjust the measured snow depths of the MCF and LCF. The correction method is as follows:

$$\alpha = P_1/P_2\,, \tag{2}$$

$$SD = \alpha * SD_{measured}\,, \tag{3}$$

where $P_1$ is the snowfall observed in the OS (**Figure 1A**), $P_2$ is the snowfall in the open area near the MCF and LCF, $SD$ is the adjusted or standardized snow depth, $SD_{measured}$ is the measured snow depth from survey, and $\alpha$ is the adjusting coefficient. According to the regional snowfall data from the two regions over the three-year period (2018–2019, 2019–2020, and 2020–2021), the coefficients $\alpha$ are $\alpha_1$ = 0.65, $\alpha_2$ = 0.63, and $\alpha_3$ = 0.62, for each year, respectively.

### 2.3.2 Calculation of Snow Density and Snow Water Equivalent

Snow density sampling at a sampling point was carried out for each layer of the snow profile and repeated on each layer three times. Finally, the density of snow for a sample was calculated as follows:

$$\rho_i = \frac{m_1 - m_2}{v}, \tag{4}$$

where $\rho_i$ is the density corresponding to a layer (g/cm$^3$), $m_1$ is the total weight of the box (g), $m_2$ is the total mass of the empty box (g), and $v$ is the internal volume (cm$^3$). The average snow density of the snow profile was calculated as follows:

$$\rho = \frac{\rho_1 d_1 + \rho_2 d_2 + \ldots + \rho_i d_i}{d_1 + d_2 + \ldots + d_i}, \tag{5}$$

where $\rho$ is the average density (g/cm$^3$) and $d_i$ is the snow depth of the corresponding layer (cm).

The snow water equivalent ($SWE$) and standard deviation ($\sigma$) at the forest stand scale were calculated as follows:

$$SWE = 10 * \rho * SD\,, \tag{6}$$

$$\sigma = \sqrt{\frac{\sum_{i=1}^{n} (x - \bar{x})^2}{n-1}}, \tag{7}$$

where $SWE$ is the snow water equivalent (mm), $SD$ is the average snow depth at the stand scale obtained by *in situ* snow depth surveys ($n$ = 36 for each plot) (cm), and $\sigma$ is the standard deviation for the survey samples within a plot.

### 2.3.3 Calculation of Canopy Snow Interception Coefficient

The interception coefficient was calculated for individual snowfall event by using variations in the snow depth before and after a single forest snowfall, at the forest site ($\Delta SD_F$) and at the open site ($\Delta SD_O$). They were observed using the time-lapse photography approach, which has been widely applied in forest snow studies (Garvelmann et al., 2012; Parajka et al., 2012; Dong and Menzel, 2017; Dong, 2018). The interception coefficient ($C_{IE}$) of forest canopy was calculated as follows:

$$C_{IE} = \left(\frac{\Delta SD_O - \Delta SD_F}{\Delta SD_O}\right), \quad (8)$$

where $\Delta SD_O$ and $\Delta SD_F$ are the variations in snow depth in the open site and in the forest site for every single snowfall event, and they were measured in the open site (OS) and forest plots at three locations in each plot simultaneously, respectively.

The cumulative value of the forest canopy interception coefficient (*Ic*) over the whole snow season or the winter period was calculated as follows:

$$Ic = \frac{\sum_n^1 (\Delta SD_O^i - \Delta SD_F^i)}{P_{snowfall}}, \quad (9)$$

where *Ic* is the cumulative interception coefficient, $\Delta SD_O^i$-$\Delta SD_F^i$ is the canopy interception of a single snowfall event *i*, the sum is the accumulated interception depth of the entire winter (cm), and $P_{snowfall}$ is the total snow depth (cm).

### 2.3.4 Calculation of Snow Sublimation by the Weighing Measurement Method

The snow sublimation in the open site (OS) was measured by the continuous daily weighing snow evaporator method (**Figure 3D**). Three circular cylindrical tubes that were 20 cm in diameter and made of white PVC plastic material were used as *in situ* snow collection device and placed in the OS site for the duration of the snow season. The height of the cylinder was able to be adjusted according to the depth of the external snow, and the connecting ring was used to increase or reduce the height of the cylinder to avoid snow exchange in the horizontal direction inside and outside of the weighing cylinder, as well as to control the disturbance caused by frequent manual measurements and to ensure the stability of the snow sample in the cylinder. The cylinder was weighed at 08:00, 12:00, and 16:00 each day, and the weight change from 16:00 on the previous day to 16:00 on the current day was measured as the snow sublimation amount of the day. The daily sublimation of snow in the OS was calculated as follows:

$$ET = 10 * \frac{M_1 - M_2 + P}{\rho_w * \pi \left(\frac{D}{2}\right)^2}, \quad (10)$$

where *ET* is the snow sublimation (mm/day); $M_1$ and $M_2$ are the weights of the cylinder for the previous day (16:00) and for the present day (16:00) (g); *P* is the snowfall occurring within the weighing interval, which is measured by other separate empty cylinders for the weighting measurement (g); $\rho_w$ is the liquid density of water (1.0 g/cm$^3$); *D* is the diameter of the snow measuring cylinder (20 cm); and $\pi$ is the circular rate constant (3.14).

### 2.3.5 Calculation of Snowmelt Rate by the Water Balance Method

To evaluate the impact of forests on the items of the snow water balance, we calculated the water balance during the snow melting period as follows:

$$Q_{SWE} = Q_{Snowfall} - Q_{E\uparrow} - Q_S, \quad (11)$$

where $Q_{SWE}$, $Q_{Snowfall}$, $Q_{E\uparrow}$, and $Q_S$ are the variation in the surface snow water equivalent during the melting period, snowfall accumulated on the snow surface, the snow sublimation, and the loss of snow *via* snowmelt which was converted into liquid water, respectively ($Q_{SWE}$ is obtained through snow surveys, and $Q_{Snowfall}$ is snowfall accumulation for each plot during the ablation period. $Q_{Snowfall}$ represents penetrating snow in forests, which is obtained from time-lapse photography of snow depths under the forest and calculated by **Eq. 6**). It is noted that no rain-on-snow events were observed during the snow ablation periods in 3 years. $Q_S$ is the loss of snow converted into liquid water in the snow layer during the ablation period and is estimated from **Eq. 11**. $Q_{E\uparrow}$ is the snow sublimation and it is the total amount water flux returned to the atmosphere in the form of sublimation. Therefore, the value ($Q_{E\uparrow}$) is the sum of the sublimation under the forest and the snow sublimation of the forest canopy which was calculated using the EC method.

In some previous studies for estimating snow water equivalent, the snow melting was calculated from meteorological data with empirical or energy-based methods [e.g., Yao et al. (2012); Yao et al. (2018)]. In our present study, the snow melting was calculated through the water balance equation (**Eq. 11**), as all other items were obtained by field measurements. The daily snowmelt rate ($S_r$) was calculated as follows, by similarly using water balance:

$$S_r = \frac{Q_{SWE}^i - Q_{SWE}^j - Q_{snowfall}^{i-j} - Q_{E\uparrow}^{i-j}}{N^{i-j}}, \quad (12)$$

where $S_r$ is the daily rate of snowmelt (mm/day), and $Q_{SWE}^i$ and $Q_{SWE}^j$ are the *SWE* of the surface snow on day *i* and day *j* during the ablation period (mm), respectively. $Q_{snowfall}^{i-j}$ is the snow accumulation on surface snow between day *i* and day *j* ($i < j$) (mm). $Q_{E\uparrow}^{i-j}$ is the total amount of snow sublimation between day *i* and day *j* (mm), and *N* is the number of days between day *i* and day *j* (days).

### 2.3.6 Quantification of the Effects of Forest on the Snow Process

To ensure that the impacts that forests have on snow processes are comparable across different years and different forest types, a forest and open site comparison method was used to calculate the effect value (*E*). This normalization method for different forest snow data was based on the effect value calculated by the reference point OS, and a method similar to that proposed by Varhola et al. (2010) was adopted, which quantified the effect uniformly over the whole season (accumulation and ablation periods). The *E* was calculated as follows:

$$E = \frac{SWE_{Forest} - SWE_{Open\ site}}{SWE_{Open\ site}}, \quad (13)$$

where $SWE_{Forest}$ is the average snow water equivalent (*SWE*) of each forest type at the plot scale, $SWE_{Open\ site}$ is the average snow water equivalent (*SWE*) of the open site (OS), which is calculated by **Eq. 6** based on the snow surveys. *E* is the effect value,

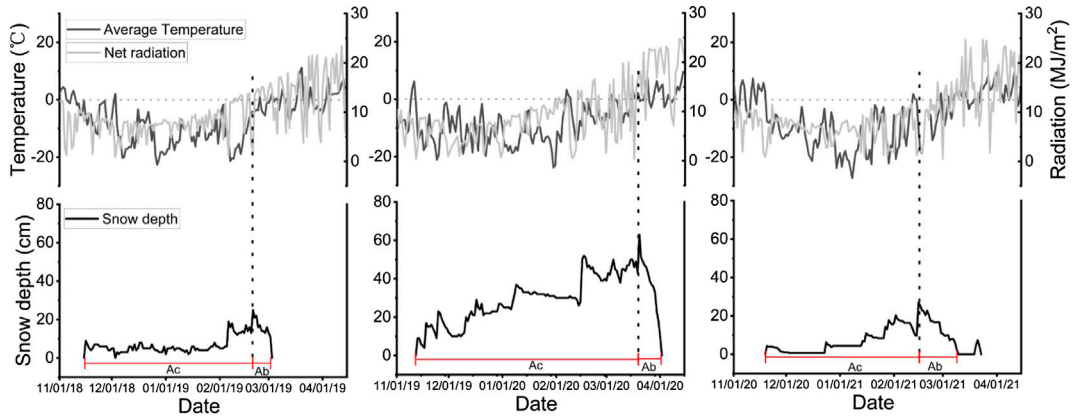


**FIGURE 4 |** Characteristics of meteorological conditions during snow accumulation and ablation processes in the open area OS, for each of the three winter seasons. The maximum snow depth appeared near the 0°C air temperature and was used as the dividing date for two periods, where *Ac* is the accumulation period that occurred before the maximum snow depth date, and *Ab* is the ablation period.

representing the average value calculated after multiple surveys throughput the entire survey period for each winter. A negative value indicates that there is a decreasing impact of the forest on the understory SWE (snow water equivalent), while a larger absolute value indicates a stronger impact of the forest on the understory SWE.

# 3 RESULTS

## 3.1 Meteorological Characteristics During the Study Period

The meteorological conditions varied throughout the whole snow cover period (**Figure 4**). The rapid shift between snow accumulation and ablation periods is strongly controlled by meteorological factors, such as snowfall, net radiation, air temperature, and other factors. According to various characteristics of meteorological elements (average temperature, net radiation, and the maximum snow depth) in the open area OS, we found that the date of the maximum snow depth appeared when the daily-average temperature was reaching 0°C in our research area, indicating the air temperature was the most important factor controlling the shift from accumulation to ablation. Therefore, the date of the maximum snow depth was used to divide the whole snow process into two periods, the *Ac* period and the *Ab* period. The maximum snow depth was reached on 20 February 2019, 20 March 2020, and 15 February 2021, respectively, for the three winter seasons. The maximum snow depth in the OS was 25 cm (2018–2019), 63 cm (2019–2020), and 27 cm (2020–2021), respectively. Overall, both air temperature ($T_a$) and net radiation ($R_a$) are the main input sources of snow ablation energy, and their values varied at different periods, which together regulate the transition between the *Ac* and *Ab* periods. Over the 3 years, the average of $T_a$ in *Ac* was about −11.2°C (2018–2019), −9.1°C (2019–2020), and −12°C (2020–2021), and the average of $R_a$ in *Ac* was 7.75 MJ/m$^2$ (2018–2019), 6.76 MJ/m$^2$ (2019–2020), and 6.6 MJ/m$^2$ (2020–2021), respectively. During the three *Ab* periods, the average of $T_a$ increased to −2.2°C (2018–2019), 1.86°C (2019–2020), and −6°C (2020–2021), and the average of $R_a$ increased to 13.1 MJ/m$^2$ (2018–2019), 18.8 MJ/m$^2$ (2019–2020), and 9.95 MJ/m$^2$ (2020–2021). The average values of $T_a$ and $R_a$ in the *Ac* period were lower than those in the *Ab* period.

The changes in $T_a$ and $R_a$ during the *Ab* period affected the pattern of snow melting and thus strongly controlled the duration of the snow. Although the maximum snow depth in 2019–2020 (63 cm) was far greater than that in the other 2 years (**Figure 4** middle column), the multi-day average of $T_a$ and $R_a$ during the *Ab* period remained the highest at 1.86°C and 18.8 MJ/m$^2$; thus, fast ablation was observed during this snowmelt period. The ablation curve was also relatively steep, and the *Ab* period lasted just 13 days. However, the maximum snow depth in 2020–2021 was only 27 cm in the OS (**Figure 4** right column). The multi-day average of $T_a$ and $R_a$ in the *Ab* period were only −6°C and 9.95 MJ/m$^2$ and showed a slow increasing trend. As a result, the snow had showed a slow ablation, and the *Ab* period lasted for the longest amount of time: 23 days (2020–2021). Correspondingly, there were 11 (2018–2019), 13 (2019–2020), and 23 (2020–2021) snow ablation days for the 3 years. Thus, the ablation pattern and ablation duration in the *Ab* period were mainly controlled by the $T_a$ and $R_a$. The higher the values of $T_a$ and $R_a$, the faster the ablation rate, and correspondingly, the shorter the ablation period.

## 3.2 Variations in Snow Density and Snow Depth at Five Sites

The snow density ($\rho$) varied largely with the day of winter (DOW) within the different land types: between 0.14 and 0.45 g/cm$^3$ at the five sites (**Figure 5**). Throughout the three winters, the $\rho$ of the five sites in the *Ac* period was smaller than that in the *Ab* period, and $\rho$ increased with the DOW. The $\rho$ during the *Ac* period was about 0.14–0.35 g/cm$^3$, while during the *Ab* period, the $\rho$ of the five sites all showed an increasing trend, varying between 0.35 and

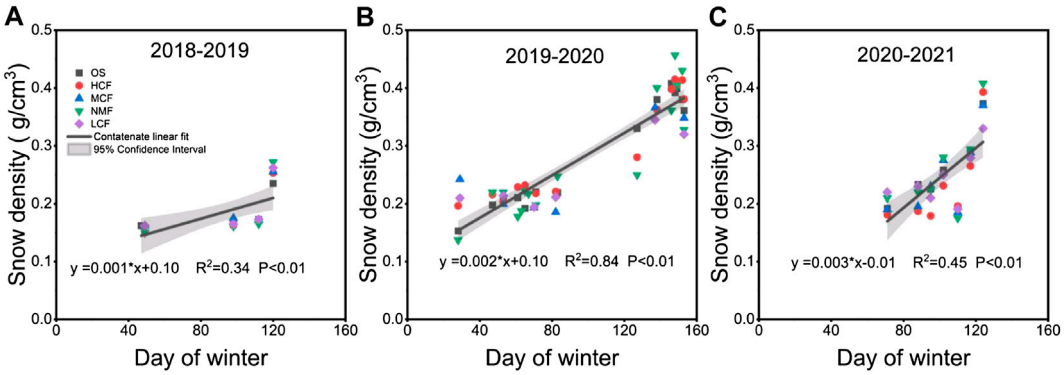


**FIGURE 5 |** Relationship of snow density ($\rho$) with day of winter (DOW) for 3 years at five sites: **(A)** 2018–2019, **(B)** 2019–2020, and **(C)** 2020–2021. Day of winter (DOW) represents the number of days, starting from November 1 to the seasonal end of April 8. The different icons indicate different land types: OS, open site; HCF, high-intensity cutting mixed forest; MCF, moderate-intensity cutting mixed forest; NMF, natural mixed forests; LCF, low-intensity cutting mixed forest. The solid line is a fitted regression for snow density and DOW for all land types, and the shaded range indicates the 95% conference interval.

**TABLE 2 |** Statistical characteristics of snowfall for 3 years.

| Year | S (cm) | Light snow (0 < d ≤ 5 cm) | Moderate snow (5 cm < d ≤ 15 cm) | Heavy snow (15 cm < d ≤ 25 cm) | Extremely heavy snow (d > 25 cm) |
|---|---|---|---|---|---|
| | | Proportion (%) | Proportion (%) | Proportion (%) | Proportion (%) |
| 2018–2019 | 91 | 63 | 37 | - | - |
| 2019–2020 | 207 | 32 | 43 | 12 | 13 |
| 2020–2021 | 75 | 48 | 28 | 24 | - |

*The single snowfall intensity was identified by a set of snow depth thresholds at the meteorological stations OS; d is the snow depth of a single snowfall event, and 0, 5, 15, and 25 cm were used as the thresholds to divide snowfall into four categories. S is the total snowfall in a season, and the proportion of one intensity category is the ratio of the cumulative value of this category against the total snowfall. "-" means not applicable.*

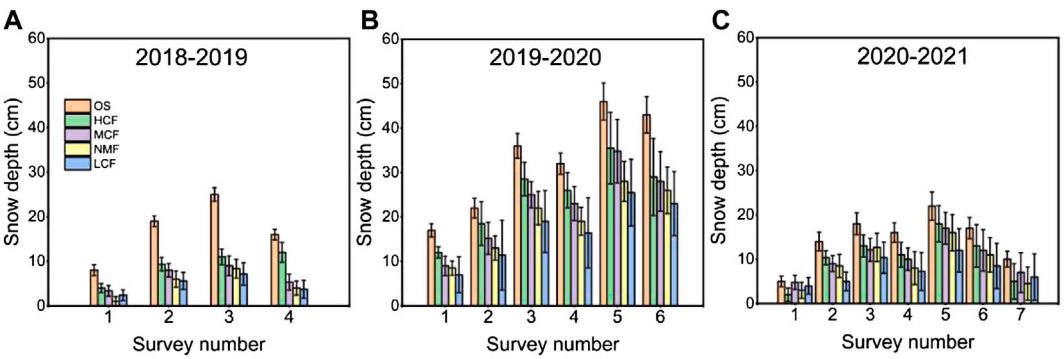


**FIGURE 6 |** Snow depth distribution characteristics at stand level for five sites in three years, **(A)** 2018–2019, **(B)** 2019–2020, and **(C)** 2020–2021. The histogram is the average snow depth (*SD*) at the plot scale, and the error bar is the standard deviation ($n$ = 36). Different color histograms indicate different sites: OS, open site; HCF, high-intensity cutting mixed forest; MCF, moderate-intensity cutting mixed forest; NMF, natural mixed forests; LCF, low-intensity cutting mixed forest; *SD* is snow depth (cm). The survey number (*SN*) is the serial number of the field snow survey conducted, and snow depth surveys were carried out weekly to bi-weekly.

0.45 g/cm$^3$. The relationship between $\rho$ and DOW of the five sites showed the best ($R^2$ = 0.84) linear correlation in 2019–2020, and the correlation results in 2018–2019 ($R^2$ = 0.34) and in 2020–2021 ($R^2$ = 0.45) were relatively weaker. Changes in meteorological conditions also affected the relationship between $\rho$ and DOW. The annual snowfall in 2019–2020 was close to the average annual snowfall in the region for many years, but 2018–2019 and 2020–2021 were abnormal years where there was less snowfall in this region (**Table 2**). Thus, in the early *Ac* period of the two snow years with less snow, the surface snow depth showed a long-term weak fluctuation in the low range (<10 cm, **Figure 4**) and snow density lacked the process of compaction due

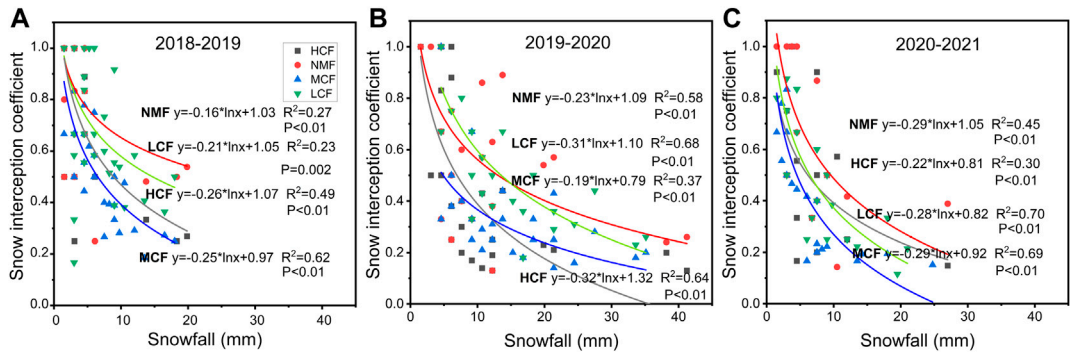


**FIGURE 7 |** Relationship between the forest canopy interception coefficient ($C_{IE}$) and snowfall for each of the three years, **(A)** 2018–2019, **(B)** 2019–2020, and **(C)** 2020–2021. The different icons indicate different forest types. One dot is for one snowfall event. The fitted curves are logarithmic functions of the snowfall.

to the small snow depth accumulation. Moreover, $T_a$ and $R_a$ in the *Ac* period were low for a long time and there existed a role for new snowfall to reduce the average snow density of the snow profile, and these factors eventually affected the evolutionary process of snow density. This was the main reason for the relatively weak relationship between $\rho$ and DOW in 2018–2019 and 2020–2021.

The snow depth in the forest correlated to the forest canopy closure (**Figure 6**). The *SD* in the OS was greater than that in all the forests for the same *SN*. Moreover, the *SD* of the four forests in the same *SN* also decreased as the closure $\theta$ increased. The size order of the *SD* was OS > HCF > MCF > NMF > LCF (**Figure 6**), but the $\theta$ order was OS < HCF < MCF < NMF < LCF (**Table 1**), showing opposite sizes. This indicated that the forest had an obvious snow depth reduction effect. Forests with a larger $\theta$ tend to have a smaller *SD*.

## 3.3 The Relationship Between Forest Canopy Interception and Snowfall

The forest canopy interception correlated fairly with snowfall (**Figure 7**). The $C_{IE}$ of the canopy decreased as the amount of snowfall increased for an event, during 2018–2021. The $C_{IE}$ of the HCF, NMF, MCF, and LCF for a single snowfall event varied from 0.1 to 0.9. A single snowfall event in the study area ranged between 1.5 and 42 mm (converted to liquid water). On the whole, the $C_{IE}$ showed interannual variation (seeing the three sub-graphs for 3 years in **Figure 7**), and the fitting effectiveness of the regression curve was better in the 2019–2020 winter than in the other two winters, which was mainly because of the higher interception effect of the canopy on light snows. The proportion of the cumulative amount of light snow in the total snowfall amount was the lowest in the 2019–2020 season (**Table 2**). **Figure 7** also shows that there was an interval difference relationship between the variation range of the interception coefficient and snowfall. The smaller the snowfall, the greater the variation range of the interception coefficient. Additionally, as snowfall increased, the variation range of the interception coefficient gradually became narrower. Furthermore, as illustrated by the fitting curves, there was a different maximum interception coefficient among different forest types. In other words, when the amount of snowfall was the same, the forest with a larger closure had a higher $C_{IE}$ (i.e., NMF > HCF, LCF > MCF).

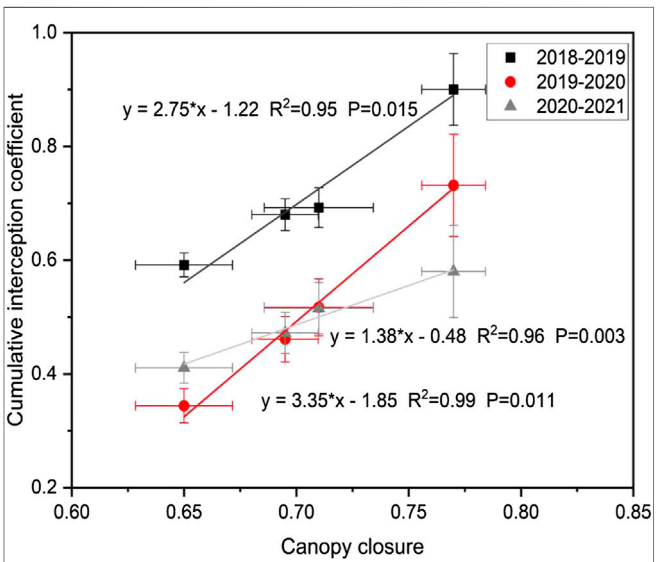


**FIGURE 8 |** Relationship between cumulative interception coefficient (*Ic*) and forest canopy closure ($\theta$). Points with different colors and shapes represent different years: the black square points represent 2018–2019, the red points represent 2019–2020, and the gray triangle points represent 2020–2021.

## 3.4 The Relationship Between Canopy Closure and Snow Interception Coefficient

The snow interception coefficient is strongly related to forest canopy closure (**Figure 8**). The *Ic* and $\theta$ had a good positive correlation, and *Ic* increased with $\theta$. This means that in the same year, when the $\theta$ of the forest was larger among the four forest plots, more snow was intercepted by the canopy. In the 2018–2019 winter, the *Ic* of the four plots varied from 0.59 to 0.9, and the forest canopy intercepted 59%–90% of the snowfall. The correlation's slope parameter was 2.75 ($R^2$ = 0.95). When the $\theta$ increased by 0.1, the *Ic* would increase by

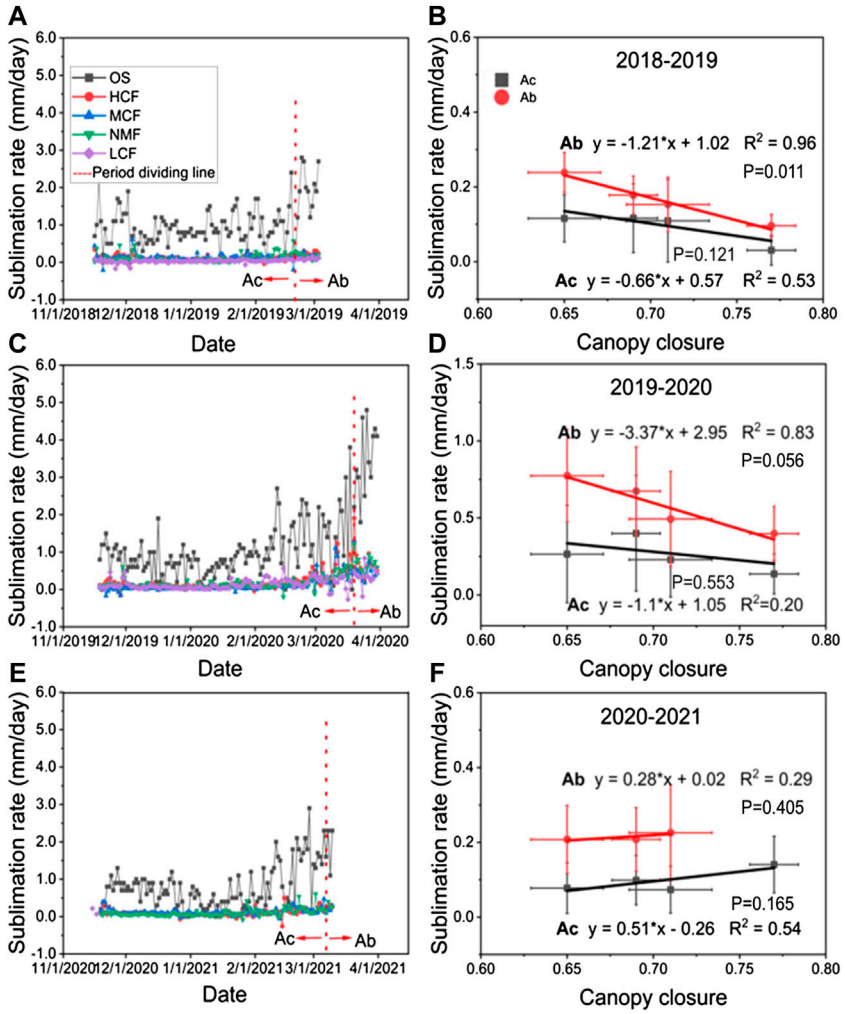


**FIGURE 9 |** Snow sublimation rate ($S_s$) daily dynamics of five sites: **(A)** 2018–2019, **(C)** 2019–2020, and **(E)** 2020–2021; the relationship between the multi-day average snow sublimation rate ($S_{s\text{-}A}$) and forest canopy closure ($\theta$) in the different periods: **(B)** 2018–2019, **(D)** 2019–2020, and **(F)** 2020–2021. *Ac* is the accumulation period (right column, grey point), *Ab* is the ablation period (right column, red point), and red dotted line (left column) is the dividing line for the *Ac* and *Ab* periods.

0.27, and the corresponding snow interception increased by 27%. In the 2019–2020 winter, the *Ic* of the four forests varied from 0.34 to 0.73, the forest intercepted 34%–73% of the snowfall that occurred. When $\theta$ increased by 0.1, the *Ic* increased by 0.33 ($R^2 = 0.98$), and the corresponding snow interception increased by 33%. In the 2020–2021 winter, the *Ic* of the four forests varied from 0.41 to 0.58, and the forest canopy intercepted 41%–58% of the total snowfall. For every 0.1 increase in $\theta$, the *Ic* increased by 0.13 ($R^2 = 0.96$), and the corresponding snowfall interception increased by 13%. Thus, we found that the relationship between *Ic* and $\theta$ was the strongest in 2019–2020, followed by in 2018–2019 and in 2020–2021. There were different linear correlations between *Ic* and $\theta$ in different years, indicating that the relationship had interannual variation that were largely related to changes in the annual snowfall and intensity composition of snowfall events.

The interception coefficients of the four mixed forests all showed a decreasing trend as the snowfall intensity increased. This feature appeared the highest with light snow, the second highest with moderate snow, and the lowest with heavy snow and extremely heavy snow (**Figure 7**). As a consequence of this, when there was a higher proportion of light snow in a year, the cumulative interception was larger (**Figure 8**, 2018–2019), which means that when more snow was lost due to canopy interception, there was less snow understory of the canopy. From **Table 2**, in 2018–2019, light snow comprised 63% of the annual snowfall, and this was why the cumulative snow interception rates at the four forests in 2018–2019 were all higher than they were in the other 2 years (**Figure 8**).

## 3.5 The Relationship Between Canopy Closure and Snow Sublimation Rate

The forest canopy closure affected the snow sublimation rate (**Figures 9A,C,E**). There were obvious differences in the snow sublimation dynamics between the OS and the four forests. The $S_s$ in the OS and the variation range in the 3 years were both much

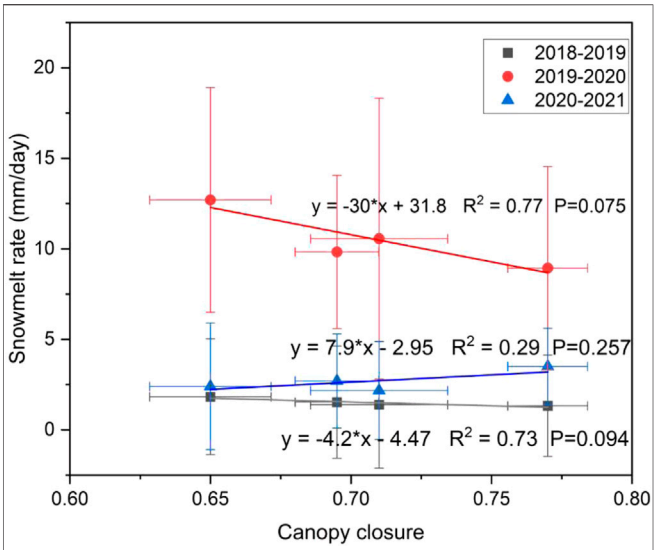


**FIGURE 10 |** Relationship between forest canopy closure ($\theta$) and snowmelt rate ($S_r$). Points of different colors and shapes represent different years. The gray square points represent 2018–2019, the red circle points represent 2019–2020, and the blue triangle points represent 2020–2021.

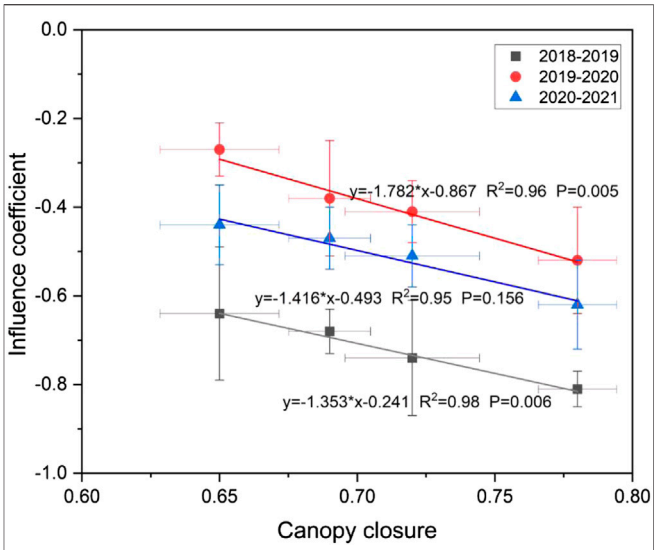


**FIGURE 11 |** Relationship between forest influence effect ($E$) on snow processes and canopy closure ($\theta$). Points of different colors and shapes represent different years.

larger than those in the four forests over the entirety of both the *Ac* and *Ab* periods. Over the course of 3 years, the $S_s$ in the OS varied from 0 to 4.5 mm/day, while the $S_s$ in the four forests (HCF, MCF, NMF, and LCF) varied from 0 to 1.0 mm/day. During the different snow periods (*Ac* and *Ab*) for the same site, the $S_s$ in the *Ab* period was greater than that during the *Ac* period (**Figures 9B,D,F**). Moreover, the $S_s$ in the OS showed a much faster increase than it did in the four forests (**Figure 9** left column).

The forest closure affected the snow sublimation rate in both the snow accumulation and ablation periods. The snow sublimation rate ($S_s$) of four forests in the accumulation period was lower than that in the ablation period (**Figures 9B,D,F**). In 2018–2019, the $S_s$ in the accumulation period was 0.3 ± 0.04–0.12 ± 0.14 mm/day, while it increased to 0.09 ± 0.03–0.24 ± 0.05 mm/day in the ablation period. In 2019–2020, the $S_s$ was 0.13 ± 0.13–0.4 ± 0.37 mm/day in the snow accumulation period, while it increased to 0.39 ± 0.18–0.77 ± 0.31 mm/day in the ablation period. In 2020–2021, the $S_s$ was 0.07 ± 0.06–0.14 ± 0.08 mm/day during the snow accumulation period and increased to 0.20 ± 0.08–0.23 ± 0.13 mm/day during the ablation period.

The effects of forest canopy closure on the snow sublimation rate showed interannual variations for both the periods. **Figures 9B,D,F** showed the relationship between $S_{s\text{-}A}$ and $\theta$ during the different periods. The $S_{s\text{-}A}$ of the four forests during the *Ac* and *Ab* periods all decreased as the $\theta$ increased for the first 2 years (2018–2019 and 2019–2020). The slope and correlation coefficient (−1.21, $R^2$ = 0.96, 2018–2019; −3.37, $R^2$ = 0.83, 2019–2020) were steeper and stronger during the *Ab* period than they were during the *Ac* period (−0.66, $R^2$ = 0.53, 2018–2019; −1.1, $R^2$ = 0.20, 2019–2020). This difference reflected how forest canopy closure had a reduction effect on $S_s$ in 2018–2019 and 2019–2020. Additionally, the effects of forest canopy closure on snow sublimation rate during the *Ab* period was stronger than that in the *Ac* period. However, for the year 2020–2021, $S_{s\text{-}A}$ and $\theta$ showed a weak positive correlation (**Figure 9F**), which was opposite to the correlations in the other 2 years. This indicated that forest canopy closure increased the snow sublimation rate slightly in 2020–2021.

## 3.6 The Relationship Between Canopy Closure and Snowmelt Rate

The snowmelt rate was also affected by forest canopy closure (**Figure 10**). The average $S_r$ in the four forests was about 1.52 mm/day (2018–2019), 10.5 mm/day (2019–2020), and 2.69 mm/day (2020–2021). The large variation in the $S_r$ among the years was related to the varying $T_a$ and $R_a$. The higher they were, the higher the $S_r$ and the faster the snowmelt. During the three *Ab* periods, there were different correlations between $\theta$ and $S_r$. The $S_r$ was negatively correlated with $\theta$ in 2018–2019 ($R^2$ = 0.73), and $S_r$ decreased by 0.4 mm/day when the $\theta$ increased by 0.1. Similarly, there was a good negative correlation between $S_r$ and $\theta$ in 2019–2020 ($R^2$ = 0.77), and $S_r$ decreased by 3 mm/day when the $\theta$ increased by 0.1. This suggested that elevated forest canopy closure reduced the snowmelt rate in two of the studied years. However, $S_r$ showed a slight increase alone with the $\theta$ in 2020–2021, which indicated that the $\theta$ increased the $S_r$ slightly during the *Ab* period ($S_r$ increased by 0.79 mm/day for every 0.1 increase in $\theta$). In summary, there was a good correlation between $\theta$ and $S_r$, and the relationship between them showed interannual variation.

### 3.7 The Relationship Between Forest Effect on the Snow Process and Canopy Closure

Forests have a significant impact on snow processes, and with the increase of forest canopy closure, the influence of forest on snow processes also increased correspondingly (**Figure 11**). All four forests show a reduction in the understory surface snow water equivalent, and there is a good linear correlation between $\theta$ and the influence effect $E$ over the 3 years. In a normal snow year (2019–2020), the $E$ ranged from −27% to −52% among the four plots, and it decreased as $\theta$ increased across plots. Four forests showed a stronger effect on the snow in extreme low snow years (2018–2019 and 2020–2021). The mean values of the effect of the four mixed forests on understory SWE (snow water equivalent) over the 3 years ranged from −45% to −65%. Therefore, the effects of canopy closure on the forest snow processes had interannual variation. The slope of the fitted linear line (**Figure 11**) showed that the relationship between $\theta$ and $E$ changed a little among different years. In 2018–2019, when $\theta$ increased by 0.1, the $E$ of the forest on the *SWE* showed a relative increase of 13% ($R^2$ = 0.98). In 2019–2020, when $\theta$ increased by 0.1, the $E$ increased by 17% ($R^2$ = 0.96), or in 2020–2021 it increased by 14% ($R^2$ = 0.95). This was mainly due to the changes in snowfall characteristics in different years (**Table 2**). Canopy closure had a negative effect on snow processes. When $\theta$ was larger, the effect was stronger, and accordingly, there was less *SWE* under the forest. The higher the proportion of light snowfall annually, the stronger the influence effect of the forest on snow processes. For example, $E$ (2019–2020) > $E$ (2020–2021) > $E$ (2018–2019), corresponding to the proportion of light snowfall to annual snowfall, which was 0.32 (2019–2020) < 0.48 (2020–2021) < 0.63 (2018–2019).

## 4 DISCUSSION

### 4.1 Influence Mechanisms of Forest on Snow Density and Snow Depth

Snow density and snow depth are indicators of the impacts that a forest has on snow processes. The duration date factors of snow (DOY, day of year or Julian day) have been used in snow density models: e.g., Sturm model (Lea et al., 2010) and Sexstone model (Sexstone and Fassnacht, 2014). Similar to the snow density research by Yao et al. (2018) at the Dorset Environment Science Centre site, we also found that there was a good correlation between density $\rho$ and DOW (day of winter) during a normal snow year ($R^2$ = 0.84, 2019–2020), indicating that the evolution of snow density can be reconstructed and characterized by DOW. However, the relationship was weak in snow-anomaly years ($R^2$ = 0.34, 2018–2019; $R^2$ = 0.45, 2020–2021). This indicates that snow depth (*SD*) should be taken into account when using the DOW to simulate snow density in less snow years. Although the snow density showed a distinguishable relationship at different sites after certain snow surveys in our study, no regular relationship was observed throughout the whole snow season. The main reason for this is that the forest canopy had a complex and persistent impact on snow density through changing a variety of comprehensive factors (such as snow depth, temperature, humidity, sublimation, and ablation), which ultimately affected the snow density under the forest canopy. A single survey event reveals only the results of the comprehensive impact of various factors on snow density in a limited period. The intensity and mechanism of different factors are changed constantly. Therefore, during the entire snow period, the snow density at various sites did not show a stable relationship with distinguishability and consistency.

The forest canopy closure affected the snow depth obviously, and the snow depth had a good relationship with the canopy closure gradient over the 3 years (**Figure 6**). When $\theta$ was larger, the *SD* was smaller. This was mainly because the greater the $\theta$, the stronger the interception effect of the canopy on snow (**Figure 8**), resulting in less snow accumulating on the ground surface.

### 4.2 Influence Mechanism of Forest Canopy Closure on the Snow Process

Canopy closure indirectly reflects the interception area in the horizontal direction of the canopy, and it is a canopy indicator that controls the energy input and mass input to the snow surface of the understory. When the interception area increases, both the snow and energy input to the surface through the canopy are weakened. Therefore, the interception effect and influence effect decreased as $\theta$ increased (**Figures 8**, **11**). In this study, the canopy's interception effect on the snow was about −34% to −73%. Similar to the study by Storck et al. (2002), Roth and Nolin (2017), and Xiao et al. (2019), canopy interception was still the strongest factor affecting understory surface snow accumulation in this region. However, we found that for extreme low snow years, the canopy interception effect was stronger than in normal snow years. Additionally, the radiation transmission and wind speed under the canopy decreased as the canopy closure increased (Stähli et al., 2009), and they further changed the snow sublimation rate and snowmelt rate. All of these is the reason why the $S_s$ in the four forests was lower than that of the open site (**Figure 9**), $S_s$ and $S_r$ both decreased as $\theta$ increased (**Figures 9**, **10**). More importantly, at the forest stand level (40 m wide) of our study, $\theta$ showed a good correlation relationship with all the snow sub-processes (interception, sublimation, and snowmelt). Similar to previous studies on the relationship between canopy closure (or LAI) and snow processes as determined using different scales and methods by Krogh et al. (2020), Broxton et al. (2021), and Russell et al. (2021), we also found that $\theta$ was an ideal canopy index factor to explain the variations in *SD*, *Ic*, $S_s$, $S_r$, and *SWE* in the mixed forests of the Changbai Mountains.

Moreover, the effects of $\theta$ on $S_s$ and $S_r$ take place during different periods and show interannual variations. The relationship between $\theta$ and $S_s$ or $S_r$ appeared to be positively correlated in two of the studied years (2018–2019 and 2019–2020) but negatively correlated in the other year (2020–2021). The sublimation results in NMF forest by Li et al. (2013) showed that the sublimation rate has quadratic curves and exponential relationships with net radiation and the average temperature, respectively. Therefore, the influence of forests on snow sublimation was highly sensitive to changes in two climate factors. The multi-day $T_a$ and $R_a$ were −6°C and

9.95 MJ/m$^2$ during the *Ab* period (2020–2021), so the energy required for snowmelt mainly came from the $R_a$. Because the extinction of short-wave radiation by canopy can increase the long-wave radiation of the trunk (Pomeroy et al., 2009), when the canopy has a greater $\theta$, more energy can be absorbed by the canopy in the form of net solar radiation. This further increased the energy supply (long-wave radiation) of the snow surface and promoted the $S_s$ and $S_r$ of the forest snow. Therefore, $S_s$ and $S_r$ increased as $\theta$ increased in 2020–2021 (**Figures 9**, **10**). The results show that the effects (positive or negative) of forest canopy closure on snow sub-processes (i.e., sublimation and snowmelt) mainly depend on the changes in different meteorological factors during the different periods.

### 4.3 Influence Mechanism of Snowfall on the Interaction Between Forest and Snow

The forest had a significant effect on reducing the amount of snow (**Figures 6**, **11**). Meanwhile, there was a good negative correlation between canopy closure and the effect value (**Figure 11**), which is consistent with the previous research results obtained by Gelfan et al. (2004) and Varhola et al. (2010). However, the results based on the 3 years of our study showed the interannual variation in the correlation between the two. One reason was the composition of snowfall. The canopy interception coefficient was the strongest for light snow, followed by moderate snow, and was the smallest in heavy snow and extremely heavy snow (**Figure 7**). Accordingly, the higher the proportion of light snow, the higher effect value on the snow process. As such, forests had a stronger effect in 2018–2019 than it did during the other 2 years (**Figure 11**). Similarly, the proportion of light snow in 2019–2020 was the smallest (32%), and the four forests showed a smaller effect value (2019–2020) than the other 2 years. In addition, the total annual snowfall was another reason, as they had a joint effect on the snow processes. Ultimately, the impact of forests on the snow process was relatively stronger in extreme low snow years than in normal snow years. Likewise, we speculated that the intensity of the nested and interactive effects of large-scale factors (climatic conditions) and small-scale factors (forest structure) likely changed over the 3 years. This indicates that in different regions, or at different spatial scales, strong local and interannual variations may happen in the relationship between canopy closure and snow processes.

Our study serves as a case study for enriching our knowledge of forest and snow interactions. The results herein also suggest that the establishment of statistical models or physical models based on canopy structure factors in forest areas need to consider interannual effects, types of snowfall, type of forest, and scale dependences. If available, the corresponding parameters of the spatiotemporal interpolation method and remote sensing algorithm, such as the pixel decomposition algorithm by Jiang et al. (2014) and Yang et al. (2019), should be flexibly adjusted according to the relationship between *SWE* and forest closure in forest areas, and this may improve the accuracy of snow estimation in forest areas. Our study presents the effect of mixed forests on snow processes in the Changbai Mountain area over the course of three snow years and will compensate for the lack of snow process research in northeast China. Moreover, it may provide helpful information for forest management, snow model verification, remote sensing product development, algorithm improvement, and verification for this region in the future.

## 5 CONCLUSION

This study explored the impact of forest canopy closure on snow processes by combining *in situ* snow survey, eddy covariance, and water balance method to research snow processes at five sites (four forest sites and an open site). We found that forest snow processes were largely controlled by the changes in snowfall or intensity, micrometeorological conditions, and forest canopy closure. The interception of snow by the forest canopy was an important factor affecting the snow depth of understory. The forest interception effect ranged from −33% to −90%. The good correlation between forest canopy closure and the interception effect also showed interannual changes, which were mainly related to different snowfall events. Changes in forest closure altered the snow sublimation and snowmelt processes, and canopy closure showed a good correlation with the snow sublimation rate and snowmelt rate. Compared to the open site, the four mixed forests affected the *SWE* of understory by −27% to −81% and strongly reduced the *SWE* over the 3 years. Canopy closure can explain well the impact of mixed forest structure changes on the snow processes in the Changbai Mountain area. We also found that there were interannual variations in the impact effects caused by forest closure on the snow processes, suggesting that dynamic effects need to be considered when comparing snow models in forest area or when conducting the snow mapping tasks. More importantly, changes in snowfall caused by future winter warming may further complicate the impact of forests on snow processes in this region.

## DATA AVAILABILITY STATEMENT

The original contributions presented in the study are included in the article/supplementary material; further inquiries can be directed to the corresponding author.

## AUTHOR CONTRIBUTIONS

YG and LS contributed to conception and design of the study. YG and RC organized the database and performed the statistical analysis. YG wrote the first draft of the manuscript. LS, AW, FY, JW, DG, and HY revised the manuscript and provided for revision. All authors contributed to manuscript revision and read and approved the submitted version.

## FUNDING

This research was supported by the National Natural Science Foundation of China (Grant Nos. 31971728, 32171873, 41975150, and 31870625).

## REFERENCES


Bebi, P., Kulakowski, D., and Rixen, C. (2009). Snow Avalanche Disturbances in Forest Ecosystems-State of Research and Implications for Management. *For. Ecol. Manag.* 257 (9), 1883–1892. doi:10.1016/j.foreco.2009.01.050

Broxton, P. D., Harpold, A. A., Biederman, J. A., Troch, P. A., Molotch, N. P., and Brooks, P. D. (2015). Quantifying the Effects of Vegetation Structure on Snow Accumulation and Ablation in Mixed-conifer Forests. *Ecohydrol.* 8 (6), 1073–1094. doi:10.1002/eco.1565

Broxton, P. D., Moeser, C. D., and Harpold, A. (2021). Accounting for Fine-Scale Forest Structure is Necessary to Model Snowpack Mass and Energy Budgets in Montane Forests. *Water Resour. Res.* 57, e2021WR029716. doi:10.1029/2021WR029716

Burles, K., and Boon, S. (2011). Snowmelt Energy Balance in a Burned Forest Plot, Crowsnest Pass, Alberta, Canada. *Hydrol. Process.* 25, 3012–3029. doi:10.1002/hyp.8067

Casteller, A., Häfelfinger, T., Cortés Donoso, E., Podvin, K., Kulakowski, D., and Bebi, P. (2018). Assessing the interaction between mountain forests and snow avalanches at Nevados de Chillan, Chile and its implications for ecosystem-based disaster risk reduction. *Nat. Hazards Earth Syst. Sci.* 18 (4), 1173–1186. doi:10.5194/nhess-18-1173-2018

Chang, J., Wang, G.-x., Gao, Y.-h., and Wang, Y.-b. (2014). The Influence of Seasonal Snow on Soil Thermal and Water Dynamics under Different Vegetation Covers in a Permafrost Region. *J. Mt. Sci.* 11 (3), 727–745. doi:10.1007/s11629-013-2893-0

Charuchittipan, D., Babel, W., Mauder, M., Leps, J.-P., and Foken, T. (2014). Extension of the Averaging Time in Eddy-Covariance Measurements and its Effect on the Energy Balance Closure. *Boundary-Layer Meteorol.* 152 (3), 303–327. doi:10.1007/s10546-014-9922-6

De Roo, F., Zhang, S., Huq, S., and Mauder, M. (2018). A Semi-empirical Model of the Energy Balance Closure in the Surface Layer. *PLoS One* 13 (12), e0209022. doi:10.1371/journal.pone.0209022

Dong, C., and Menzel, L. (2017). Snow Process Monitoring in Montane Forests with Time-Lapse Photography. *Hydrol. Process.* 31 (16), 2872–2886. doi:10.1002/hyp.11229

Dong, C. (2018). Remote Sensing, Hydrological Modeling and *In Situ* Observations in Snow Cover Research: A Review. *J. Hydrol.* 561, 573–583. doi:10.1016/j.jhydrol.2018.04.027

Ellis, C. R., Pomeroy, J. W., Brown, T., and MacDonald, J. (2010). Simulation of Snow Accumulation and Melt in Needleleaf Forest Environments. *Hydrol. Earth Syst. Sci.* 14 (6), 925–940. doi:10.5194/hess-14-925-2010

Frazer, G. W., Canham, C. D., and Lertzman, K. P. (1999). *Gap Light Analyzer (GLA): Imaging Software to Extract Canopy Structure and Gap Light Transmission Indices from True-Colour Fisheye Photographs, Users Manual and Program Documentation*. Burnaby, Millbrook, NY: Simon Fraser University, Institute of Ecosystem Studies.

Frei, A., Tedesco, M., Lee, S., Foster, J., Hall, D. K., Kelly, R., et al. (2012). A Review of Global Satellite-Derived Snow Products. *Adv. Space Res.* 50 (8), 1007–1029. doi:10.1016/j.asr.2011.12.021

Garvelmann, J., Pohl, S., and Weiler, M. (2012). Applying a Time-Lapse Camera Network to Observe Snow Processes in Mountainous Catchments. doi:10.5194/hessd-9-10687-2012

Gelfan, A. N., Pomeroy, J. W., and Kuchment, L. S. (2004). Modeling Forest Cover Influences on Snow Accumulation, Sublimation, and Melt. *J. Hydrometeorol.* 5 (5), 785–803. doi:10.1175/1525-7541(2004)005<0785:mfcios>2.0.co;2

Guan, D.-X., Wu, J.-B., Zhao, X.-S., Han, S.-J., Yu, G.-R., Sun, X.-M., et al. (2006). CO2 Fluxes over an Old, Temperate Mixed Forest in Northeastern China. *Agric. For. Meteorol.* 137 (3-4), 138–149. doi:10.1016/j.agrformet.2006.02.003

Hao, J., Mind'je, R., Feng, T., and Li, L. (2021). Performance of Snow Density Measurement Systems in Snow Stratigraphies. *Hydrol. Res.* 52 (4), 834–846. doi:10.2166/nh.2021.133

Harpold, A. A., Guo, Q., Molotch, N., Brooks, P. D., Bales, R., Fernandez-Diaz, J. C., et al. (2014). LiDAR-derived Snowpack Data Sets from Mixed Conifer Forests across the Western United States. *Water Resour. Res.* 50 (3), 2749–2755. doi:10.1002/2013wr013935

Henderson, G. R., Peings, Y., Furtado, J. C., and Kushner, P. J. (2018). Snow-atmosphere Coupling in the Northern Hemisphere. *Nat. Clim. Change* 8 (11), 954–963. doi:10.1038/s41558-018-0295-6

Hojatimalekshah, A., Uhlmann, Z., Glenn, N. F., Hiemstra, C. A., Tennant, C. J., Graham, J. D., et al. (2021). Tree Canopy and Snow Depth Relationships at Fine Scales with Terrestrial Laser Scanning. *Cryosphere* 15 (5), 2187–2209. doi:10.5194/tc-15-2187-2021

Jacobs, J. M., Hunsaker, A. G., Sullivan, F. B., Palace, M., Burakowski, E. A., Herrick, C., et al. (2021). Snow Depth Mapping with Unpiloted Aerial System Lidar Observations: a Case Study in Durham, New Hampshire, United States. *Cryosphere* 15 (3), 1485–1500. doi:10.5194/tc-15-1485-2021

Jiang, L., Wang, P., Zhang, L., Yang, H., and Yang, J. (2014). Improvement of Snow Depth Retrieval for FY3B-MWRI in China. *Sci. China Earth Sci.* 57 (6), 1278–1292. doi:10.1007/s11430-013-4798-8

Krinner, G., Derksen, C., Essery, R., Flanner, M., Hagemann, S., Clark, M., et al. (2018). ESM-SnowMIP: Assessing Snow Models and Quantifying Snow-Related Climate Feedbacks. *Geosci. Model Dev.* 11 (12), 5027–5049. doi:10.5194/gmd-11-5027-2018

Krogh, S. A., Broxton, P. D., Manley, P. N., and Harpold, A. A. (2020). Using Process Based Snow Modeling and Lidar to Predict the Effects of Forest Thinning on the Northern Sierra Nevada Snowpack. *Front. For. Glob. Change* 3, 21. doi:10.3389/ffgc.2020.00021

Lea, J., Jonas, T., Derksen, C., Liston, G.E., Taras, B., and Sturm, M. (2010). Estimating Snow Water Equivalent Using Snow Depth Data and Climate Classes. *J. Hydrometeorol.* 11 (6), 1380–1394. doi:10.1175/2010jhm1202.1

Lendzioch, T., Langhammer, J., and Jenicek, M. (2019). Estimating Snow Depth and Leaf Area Index Based on UAV Digital Photogrammetry. *Sensors* 19 (5), 1027. doi:10.3390/s19051027

Li, H. D., Guan, D. X., Wang, A. Z., Wu, J. B., Jin, C. J., and ShiI, T. T. (2013). Characteristics of Evaporation over Broadleaved Korean Pine Forest in Changbai Mountains, Northeast China during Snow Cover Period in Winter. *Ying Yong Sheng Tai Xue Bao* 24 (4), 1039–1046. doi:10.13287/j.1001-9332.2013.0278

Li, H., Wang, A., Guan, D., Jin, C., Wu, J., Yuan, F., et al. (2016). Empirical Model Development for Ground Snow Sublimation beneath a Temperate Mixed Forest in Changbai Mountain. *J. Hydrol. Eng.* 21 (11), 04016040. doi:10.1061/(asce)he.1943-5584.0001415

López-Moreno, J. I., and Nogués-Bravo, D. (2006). Interpolating Local Snow Depth Data: an Evaluation of Methods. *Hydrol. Process.* 20 (10), 2217–2232. doi:10.1002/hyp.6199

Lopez-Moreno, J. I., and Stahli, M. (2008). Statistical Analysis of the Snow Cover Variability in a Subalpine Watershed: Assessing the Role of Topography and Forest, Interactions. *J. Hydrol.* 348 (3-4), 379–394. doi:10.1016/j.jhydrol.2007.10.018

Lundquist, J. D., Dickerson-Lange, S. E., Lutz, J. A., and Cristea, N. C. (2013). Lower Forest Density Enhances Snow Retention in Regions with Warmer Winters: A Global Framework Developed from Plot-Scale Observations and Modeling. *Water Resour. Res.* 49 (10), 6356–6370. doi:10.1002/wrcr.20504

Lyu, Z., and Zhuang, Q. (2018). Quantifying the Effects of Snowpack on Soil Thermal and Carbon Dynamics of the Arctic Terrestrial Ecosystems. *J. Geophys. Res. Biogeosci.* 123 (4), 1197–1212. doi:10.1002/2017jg003864

Mauder, M., Cuntz, M., Drüe, C., Graf, A., Rebmann, C., Schmid, H. P., et al. (2013). A Strategy for Quality and Uncertainty Assessment of Long-Term Eddy-Covariance Measurements. *Agric. For. Meteorol.* 169, 122–135. doi:10.1016/j.agrformet.2012.09.006

Maurer, G. E., and Bowling, D. R. (2014). Seasonal Snowpack Characteristics Influence Soil Temperature and Water Content at Multiple Scales in Interior Western U.S. Mountain Ecosystems. *Water Resour. Res.* 50 (6), 5216–5234. doi:10.1002/2013wr014452

Maxwell, J. D., Call, A., and St. Clair, S. B. (2019). Wildfire and Topography Impacts on Snow Accumulation and Retention in Montane Forests. *For. Ecol. Manag.* 432, 256–263. doi:10.1016/j.foreco.2018.09.021

Montesi, J., Elder, K., Schmidt, R. A., and Davis, R. E. (2004). Sublimation of Intercepted Snow within a Subalpine Forest Canopy at Two Elevations. *J. Hydrometeorol.* 5 (5), 763–773. doi:10.1175/1525-7541(2004)005<0763:soiswa>2.0.co;2

Musselman, K. N., Molotch, N. P., Margulis, S. A., Kirchner, P. B., and Bales, R. C. (2012). Influence of Canopy Structure and Direct Beam Solar Irradiance on Snowmelt Rates in a Mixed Conifer Forest. *Agric. For. Meteorol.* 161, 46–56. doi:10.1016/j.agrformet.2012.03.011

Napoly, A., Boone, A., and Welfringer, T. (2020). ISBA-MEB (SURFEX v8.1): Model Snow Evaluation for Local-Scale Forest Sites. *Geosci. Model Dev.* 13 (12), 6523–6545. doi:10.5194/gmd-13-6523-2020

O'Gorman, P. A. (2014). Contrasting Responses of Mean and Extreme Snowfall to Climate Change. *Nature* 512 (7515), 416–418. doi:10.1038/nature13625

Parajka, J., Haas, P., Kirnbauer, R., Jansa, J., and Blöschl, G. (2012). Potential of Time-Lapse Photography of Snow for Hydrological Purposes at the Small Catchment Scale. *Hydrol. Process.* 26 (22), 3327–3337. doi:10.1002/hyp.8389

Parajuli, A., Nadeau, D. F., Anctil, F., Parent, A.-C., Bouchard, B., Girard, M., et al. (2020). Exploring the Spatiotemporal Variability of the Snow Water Equivalent in a Small Boreal Forest Catchment through Observation and Modelling. *Hydrol. Process.* 34 (11), 2628–2644. doi:10.1002/hyp.13756

Perrot, D., Molotch, N. P., Musselman, K. N., and Pugh, E. T. (2014). Modelling the Effects of the Mountain Pine Beetle on Snowmelt in a Subalpine Forest. *Ecohydrol.* 7 (2), 226–241. doi:10.1002/eco.1329

Pomeroy, J. W., Gray, D. M., Hedstrom, N. R., and Janowicz, J. R. (2002). Prediction of Seasonal Snow Accumulation in Cold Climate Forests. *Hydrol. Process.* 16 (18), 3543–3558. doi:10.1002/hyp.1228

Pomeroy, J. W., Gray, D. M., Brown, T., Hedstrom, N. R., Quinton, W. L., Granger, R. J., et al. (2007). The Cold Regions Hydrological Model: a Platform for Basing Process Representation and Model Structure on Physical Evidence. *Hydrol. Process.* 21 (19), 2650–2667. doi:10.1002/hyp.6787

Pomeroy, J. W., Marks, D., Link, T., Ellis, C., Hardy, J., Rowlands, A., et al. (2009). The Impact of Coniferous Forest Temperature on Incoming Longwave Radiation to Melting Snow. *Hydrol. Process.* 23 (17), 2513–2525. doi:10.1002/hyp.7325

Pomeroy, J., Fang, X., and Ellis, C. (2012). Sensitivity of Snowmelt Hydrology in Marmot Creek, Alberta, to Forest Cover Disturbance. *Hydrol. Process.* 26 (12), 1891–1904. doi:10.1002/hyp.9248

Pugh, E., and Gordon, E. (2013). A Conceptual Model of Water Yield Effects from Beetle-Induced Tree Death in Snow-Dominated Lodgepole Pine Forests. *Hydrol. Process.* 27 (14), 2048–2060. doi:10.1002/hyp.9312

Reichstein, M., Falge, E., Baldocchi, D., Papale, D., Aubinet, M., Berbigier, P., et al. (2005). On the Separation of Net Ecosystem Exchange into Assimilation and Ecosystem Respiration: Review and Improved Algorithm. *Glob. Change Biol.* 11 (9), 1424–1439. doi:10.1111/j.1365-2486.2005.001002.x

Revuelto, J., López-Moreno, J.-I., Azorin-Molina, C., Alonso-González, E., and Sanmiguel-Vallelado, A. (2016). Small-Scale Effect of Pine Stand Pruning on Snowpack Distribution in the Pyrenees Observed with a Terrestrial Laser Scanner. *Forests* 7 (8), 166. doi:10.3390/f7080166

Roth, T. R., and Nolin, A. W. (2017). Forest Impacts on Snow Accumulation and Ablation across an Elevation Gradient in a Temperate Montane Environment. *Hydrol. Earth Syst. Sci.* 21 (11), 5427–5442. doi:10.5194/hess-21-5427-2017

Russell, M., Eitel, J. U. H., Link, T. E., and Silva, C. A. (2021). Important Airborne Lidar Metrics of Canopy Structure for Estimating Snow Interception. *Remote Sens.* 13 (20), 4188. doi:10.3390/rs13204188

Rutter, N., Essery, R., Pomeroy, J., Altimir, N., Andreadis, K., Baker, I., et al. (2009). Evaluation of Forest Snow Processes Models (SnowMIP2). *J. Geophys. Res.* 114, D06111. doi:10.1029/2008JD011063

Schelker, J., Kuglerová, L., Eklöf, K., Bishop, K., and Laudon, H. (2013). Hydrological Effects of Clear-Cutting in a Boreal Forest - Snowpack Dynamics, Snowmelt and Streamflow Responses. *J. Hydrol.* 484, 105–114. doi:10.1016/j.jhydrol.2013.01.015

Schwartz, A. J., McGowan, H., and Callow, N. (2020). Impact of Fire on Montane Snowpack Energy Balance in Snow Gum Forest Stands. *Agric. For. Meteorol.* 294, 108164. doi:10.1016/j.agrformet.2020.108164

Sexstone, G. A., and Fassnacht, S. R. (2014). What Drives Basin Scale Spatial Variability of Snowpack Properties in Northern Colorado? *Cryosphere* 8 (2), 329–344. doi:10.5194/tc-8-329-2014

Sexstone, G. A., Clow, D. W., Fassnacht, S. R., Liston, G. E., Hiemstra, C. A., Knowles, J. F., et al. (2018). Snow Sublimation in Mountain Environments and its Sensitivity to Forest Disturbance and Climate Warming. *Water Resour. Res.* 54 (2), 1191–1211. doi:10.1002/2017wr021172

Stähli, M., Jonas, T., and Gustafsson, D. (2009). The Role of Snow Interception in Winter-Time Radiation Processes of a Coniferous Sub-alpine Forest. *Hydrol. Process.* 23 (17), 2498–2512. doi:10.1002/hyp.7180

Steele, C., Dialesandro, J., James, D., Elias, E., Rango, A., and Bleiweiss, M. (2017). Evaluating MODIS Snow Products for Modelling Snowmelt Runoff: Case Study of the Rio Grande Headwaters. *Int. J. Appl. Earth Observ, Geoinf.* 63, 234–243. doi:10.1016/j.jag.2017.08.007

Storck, P., Lettenmaier, D. P., and Bolton, S. M. (2002). Measurement of Snow Interception and Canopy Effects on Snow Accumulation and Melt in a Mountainous Maritime Climate, Oregon, United States. *Water Resour. Res.* 38 (11), 5–1516. doi:10.1029/2002wr001281

Varhola, A., and Coops, N. C. (2013). Estimation of Watershed-Level Distributed Forest Structure Metrics Relevant to Hydrologic Modeling Using LiDAR and Landsat. *J. Hydrol.* 487, 70–86. doi:10.1016/j.jhydrol.2013.02.032

Varhola, A., Coops, N. C., Weiler, M., and Moore, R. D. (2010). Forest Canopy Effects on Snow Accumulation and Ablation: An Integrative Review of Empirical Results. *J. Hydrol.* 392 (3-4), 219–233. doi:10.1016/j.jhydrol.2010.08.009

Veatch, W., Brooks, P. D., Gustafson, J. R., and Molotch, N. P. (2009). 'Quantifying the Effects of Forest Canopy Cover on Net Snow Accumulation at a Continental, Mid-latitude Site'. *Ecohydrol.* 2 (2), 115–128. doi:10.1002/eco.45

Watson, F. G. R., Anderson, T. N., Newman, W. B., Alexander, S. E., and Garrott, R. A. (2006). Optimal Sampling Schemes for Estimating Mean Snow Water Equivalents in Stratified Heterogeneous Landscapes. *J. Hydrol.* 328 (3-4), 432–452. doi:10.1016/j.jhydrol.2005.12.032

Webb, E. K., Pearman, G. I., and Leuning, R. (1980). Correction of Flux Measurements for Density Effects Due to Heat and Water Vapour Transfer. *Q.J R. Metall. Soc.* 106, 85–100. doi:10.1002/qj.49710644707

Wilczak, J. M., Oncley, S. P., and Stage, S. A. (2001). Sonic Anemometer Tilt Correction Algorithms. *Boundary-Layer Meteorol.* 99 (1), 127–150. doi:10.1023/A:1018966204465

Woods, S. W., Ahl, R., Sappington, J., and McCaughey, W. (2006). Snow Accumulation in Thinned Lodgepole Pine Stands, Montana, USA. *For. Ecol. Manag.* 235 (1-3), 202–211. doi:10.1016/j.foreco.2006.08.013

Wu, J., Guan, D., Yuan, F., Yang, H., Wang, A., and Jin, C. (2012). Evolution of Atmospheric Carbon Dioxide Concentration at Different Temporal Scales Recorded in a Tall Forest. *Atmos. Environ.* 61, 9–14. doi:10.1016/j.atmosenv.2012.07.013

Xiao, Y., Li, X., Zhao, S., and Song, G. (2019). Characteristics and Simulation of Snow Interception by the Canopy of Primary Spruce-fir Korean Pine Forests in the Xiaoxing'an Mountains of China. *Ecol. Evol.* 9 (10), 5694–5707. doi:10.1002/ece3.5152

Yang, J., Jiang, L., Dai, L., Pan, J., Wu, S., and Wang, G. (2019). The Consistency of SSM/I vs. SSMIS and the Influence on Snow Cover Detection and Snow Depth Estimation over China. *Remote Sens.* 11 (16), 1879. doi:10.3390/rs11161879

Yao, H., McConnell, C., James, A., and Fu, C. (2012). Comparing and Modifying Eight Empirical Models of Snowmelt Using Data from Harp Experimental Station in Central Ontario. *Br. J. Environ. Clim. Change* 2, 259–277. doi:10.9734/bjecc/2012/2249

Yao, H., Field, T., McConnell, C., Beaton, A., and James, A. L. (2018). Comparison of Five Snow Water Equivalent Estimation Methods across Categories. *Hydrol. Process.* 32 (12), 1894–1908. doi:10.1002/hyp.13129

Zhang, Y., Yan, S., and Lu, Y. (2010). Snow Cover Monitoring Using MODIS Data in Liaoning Province, Northeastern China. *Remote Sens.* 2 (3), 777–793. doi:10.3390/rs2030777

**Conflict of Interest:** The authors declare that the research was conducted in the absence of any commercial or financial relationships that could be construed as a potential conflict of interest.

frontiers | Frontiers in Environmental Science

ORIGINAL RESEARCH
published: 13 July 2022
doi: 10.3389/fenvs.2022.942974

# Reforestation in Southern China Enhances the Convective Afternoon Rainfall During the Post-flood Season

*Xing Li[1,2]*, Xiao Li[1,3], Hedi Ma[4], Wenjian Hua[3], Haishan Chen[3], Xiaohang Wen[1], Wanxin Zhang[1], Yiwen Lu[2], Xueqi Pang[5] and Xuanwen Zhang[5]*

*[1]Plateau Atmosphere and Environment Key Laboratory of Sichuan Province, College of Atmospheric Science, Chengdu University of Information Technology, Chengdu, China, [2]Shanghai Ecological Forecasting and Remote Sensing Center, Shanghai Meteorological Service, Shanghai, China, [3]Key Laboratory of Meteorological Disaster, Ministry of Education (KLME)/Joint International Research Laboratory of Climate and Environment Change (ILCEC)/Collaborative Innovation Center on Forecast and Evaluation of Meteorological Disasters (CIC-FEMD), Nanjing University of Information Science and Technology, Nanjing, China, [4]Hubei Key Laboratory for Heavy Rain Monitoring and Warning Research, Institute of Heavy Rain, China Meteorological Administration, Wuhan, China, [5]Department of Atmospheric and Oceanic Sciences, Fudan University, Shanghai, China*

OPEN ACCESS

**Edited by:**
*Bo Huang,*
*Norwegian University of Science and Technology, Norway*

**Reviewed by:**
*Jun Ge,*
*Nanjing University, China*
*Lian Chen,*
*Shanghai Institute of Satellite Engineering, China*

***Correspondence:**
*Xing Li*
*LX_CUIT@163.com*

**Specialty section:**
*This article was submitted to Interdisciplinary Climate Studies, a section of the journal Frontiers in Environmental Science*

**Received:** *13 May 2022*
**Accepted:** *20 June 2022*
**Published:** *13 July 2022*

**Citation:**
*Li X, Li X, Ma H, Hua W, Chen H, Wen X, Zhang W, Lu Y, Pang X and Zhang X (2022) Reforestation in Southern China Enhances the Convective Afternoon Rainfall During the Post-flood Season. Front. Environ. Sci. 10:942974. doi: 10.3389/fenvs.2022.942974*

Dynamic and continuous land use and cover change (LUCC) is one of the external forcing factors affecting regional climate in China. Based on the annual dynamic global land cover dataset derived from the Global Land Surface Satellite (GLASS-GLC), this paper modelled and investigated the effects of annual transient LUCC on precipitation over China using the regional climate model RegCM4.8.2. Analysis of the GLASS-GLC data revealed that considerable conversions of cropland to forest, grassland to cropland and bare ground to grassland had occurred during the last 3 decades (1984–2013) in southern, northeastern and northwestern China respectively. By comparing the differences between the two sets of experiments under the fixed LUCC and dynamic LUCC scenarios, the results showed that reforestation in southern China during the past 3 decades significantly enhanced local convective afternoon rainfall (CAR; ~2 mm/day) during the post-flood season (POF; July-August-September). This reforestation effect on CAR also increased with the intensity of LUCC. However, the realistic LUCC effects were weak and negligible for other periods, regions and large-scale precipitation. Furthermore, we have identified two possible reasons that favored the occurrence of POFCAR, namely that the moisture and instability conditions required to trigger convections were both enhanced by reforestation. This was evidenced by increases (decreases) in convective available potential energy (lifting condensation level), increases in atmospheric water vapor content and declining tendencies of equivalent potential temperature with height. Overall, this study highlights the importance of reforestation impacts on the diurnal variations of the precipitation.

**Keywords: land use and cover change, regional climate modeling, convective precipitation, GLASS-GLC, southern China**

## INTRODUCTION

Land use and cover change (LUCC) is one of the anthropogenic external forcing factors that affect global and regional climate (IPCC, 2013; IPCC, 2021). According to the latest Intergovernmental Panel on Climate Change (IPCC) Special Report on Climate Change and Land (SRCCL), 71% of the global ice-free land has been used by humans over the historical period, and 24% of the land has also undergone land cover conversion (Arneth et al., 2019). Such intense LUCC can exert influences on local, regional and even global scale weather and climate through two pathways, namely biogeophysical (e.g., Bright, 2015; Chen and Dirmeyer, 2016; Li et al., 2017; Winckler et al., 2017; Hirsch et al., 2018; Li et al., 2018) and biogeochemical (e.g., Claussen et al., 2001; Cherubini et al., 2012; Ciais et al., 2013; Ward et al., 2014) mechanisms. On the one hand, LUCC can modulate the local energy-water balance by changing albedo, evapotranspiration, and roughness, causing changes in weather and climate (e.g., Bonan, 2008; Davin and de Noblet-Ducoudré, 2010; Devaraju et al., 2018). On the other hand, LUCC can also alter the biogeochemical cycle by changing the biomass and the associated atmospheric composition, further affecting climate change and the provision of ecosystem services (Pielke, 2005; Reyers et al., 2009; Devaraju et al., 2015). However, the impact of LUCC on climate is subject to considerable uncertainties and challenges (e.g., Pitman et al., 2009; Pitman et al., 2011; Houghton et al., 2012; Li et al., 2018; Ge et al., 2019), and the IPCC gives only medium confidence in the net global effects of LUCC (IPCC, 2021).

A large number of observational and numerical modeling studies have highlighted the much more significant impacts of LUCC on local and regional climates than the global mean (e.g., Lohila et al., 2010; Lee et al., 2011; Pielke Sr et al., 2011; Hua and Chen, 2013; Mahmood et al., 2014; Lawrence and Vandecar, 2015). However, due to the long-time scales of LUCC and the insufficient accumulation of observations, the regional LUCC effects have been assessed mainly through the global land-use model-based reconstructed LUCC datasets (e.g., the Land-Use Harmonization datasets; Hurtt et al., 2011; Hurtt et al., 2020) and numerical simulations. This results in the confidence in the quantitative impact of LUCC being highly reliant on the model's representations of the LUCC-related processes and the accuracy of the data used to characterize LUCC (Prestele et al., 2017). Numerous studies have used reconstructed data or idealized LUCC scenarios (e.g., complete deforestation) to reveal the effects and mechanisms of historical LUCC on regional and global climate (e.g., Pitman et al., 2012; Chen and Dirmeyer, 2017; Li et al., 2017; Li et al., 2022). These studies generally reached similar conclusions: large-scale and high-intensity LUCCs had considerable regional effects on temperatures and the related extremes, while being relatively weak and more uncertain for precipitation. Due to the relatively coarse resolution of the global model, it is likely that LUCC effects on small-scale processes, such as local wind systems, convections, boundary layer processes and scale-interactions are ignored (Mahmood et al., 2014). Therefore, to better assess the role of LUCC in climate change, more refined representations and explanations of the realistic LUCC and its impacts and mechanisms on climate are needed. Meanwhile, Lawrence and Vandecar (2015) and Mahmood et al. (2016) also pointed out that the quantitative assessments derived from simulations using state-of-the-art mesoscale models and more realistic LUCC scenarios are helpful and useful for local policymakers.

After the 1980s, as satellite data accumulated, satellite-based LUCC datasets with the high resolution and long time series, were developed. For example, the Terra and Aqua combined Moderate Resolution Imaging Spectroradiometer (MODIS) yearly land cover type dataset (e.g., MCD12C1; Sulla-Menashe and Friedl, 2018), the European Space Agency (ESA)-Climate Change Initiative (CCI)-Land Cover (LC) dataset (ESA-CCI-LC; ESA, 2017) and the Global Land Surface Satellite Climate Data Records-derived land cover dataset (GLASS-GLC; Liu et al., 2020). Among these, the GLASS-GLC dataset is the most recent, longest time series and highest average accuracy product of the three popular LUCC datasets mentioned above (Liu et al., 2020). It also provides a reliable data source for the use of regional climate models to simulate the weather-climate effects of the realistic and long-term dynamics of LUCC. Based on the LUCC scenarios characterized by satellite data, a growing number of studies in recent years have also assessed the impacts of realistic LUCC using regional climate models (e.g., Chen et al., 2015; Hu et al., 2015; Zhang et al., 2021). For example, Hu et al. (2015) used the Weather Research and Forecasting (WRF) model to reveal that LUCC (1980 versus 2000s) cooled the surface air temperature in northern China by 0.3–0.5°C and increased summer precipitation in southern China by ~6–7%. Zhang et al. (2021) also used the WRF model and similar LUCC scenarios and experiments to highlight that the impact of LUCC on precipitation in eastern China may be strongly influenced by the large-scale background climate. The vast majority of these studies have assessed the impacts of LUCC based on the comparison of the differences in climate state between the two fixed LUCC scenarios, with no consideration of the interannual variability of LUCC dynamics.

China has experienced the remarkable forest restoration over the last 3 decades, especially in southern China, leading the way in global greening (Chen et al., 2019). In terms of local ecological restoration, afforestation/reforestation significantly reverses land degradation and increases forest carbon sinks to potentially mitigate GHG-induced global warming (e.g., Pan et al., 2011; Bryan et al., 2018). However, afforestation/reforestation as a possible greenhouse gas mitigation strategy to meet climate targets (Grassi et al., 2017), the impacts of its biogeophysical effects (e.g., albedo, roughness and evapotranspiration) in the realistic LUCC scenario, also need to be fully assessed and understood (e.g., Betts, 2000; Bonan, 2008; Davin and de Noblet- Ducoudré, 2010; Perugini et al., 2017; Duveiller et al., 2018). In particular, the effects of forests on precipitation are largely unknown and uncertain, both in terms of their extent and physical mechanisms. This is where the previous researches were highly inadequate. Therefore, based on the above considerations and gaps, this paper explores the effects of realistic LUCC on precipitation over China by using the latest satellite-based LUCC dataset to conduct numerical simulations with a state-of-the-art

regional climate model, focusing on: 1) The quantitative assessment of realistic LUCCs on precipitation, especially the relative contribution of convective and large-scale precipitation responses. 2) The associated physical mechanisms.

# DATA, MODEL AND METHODOLOGY

## Regional Climate Model

The state-of-the-art regional climate model used in this study to investigate the realistic LUCC effects in China is the Regional Climate Model system (RegCM) developed by the International Centre for Theoretical Physics (ICTP). We use RegCM version 4.8.2 and select the Community Land Model version 4.5 (CLM4.5; Oleson et al., 2013) from the United States National Center for Atmospheric Research (NCAR) as the land surface component. RegCM was originally developed by Dickinson et al. (1989) and Giorgi and Bates (1989) for dynamical downscaling in limited-area regional climate modeling. To date, RegCM has been updated to its fourth generation (Giorgi et al., 2012; Coppola et al., 2021) and the fifth generation (preview version can be found at https://github.com/ICTP/RegCM/tree/Version5) will be released soon. RegCM4 is one of the most widely used regional climate models in multiple fields over the last decades (e.g., Gao and Giorgi, 2017). Particularly for East Asia, RegCM4 has become one of the most popular tools for exploring regional climate change and projections, aerosols and LUCCs (e.g., Chen et al., 2015), because of its good capability to reproduce both mean and extreme climates (e.g., Ji and Kang, 2015; Hu et al., 2016). The up-to-date source code of RegCM4 can be obtained from https://github.com/ICTP/RegCM/.

## Satellite Data and Pre-Processing Procedure

The GLASS-GLC land cover dataset is used to characterize a realistic LUCC scenario in our study, which contains the most recently released global annual land cover maps produced using machine learning techniques with a horizontal resolution of 5 km (Liu et al., 2020). The GLASS-GLC has the highest averaged accuracy and the longest time coverage compared to other popular satellite-based land cover datasets such as MCD12C1 and ESA-CCI-LC (Liu et al., 2020). This dataset has seven major land cover types, i.e., cropland, forest, grassland, shrubland, tundra, bare land, and snow/ice and covers a total of 34 global land cover maps for the period 1982–2015. Details of the production of GLASS-GLC can be found in Liu et al. (2020). The raw data can be downloaded from https://store.pangaea.de/Publications/LiuH-etal_2020/GLASS-GLC.zip.

The land surface component of RegCM4, i.e., CLM4.5, has the ability to simulate annual transient LUCC, updating not only the change in PFT percentage every day, but also the associated balance of mass and energy fluxes (Oleson et al., 2013). In order to extract and merge annual dynamic LUCC information from the original GLASS-GLC into the initial and boundary forcings of the land surface model of RegCM4 (i.e., CLM4.5), we need to address the following issues. 1) The conversions of land cover "type" data from the original GLASS-GLC to the plant function type (PFT) "percentage" data required by the CLM. 2) Minimizing the possible year-to-year fluctuations in the original satellite data; 3) Matching the LUCC information from GLASS-GLC as much as possible to the other initial and boundary conditions of CLM4.5 (e.g., leaf area index; LAI). Based on the above consideration, we preprocessed the GLASS-GLC data by closely following the similar procedures to that of Liu et al. (2021b). The detailed processes can be found in the Supporting Information (**Supplementary Appendix S1**). The final pre-processed GLASS-GLC-based land cover forcing data have exactly the same structure as the model default data for simulating dynamic LUCC (i.e., annually percentage information for 17 PFTs: bare ground, eight trees, three shrubs, three grasses and two crop types). In addition, the "urban" type is not included in the GLASS-GLC data, so the realistic LUCC scenario in our study only involves vegetation changes. The urban PFT information remains default and fixed throughout the simulation period. We also emphasize that only the PFT percentage information in the forcing data was changed in this study based on information from GLASS-GLC, and the associated grid-level vegetation parameters (e.g., LAI) changed with annual dynamic PFT-based updates. However, the prescribed PFT-specific vegetation structure values (e.g., LAI, stem area indices and canopy top and bottom heights) for calculating grid-level vegetation parameters remained unchanged.

We first fully examined the spatio-temporal characteristics of the realistic LUCC using two methods, namely the linear trends (**Figure 1**) and the empirical orthogonal function (EOF) leading modes (**Supplementary Figure S1**). **Figure 1** shows the linear trends of four major PFTs (i.e., bare ground, grassland, forests and cropland) percentages during 1984–2013. In short, three evident LUCC regions are detected from the spatial modes: i.e., conversions from cropland to forest in southern China, conversions from grassland to cropland in northeastern China and the conversions from bare ground to grassland major in northwestern China (i.e., parts of Xinjiang province, Tibet and the Hetao region; **Figures 1A–D**). In addition, the EOF results also indicate that dominant spatio-temporal patterns for all types of LUCC in China during the past 30 years have been characterized by overall long-term trends.

## Experimental Design

To investigate the transient LUCC effects and mechanisms on precipitation over China, we conduct two groups of long-term simulations (from 1983 to 2013) using RegCM4. 1) FIXED experiment: the simulation forced by land covers fixed at 1984; 2) TRANS experiment: simulations forced by annual transient land cover maps from 1984–2013. Additionally, to reduce the uncertainty in the results, two additional perturbation runs of the TRANS experiment, noted as TRANS_p1 and TRANS_p2, are performed with limited computational resources. These two perturbed runs randomly perturb the atmospheric temperature and humidity boundary conditions 6-hourly (i.e., add perturbations when update the boundary conditions), with the maximum amplitude being

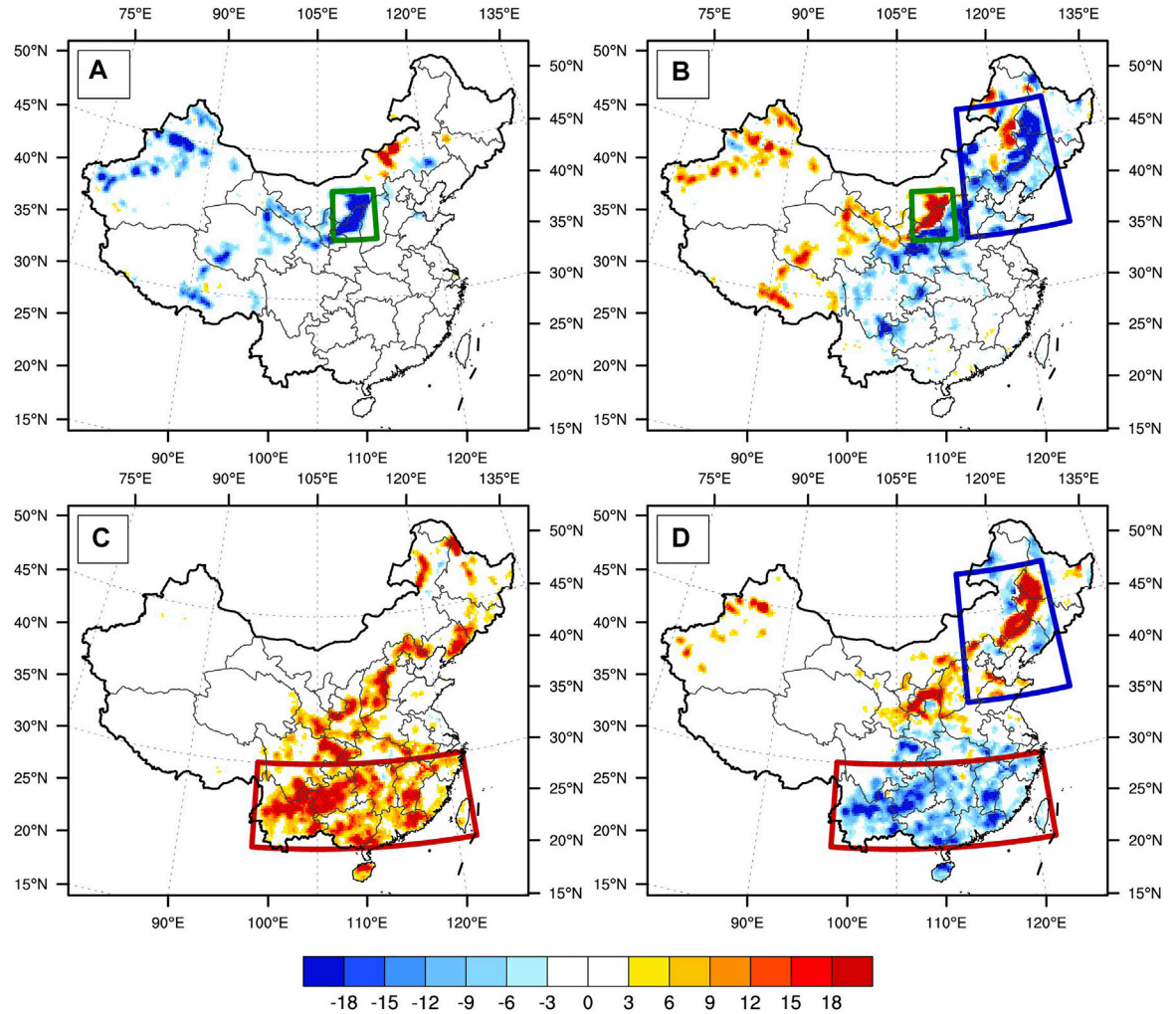


**FIGURE 1 |** The linear trends of four major PFTs percentages during 1984–2013: **(A)** bare ground, **(B)** grassland, **(C)** forest and **(D)** cropland in China, units: %/30a. Note that the red, blue and green rectangles in the figure represent the main cropland-to-forest (21.5–30°N; 98–122°E), grassland-to-cropland (36–49°N; 114–127°E) and bare groud-to-grassland (36–41°N; 107–112.5°E) transition areas, respectively. All colored values in the plots are statistically significant at 95% confidence level.

approximately $10^{-5}$ of the standard deviation of that variable. It should be noted that we change only the land cover maps between the two groups of experiments within China. The land cover information for the rest of the simulated domain (see **Figure 2**) outside of China (e.g., India and Mainland Southeast Asia) is fixed as the default land cover map (i.e., MODIS; Lawrence and Chase, 2007) through the whole simulation periods. All simulations (i.e., both FIXED and TRANS groups) are setup consistently according to the framework of the East Asia domain of the Coordinated Regional Downscaling Experiment (CORDEX) Phase II. In detail, we configure the RegCM computational domain based on the Rotated Mercator map projection centered at (35°N, 116°E) with a total of 280 (north-south) × 428 (west-east) grid points at 25 km spacing, as shown in **Figure 2**. The simulations are driven by the European Center for Medium-Range Weather Forecasts (ECMWF) Interim reanalysis (i.e., ERA-Interim; Dee et al., 2011), which initiate on 1 Jan 1983 and integrate continuously through 31 December 2013. The first year is considered as the spin-up time and is not included in the results below. The sea surface temperatures are prescribed from the monthly sea surface temperature from Hadley Centre (HadISST). The selections of other configurations and various physical parameterizations schemes are listed in **Table 1**. We chose combinations of these schemes because they have been proven to be the "best" combination for modeling the regional climate of East Asia (Han et al., 2015; Gao et al., 2016; Gao et al., 2017).

To better interpret the changes in the PFT and their associated vegetation parameters, we also examined the linear trends of various vegetation parameters (e.g., LAI, surface roughness length and albedo) in the TRANS group, as shown in **Figure 3**. It is clear that the LAI and surface roughness (surface albedo) tend to increase (decrease) due to the reforestation in southern China (**Figure 3**). The conversions of bare ground to grassland in the Hetao area also resulted in a significant increase (decrease) in LAI

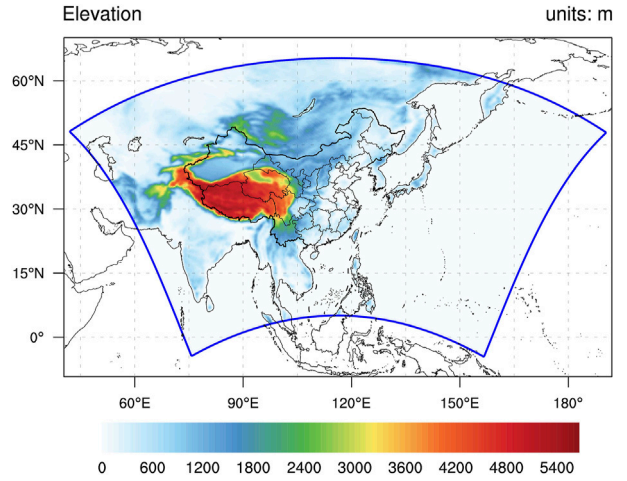


**FIGURE 2 |** The simulation domain and elevations (units: m) of the model. The blue lines indicate the boundary of the simulation domain.

(surface albedo). In addition, the conversion of grassland to cropland in northern China seems to have produced no change in vegetation parameters (**Figure 3**), probably because the vegetation structure values for grassland and cropland in the PFT-specific look-up tables are very close.

## Other Methodology

To measure the significance of the differences between the two experiments (i.e., the LUCC effect), we use a two-tailed modified student *t*-test (Zwiers and von Storch, 1995). By subtracting FIXED simulation from each simulation in TRANS group, we can obtain the LUCC effects in each pair of simulations. Then, we can calculate the multiyear monthly/seasonal ensemble mean to quantify the effects of realistic LUCC. Note that the results in the following sections are represented by the ensemble means. The degrees of consistency (i.e., uncertainties) are defined as follows: "strong" when the LUCC-induced changes have the same sign and are statistically significant (at the 90% confidence level) in all three paired simulations; "moderate" when two of the simulations have the same sign as the ensemble mean and are statistically significant; "weak" when only one simulation is statistically significant; "insignificant" when none of the paired simulations are significant. In addition, some general statistical methods used in this paper (e.g., linear trend) will not be repeatedly described here.

## RESULTS

Previous studies had shown that LUCC effects on daily/monthly mean precipitation were weak and uncertain (e.g.,

**TABLE 1 |** The configurations of the model and the selections of the parameterization schemes.

| Contents | Configurations |
|---|---|
| Dynamical configuration | MM5 hydrostatic dynamic core (Grell et al., 1994) with 23 levels-$\sigma$ coordinate (top at 50 hPa) |
| Cumulus parameterizations | MIT-Emanuel (Emanuel and Živković-Rothman, 1999) for both land and ocean |
| Land surface scheme | NCAR CLM4.5 (Oleson et al., 2013) |
| Planetary boundary layer scheme | Modified Holtslag (Holtslag et al., 1990) |
| Explicit moisture scheme | SUBEX (Pal et al., 2000) |
| Radiation scheme | Modified CCM3 (Kiehl et al., 1996) |
| Ocean flux scheme | Zeng et al., (1998) |

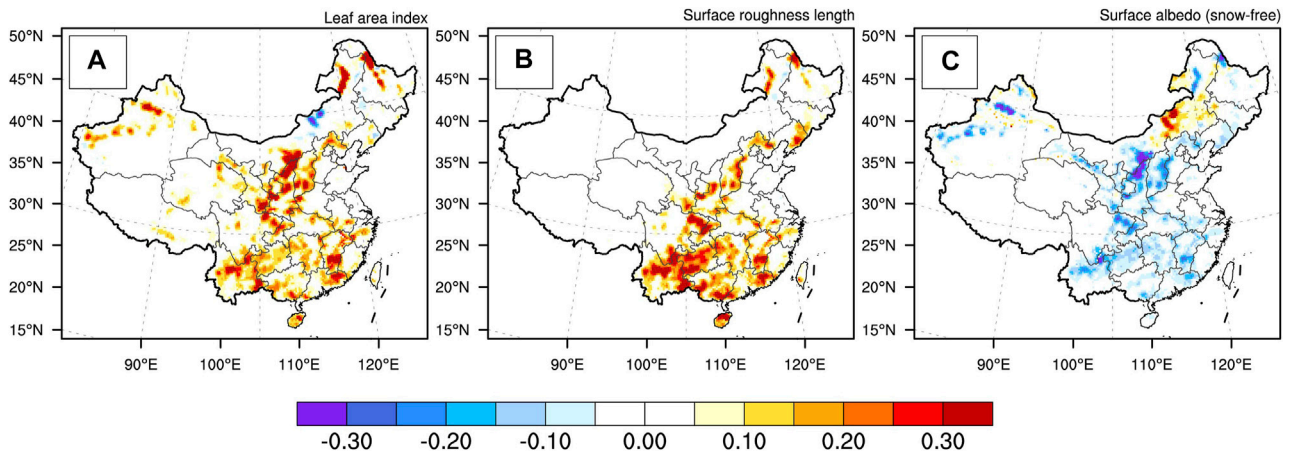


**FIGURE 3 |** The linear trends of various vegetation parameters during 1984–2013 in the TRANS experiment: **(A)** leaf area index, units: $m^2$ $m^{-2}$/30a; **(B)** surface roughness length, units: m/30a; and **(C)** snow-free surface albedo, units: $10^{-1}$/30a. All colored values in the plots are statistically significant at 95% confidence level.

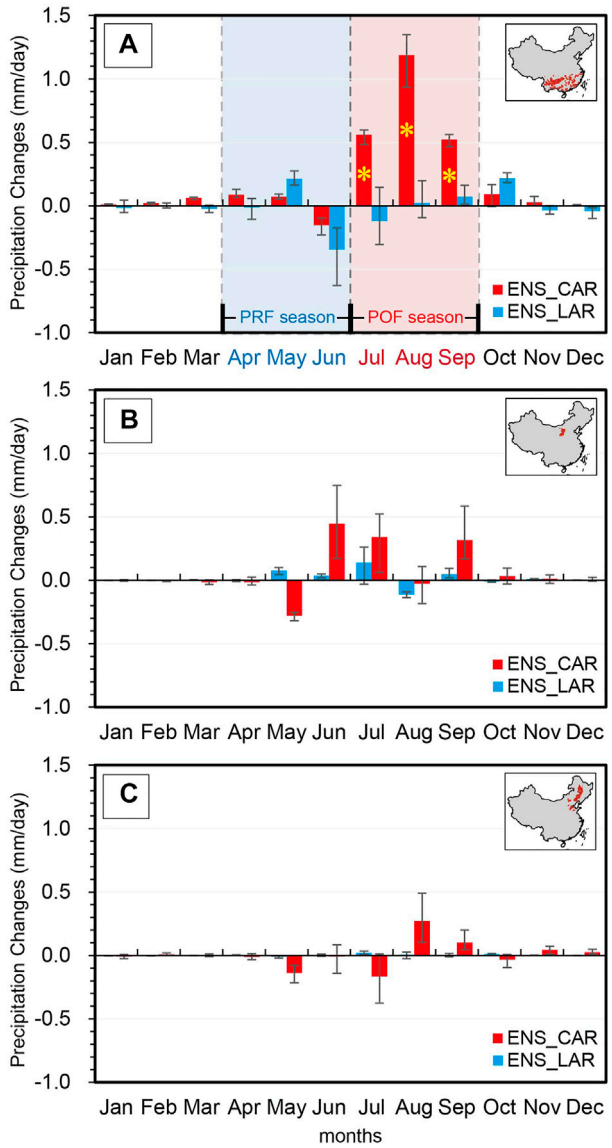


**FIGURE 4 |** The multi-year mean monthly variations of the regional averaged realistic LUCC-induced changes in afternoon convective (red, "CAR") and large-scale (blue, "LAR") rainfall (units: mm/day) for three typical LUCC regions: **(A)** cropland-to-forest transitions in southern China, **(B)** bare ground-to-grassland transitions in Hetao region and **(C)** the grassland-to-cropland transitions in northeastern China. Note that the grids involved in the regional mean calculation are shown in the subplots in the top right corner of each figure. The bars with yellow asterisks inside indicate a greater than "moderate" degree of consistency among the results of the ensemble members. Error bars denote ensemble spread of the changes.

Pitman et al., 2009), however, its effects on sub-daily precipitation may be non-neglighable (e.g., Wang et al., 2000; Chen and Dirmeyer, 2017). During the hot season (especially summer), precipitations often manifest distinct diurnal signals along the southeast coast of China, which are mainly associated with local convective afternoon rainfall events due to local secondary circulations (e.g., sea-land breezes). During the last 30 years, parts of the realistic LUCCs also coincide in southern China (**Figures 1C,D**), where afternoon convection events are frequent during the rainy season. Therefore, in contrast to previous studies that explored the influence of LUCC on precipitation from a daily mean perspective, we focus mainly on the variations of afternoon precipitation in the following results. Because of the wide range of regional longitudes (time zones) spanning in China, it is difficult to characterize the afternoon moment for the whole region with a specific moment at a coarse resolution of 6-hourly. So we define the moment when the daily maximum temperature occurs for a given day at a specific grid point as the local afternoon. All relevant variables, such as precipitation and temperature, shown in the following results refer to the values at that moment. It should also be noted that we separated the total afternoon precipitation into the large-scale and convective precipitation (short for LAR and CAR, respectively) for further investigations.

## Seasonal Afternoon Precipitation Changes in Response to LUCC

We first examine the variations in monthly afternoon precipitation induced by realistic LUCCs over three regions with intense LUCCs, shown as multi-year monthly means of regional averages (**Figure 4**). In general, the responses of afternoon precipitation due to realistic LUCCs are limited. Among the three typical LUCC regions, only the reforestation in southern China have caused significant changes in CAR during the post-flood season of southern China (i.e., July-August-September, short for POF hereinafter), while the other LUCC conversions in the Hetao region (i.e., bare ground-to-grassland conversions) and northern China (i.e., grassland-to-cropland conversions) basically lead to slight and insignificant changes in the LAR and CAR (**Figure 4**). In detail for southern China, reforestation significantly increases the CAR during the POF season (POFCAR hereinafter), with the highest increases of 1.19 mm/day in August, followed by 0.56 mm/day in July and 0.52 mm/day in September, respectively (**Figure 4A**). Meanwhile, the inter-sample uncertainty of the LUCC-induced POFCAR responses is small, i.e., the averaged inter-sample standard deviation of the POFCAR is only 0.11 mm/day (**Figure 4A**). In other months, however, reforestation causes little change (within ± 0.15 mm/day) in CAR, even during the other rainy season in southern China (i.e., the pre-flood season, April-May-June, PRF hereinafter). Furthermore, for the LAR in southern China, reforestation has not caused considerable changes, and the responses to LAR are within ± 0.3 mm/day for all months (**Figure 4A**). In addition, bare ground-to-grassland conversions over the Hetao region induce moderate increases in CAR (~0.3–0.5 mm/day) during part of summer and autumn months, but the responses are not significant (**Figure 4B**). For grassland-to-cropland conversions in northern China, no significant responses of LAR and CAR are detected and the LUCC-induced changes in precipitation are very slight (within ± 0.2 mm/day) in all months (**Figure 4C**).

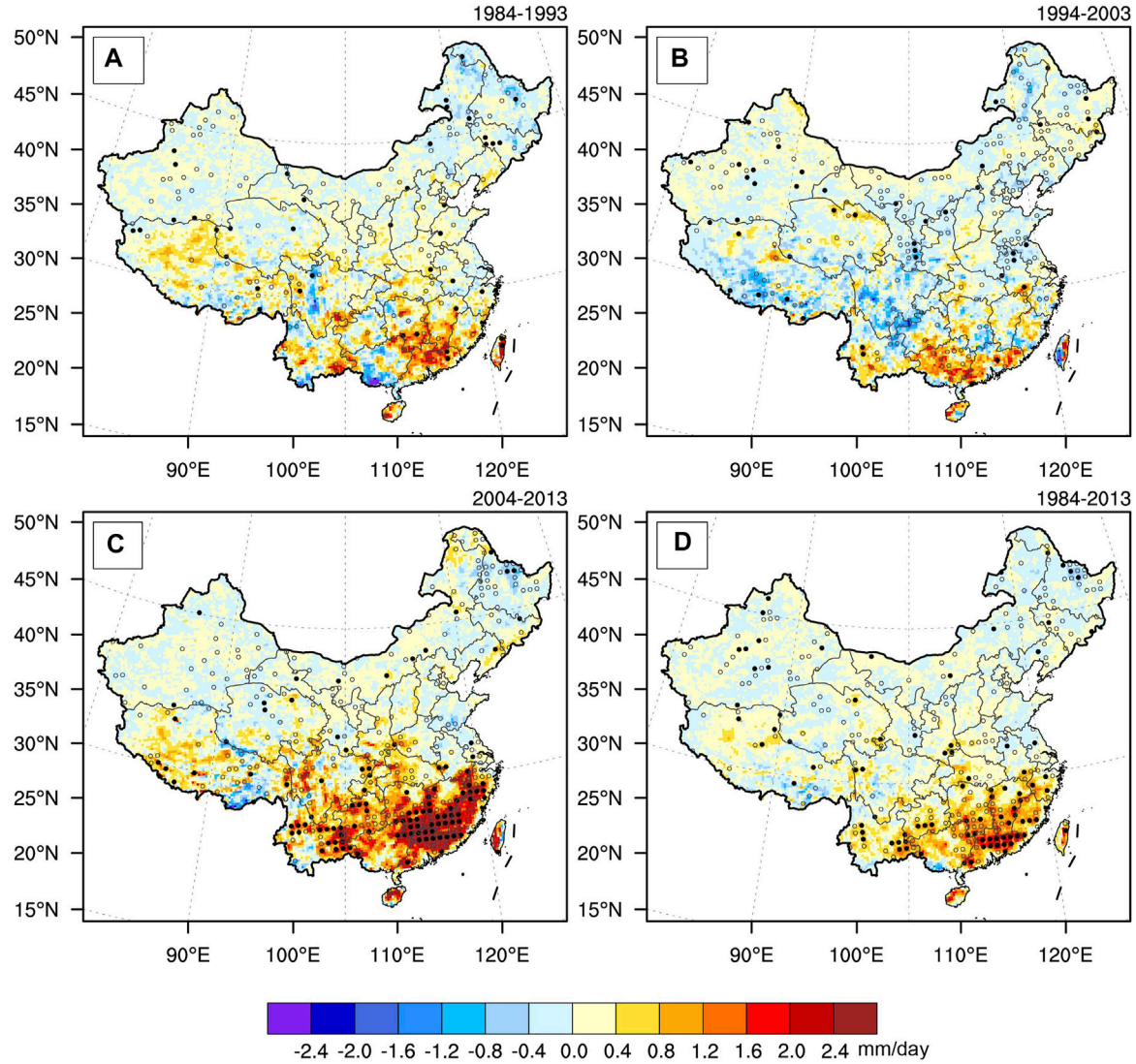


**FIGURE 5 |** The ensemble mean results of realistic LUCC-induced changes in convective afternoon rainfall (CAR; units: mm/day) in the post-flood season (POF; July-August-September) during multiple periods over China: **(A)** 1984–1993, **(B)** 1994–2003, **(C)** 2004–2013, and **(D)** 1984–2013. The solid (hollow) black dots in the figures denote a greater than "moderate" ("weak") degree of consistency among the results of the ensemble members.

## Interannual Variability of Afternoon Precipitation Responses to Reforestation in Southern China

Furthermore, since the realistic and transient LUCC scenario (i.e., the TRANS experiments) would cause the intensity of LUCC to increase over time when compared to the fixed LUCC scenario (i.e., the FIXED experiment), it is likely that the effect of LUCC would also be enhanced in the meantime (e.g., Li et al., 2017). Therefore, we also investigate the spatial patterns of LUCC effects on POFCAR at different decades and the regional averaged interannual variability of POFCAR over southern China due to reforestation to see whether there are enhanced LUCC effects over time. The results are shown in **Figures 5**, **6** respectively. It should be noted that we divided the 30-years simulation period into three sub-periods of equal length (i.e., 1984–1993, 1994–2003, 2004–2013). **Figure 5** shows the spatial differences of LUCC-induced changes in POFCAR during three sub-periods (**Figures 5A–C**) and the entire simulation period (**Figure 5D**). Overall, the impacts of realistic LUCC on POFCAR do vary considerably at different periods (**Figure 5**). In detail, the spatial results show that among the three evident LUCC regions, indeed only the southern reforestation leads to significantly enhanced local POFCAR responses, regardless of whether they are averaged over the entire period (**Figure 5D**) or across the three different decades (**Figures 5A–C**). These results are also in good agreement with the previous regional averaging results. Moreover, the enhancement of LUCC-induced POFCAR over southern China does increase with intensified LUCC strength (**Figures 5A–C**). For example, during periods of weak

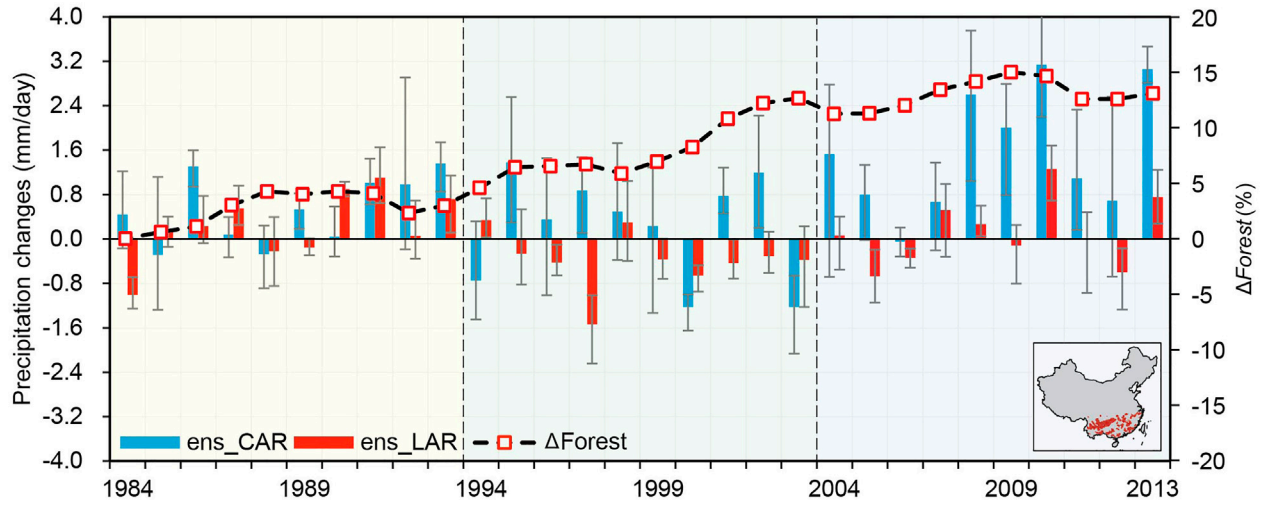


**FIGURE 6 |** The interannual variations (bars) in the regional means of LUCC-induced changes in CAR (red) and LAR (blue) during POF season, units: mm/day, the corresponding uncertainties (error bars) and the intensity of forests (dash lines) over southern China. Note that the precipitation changes are corresponding to the *y*-axis on the left. The dash lines with red hollow square denote Δ*Forest* ("Δ" denotes TRANS minus FIXED), corresponding to the *y*-axis on the right, units: %. The error bars are represented by the ensemble spread of the precipitation changes due to LUCC. The meaning of subplot at the bottom right corner is the same as **Figure 3A**. The different translucent backgrounds in the figure indicate decades with different LUCC intensities (light yellow: 1984–1993; light green: 1994–2003; light blue: 2004–2013).

(i.e., 1984–1993; **Figure 5A**) to moderate LUCC (i.e., 1994–2003; **Figure 5B**), although there are also some enhancements of POFCAR in southern reforestation areas, they are weak in both magnitudes and significances. In contrast, the responses of POFCAR to southern reforestation become very robust and significant during the period of intense LUCC (i.e., 2004–2013; **Figure 5C**). Specifically, reforestation-induced POFCAR show broad and significant enhancements across southern China during 2004–2013, with the magnitude can even exceed 2.4 mm/day (**Figure 5C**). For the entire simulation period, the southern reforestation regions similarly show significant POFCAR enhancements (~1.6–2.0 mm/day) and are likely due to the contribution of the LUCC effects in the last decade (i.e., 2004–2013; **Figure 5D**). Moreover, we examined the percentage changes in CAR due to LUCC to confirm the robustness of the aforementioned absolute changes in CAR (**Supplementary Figure S2**). The results showed that the reforestation in southern China can increase CAR by 10%–20% (20%–30%) during 1984–2013 (2004–2013), which are indeed marked increases. In addition, the CAR responses have some sporadic and weak significant signals in other LUCC areas (e.g., along the Qinghai-Tibet Railway with significant decreases in CAR during 1994–2003). However, the interdecadal variations of such signal are large and not clearly related to the LUCC intensity, which may due to the internal noise of the model.

Besides the CAR, we also examine the spatial patterns of LUCC-induced LAR during the POF season at different decades, and the responses of LAR show sporadic and insignificant variations during all periods (**Supplementary Figure S3**), which are also probably due to the internal noise. In addition, as we mentioned above, POFCAR only responded to reforestation in southern China, whereas the other intense LUCC regions and types (e.g., bare ground-to-grassland in Hetao area and grassland-to-cropland in northeastern China) did not cause significant changes in CAR (almost zero) at any time periods. This may be due to the weak changes in surface properties (e.g., surface roughness, **Figure 3B**) caused by the increase in grassland or the conversion of grassland to cropland when compared to reforestation, which in turn may not be able to produce pronounced changes in CAR through land-atmosphere interactions either.

Furthermore, we also investigate the interannual variability of the regional averaged LUCC-induced LAR and CAR during POF over the southern reforestation region, as shown in **Figure 6**. Obviously, the responses of POFCAR to reforestation are similar to the above findings, i.e., the reforestation-induced enhancement of POFCAR shows a clear increasing tendency over time, which is generally consistent with the intensity of reforestation (**Figure 6**). Meanwhile, the effect of reforestation appears to be effective only for the CAR and not for the LAR, and the LAR shows weak and highly uncertain responses due to reforestation (**Figure 6**). In conclusion, the overall impact of realistic LUCC on precipitation in China is limited, but for specific seasons (i.e., POF) and types of LUCC (i.e., reforestation), it can cause non-negligible changes in CAR. Several studies have also highlighted the effects of LUCC on precipitation from various perspectives and scenarios (e.g., Chen and Dirmeyer, 2017; Wang et al., 2020; Wang et al., 2021). In particular, Chen and Dirmeyer (2017) revealed that deforestation could lead to a reduction in precipitation and CAR, which are opposite to our LUCC scenario and sign of precipitation responses. This further suggests that the current results are intrinsically consistent with these previous findings. What are the mechanisms of the reforestation-induced enhancement of

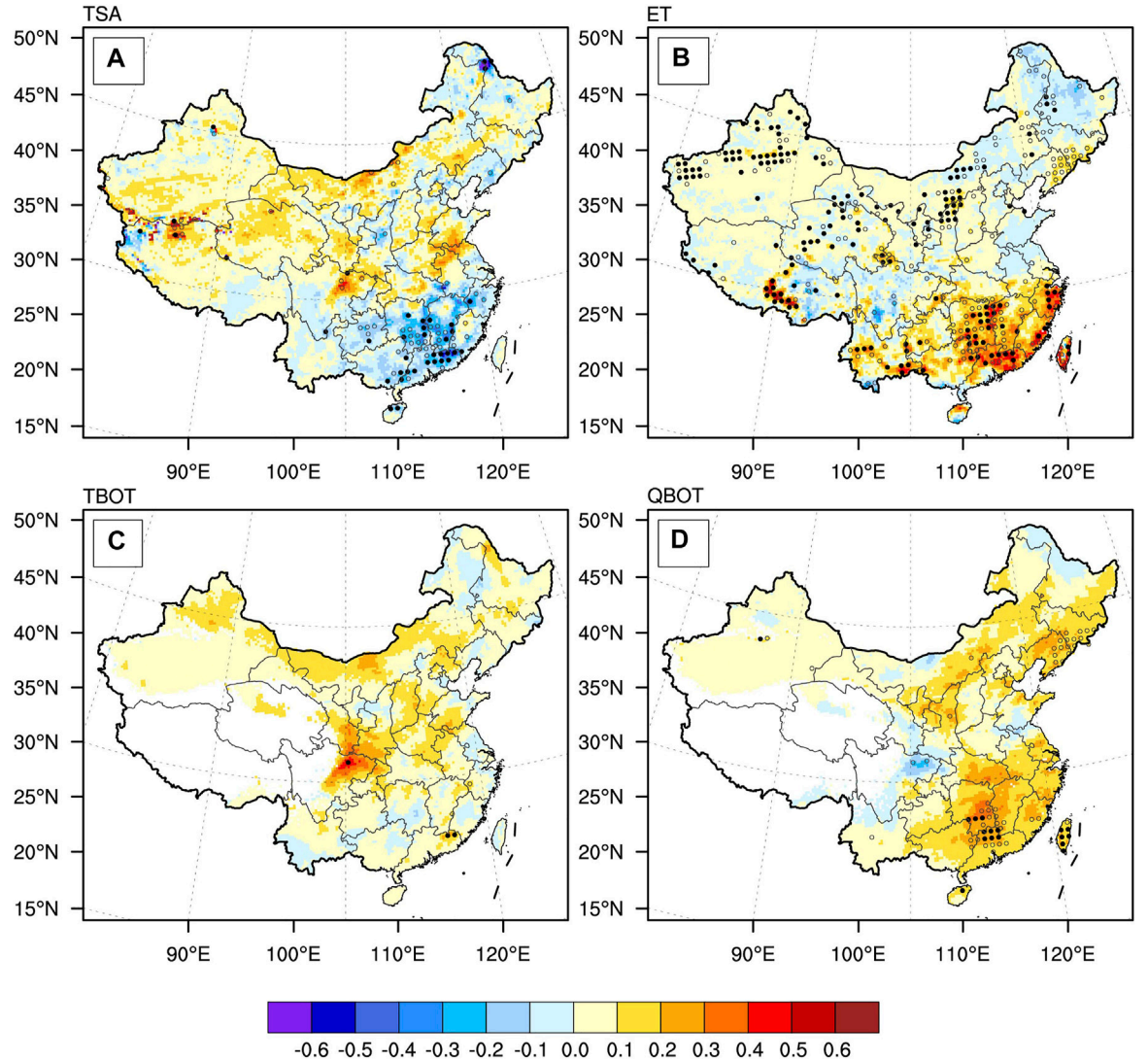


**FIGURE 7 |** The ensemble mean results of realistic LUCC-induced changes in multiple near-surface temperature and humidity variables in POF season during 1984–2013: **(A)** 2 m air temperature (units: °C), **(B)** canopy evapotranspiration (units: $10^1$ W m$^{-2}$), **(C)** atmospheric air temperature at the lowest model level (units: °C) and **(D)** atmospheric specific humidity at the lowest model level (units: g/kg). The meaning of the solid (hollow) black dots is the same as in **Figure 5**. Note that the LUCC-induced changes in the area above 3000 m are masked.

POFCAR in southern China? We will investigate this further in the next section.

## Possible Causes of the Enhanced POFCAR in Southern China

Convective rainfall can theoretically be more effectively triggered by the release of more heat into the planetary boundary layer (PBL) on the one hand, which favors the development of the PBL and the formation of clouds. On the other hand, adding moisture to the lower atmosphere could also lead to moist convection initiations (Findell and Eltahir, 2003a; Findell and Eltahir, 2003b). Therefore, in order to interpret the enhanced POFCAR in southern China, we first examine the realistic LUCC-induced changes in temperature and humidity conditions during POF at the surface and lower atmosphere (i.e., the lowest model level).

**Figure 7** shows the LUCC-induced changes in near-surface air temperature, canopy evapotranspiration, atmospheric temperature and specific humidity at the lowest model level during POF. Generally speaking, reforestation leads to a cooler (**Figure 7A**) and wetter (**Figure 7B**) surface condition in southern China, which probably due to the evaporative cooling effect of forests (Li et al., 2015; Bright et al., 2017; Zeng et al., 2017; Burakowski et al., 2018). In detail, for the surface air temperature, moderate coolings (−0.3~−0.5°C) due to reforestation are generally observed only in the southern China, but their significances show weak and sporadic features (**Figure 7A**). The canopy evapotranspiration (ET) flux is significantly enhanced by 4–6 W m$^{-2}$ due to

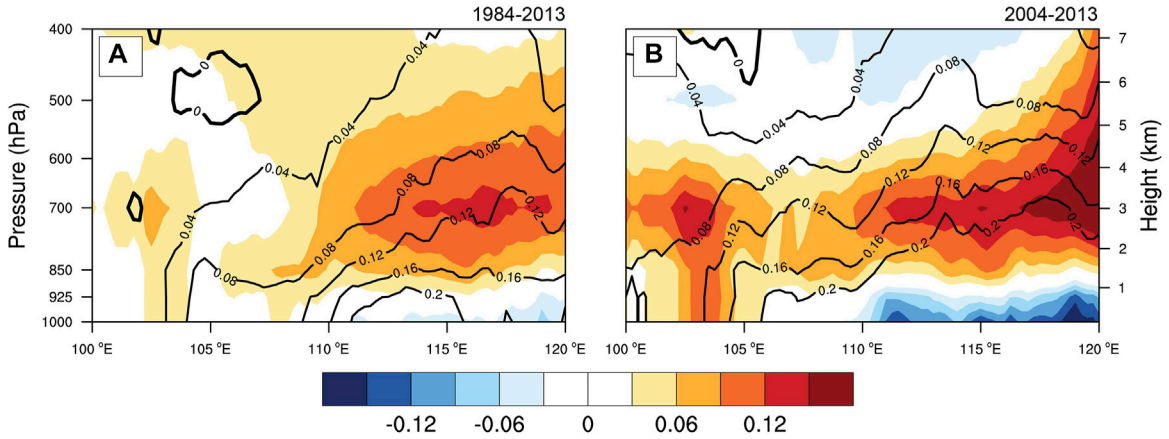


**FIGURE 8 |** The meridional sections (longitude-height) of the LUCC-induced changes in equivalent potential temperature (filled color; units: K) and atmospheric specific humidity (contours; units: g/kg) for the southern China (averaged over 21.5–30 °N) in the POF season during **(A)** 1984–2013 and **(B)** 2004–2013.

reforestation in southern China. In addition, in parts of northwestern China, the conversion of bare ground to grassland also results in slight but significant increases of ET (**Figure 7B**). From changes in surface temperature and humidity, we can infer that the forests probably transport more surface moisture through the canopy and then release them into the atmospheric boundary layer. Furthermore, we also examine the LUCC-induced changes in temperature and humidity conditions at the lower atmosphere (**Figures 7C,D**). The results show that the cooling effect of reforestation in southern China is substantially weakened at the lower atmosphere, with only very slight responses (within ± 0.1°C) remaining (**Figure 7C**). However, for changes in humidity, the enhanced ET at the surface simultaneously results in significant increases in moisture in the lower atmosphere (up to 0.3 g/kg; **Figure 7D**). These results suggest that the enhanced humidity caused by reforestation not only changes the moisture condition at the surface, but also has a broader effect on the boundary layer and lower atmosphere, while the cooling of temperature is generally limited at the surface.

To further understand the responses of reforestation-induced temperature and humidity states (expressed as specific humidity and equivalent potential temperature) in the low-to-mid atmosphere, longitude-height profiles (averaged over 21.5–30 °N) for the southern reforested regions are performed, as shown in **Figure 8**. In terms of water vapor, reforestation causes overall increases in humidity throughout the lower troposphere (i.e., 1000–500 hPa), with the greatest response detected at the surface, and the magnitude of the increase in humidity decreases with height (**Figure 8A**). This considerable increase in the humidity at the lower troposphere is highly corresponding to the previous result of enhanced ET caused by reforestation in southern China during POF (i.e., **Figures 7B,D**). It is noted that the increases in specific humidity provide the necessary moisture conditions for precipitation on the one hand, and on the other hand their vertical characteristics also favor the establishment of a "dry top and wet bottom" stratification, which has the potential to increase the convective instability energy. The equivalent potential temperature ($\theta_e$) is an important parameter for representing the combined features of temperature and humidity, and it is also closely related to the convective available potential energy (CAPE; Machado et al., 2002; Parker 2002; Kalthoff et al., 2011). For the $\theta_e$, it is clear that the highest warming is located at about 700 hPa (~0.15 K; **Figure 7A**), which could lead to increased convective instability in the mid-to-upper troposphere and favoring the vertical stretching of the convection system.

**Figure 9** shows the LUCC-induced changes in convective-related variables associated with the CAR, i.e., CAPE, convection inhibition energy (CIN), atmospheric water vapor content (PRW) and lifting condensation level (LCL). Not surprisingly, there are moderate increases in CAPE due to reforestation in southern China, with an averaged enhancement of approximately 40–60 J $kg^{-1}$ (**Figure 9A**). This is highly correlated with the observed enhancement of CAR in southern reforested regions (i.e., **Figures 4–6**). These results indicate that more days have afternoon convective precipitation triggered when croplands are replaced by forests, leading to increased CAR over this region. In addition to this, we have also detected significant decreases in CAPE over the Yangtze-Huai River Basin, but there is no significant change in either CAR or temperature and humidity state parameters for this area, which is likely due to the remote effects of LUCC or to the internal noise of the model (**Figure 9A**). However, for CIN, little LUCC-induced changes are observed (**Figure 9B**), suggesting that the net instability energy is dominated by LUCC-induced changes in CAPE. The observed response of PRW also shows large increasements in the southern reforested regions, but the significance is relatively weak (**Figure 9C**). Moreover, the LUCC-induced changes in LCL are also examined, as shown in **Figure 9D**. It is clear that the changes of LCL height induced by LUCC strongly reduce by 40–60 m, indicating that the cloud base height is decreasing (**Figure 9D**), which may also favor the initiation of convection.

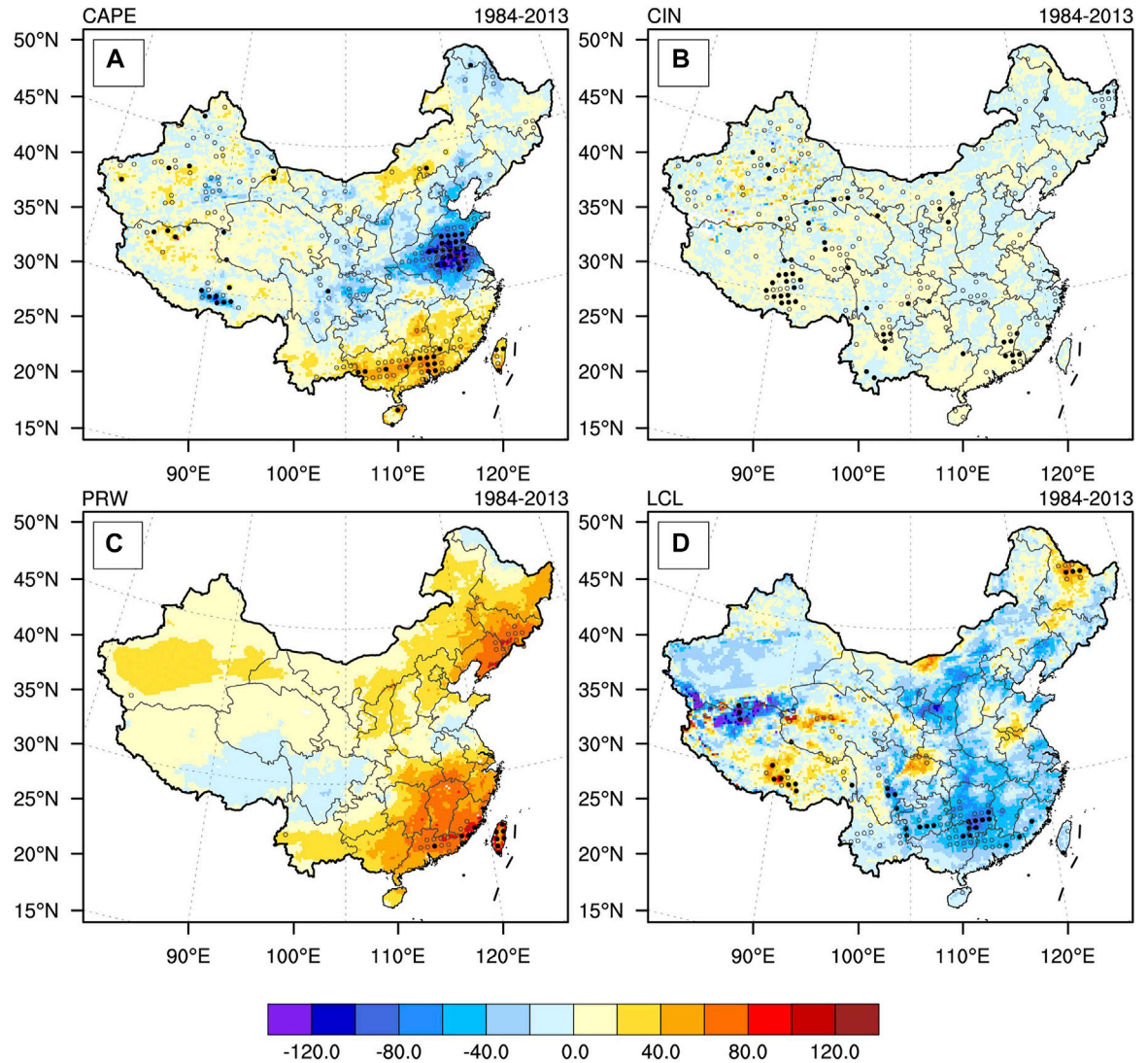


**FIGURE 9 |** Same as **Figure 7**, but for **(A)** convective available potential energy (units: J/kg), **(B)** convection inhibition energy (units: J/kg), **(C)** atmospheric water vapor content (units: $10^{-2}$ mm) and **(D)** lifting condensation level (units: m). The meaning of the solid (hollow) black dots is the same as in **Figure 5**.

In conclusion, these convective-related variables presented above reflect the vertically integrated moisture, instability and condensation needed for the generation and development of CAR, with wetter atmosphere, higher CAPE and lower LCL favoring CAR more. The current mechanism is highly consistent with previous similar studies (e.g., Chen and Dirmeyer, 2017) in which LUCC-induced changes in CAPE dominate changes in convective precipitation.

## DISCUSSION

In the previous part, we modeled the effects of realistic LUCC on the CAR based on the GLASS-GLC-based annual dynamic LUCC information. We found a robust enhancement of POFCAR due to reforestation in southern China, mainly as a result of a combined increase in atmospheric humidity and convective instability energy. Although the current results highlight the non-negligible role of realistic LUCC on the change of CAR, there are still caveats and uncertainties that should be fully discussed. In this section, we will discuss the possible uncertainties of our finding in terms of data, model and mechanisms.

Firstly, the accuracy of LUCC data is crucial to the reliability of modeling results. Although the GLASS-GLC data we used are synthetically the relatively reliable data at present, other datasets do better than GLASS-GLC data in specific aspects. For example, according to Liu et al. (2020), for the cropland type, the accuracy of ESA-CCI-LC data (94.19%) is better than that of GLASS-GLC data (73.26%), when compared with FLUXNET test samples. However, the relatively low classification accuracy may lead to misclassification of the model's grid-level PFT types, which is likely to cause significant changes in surface energy budget and

repartitioning, ultimately involving uncertainty in the model's temperature and precipitation responses (Ge et al., 2019). On the other hand, as the long-term series of LUCC information derived from GLASS-GLC data is limited to changes in the five major land cover types, other realistic land changes that may have potential impacts on climate (e.g., urbanization and irrigation) are not included in our study. For example, Zhong et al. (2017) highlighted that urban heat islands in the Yangtze River Delta urban cluster can increase extreme summer rainfall through enhanced afternoon convergence and updrafts. Liu et al. (2021a) revealed that the cooling and wetting effects of irrigation exerted opposite impacts on convective precipitation over China. To better assess the climate effects of realistic LUCCs, the effects of vegetation changes, urbanization and land management changes (e.g., irrigation) on regional climate need to be considered and quantified simultaneously in future studies.

Furthermore, while our study identified significant impacts of realistic LUCC on POFCAR and its corresponding mechanisms, it is also true that we based on the modeling results of a single regional climate model. Even though our use of limited ensemble simulations can enhance the confidence of the current conclusions, the impacts of LUCC on regional climate, especially on precipitation, are highly uncertain among the multi-models. Using the results of multi-model intercomparison projects (e.g., CMIP5/6 and LUCID), several studies have highlighted the high degree of uncertainty in multi-model quantifications of LUCC impacts (e.g., Pitman et al., 2009; Pitman et al., 2012; Li et al., 2018). In particular, for precipitation, most multi-model responses to LUCC, both in terms of its local and remote responses, were not consistent and significant over most of the globe (Pitman et al., 2009; Pitman et al., 2012). This is closely related to the inter-model descriptions of surface parameters (e.g., albedo, evapotranspiration), the land-atmosphere coupling strength and the selections of multiple parameterizations schemes specified by individual models (e.g., Koster et al., 2006; Pitman et al., 2009; Hirsch et al., 2014; Li et al., 2018). Specifically for RegCM, two additional caveats should be mentioned here. On the one hand, the empirical look-up tables used to determine PFT-specific vegetation parameters are actually inaccurate (Ge et al., 2021), which may further introduce uncertainties to the simulated climate effects of LUCC via influencing surface energy budget, etc. Several recent studies also highlighted the importance of changing vegetation parameters (e.g., LAI) on the regional climate of China, which are critical for improving the model performance in simulating realistic LUCC effects the (e.g., Li et al., 2020; Yu et al., 2020). On the other hand, regional climate models such as RegCM are noted to be less capable of modeling repartitioning effects between latent and sensible heat fluxes (e.g., Ge et al., 2021). This is highly crucial for the confidence of the modeling-derived effects of reforestation/afforestation. Hence, in order to assess the impact of realistic LUCC more accurately, parallel simulations of multiple improved models with multiple ensemble realizations are necessary in future studies. Recently, the Land Use and Climate Across Scales (LUCAS) initiative has been designed for integrating LUCC effects over Europe in RCMs. This is also the first RCM intercomparison project that will go from idealized (phase 1) to realistic high-resolution LUCC scenarios (phases 2 and 3), which is highly consistent with the views and insights expressed in our study. We emphasize the need for more parallel efforts to understand and quantify realistic LUCC impacts - as a potential pathway that could be useful for tackling future climate change. In addition, due to computational resource limitations, we can only conduct simulations of realistic LUCC effects at a relatively coarse (e.g., 25 km) horizontal resolution. It is feasible to describe subgrid-scale precipitation at such a resolution by selecting a convective parameterization scheme, however, this also means that the response of the CARs we have found may depend entirely on the parameterization that we have chosen. In future studies, simulations at a convective-permitting resolution (e.g., <3 km) are also needed in order to better understand the mechanisms of realistic LUCC effects on the convective precipitation.

Last but not least, the current responses of CAR due to reforestation in southern China seem to be valid only during POF, why not for the other seasons or periods? In addition to the POF results presented in the previous section, we carried out the same analysis for atmospheric hydrothermal conditions during the PRF season (**Supplementary Figures S4 and S5**). The results show that for the PRF, the reforestation in southern China does not exert a significant influence on surface and atmospheric humidity and instability energy as it does during the POF period. Thus, in comparison, the weak changes in CAR during the PRF period may be mainly due to the lack of moisture and instability energy conditions that is critical for the development of the convections. This also implies that the alteration of surface energy budget by LUCC can be significantly distinct in the context of different seasonal atmospheric environmental conditions. The influence of the climatic background on LUCC effects has also been widely noted (e.g., Pitman et al., 2011; Hua and Chen, 2013; Li et al., 2018). The detailed mechanisms will need to be examined more specifically in future studies. Furthermore, the effects of reforestation on CAR that we have identified in this study appear to be dominated by local effects. It should be noted that the prescribed sea surface temperatures were used as oceanic forcings in our regional climate simulations, which in fact ignored the indirect effects of LUCC via ocean-atmosphere interactions (e.g., de Noblet-Ducoudré et al., 2012). Ma et al. (2013) also highlighted the significant hydrologic responses in East China to afforestation only occurred when land-ocean-atmosphere coupling was involved. This further implies that the effects (mostly the nonlocal effects) of LUCC are likely underestimated by the current study. Besides, the effects and mechanisms of forests on precipitation, particularly their indirect and remote responses, are still largely unknown. For example, forests are known to be more efficient than the open lands in transporting sensible and latent heat fluxes from the ground to the boundary layer through canopy (Wang et al., 2000; Fisch et al., 2004; Li et al., 2015). As a result, de-/reforestation can not only exert considerable impacts on local climate, but can also cause remote impacts through modulating the atmospheric circulation (e.g., van der Ent et al., 2010). However, the above-mentioned effects of forests show large divergence in the multi-model results particularly for the remote effects, which may be due to large differences in evapotranspiration and atmospheric moisture responses (e.g., Pitman et al., 2009). Besides, a recent study by Xu et al. (2022) also revealed that forests may have completely opposite effects on cloudiness in different areas, which was linked to their specific small-scale heterogeneous landscapes. In short, in addition to the

uncertainties mentioned above, our study obtained certain signals in precipitation in the realistic and dynamic LUCC scenario from numerical experiments, which are helpful for understanding and assessing the real impact of LUCC. A comprehensive understanding of the quantitative impacts of realistic LUCC on regional climate will therefore require detailed researches to further advance.

Despite all the caveats mentioned above, the most important added value of the current study is the uncovering of a non-negligible response of CAR due to LUCC in a realistic scenario. This provides a new insight to revisit the regional climate effects of LUCC and especially its impact on precipitation at sub-daily scale.

## CONCLUSION

This paper used the state-of-the-art regional climate model RegCM4.8.2 to simulate and investigate the impact of annual dynamic realistic LUCC on precipitation in China based on the GLASS-GLC satellite data. Overall, the realistic LUCC has occurred in three main areas over the past 3 decades: the cropland-forest transition zone in southern China, the grassland-cropland transition zone in northeastern China and the bare ground-grassland transition zone in northwestern China. In the context of such realistic LUCC scenario, through the ensemble comparative experiments we found robust enhancements of POFCAR in the LUCC-induced reforestation areas of southern China, with increases in CAR magnitudes of up to 2 mm/day. In contrast, the changes in large-scale precipitation in the afternoon were less pronounced. We also found that this increase in reforestation-induced CAR was enhanced with increasing LUCC intensity in terms of interannual variations. Further analysis revealed that the increase in CAR was most pronounced in the years 2004–2013 (i.e., the decade of greatest LUCC intensity), both in terms of the spatial extent of its significant changes (in almost all southern reforestation areas) and its intensity (which can exceed 2.4 mm/day). However, apart from the above responses, no significant changes in both large-scale and convective precipitation were observed in the other considerable LUCC areas.

Furthermore, we explored the possible mechanisms for the enhanced POFCAR induced by reforestation. Results showed that the changes in POFCAR can be attributed to two possible factors: On the one hand, the reforestation significantly enhanced the evapotranspiration at the surface, resulting in a significant increase in water vapor at the surface and in the lower atmosphere, which provided favorable moisture conditions for the generation of CAR. On the other hand, the enhancement of water vapor was more evident in the lower atmosphere than in the higher atmosphere, thus leading to an unstable "dry-on-top, wet-on-bottom" state of the atmosphere's stratification. In addition, the simultaneous decreases in LCL, the increases in CAPE and the tendency for the equivalent potential temperature to decrease with height all matched such unstable stratification and provided instability energy conditions for the CAR generation. Finally, a wetter atmosphere, higher CAPE and lower LCL induced by intense reforestation produced more CAR.

In summary, our current study uncovered significant effects of realistic LUCC on CAR in southern China. To date, our study is one of the few to use dynamic LUCC forcing rather than fixed LUCC forcing in regional climate simulations to study the climate impacts of regional LUCC in China. Although our study is only the result of a single model, we again emphasize the importance of anthropogenic interventions in forest changes as a potentially critical strategy for tackling climate change. In future studies, multi-model ensemble comparisons under a unified framework are required to better assess the biogeophysical effects of historical and future LUCC and forest changes.

## DATA AVAILABILITY STATEMENT

The data analyzed in this study is subject to the following licenses/restrictions: The GLASS-GLC data is openly available at https://store.pangaea.de/Publications/LiuH-etal_2020/GLASS-GLC.zip. The ERA-interim and HadISST data used for running the model can be obtained from https://apps.ecmwf.int/datasets/data/interim-full-daily/levtype=pl/ and https://www.metoffice.gov.uk/hadobs/hadisst/data/download.html, respectively. The source code of the RegCM model can be obtained from https://github.com/ICTP/RegCM/. We thank the relevant institutions for offering the data and codes. The raw model data supporting the conclusions of this article will be made available by the authors, without undue reservation.

## AUTHOR CONTRIBUTIONS

XnL, HM, WH, HC, and XW contributed to conception and design of the study. XP and XZ organized the database. XnL, XaL, WZ, and YL performed the statistical analysis. XnL and XaL wrote the first draft of the manuscript. XnL, HM, and WH wrote sections of the manuscript. All authors contributed to manuscript revision, read and approved the submitted version.

## FUNDING

This study was jointly supported by the Shanghai Sailing Program (19YF1443800), the National Natural Science Foundation of China (41905065, 41905080), the Natural Science Foundation of Jiangsu Province (BK20200096), the Joint Open Project of KLME and CIC-FEMD, NUIST (KLME202002), the Scientific Research Foundation of CUIT (KYTZ202124, KYTZ202123) and the Innovation Team Fund of Southwest Regional Meteorological Center, China Meteorological Administration.

## SUPPLEMENTARY MATERIAL

The Supplementary Material for this article can be found online at: https://www.frontiersin.org/articles/10.3389/fenvs.2022.942974/full#supplementary-material

## REFERENCES


Arneth, A., Denton, F., Agus, F., Elbehri, A., Erb, K., Osman Elasha, B., et al. (2019). "Framing and Context," in *Climate Change and Land: An IPCC Special Report on Climate Change, Desertification, Land Degradation, Sustainable Land Management, Food Security, and Greenhouse Gas Fluxes in Terrestrial Ecosystems*. Editors P. R. Shukla, J. Skea, E. Calvo Buendia, V. Masson-Delmotte, H.-O. Pörtner, D. C. Roberts, et al. In press. https://www.ipcc.ch/site/assets/uploads/sites/4/2019/12/04_Chapter-1.pdf.

Betts, R. A. (2000). Offset of the Potential Carbon Sink from Boreal Forestation by Decreases in Surface Albedo. *Nature* 408 (6809), 187–190. doi:10.1038/35041545

Bonan, G. B. (2008). Forests and Climate Change: Forcings, Feedbacks, and the Climate Benefits of Forests. *Science* 320 (5882), 1444–1449. doi:10.1126/science.1155121

Bright, R. M., Davin, E., O'Halloran, T., Pongratz, J., Zhao, K., and Cescatti, A. (2017). Local Temperature Response to Land Cover and Management Change Driven by Non-radiative Processes. *Nat. Clim. Change* 7 (4), 296–302. doi:10.1038/nclimate3250

Bright, R. M. (2015). Metrics for Biogeophysical Climate Forcings from Land Use and Land Cover Changes and Their Inclusion in Life Cycle Assessment: a Critical Review. *Environ. Sci. Technol.* 49 (6), 3291–3303. doi:10.1021/es505465t

Bryan, B. A., Gao, L., Ye, Y., Sun, X., Connor, J. D., Crossman, N. D., et al. (2018). China's Response to a National Land-System Sustainability Emergency. *Nature* 559 (7713), 193–204. doi:10.1038/s41586-018-0280-2

Burakowski, E., Tawfik, A., Ouimette, A., Lepine, L., Novick, K., Ollinger, S., et al. (2018). The Role of Surface Roughness, Albedo, and Bowen Ratio on Ecosystem Energy Balance in the Eastern United States. *Agric. For. Meteorology* 249, 367–376. doi:10.1016/j.agrformet.2017.11.030

Chen, C., Park, T., Wang, X., Piao, S., Xu, B., Chaturvedi, R. K., et al. (2019). China and India Lead in Greening of the World through Land-Use Management. *Nat. Sustain* 2 (2), 122–129. doi:10.1038/s41893-019-0220-7

Chen, H., Li, X., and Hua, W. (2015). Numerical Simulation of the Impact of Land Use/land Cover Change over China on Regional Climates during the Last 20 Years. *Chin. J. Atmos. Sci. (in Chinese)* 39 (2), 357–369. doi:10.3878/j.issn.1006-9895.1404.14114

Chen, L., and Dirmeyer, P. A. (2016). Adapting Observationally Based Metrics of Biogeophysical Feedbacks from Land Cover/land Use Change to Climate Modeling. *Environ. Res. Lett.* 11 (3), 034002. doi:10.1088/1748-9326/11/3/034002

Chen, L., and Dirmeyer, P. A. (2017). Impacts of Land-Use/land-Cover Change on Afternoon Precipitation over North America. *Journal of Climate* 30 (6), 2121–2140. doi:10.1175/jcli-d-16-0589.1

Cherubini, F., Bright, R. M., and Strømman, A. H. (2012). Site-specific Global Warming Potentials of Biogenic CO 2 for Bioenergy: Contributions from Carbon Fluxes and Albedo Dynamics. *Environ. Res. Lett.* 7 (4), 045902. doi:10.1088/1748-9326/7/4/045902

Ciais, P., Sabine, C., Bala, G., Bopp, L., Brovkin, V., Canadell, J., et al. (2013). "Carbon and Other Biogeochemical Cycles," in *Climate Change 2013: The Physical Science Basis. Contribution of Working Group I to the Fifth Assessment Report of the Intergovernmental Panel on Climate Change*. Editors T. F. Stocker, D. Qin, G.-K. Plattner, M. Tignor, S. K. Allen, J. Boschung, et al. (Cambridge, United Kingdom and New York, NY, USA: Cambridge University Press), 465–570. doi:10.1017/CBO9781107415324.015

Claussen, M., Brovkin, V., and Ganopolski, A. (2001). Biogeophysical versus Biogeochemical Feedbacks of Large-Scale Land Cover Change. *Geophys. Res. Lett.* 28 (6), 1011–1014. doi:10.1029/2000gl012471

Coppola, E., Stocchi, P., Pichelli, E., Torres Alavez, J. A., Glazer, R., Giuliani, G., et al. (2021). Non-Hydrostatic RegCM4 (RegCM4-NH): Model Description and Case Studies over Multiple Domains. *Geosci. Model. Dev.* 14 (12), 7705–7723. doi:10.5194/gmd-14-7705-2021

Davin, E. L., and de Noblet-Ducoudré, N. (2010). Climatic Impact of Global-Scale Deforestation: Radiative versus Nonradiative Processes. *Journal of Climate* 23 (1), 97–112. doi:10.1175/2009jcli3102.1

de Noblet-Ducoudré, N., Boisier, J.-P., Pitman, A., Bonan, G. B., Brovkin, V., Cruz, F., et al. (2012). Determining Robust Impacts of Land-Use-Induced Land Cover Changes on Surface Climate over North America and Eurasia: Results from the First Set of LUCID Experiments. *Journal of Climate* 25 (9), 3261–3281. doi:10.1175/JCLI-D-11-00338.1

Dee, D. P., Uppala, S. M., Simmons, A. J., Berrisford, P., Poli, P., Kobayashi, S., et al. (2011). The ERA-Interim Reanalysis: Configuration and Performance of the Data Assimilation System. *Q.J.R. Meteorol. Soc.* 137 (656), 553–597. doi:10.1002/qj.828

Devaraju, N., Bala, G., and Nemani, R. (2015). Modelling the Influence of Land-Use Changes on Biophysical and Biochemical Interactions at Regional and Global Scales. *Plant Cell. Environ* 38 (9), 1931–1946. doi:10.1111/pce.12488

Devaraju, N., de Noblet-Ducoudré, N., Quesada, B., and Bala, G. (2018). Quantifying the Relative Importance of Direct and Indirect Biophysical Effects of Deforestation on Surface Temperature and Teleconnections. *Journal of Climate* 31 (10), 3811–3829. doi:10.1175/jcli-d-17-0563.1

Dickinson, R. E., Errico, R. M., Giorgi, F., and Bates, G. T. (1989). A Regional Climate Model for the Western United States. *Climatic Change* 15 (3), 383–422. doi:10.1007/bf00240465

Duveiller, G., Forzieri, G., Robertson, E., Li, W., Georgievski, G., Lawrence, P., et al. (2018). Biophysics and Vegetation Cover Change: A Process-Based Evaluation Framework for Confronting Land Surface Models With Satellite Observations. *Earth Syst. Sci. Data*. 10 (3), 1265–1279. doi:10.5194/essd-10-1265-2018

Emanuel, K. A., and Živković-Rothman, M. (1999). Development and Evaluation of a Convection Scheme for Use in Climate Models. *J. Atmos. Sci.* 56 (11), 1766–1782. doi:10.1175/1520-0469(1999)056<1766:daeoac>2.0.co;2

ESA (2017). Land Cover CCI Product User Guide Version 2. Available at: https://maps.elie.ucl.ac.be/CCI/viewer/download/ESACCI-LC-Ph2-PUGv2_2.0.pdf. (Accessed June 29, 2022).

Findell, K. L., and Eltahir, E. A. B. (2003a). Atmospheric Controls on Soil Moisture-Boundary Layer Interactions. Part I: Framework Development. *J. Hydrometeor* 4 (3), 552–569. doi:10.1175/1525-7541(2003)004<0552:acosml>2.0.co;2

Findell, K. L., and Eltahir, E. A. B. (2003b). Atmospheric Controls on Soil Moisture-Boundary Layer Interactions. Part II: Feedbacks within the Continental United States. *J. Hydrometeor* 4 (3), 570–583. doi:10.1175/1525-7541(2003)004<0570:acosml>2.0.co;2

Fisch, G., Tota, J., Machado, L. A. T., Silva Dias, M. A. F., Lyra, R. F. d. F., Nobre, C. A., et al. (2004). The Convective Boundary Layer over Pasture and Forest in Amazonia. *Theoretical and Applied Climatology* 78 (1), 47–59. doi:10.1007/s00704-004-0043-x

Gao, X.-J., Shi, Y., and Giorgi, F. (2016). Comparison of Convective Parameterizations in RegCM4 Experiments over China with CLM as the Land Surface Model. *Atmospheric and Oceanic Science Letters* 9 (4), 246–254. doi:10.1080/16742834.2016.1172938

Gao, X., and Giorgi, F. (2017). Use of the RegCM System over East Asia: Review and Perspectives. *Engineering* 3 (5), 766–772. doi:10.1016/j.eng.2017.05.019

Gao, X., Shi, Y., Han, Z., Wang, M., Wu, J., Zhang, D., et al. (2017). Performance of RegCM4 over Major River Basins in China. *Adv. Atmos. Sci.* 34 (4), 441–455. doi:10.1007/s00376-016-6179-7

Ge, J., Pitman, A. J., Guo, W., Wang, S., and Fu, C. (2019). Do uncertainties in the Reconstruction of Land Cover Affect the Simulation of Air Temperature and Rainfall in the CORDEX Region of East Asia? *J. Geophys. Res. Atmos.* 124 (7), 3647–3670. doi:10.1029/2018jd029945

Ge, J., Qiu, B., Chu, B., Li, D., Jiang, L., Zhou, W., et al. (2021). Evaluation of Coupled Regional Climate Models in Representing the Local Biophysical Effects of Afforestation over Continental China. *Journal of Climate* 34 (24), 9879–9898. doi:10.1175/jcli-d-21-0462.1

Giorgi, F., and Bates, G. T. (1989). The Climatological Skill of a Regional Model over Complex Terrain. *Mon. Wea. Rev.* 117 (11), 2325–2347. doi:10.1175/1520-0493(1989)117<2325:tcsoar>2.0.co;2

Giorgi, F., Coppola, E., Solmon, F., Mariotti, L., Sylla, M., Bi, X., et al. (2012). RegCM4: Model Description and Preliminary Tests over Multiple CORDEX Domains. *Clim. Res.* 52, 7–29. doi:10.3354/cr01018

Grassi, G., House, J., Dentener, F., Federici, S., den Elzen, M., and Penman, J. (2017). The Key Role of Forests in Meeting Climate Targets Requires Science for Credible Mitigation. *Nature Clim Change* 7 (3), 220–226. doi:10.1038/nclimate3227

Grell, G. A., Dudhia, J., and Stauffer, D. R. (1994). *A Description of the Fifth-Generation Penn State/NCAR Mesoscale Model (MM5)*. Boulder, CO: NCAR.

Han, Z., Gao, X., Shi, Y., Wu, J., Wang, M., and Giorgi, F. (2015). Development of Chinese High Resolution Land Cover Data for the RegCM4/CLM and its

Impact on Regional Climate Simulation. *Journal of Glaciology Geocryology (in Chinese)* 37 (4), 857–866. doi:10.7522/j.issn.1000-0240.2015.0095

Hirsch, A. L., Guillod, B. P., Seneviratne, S. I., Beyerle, U., Boysen, L. R., Brovkin, V., et al. (2018). Biogeophysical Impacts of Land-Use Change on Climate Extremes in Low-Emission Scenarios: Results from HAPPI-Land. *Earth's Future.* 6 (3), 396–409. doi:10.1002/2017ef000744

Hirsch, A. L., Pitman, A. J., and Kala, J. (2014). The Role of Land Cover Change in Modulating the Soil Moisture-Temperature Land-Atmosphere Coupling Strength over Australia. *Geophys. Res. Lett.* 41 (16), 5883–5890. doi:10.1002/2014gl061179

Holtslag, A. A. M., De Bruijn, E. I. F., and Pan, H.-L. (1990). A High Resolution Air Mass Transformation Model for Short-Range Weather Forecasting. *Mon. Wea. Rev.* 118 (8), 1561–1575. doi:10.1175/1520-0493(1990)118<1561:ahramt>2.0.co;2

Houghton, R. A., House, J. I., Pongratz, J., van der Werf, G. R., DeFries, R. S., Hansen, M. C., et al. (2012). Carbon Emissions from Land Use and Land-Cover Change. *Biogeosciences* 9 (12), 5125–5142. doi:10.5194/bg-9-5125-2012

Hu, Y., Zhang, X.-Z., Mao, R., Gong, D.-Y., Liu, H.-b., and Yang, J. (2015). Modeled Responses of Summer Climate to Realistic Land Use/cover Changes from the 1980s to the 2000s over Eastern China. *J. Geophys. Res. Atmos.* 120 (1), 167–179. doi:10.1002/2014jd022288

Hu, Y., Zhong, Z., Lu, W., Zhang, Y., and Sun, Y. (2016). Evaluation of RegCM4 in Simulating the Interannual and Interdecadal Variations of Meiyu Rainfall in China. *Theoretical and Applied Climatology* 124 (3), 757–767. doi:10.1007/s00704-015-1459-1

Hua, W., and Chen, H. (2013). Recognition of Climatic Effects of Land Use/land Cover Change under Global Warming. *Chin. Sci. Bull.* 58 (31), 3852–3858. doi:10.1007/s11434-013-5902-3

Hurtt, G. C., Chini, L. P., Frolking, S., Betts, R. A., Feddema, J., Fischer, G., et al. (2011). Harmonization of Land-Use Scenarios for the Period 1500–2100: 600 Years of Global Gridded Annual Land-Use Transitions, Wood Harvest, and Resulting Secondary Lands. *Climatic Change* 109 (1), 117. doi:10.1007/s10584-011-0153-2

Hurtt, G. C., Chini, L., Sahajpal, R., Frolking, S., Bodirsky, B. L., Calvin, K., et al. (2020). Harmonization of Global Land Use Change and Management for the Period 850-2100 (LUH2) for CMIP6. *Geosci. Model. Dev.* 13 (11), 5425–5464. doi:10.5194/gmd-13-5425-2020

Ji, Z., and Kang, S. (2015). Evaluation of Extreme Climate Events Using a Regional Climate Model for China. *Int. J. Climatol.* 35 (6), 888–902. doi:10.1002/joc.4024

Kalthoff, N., Kohler, M., Barthlott, C., Adler, B., Mobbs, S. D., Corsmeier, U., et al. (2011). The Dependence of Convection-Related Parameters on Surface and Boundary-Layer Conditions Over Complex Terrain. *Q. J. R. Meteorol. Soc.* 137 (S1), 70–80. doi:10.1002/qj.686

Kiehl, J. T., Hack, J. J., Bonan, G. B., Boville, B. A., Briegleb, B. P., Williamson, D. L., et al. (1996). *Description of the NCAR Community Climate Model (CCM3). Technical Note*. Boulder, CO: NCAR.

Koster, R. D., Sud, Y. C., Guo, Z., Dirmeyer, P. A., Bonan, G., Oleson, K. W., et al. (2006). GLACE: The Global Land-Atmosphere Coupling Experiment. Part I: Overview. *Journal of Hydrometeorology* 7 (4), 590–610. doi:10.1175/jhm510.1

Lawrence, P. J., and Chase, T. N. (2007). Representing a New MODIS Consistent Land Surface in the Community Land Model (CLM 3.0). *J. Geophys. Res.* 112 (G1), G01023. doi:10.1029/2006JG000168

Lawrence, D., and Vandecar, K. (2015). Effects of Tropical Deforestation on Climate and Agriculture. *Nature Clim Change* 5 (1), 27–36. doi:10.1038/nclimate2430

Lee, X., Goulden, M. L., Hollinger, D. Y., Barr, A., Black, T. A., Bohrer, G., et al. (2011). Observed Increase in Local Cooling Effect of Deforestation at Higher Latitudes. *Nature* 479 (7373), 384–387. doi:10.1038/nature10588

Li, X., Chen, H., Liao, H., Hua, W., Sun, S., Ma, H., et al. (2017). Potential Effects of Land Cover Change on Temperature Extremes over Eurasia: Current versus Historical Experiments. *Int. J. Climatol* 37 (S1), 59–74. doi:10.1002/joc.4976

Li, X., Chen, H., Wei, J., Hua, W., Sun, S., Ma, H., et al. (2018). Inconsistent Responses of Hot Extremes to Historical Land Use and Cover Change Among the Selected CMIP5 Models. *J. Geophys. Res. Atmos.* 123 (7), 3497–3512. doi:10.1002/2017jd028161

Li, Y., Brando, P. M., Morton, D. C., Lawrence, D. M., Yang, H., and Randerson, J. T. (2022). Deforestation-induced Climate Change Reduces Carbon Storage in Remaining Tropical Forests. *Nat Commun* 13 (1), 1964. doi:10.1038/s41467-022-29601-0

Li, Y., Piao, S., Chen, A., Ciais, P., and Li, L. Z. X. (2020). Local and Teleconnected Temperature Effects of Afforestation and Vegetation Greening in China. *National Science Review* 7 (5), 897–912. doi:10.1093/nsr/nwz132

Li, Y., Zhao, M., Motesharrei, S., Mu, Q., Kalnay, E., and Li, S. (2015). Local Cooling and Warming Effects of Forests Based on Satellite Observations. *Nat Commun* 6 (1), 6603. doi:10.1038/ncomms7603

Liu, G., Wang, W., Shao, Q., Wei, J., Zheng, J., Liu, B., et al. (2021a). Simulating the Climatic Effects of Irrigation over China by Using the WRF-Noah Model System with Mosaic Approach. *Journal of Geophysical Research Atmospheres* 126 (15), e2020JD034428. doi:10.1029/2020jd034428

Liu, H., Gong, P., Wang, J., Clinton, N., Bai, Y., and Liang, S. (2020). Annual Dynamics of Global Land Cover and its Long-Term Changes from 1982 to 2015. *Earth Syst. Sci. Data* 12 (2), 1217–1243. doi:10.5194/essd-12-1217-2020

Liu, S., Liu, X., Yu, L., Wang, Y., Zhang, G. J., Gong, P., et al. (2021b). Climate Response to Introduction of the ESA CCI Land Cover Data to the NCAR CESM. *Climate Dynamics* 56 (11), 4109–4127. doi:10.1007/s00382-021-05690-3

Lohila, A., Minkkinen, K., Laine, J., Savolainen, I., Tuovinen, J.-P., Korhonen, L., et al. (2010). Forestation of Boreal Peatlands: Impacts of Changing Albedo and Greenhouse Gas Fluxes on Radiative Forcing. *J. Geophys. Res.* 115 (G4), G04011. doi:10.1029/2010jg001327

Ma, D., Notaro, M., Liu, Z., Chen, G., and Liu, Y. (2013). Simulated Impacts of Afforestation in East China Monsoon Region as Modulated by Ocean Variability. *Climate Dynamics* 41 (9), 2439–2450. doi:10.1007/s00382-012-1592-9

Machado, L. A. T., Laurent, H., and Lima, A. A. (2002). Diurnal March of the Convection Observed During TRMM-WETAMC/LBA. *J. Geophys. Res.* 107 (D20), 8064. doi:10.1029/2001JD000338

Mahmood, R., Pielke, R. A., Hubbard, K. G., Niyogi, D., Dirmeyer, P. A., McAlpine, C., et al. (2014). Land Cover Changes and Their Biogeophysical Effects on Climate. *Int. J. Climatol.* 34 (4), 929–953. doi:10.1002/joc.3736

Mahmood, R., Pielke, R. A., and McAlpine, C. A. (2016). Climate-relevant Land Use and Land Cover Change Policies. *Bulletin of the American Meteorological Society* 97 (2), 195–202. doi:10.1175/bams-d-14-00221.1

IPCC (2021). "Summary for Policymakers," in *Climate Change 2021: The Physical Science Basis. Contribution of Working Group I to the Sixth Assessment Report of the Intergovernmental Panel on Climate Change*. Editors V. Masson Delmotte, P. Zhai, A. Pirani, S. L. Connors, C. Péan, S. Berger, et al. (Cambridge, United Kingdom: Cambridge University Press). In Press. https://www.ipcc.ch/report/ar6/wg1/downloads/report/IPCC_AR6_WGI_SPM_final.pdf

Oleson, K., Lawrence, D., Bonan, G., Drewniak, B., Huang, M., Koven, C., et al. (2013). *Technical Description of Version 4.5 of the Community Land Model (CLM)*. Boulder, CO: NCAR.

Pal, J. S., Small, E. E., and Eltahir, E. A. B. (2000). Simulation of Regional-Scale Water and Energy Budgets: Representation of Subgrid Cloud and Precipitation Processes within RegCM. *J. Geophys. Res.* 105 (D24), 29579–29594. doi:10.1029/2000jd900415

Pan, Y., Birdsey, R. A., Fang, J., Houghton, R., Kauppi, P. E., Kurz, W. A., et al. (2011). A Large and Persistent Carbon Sink in the World's Forests. *Science* 333 (6045), 988–993. doi:10.1126/science.1201609

Parker, D.J. (2002). The Response of CAPE and CIN to Tropospheric Thermal Variations. *Q. J. R. Meteorol. Soc.* 128 (579), 119–130. doi:10.1256/00359000260498815

Perugini, L., Caporaso, L., Marconi, S., Cescatti, A., Quesada, B., de Noblet-Ducoudré, N., et al. (2017). Biophysical Effects on Temperature and Precipitation Due to Land Cover Change. *Environ. Res. Lett.* 12 (5), 053002. doi:10.1088/1748-9326/aa6b3f

Pielke, R. A. (2005). Land Use and Climate Change. *Science* 310 (5754), 1625–1626. doi:10.1126/science.1120529

Pielke Sr, R. A., Pitman, A., Niyogi, D., Mahmood, R., McAlpine, C., Hossain, F., et al. (2011). Land Use/land Cover Changes and Climate: Modeling Analysis and Observational Evidence. *WIREs Clim Change* 2 (6), 828–850. doi:10.1002/wcc.144

Pitman, A. J., Avila, F. B., Abramowitz, G., Wang, Y. P., Phipps, S. J., and de Noblet-Ducoudré, N. (2011). Importance of Background Climate in Determining

Impact of Land-Cover Change on Regional Climate. *Nature Clim Change* 1 (9), 472–475. doi:10.1038/nclimate1294

Pitman, A. J., de Noblet-Ducoudré, N., Avila, F. B., Alexander, L. V., Boisier, J.-P., Brovkin, V., et al. (2012). Effects of Land Cover Change on Temperature and Rainfall Extremes in Multi-Model Ensemble Simulations. *Earth Syst. Dynam.* 3 (2), 213–231. doi:10.5194/esd-3-213-2012

Pitman, A. J., de Noblet-Ducoudré, N., Cruz, F. T., Davin, E. L., Bonan, G. B., Brovkin, V., et al. (2009). Uncertainties in Climate Responses to Past Land Cover Change: First Results from the LUCID Intercomparison Study. *Geophys. Res. Lett.* 36 (14), L14814. doi:10.1029/2009gl039076

Prestele, R., Arneth, A., Bondeau, A., de Noblet-Ducoudré, N., Pugh, T. A. M., Sitch, S., et al. (2017). Current Challenges of Implementing Anthropogenic Land-Use and Land-Cover Change in Models Contributing to Climate Change Assessments. *Earth Syst. Dynam.* 8 (2), 369–386. doi:10.5194/esd-8-369-2017

Reyers, B., O'Farrell, P. J., Cowling, R. M., Egoh, B. N., Le Maitre, D. C., and Vlok, J. H. J. (2009). Ecosystem Services, Land-Cover Change, and Stakeholders Finding a Sustainable Foothold for a Semiarid Biodiversity Hotspot. *Ecology and Society* 14 (1), 38. doi:10.5751/es-02867-140138

IPCC (2013). "Summary for Policymakers," in *Climate Change 2013: The Physical Science Basis. Contribution of Working Group I to the Fifth Assessment Report of the Intergovernmental Panel on Climate Change*. Editors T. F. Stocker, D. Qin, G.-K. Plattner, M. Tignor, S. K. Allen, J. Boschung, et al. (Cambridge, United Kingdom and New York, NY, USA: Cambridge University Press), 1–30.

Sulla-Menashe, M., and Friedl, M. A. (2018). User Guide to Collection 6 MODIS Land Cover (MCD12Q1 and MCD12C1) Product. USGS Doc. 28. Available at: https://lpdaac.usgs.gov/documents/101/MCD12_User_Guide_V6.pdf. (Accessed June 29, 2022).

van der Ent, R. J., Savenije, H. H. G., Schaefli, B., and Steele-Dunne, S. C. (2010). Origin and Fate of Atmospheric Moisture over Continents. *Water Resources Research* 46 (9), W09525. doi:10.1029/2010wr009127

Wang, J., Bras, R. L., and Eltahir, E. A. B. (2000). The Impact of Observed Deforestation on the Mesoscale Distribution of Rainfall and Clouds in Amazonia. *J. Hydrometeor* 1 (3), 267–286. doi:10.1175/1525-7541(2000)001<0267:tioodo>2.0.co;2

Wang, Q., Yan, M., Liu, J., and Ning, L. (2021). Impacts of Land Use/cover Change on Spatial Patterns of Summer Precipitation at Decadal Scale over Eastern China. *Intl Journal of Climatology* 41 (3), 1939–1951. doi:10.1002/joc.6939

Wang, X., Zhang, B., Xu, X., Tian, J., and He, C. (2020). Regional Water-Energy Cycle Response to Land Use/cover Change in the Agro-Pastoral Ecotone, Northwest China. *Journal of Hydrology* 580, 124246. doi:10.1016/j.jhydrol.2019.124246

Ward, D. S., Mahowald, N. M., and Kloster, S. (2014). Potential Climate Forcing of Land Use and Land Cover Change. *Atmos. Chem. Phys.* 14 (23), 12701–12724. doi:10.5194/acp-14-12701-2014

Winckler, J., Reick, C. H., and Pongratz, J. (2017). Robust Identification of Local Biogeophysical Effects of Land-Cover Change in a Global Climate Model. *Journal of Climate* 30 (3), 1159–1176. doi:10.1175/jcli-d-16-0067.1

Xu, R., Li, Y., Teuling, A. J., Zhao, L., Spracklen, D. V., Garcia-Carreras, L., et al. (2022). Contrasting Impacts of Forests on Cloud Cover Based on Satellite Observations. *Nat Commun* 13 (1), 670. doi:10.1038/s41467-022-28161-7

Yu, L., Liu, Y., Liu, T., and Yan, F. (2020). Impact of Recent Vegetation Greening on Temperature and Precipitation over China. *Agricultural and Forest Meteorology* 295, 108197. doi:10.1016/j.agrformet.2020.108197

Zeng, X., Zhao, M., and Dickinson, R. E. (1998). Intercomparison of Bulk Aerodynamic Algorithms for the Computation of Sea Surface Fluxes Using TOGA COARE and TAO Data. *J. Climate* 11 (10), 2628–2644. doi:10.1175/1520-0442(1998)011<2628:iobaaf>2.0.co;2

Zeng, Z., Piao, S., Li, L. Z. X., Zhou, L., Ciais, P., Wang, T., et al. (2017). Climate Mitigation from Vegetation Biophysical Feedbacks during the Past Three Decades. *Nature Clim Change* 7 (6), 432–436. doi:10.1038/nclimate3299

Zhang, X., Chen, J., and Song, S. (2021). Divergent Impacts of Land Use/cover Change on Summer Precipitation in Eastern China from 1980 to 2000. *Int J Climatol* 41 (4), 2360–2374. doi:10.1002/joc.6963

Zhong, S., Qian, Y., Zhao, C., Leung, R., Wang, H., Yang, B., et al. (2017). Urbanization-induced Urban Heat Island and Aerosol Effects on Climate Extremes in the Yangtze River Delta Region of China. *Atmos. Chem. Phys.* 17 (8), 5439–5457. doi:10.5194/acp-17-5439-2017

Zwiers, F. W., and von Storch, H. (1995). Taking Serial Correlation into Account in Tests of the Mean. *J. Climate* 8 (2), 336–351. doi:10.1175/1520-0442(1995)008<0336:tsciai>2.0.co;2

**Conflict of Interest:** The authors declare that the research was conducted in the absence of any commercial or financial relationships that could be construed as a potential conflict of interest.

**Publisher's Note:** All claims expressed in this article are solely those of the authors and do not necessarily represent those of their affiliated organizations, or those of the publisher, the editors and the reviewers. Any product that may be evaluated in this article, or claim that may be made by its manufacturer, is not guaranteed or endorsed by the publisher.

frontiers | Frontiers in Environmental Science

TYPE Original Research
PUBLISHED 10 August 2022
DOI 10.3389/fenvs.2022.916748



OPEN ACCESS

EDITED BY
Yan Li,
Beijing Normal University, China

REVIEWED BY
Rudy Calif,
Université des Antilles, Guadeloupe
Keyan Fang,
Fujian Normal University, China

*CORRESPONDENCE
Liang Qiao,
19113020001@fudan.edu.cn

SPECIALTY SECTION
This article was submitted to Land Use Dynamics, a section of the journal Frontiers in Environmental Science

RECEIVED 10 April 2022
ACCEPTED 13 July 2022
PUBLISHED 10 August 2022

CITATION
Jin H, Wang S, Yan P, Qiao L, Sun L and Zhang L (2022), Spatial and temporal characteristics of surface solar radiation in China and its influencing factors. *Front. Environ. Sci.* 10:916748. doi: 10.3389/fenvs.2022.916748



# Spatial and temporal characteristics of surface solar radiation in China and its influencing factors

Hongmei Jin[1,2], Suichan Wang[1], Pengcheng Yan[3], Liang Qiao[4]*, Linhua Sun[2] and Ling Zhang[1]

[1]Gansu Meteorological Information and Technical Equip Safeguard Center, Gansu Meteorological Bureau, Lanzhou, China, [2]Lanzhou Resources & Environment Voc-Tech University, Key Laboratory of Climate Resources Utilization and Disaster Prevention and Mitigation of Gansu Province, Lanzhou, China, [3]Institute of Arid Meteorology of CMA, Key Open Laboratory of Arid Climatic Change and Disaster Reduction of CMA, Key Laboratory of Arid Climatic Change and Reducing Disaster of Gansu Province, Lanzhou, China, [4]Department of Atmospheric and Oceanic Sciences/Institute of Atmospheric Sciences, Fudan University, Shanghai, China

The total-sky direct solar radiation at Earth's surface (SRS) not only has an important impact on the earth's climate and ecology, but also is a crucial parameter for solar photovoltaic power. SRS determines whether photovoltaic power plants can be built in the region and directly affects the efficiency of photovoltaic power generation. Therefore, the spatial and temporal distribution characteristics of SRS have a very important guiding significance for the construction of photovoltaic power stations. This study discusses the temporal and spatial characteristics of SRS and its influencing factors in China during 1961–2020 using ERA5 data and the empirical orthogonal function (EOF), rotated empirical orthogonal function (REOF), and ensemble empirical model decomposition (EEMD) methods. Our investigation reveals that the high-value SRS center is located on the southwestern Tibetan Plateau, while the low-value center occurs on the northeastern Yunnan–Guizhou Plateau and in the Sichuan Basin. Seasonal variability in SRS means that maximum values occur uniformly in summer, followed sequentially by spring, autumn, and winter. The spatial distribution of the leading SRS EOF mode exhibits a dipole pattern between the southern Tibetan Plateau and other regions. Combined with the time series, SRS in China underwent an interdecadal transition around the year 2000. The regression analysis shows that this pattern is mainly affected by surface air temperature, total precipitation, relative humidity and cloud cover. The time series evolution of SRS primarily reflects the interannual variability in annual-mean and four seasons; the variance contributions of decadal variability and secular trend are minor through the EEMD. The REOF separates Chinese SRS into 11 central regions, the top 5 being the western Tibetan Plateau, western Northwest China, the eastern Tibetan Plateau, northern Xinjiang, and North China. The relationship between SRS and meteorological parameters shows that SRS is positively correlated with surface air temperature and wind speed but negatively correlated with total precipitation, relative humidity, low and total cloud cover, and aerosol concentrations.

KEYWORDS

solar radiation, China, temporal and spatial characteristics, influence factor, EEMD decomposition

## Introduction

Solar radiation is the dominant source of energy received by Earth's surface, where it not only constitutes a valuable source of renewable energy for use by humans but also plays a driving role in global climate (Dickinson and Cheremisinoff, 1980; Yan et al., 2014; Huang et al., 2017). Climate change is closely related to the solar radiation reaching Earth's surface; changes in insolation directly affect surface temperature, and in turn evaporation, hydrology, human living environments, and ecosystem. Consequently, spatial and temporal variability in solar radiation also influences the distribution of all climate-related resources (Wu et al., 2009; You et al., 2013; Wang, 2015; Jin et al., 2019; Zhang et al., 2020). As the primary energy source for biological, physical, and chemical processes at Earth's surface, solar radiation plays a central role in local climate and the development of plant communities and forms a key parameter in numerical models simulating the land surface, hydrology, ecology, climate, and environment. Ultimately, a robust understanding of solar radiation is vital to these research fields (Meza and Varas, 2000; Winslow et al., 2001; Zhou et al., 2012; Blanka et al., 2017; Huang et al., 2017; Guan et al., 2018). To support the development and utilization of solar energy resources, it is first necessary to critically assess the distribution and variability of solar energy resources (Xu et al., 2010). As an essential input parameter for net primary productivity of vegetation, the accuracy and quantitative evaluation of solar radiation can help refine our knowledge of regional and global carbon cycles (Zhang et al., 2020).

To accurately evaluate the nature of solar energy resources throughout China, we first need to understand the spatial and temporal distribution characteristics of solar radiation (He et al., 2003; Huang et al., 2017). In their study of regional insolation characteristics, Wen et al. (2008) employed ground radiation observational data collected by 122 radiation stations throughout China between 1961 and 2000 to study the regional characteristics of solar radiation in China. Similarly, Li et al. explored spatial and temporal variability in surface solar radiation, and the factors influencing this variability, in China for the period 2003–2012. The results of both studies indicate that insolation is highest on the Tibetan Plateau and lowest in the Sichuan Basin, and suggest that the receipt of solar radiation in China is impacted by both seasonal and interannual variations. Meanwhile, Yang et al. (2007) analyzed monthly averaged total radiation data from sixty stations in mainland China between 1961 and 2002. They observed that most stations reported a declining trend over the 40-year period, with the decline being significantly greater in eastern regions than in the west. More recently, Tao et al. (2016) proposed that spatial variability in seasonal trends of total solar radiation varies considerably throughout China, and Qi et al., 2014, Qi et al. (2015) implicated aerosol pollution arising from urbanization and industrialization in the observed insolation decrease. As the primary factor is the dispersal of atmospheric pollutants, wind plays a central role in the impact of tropospheric haze on insolation levels. This relationship supports the model that air pollution is an increasingly important driver of changes in surface solar radiation, especially in eastern China. Climatically, Shen and Wang, 2011 reported that observed changes in surface solar radiation have played a significant role in climate change in southeast China over the past 50 years. Where radiation increased, average surface air temperatures have also risen, and vice versa.

A key limitation of the existing body of research is that most studies are based on short time series of comparatively low temporal and spatial resolution. At present, there are few studies of Chinese insolation spanning more than a few decades and utilizing high-resolution radiation data. To help address this shortcoming, we utilized total-sky direct solar radiation data derived from ERA5 reanalysis for the period 1961–2020 to 1) analyze the spatial and temporal distribution characteristics of solar radiation throughout China and 2) identify the factors influencing these characteristics. Our overarching goal in this research is to deliver valuable new insight into the effective development of solar energy resources in China and scientific support for the siting of photovoltaic power stations, both of which are vital to growing the viability of clean energy, helping China achieve carbon neutrality, and slowing the rate of global warming.

## Data and methods

### Data

ERA5 is the most up to date set of global atmospheric, land, and oceanic reanalysis products derived from the European Centre for Medium-Range Weather Forecasts (Hersbach et al., 2020). In this paper, we used ERA5 monthly total-sky direct solar radiation at the surface (SRS) data, with a spatial resolution of $0.25^{\circ} \times 0.25^{\circ}$, for the period 1961–2020. Specifically, these data are used to represent atmospheric forcing in the land surface model and thus have key applications in regional climate assessment, agriculture, and solar energy resources. Zhang et al. (2021) evaluated ERA5 surface-received solar radiation data on multiple spatio-temporal scales and demonstrated the suitability of this dataset for mainland China.

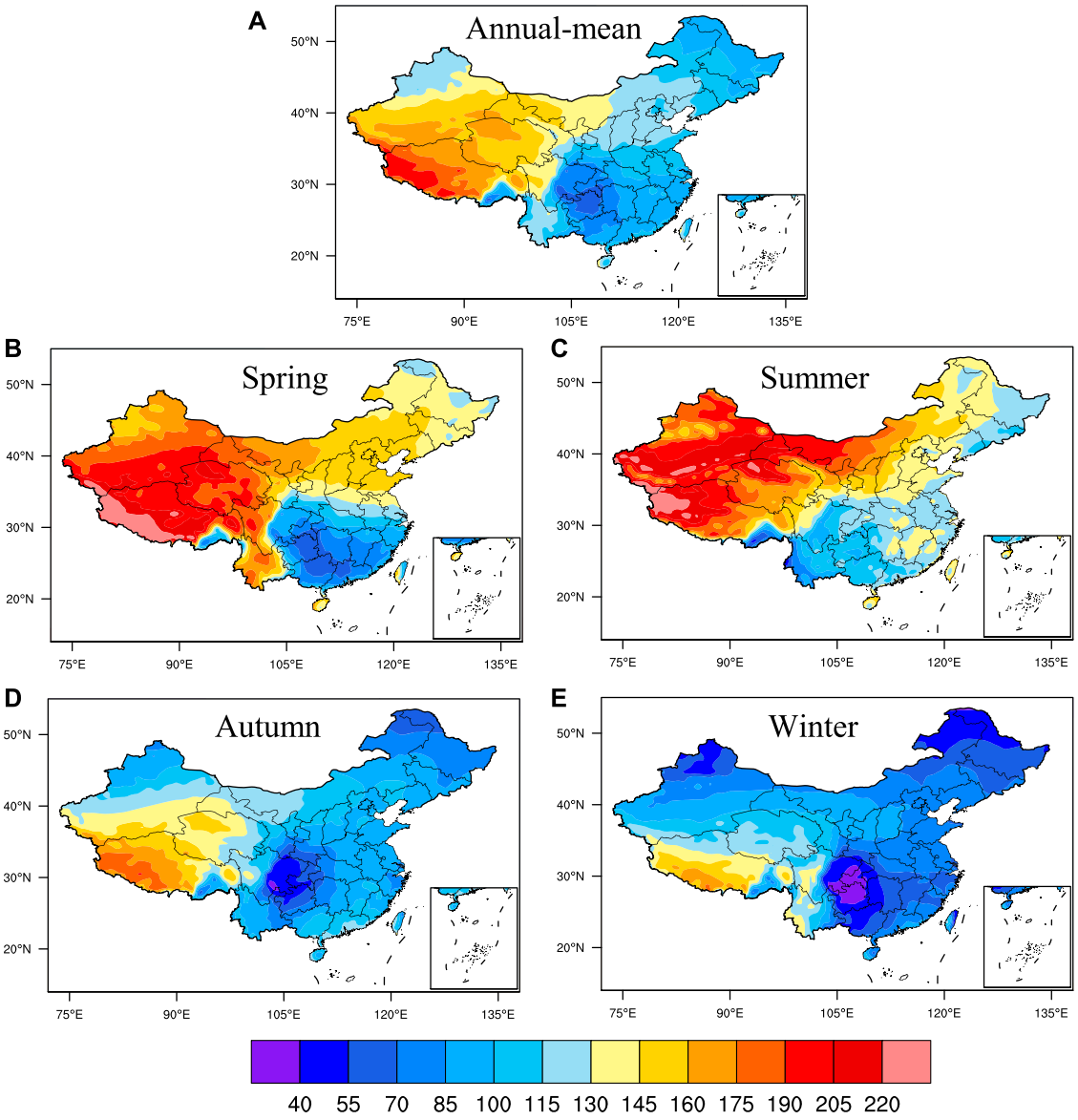


FIGURE 1
Spatial distribution of SRS (W/m$^2$) climate states in China during the period 1961–2020. **(A)** is annual-mean, **(B)** is spring, **(C)** is summer, **(D)** is autumn, and **(E)** is winter.

## Methods

We applied linear least-squares regression to analyze trends in SRS variability, and the empirical orthogonal function (EOF) to evaluate SRS temporal and spatial variation characteristics. In addition, we used ensemble empirical model decomposition (EEMD) to decompose the SRS time series into specific oscillation components for various timescales (Wu and Huang, 2009) and the rotated empirical orthogonal function (REOF) to divide spatial distribution characteristics for China. Finally, the spatial distribution of the correlation between SRS and other meteorological variables affords a means for assessing the influence of each variable on SRS in different regions.

The EOF method is an effective tool for decomposing climatic variable fields into a space field and time period, and the EOF method has been widely used in climate diagnosis (Dommenget and Latif, 2002; Fan et al., 2011; Li and Xie, 2014; Zuo et al., 2018; Qiao et al., 2022). Building on EOF, REOF applies rotation technology to also realize the climate variable field. Rotation serves to reveal typical spatial structures that can reflect not only changes among different regions, but also the relevant distribution of those regions. REOF is a widely

used method for investigating meteorological elements in different regions (Li et al., 1997; Zhang et al., 2016).

The EEMD method is a relatively new, self-adaptive time series analysis technique that is suitable for analyzing nonlinear and non-stationary datasets (e.g., climate data). Specifically, EEMD decomposes a complex time series into finite oscillation components on different time scales, thereby permitting the analysis of meteorological elements. The advantage of EEMD is that, rather than relying on other functions, time series decomposition is based on the adaptive filtering of the data themselves. By adding an appropriate degree of white noise to the original data to simulate multiple observation scenarios, and through multiple calculations, realistic results can be derived from the ensemble average (Qian et al., 2012). In recent years, the EEMD method has been applied widely in climate change research (Franzke 2010; Qian et al., 2011; Gao et al., 2015; Cornes et al., 2017; Zhang et al., 2018; Zuo et al., 2018; Thomas et al., 2020). In the current study, we employed EEMD to analyze SRS time series throughout China.

# Results

## SRS variation characteristics on multiple time scales

To explore the spatial distribution characteristics of SRS in China, we analyzed the climatic state of SRS ($W/m^2$; Figure 1) for the period 1961–2020 from ERA5 monthly dataset. According to the annual-mean SRS (Figure 1A), the highest SRS values occur in western China, with a maximum over the southwest Tibetan Plateau, whereas the lowest values occur in the east and are centered on the northeastern Yunnan–Guizhou Plateau and in the Sichuan Basin. With an average elevation of >4,000 m, the Tibetan Plateau is the highest in the world. We note that maximum SRS values coincide with the highest parts of this plateau, where the thin, dry nature of the air column results in high atmospheric transparency and minimal scattering of incoming shortwave radiation. The Tibetan Plateau also experiences generally clear conditions, thereby enhancing the receipt of solar radiation. In contrast, the Yunnan–Guizhou Plateau and Sichuan Basin experience a monsoonal climate that, during the rainy season, results in high rainfall, cloudy days, and less direct sunshine, all of which serve to reduce surface insolation.

To explore the spatial distribution of SRS characteristics further (Figures 1B–E), we next defined the mean value for December–February as winter, the mean March–May value as spring, the mean June–August value as summer, and the mean September–November value as autumn. Recognizing that the spatial distribution of SRS during different seasons is broadly similar to the annual-mean, there are nonetheless several clear differences among them. On the whole, summer exhibits the highest SRS value, followed by spring, autumn, and winter. This general pattern confirms that the receipt of solar radiation at the surface is greatest in summer and weakest in winter, reflecting China's position in the Northern Hemisphere. We also note that during both spring and summer, SRS in northwest China increased considerably relative to the annual-mean. In summertime especially, the center of maximum values underwent a significant expansion and northward shift, a pattern that was accompanied by drought and generally clear sky over northwest China.

We used least-squares linear regression to analyze trends in SRS ($W/m^2$/decade) between 1961 and 2020 (Figure 2). In terms of annual-mean SRS, positive trends occurred in Northeast China, North China, Southwest China, South China, and Xinjiang, with a high value center located in Yunnan. Conversely, the Tibetan Plateau exhibited a generally negative trend; the low value center is located in central Sichuan. SRS trends vary considerably by season. In spring, SRS increases over most parts of China except the Tibetan Plateau, with the highest values observed in North China, eastern Central China, and Eastern China. During summer, SRS declines throughout most regions, with the exception of northeast China, Hebei, northern Xinjiang, Yunnan, and South China. The lowest value centers during that season are located primarily on the northwest Tibetan Plateau and in East China. SRS trends in autumn and winter are weak, with the highest values centered on Yunnan. Overall, the degree of variability among SRS trends is greatest in spring and summer, with significant springtime increases in eastern China followed by decreasing trends in most areas during summer. We note that the Tibetan Plateau, with the highest overall SRS values, exhibits negative trends in both spring and summer. Meanwhile, SRS trends in Yunnan and Northeast China were positive in all four seasons.

To investigate SRS stability between 1961 and 2020, we analyzed the spatial distribution of the SRS standard deviation ($W/m^2$; Figure 3). Our results show that the annual-mean standard deviation decreases gradually from southeast to northwest, a pattern that is mirrored by all four seasonal trends. The center of maximum SRS standard deviation is located generally in Eastern China during spring and summer, but shifts towards Southern China during summer and autumn. This behavior indicates that SRS in Southeast China exhibits a greater degree of variability relative to SRS in northwest and northeast regions, a pattern that is consistent with the respective meteorologic and climatic characteristics of each regions. For instance, occupying a relatively interior position, Northwest China is largely unaffected by monsoon circulation and consequently experiences dry, sunny conditions and minor variability in the receipt of solar radiation. Southeast China, in

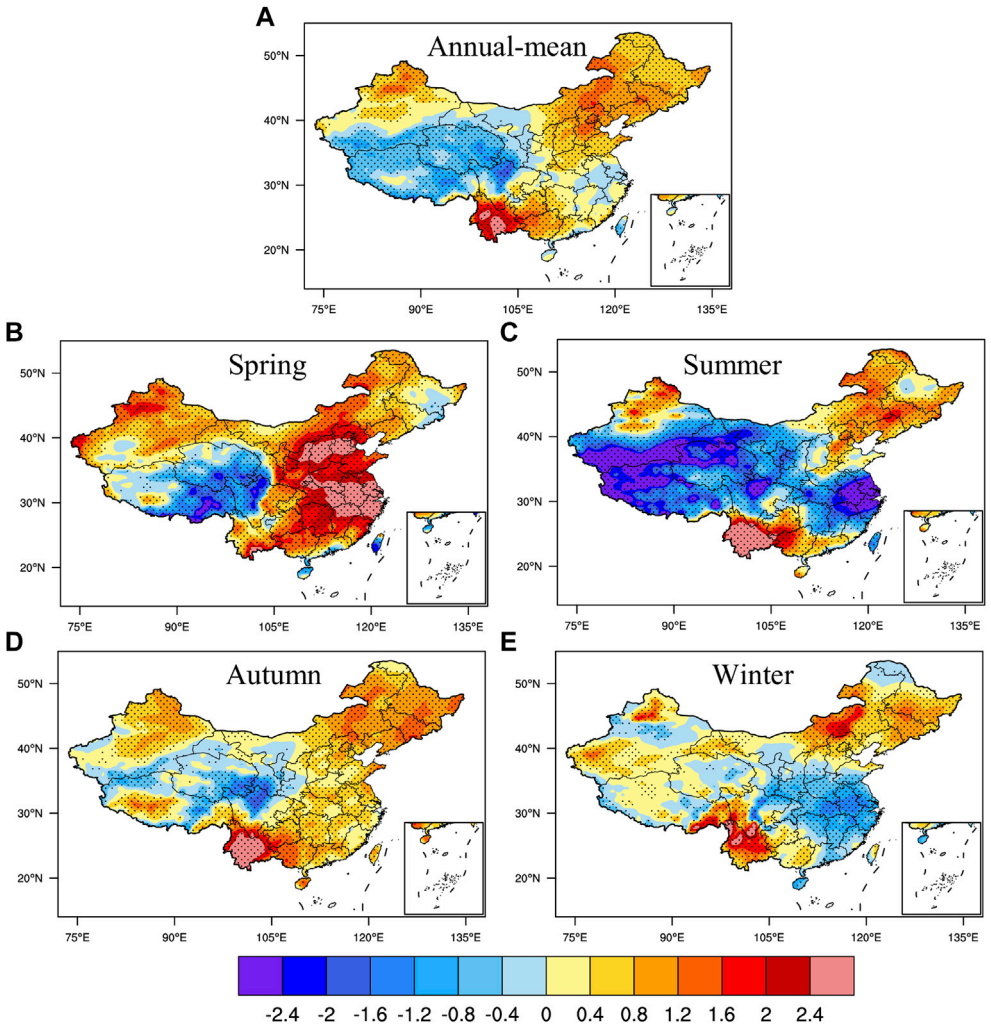


FIGURE 2
Same as in Figure 1, but for trends in SRS (W/m$^2$/decade). **(A)** is annual-mean, **(B)** is spring, **(C)** is summer, **(D)** is autumn, and **(E)** is winter.

contrast, is dominated by the East Asian monsoon, which brings heavy rainfall and results in a greater degree of insolation variability.

Using EOF, we decomposed annual-mean and seasonal SRS values for the 1961–2020 study period to explore spatio-temporal variations throughout China, with a specific focus on the first two modes (Figure 4). For annual-mean SRS, the explained variances of the first and second modes are 26.4 and 11.9%, respectively. The spatial distribution of the first EOF mode exhibits a dipole pattern between the southern Tibetan Plateau and other regions, with the center of highest values located in Central China. Combined with the time period to the first mode, it can be seen that the first mode is mainly reflected in the interdecadal variation characteristics, and SRS in China showed an obvious interdecadal transition around year 2000, when the periodicity changed from its negative to positive phase. In other words, with the exception of the southern Tibetan Plateau, most of China was dominated by negative anomalies prior to 2000, after which the opposite pattern was established. The spatial distribution of the second EOF mode is bounded by 32°N, with the negative phase dominating the southeast region and positive phase elsewhere. This time series primarily reflects interannual variability.

Figures 4B–E depicts the results of EOF analysis of SRS during different seasons. During spring, the explained variances of the first and second EOF modes are 29.8 and 12.4%, respectively. Moreover, the spatial distribution of first mode exhibits a "negative–positive–negative" tripole pattern extending from northeast to southwest, by which Northeast (Heilongjiang, Inner Mongolia) and Southwest China (Tibet, Sichuan, Yunnan) experience the negative phase, while other

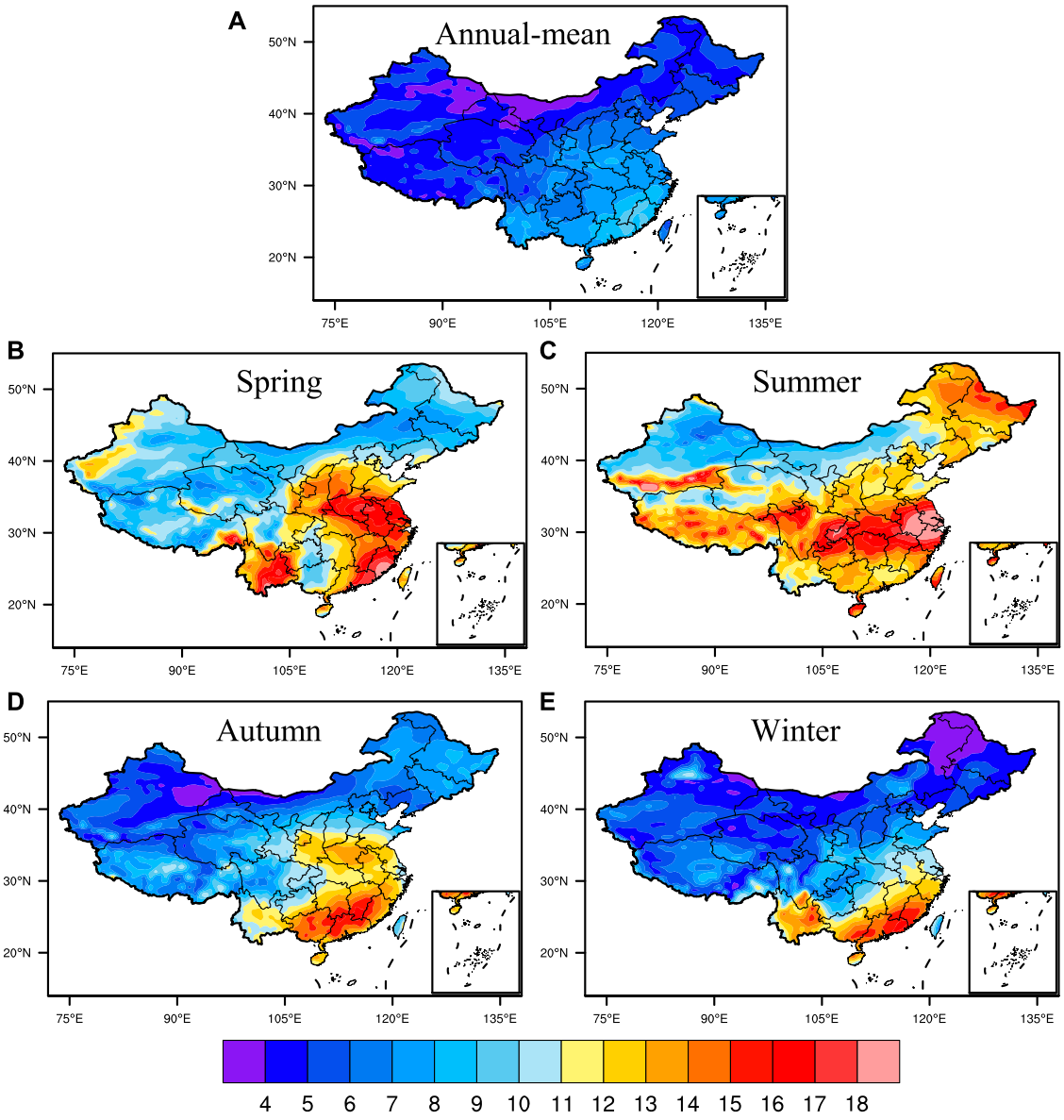


FIGURE 3
Same as in Figure 1, but for the standard deviation of SRS (W/m$^2$). **(A)** is annual-mean, **(B)** is spring, **(C)** is summer, **(D)** is autumn, and **(E)** is winter.

regions experience the positive phase. The corresponding high-value centers are expansive and include most of Central and Eastern China. During spring, the time period of the first mode exhibits an obvious interdecadal transition around the year 2000, when the negative phase was replaced by the positive phase. The spatial distribution of the second mode reveals a similar springtime tripole pattern but in reverse ("positive–negative–positive"). In this mode, the majority of North China, central and northern East China, central and northern Central China, and northern Northwest China experience the negative phase, while the remaining regions are largely positive. The time period of the second mode is similar to that of the first mode, including the marked transition around the year 2000.

During summer, the explained variances of the first and second EOF modes are 17.4 and 13.7%, respectively. These values are the smallest of the four seasons, indicating that the corresponding SRS mode is more complex and changeable in summer. As is evident from the spatial distribution of EOF1, the negative phase dominates in southwest Tibet, southeast coastal areas, and North China, whereas other regions are characterized by the positive phase. We also note that the time

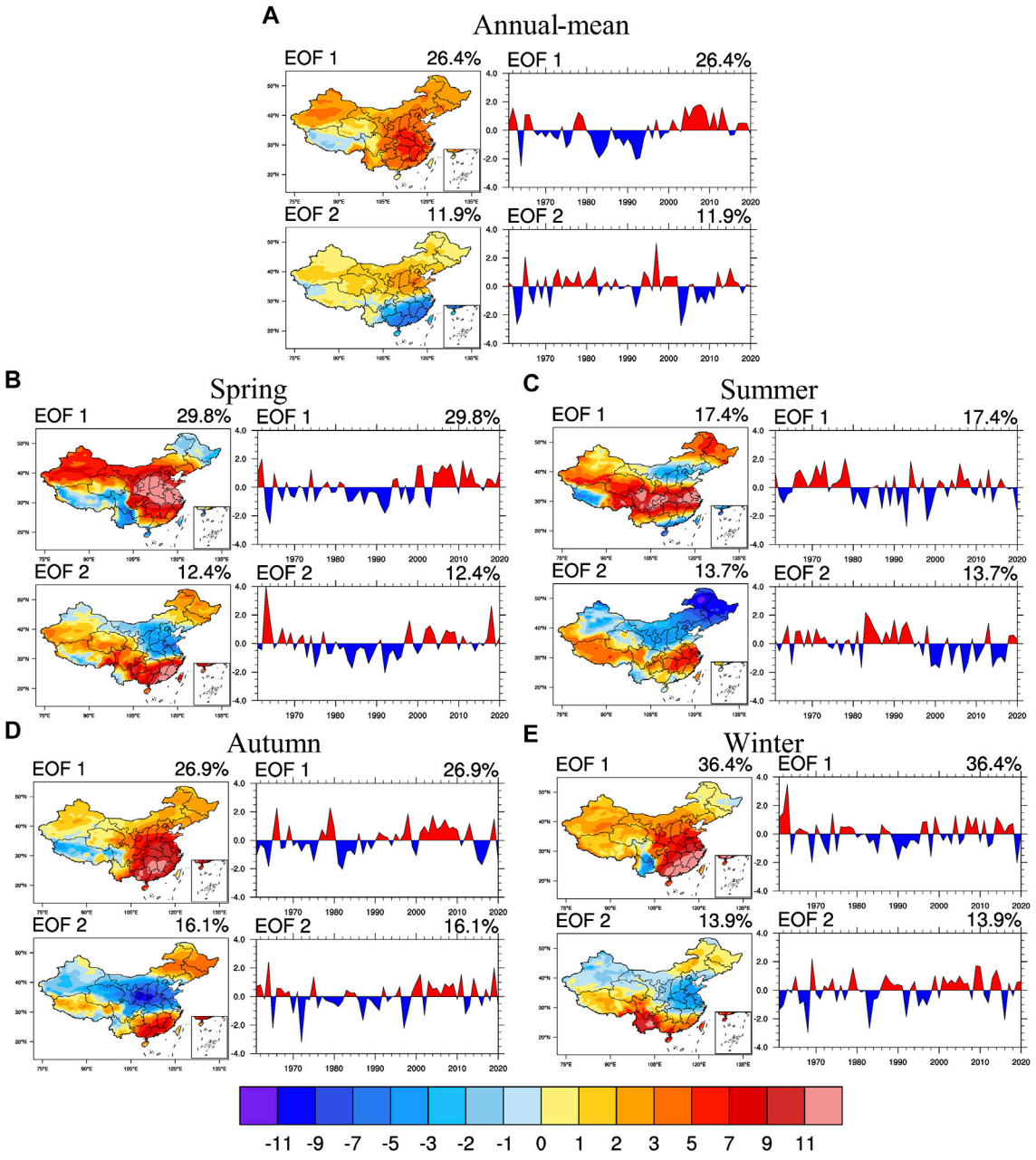


FIGURE 4
EOF decomposition of SRS in China from 1961 to 2020. **(A)** is annual-mean, **(B)** is spring, **(C)** is summer, **(D)** is autumn, and **(E)** is winter.

period of variability is interannual. The spatial distribution of summertime EOF2 exhibits a meridional dipole pattern, and the time period is mainly characterized by interdecadal variation. There was an obvious shift from the positive to negative phase occurred around 1998. During autumn, the explained variance of the first and second EOF modes are 26.9 and 16.1%, respectively. The spatial distribution of the first mode reveals that, with the notable exception of Tibet, China experiences a generally positive phase with positive centers located in Hunan and Jiangxi. The autumn time period in EOF1 is dominated by interannual variability. The spatial distribution of the second mode displays a northeast–southwest "positive–negative–positive" tripole pattern, and the time period is mainly interannual. The explained variances of the first and second EOF mode in winter are 36.4 and 13.9%, respectively, and are the highest

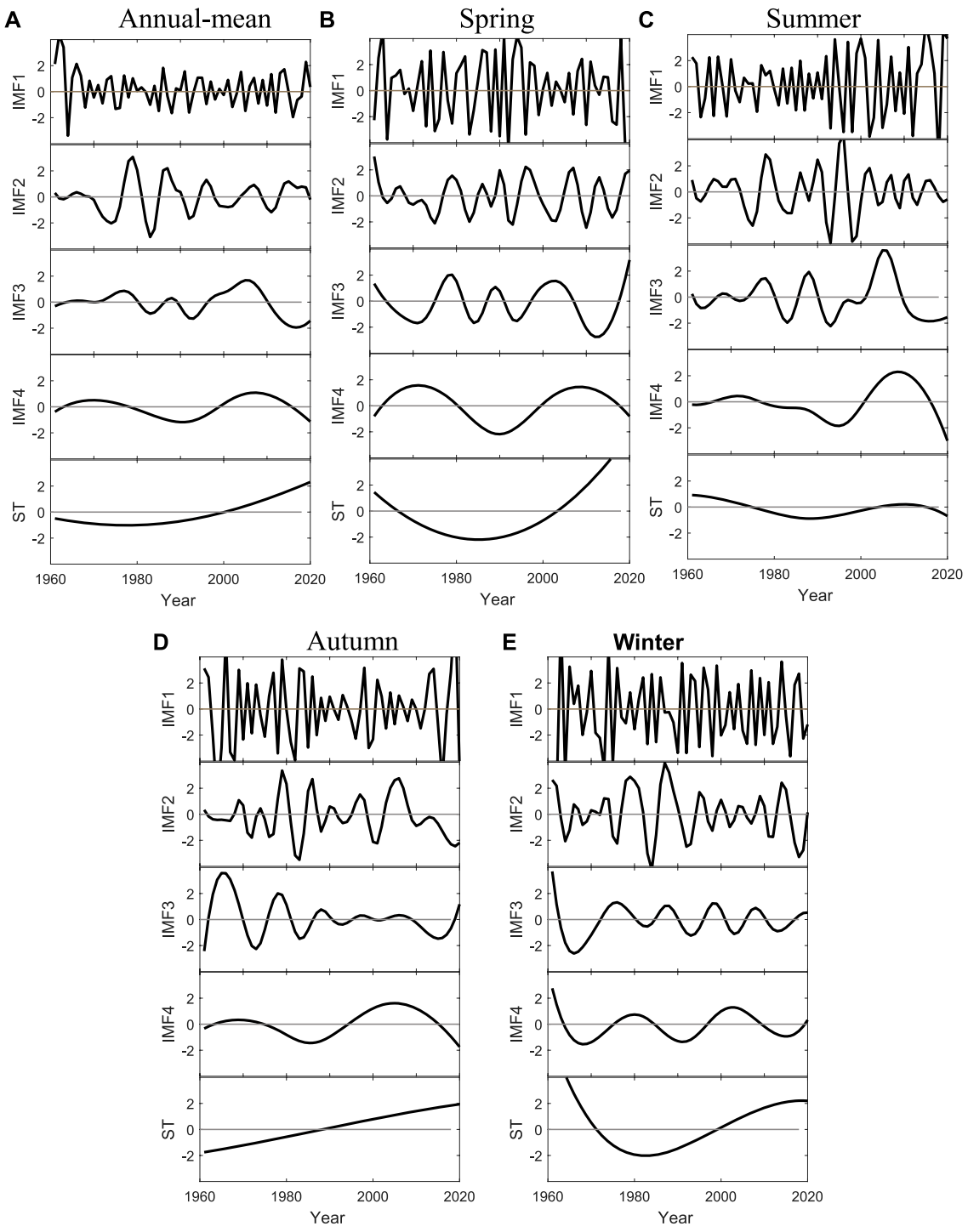


FIGURE 5
EEMD decomposition of SRS time series throughout China from 1961 to 2020. **(A)** is annual-mean, **(B)** is spring, **(C)** is summer, **(D)** is autumn, and **(E)** is winter.

values of the four seasons. Our results indicate that the spatial distribution of the first mode is largely positive phase, and the time period is interannual variation. The spatial distribution of the second mode exhibits a "negative–position–negative" tripole pattern from northeast to southwest, and the time period is primarily interannual.

TABLE 1 Periods and variance contributions in different timescales for the annual-mean and four seasons through the EEMD decompositions.

| | | IMF1 | IMF2 | IMF3 | IMF4 | ST |
|---|---|---|---|---|---|---|
| Annual | Period (Year) | 2.6 | 7.5 | 12.0 | 29.9 | 118.3 |
| | Variance (%) | 33.0 | 26.1 | 15.3 | 8.4 | 17.2 |
| spring | Period (Year) | 3.0 | 6.7 | 15.0 | 32.2 | 60.0 |
| | Variance (%) | 39.1 | 11.1 | 11.3 | 9.6 | 28.9 |
| summer | Period (Year) | 2.6 | 5.5 | 10.0 | 25.7 | 46.2 |
| | Variance (%) | 47.7 | 21.0 | 15.8 | 12.7 | 2.8 |
| autumn | Period (Year) | 3.2 | 6.0 | 10.0 | 31.2 | 126.2 |
| | Variance (%) | 56.3 | 15.5 | 12.9 | 7.0 | 8.3 |
| winter | Period (Year) | 2.7 | 5.5 | 12.0 | 21.2 | 62.3 |
| | Variance (%) | 50.9 | 16.4 | 6.6 | 4.6 | 21.5 |

The EEMD method is used to decompose the SRS time series into specific oscillation components on different time scales (Figure 5 and Table 1). Here, the annual-mean and seasonal time series can be decomposed into four intrinsic mode functions (IMFs) and a residual secular trend (ST). For both the annual-mean and seasonal IMF1, the periods are 2–3 years, and the variance contributions (33.0%–56.3%) that are greatest with other IMFs and ST. This outcome indicates that the Chinese SRS time series are dominated by a 2–3-years variability, and also that the amplitude of summertime IMF1 increased significantly after 1990. Both the annual-mean and four-season series exhibit similar periods in IMFs and ST, namely 5–15 years under IMF2, 10–15 years under IMF3, and 21–32 years under IMF4. Of these, the variance contribution of IMF4 accounts for the smallest proportion in all time scales. In terms of the interdecadal change characteristics, we note that the annual-mean, spring, summer, and autumn series all display phase changes from negative phase to positive phase during the period 1995–2000, consistent with the interdecadal EOF transition described above. Meanwhile, ST exhibits a long-term trend in both annual-mean and four-season time series, with relatively minor variance contributions. Both the annual-mean and autumn ST reveal a long-term increasing trend, whereas the summer ST is relatively weak. During spring and winter, ST exhibited an initial decrease and subsequent increase, with a clear phase transition from negative to positive in 2000. Finally, results of the EEMD method confirm that SRS time series for China display a predominantly interannual variability (at least between 1961-2020), consistent with the periodicity of the principal EOF mode.

## Meteorological factors influencing SRS

Representing the total direct solar radiation received at Earth's surface, SRS is impacted not only by seasonal insolation variability and solar activity but also by weather conditions (e.g., cloud cover and atmospheric transparency). Therefore, we conducted correlation analyses between annual-mean SRS and key meteorological factors, namely surface air temperature (SAT), surface air pressure, total precipitation, relative humidity, low cloud cover, total cloud cover, 10-m wind speed, and aerosol content, to establish which factors exert the strongest influence on SRS in various regions. Figure 6 displays the spatial distribution of correlation coefficients between annual mean SRS and each meteorological element. We note that, although solar radiation is directly impacted by aerosols, the ERA5 dataset does not include aerosol variables (e.g., aerosol optical thickness, atmospheric turbidity). To circumvent this limitation, we calculated the clear sky index:

$$\left(\left(\text{clear}-\text{sky solar radiation at surface}-\text{solar radiation at surface}\right)/\text{clear}-\text{sky solar radiation at surface}\right)$$

To quantify the absorption and scattering of solar radiation by clouds and aerosols. To minimize the influence of clouds, we calculated the partial correlation between this ratio and SRS to eliminate total cloud cover, thereby obtaining the SRS-aerosol correlation distribution (Figure 6H).

As individual meteorological factors can exhibit considerable spatial heterogeneity, the impact of specific elements on SRS is regionally variable. For instance, although SAT and SRS are positively correlated in most regions, with the strongest correlation on the Yunnan–Guizhou Plateau and in Xinjiang, we also observed a weak (do not pass the 95% significance test.) negative correlation between the two over parts of the Tibetan Plateau. Consequently, we infer that SRS is highly sensitive to SAT on the Yunnan–Guizhou Plateau and in Xinjiang, but relatively insensitive to this factor on the Tibetan Plateau. For all regions, the correlation between surface pressure and SRS is weak; only minor areas (e.g., Yunnan and central Inner Mongolia) pass the 95% significance test, indicating that air pressure has little influence on SRS. In contrast, total precipitation, relative humidity, low cloud cover, and total cloud cover all exhibit significant negative correlations with SRS. These factors typically correspond to cloudier conditions with reduced atmospheric transparency, leading to an inverse relationship between SRS and these meteorological elements. Whereas the influence on SRS of total precipitation is broadly uniform throughout China, the relative humidity in Yunnan, low cloud cover in South and Northeast China, and total cloud cover in Central and Eastern China all result in strong negative correlations in those regions. With the exception of parts of Xinjiang, the Tibetan Plateau, and Northeast China, we observed a positive correlation between wind speed and SRS in most regions, potentially due to the higher atmospheric transparency that tends to accompany windy days. Finally, we note that SRS is negatively correlated (at 95% significance) with

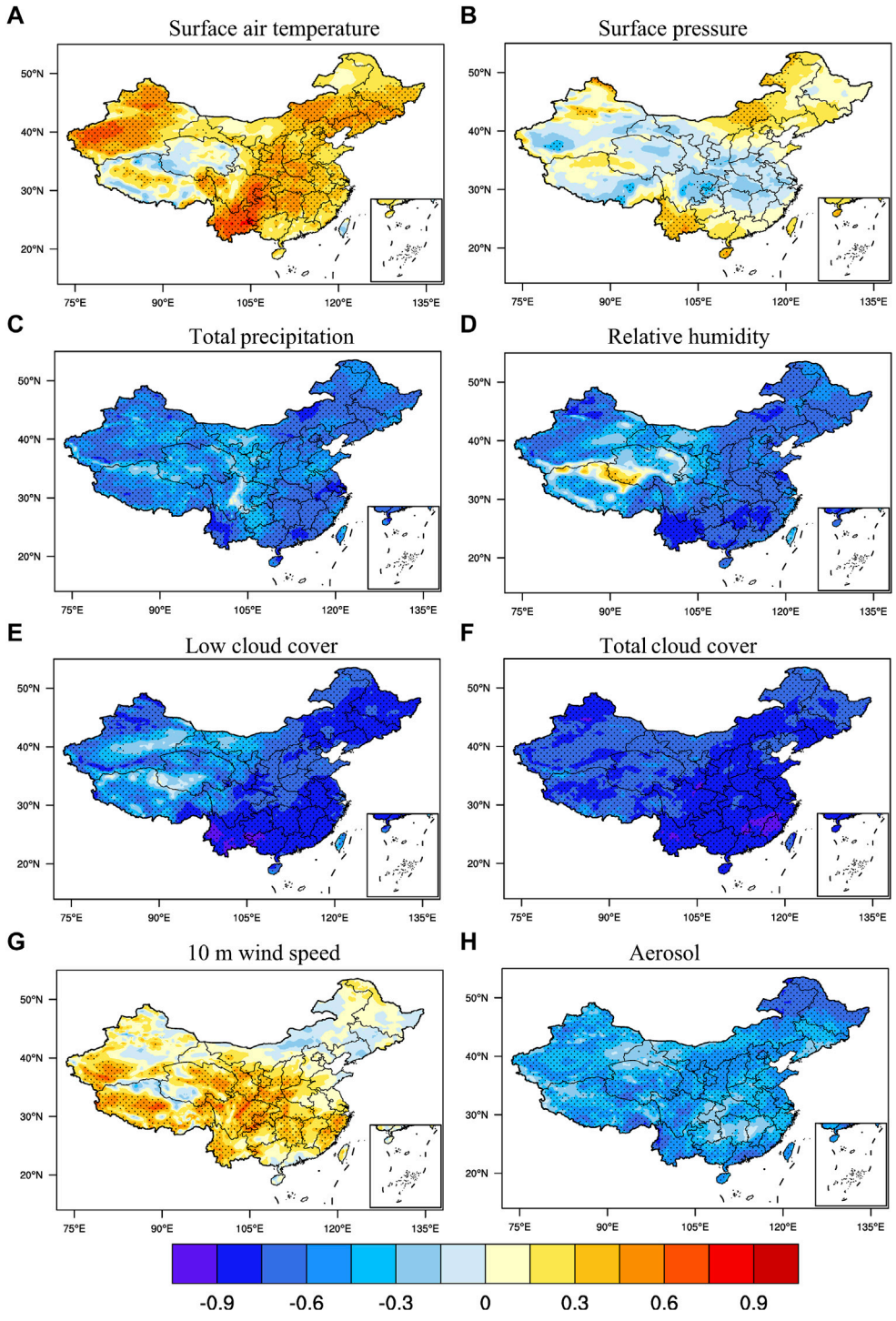


FIGURE 6
Spatial distributions of correlation coefficients between SRS and meteorological elements during the period 1961–2020. **(A)** is SAT, **(B)** is surface pressure, **(C)** is total precipitation, **(D)** is relative humidity, **(E)** is low cloud cover, **(F)** is total cloud cover, **(G)** is 10 m wind speed, and **(H)** is aerosol. Black dots indicate where a given area passes the 95% significance test.

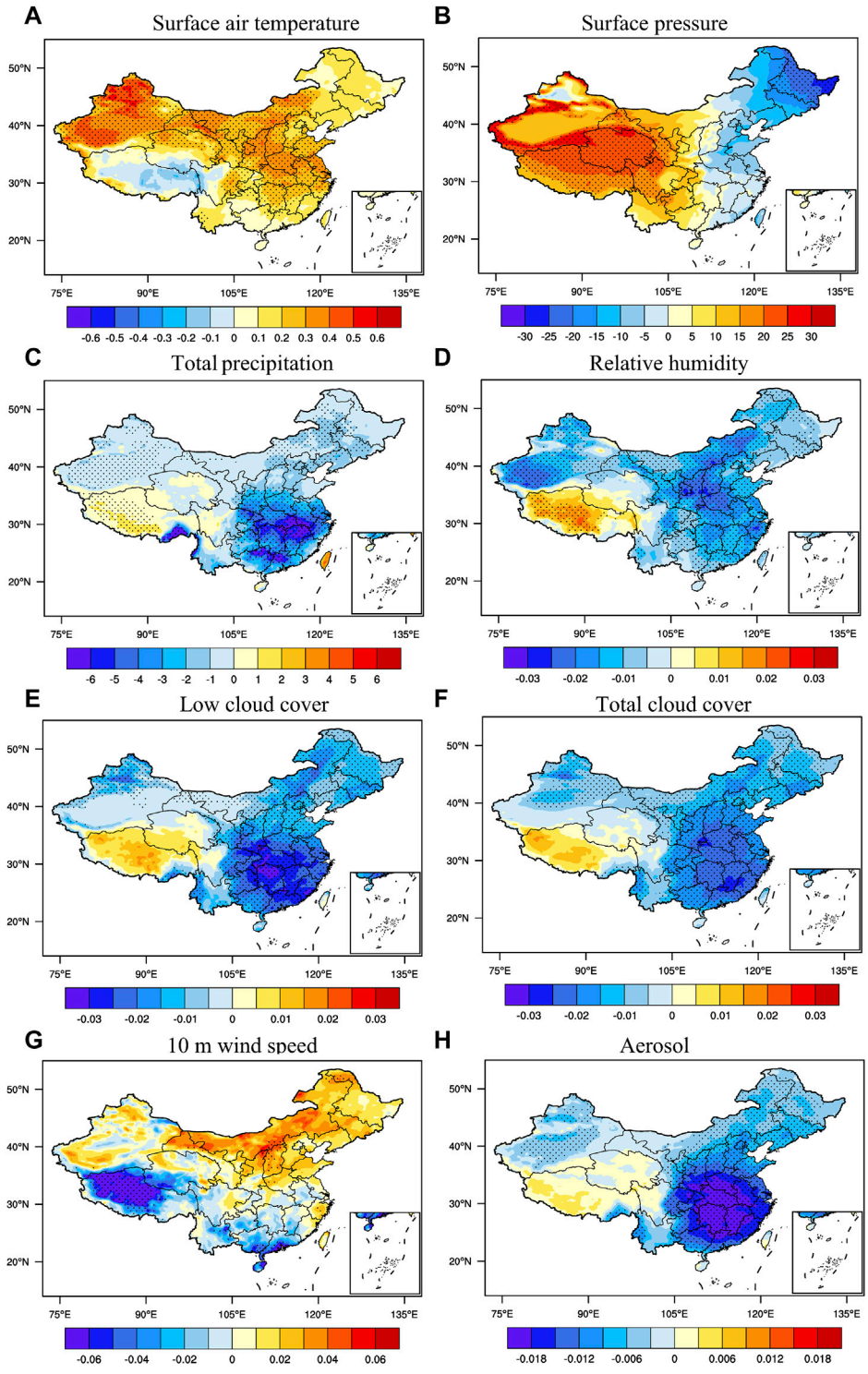


FIGURE 7
Meteorological elements regressed upon the normalized time series corresponding to EOF1 of annual-mean SRS. **(A)** is SAT (°C), **(B)** is surface pressure (Pa), **(C)** is total precipitation (mm), **(D)** is relative humidity (ratio), **(E)** is low cloud cover (ratio), **(F)** is total cloud cover (ratio), **(G)** is 10 m wind speed (m/s), and **(H)** is aerosol (ratio). Black dots indicate where a given area passes the 95% significance test.

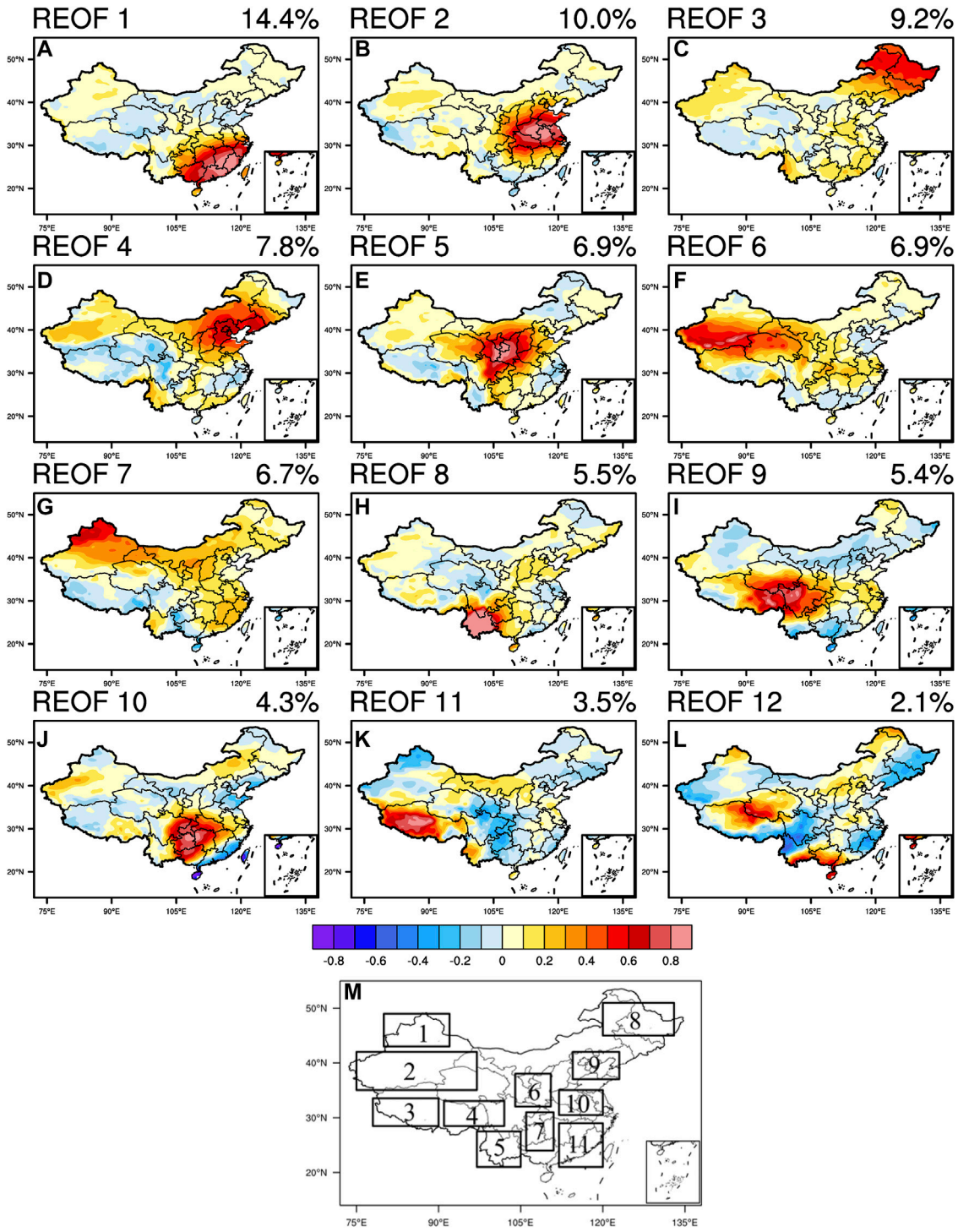


FIGURE 8
**(A–L)** Spatial distributions of the 12 eigenvector fields obtained from REOF decomposition of SRS between 1961 and 2020. Panel **(M)** represents the regional distribution of the first 11 eigenvector fields. Since the 12th eigenvector field is not significant, we determined the regional division from the first 11. The divided regions are as follows: northern Xinjiang (r1: 43°–49°N, 80°–92°E), western Northwest (r2: 35°–42°N, 75°–97°E), western Tibet Plateau (r3: 28.5°–33.5°N, 78°–90°E), eastern Tibet Plateau (r4: 28.5°–33°N, 91°–102°E), Yunnan (r5: 21°–27.5°N, 97°–105°E), Loess Plateau (r6: 32°–38°N, 104°–110.5°E), Central China (r7: 24°–31°N, 106°–111°E), Northeast China (r8: 45°–51°N, 120°–133°E), North China (r9: 37°–42°N, 114.5°–123°E), East China (r10: 30.5°–35°N, 112°–120°E), southeast China (r11: 21°–29°N, 112°–120°E).

TABLE 2 Correlation coefficients between SRS and meteorological elements in 11 regions in China during 1961-2020. SAT is surface air temperature, SP is surface pressure, PRE is total precipitation, RH is relative humidity, LC is low cloud cover, TC is total cloud cover, WC is 10 m wind speed, AER is aerosol. The regions r1-r11 same as in Figure 8.

| | SAT | SP | PRE | RH | LC | TC | WS | AER |
|---|---|---|---|---|---|---|---|---|
| r1 | 0.41** | 0.23 | −0.72** | −0.73** | −0.81** | −0.80** | −0.07 | −0.27 |
| r2 | 0.37** | −0.01 | −0.68** | −0.48** | −0.66** | −0.80** | 0.11 | −0.17 |
| r3 | −0.03 | −0.06 | −0.52** | −0.29* | −0.50** | −0.75** | 0.47** | −0.16 |
| r4 | 0.18 | −0.03 | −0.53** | −0.47** | −0.47** | −0.74** | 0.19 | -0.25 |
| r5 | 0.68** | 0.42** | −0.78** | −0.83** | −0.89** | −0.86** | 0.15 | −0.39* |
| r6 | 0.37** | −0.14 | −0.51** | −0.49** | −0.79** | −0.84** | 0.45** | −0.34* |
| r7 | 0.46** | −0.03 | −0.52** | −0.67** | −0.83** | −0.85** | 0.28 | 0.01 |
| r8 | 0.27* | 0.12 | −0.75** | −0.74** | −0.83** | −0.77** | 0.01 | −0.60** |
| r9 | 0.42** | 0.16 | −0.69** | −0.71** | −0.75** | −0.76** | −0.03 | −0.34* |
| r10 | 0.36** | −0.13 | −0.70** | −0.72** | −0.78** | −0.83** | 0.12 | −0.28 |
| r11 | 0.25 | 0.03 | −0.76** | −0.72** | −0.85** | −0.91** | 0.16 | −0.17 |

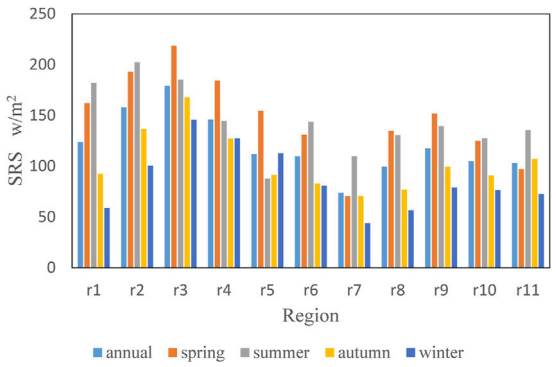


FIGURE 9
Annual-mean and seasonal SRS for 11 regions between 1961 and 2020. Regions r1–r11 are the same as in Figure 8.

aerosols throughout China, confirming that air pollution reduces SRS. In order to explore the possible causes of the dipole pattern of annual-mean SRS EOF1 between the southern Tibetan Plateau and the rest of China (Figure 4A). The relevant meteorological element fields regressed upon the normalized time series corresponding to annual-mean SRS EOF1 are analyzed (Figure 7). The results show that the SAT, total precipitation, relative humidity, low cloud cover, and total cloud cover had a similar pattern to the regional pattern of annual-mean SRS EOF1, which means that the dipole pattern is strongly related to these elements.

On the basis of these analyses, we conclude that the spatial distribution of SRS throughout China exhibits considerable regional differences in climate state, trend, standard deviation, and spatial EOF mode. Consequently, we utilized REOF to examine the spatial distribution of SRS in more detail (Figure 8). According to the REOF variance contribution, the spatial distribution of Chinese SRS can be subdivided into 11 major radiation regions (see Figure 7M): northern Xinjiang (r1: 43°–49°N, 80°–92°E), western Northwest China (r2: 35°–42°N, 75°–97°E), western Tibetan Plateau (r3: 28.5°–33.5°N, 78°–90°E), eastern Tibetan Plateau (r4: 28.5°–33°N, 91°–102°E), Yunnan (r5: 21°–27.5°N, 97°–105°E), Loess Plateau (r6: 32°–38°N, 104°–110.5°E), Central China (r7: 24°–31°N, 106°–111°E), Northeast China (r8: 45°–51°N, 120°–133°E), North China (r9: 37°–42°N, 114.5°–123°E), East China (r10: 30.5°–35°N, 112°–120°E), and Southeast China (r11: 21°–29°N, 112°–120°E).

Figure 9 compares the annual-mean and seasonal SRS values for the 11 regions delineated by REOF decomposition. For r1, r2, r6, r7, r10, and r11, maximum SRS values occur in summer; in r3, r4, r5, r8, and r9, peak SRS is attained in spring. With the exception of r5, minimum values for all regions occur in winter. Viewed as a whole, therefore, peak SRS in China (except for r5) coincides with the spring–summer warm season and minimum SRS with winter conditions, a pattern that generally reflects Northern Hemisphere insolation. Concurrently, we ranked the annual-mean SRS values for each region, from largest to smallest, as follows: r3, r2, r4, r1, r9, r5, r6, r10, r11, r8, r7. The higher the value, the greater the amount of solar radiation received at the surface, and vice versa.

To refine our understanding of how weather conditions impact SRS on a regional basis, we analyzed the correlations between SRS and various meteorological elements in each region (Table 2). We observed that, for all regions, precipitation, relative humidity, low cloud cover, total cloud cover, and aerosol all exhibit significant negative correlations, consistent with the findings shown in Figure 6. Correlations for both SAT and SRS are largely positive, with r1, r2, r5, r6, r7, r9, and r10 passing the 99% significance test. However, correlations for r3, r4, and r11 are relatively weak, indicating that SRS in those regions is less impacted by SAT. We observed no correlation between surface pressure and SRS in any region,

with the exception of r5. Whereas significant positive correlations (at 99% significance) exist between wind speed and SRS in r3 and r6, this relationship returns only weak positive correlations in other regions, and even a weak negative correlation in r1. Therefore, although SAT and wind speed both influence SRS, wind speed only passes the significance test in r3 and r6 regions. Overall, among the eight meteorological influence factors which can enhance SRS are SAT and wind speed, but wind speed only passes the significance test in r3 and r6 regions. Meanwhile, cloud cover, precipitation, relative humidity, and aerosol are the main weakening influence factors.

## Conclusion

This paper used ERA5 reanalysis to investigate the spatial and temporal distributions of SRS throughout China for the period 1961–2020 and to evaluate correlations between SRS and meteorological factors. From this assessment, we draw the following conclusions:

1) SRS high value centers are located primarily on the southwest Tibetan Plateau, whereas the low value center occurs on the northeast Yunnan–Guizhou Plateau and in the Sichuan Basin. SRS values are highest in summer, followed by spring, autumn, and winter. The annual-mean of SRS is increasing in Northeast China, North China, Southwest China, South China, and Xinjiang, whereas the Tibetan Plateau is experiencing a declining trend. SRS trends vary significantly among the four seasons, being greatest in Eastern China and lowest in Western China.
2) The spatial distribution of the first mode of EOF indicates that, between 1961 and 2020, annual-mean SRS on the southern Tibetan Plateau was anti-phased with that of other regions. Combined with the time period, the SRS throughout China underwent a decadal transition around the year 2000, after which most parts of China experienced positive SRS anomalies. This pattern is mainly affected by SAT, total precipitation, relative humidity and cloud cover. Only the southern part of the Tibetan Plateau was dominated by negative anomalies. The spatial distribution of the second mode of EOF reveals a “positive north and negative south” pattern of annual-mean SRS, with a predominantly interannual variability. Using the EEMD method, we found that the temporal evolution of SRS is largely interannual.
3) By analyzing potential influencing factors, we observed that SAT and wind speed are both positively correlated with SRS. In contrast, precipitation, relative humidity, cloud cover, and aerosol are negatively correlated with SRS, suggesting that, although SAT and wind speed serve to enhance SRS, precipitation, relative humidity, cloud cover, and aerosol weaken SRS. We employed REOF to divide Chinese SRS into 11 specific regions. For each region, maximum SRS values occurred in the spring or summer (warm season), whereas minimum values largely coincide with winter. In terms of annual-mean SRS, the top five regions (from largest to smallest) are the western Tibetan Plateau, western Northwest China, the eastern Tibetan Plateau, northern Xinjiang, and North China.

## Data availability statement

Publicly available datasets were analyzed in this study. This data can be found here: ERA5 reanalysis datasets during this study are openly available from the European Centre for Medium-Range Weather Forecasts at https://cds.climate.copernicus.eu/cdsapp#!/search?type=dataset.

## Author contributions

LQ and HJ conceived and designed the research, SW and PY processed the data. HJ analysed the data and wrote the manuscript. LS and LZ reviewed the paper.

## Funding

This work was supported by the Industry Support Project of University in Gansu Province (Grant Nos. 2020C-34), the National Natural Science Foundation of China (Grant Nos. 42005056, 42005058), and the Meteorological scientific research project of Gansu Meteorological Bureau (grant no. ZcZd2022-25).

## Conflict of interest

The authors declare that the research was conducted in the absence of any commercial or financial relationships that could be construed as a potential conflict of interest.

## Publisher’s note

# References


Blanka, B., Martin, W., Doris, F., Daniel, L., Sven, K., Christoph, S., et al. (2017). Projected changes in surface solar radiation in CMIP5 global climate models and in EURO-CORDEX regional climate models for Europe. *Clim. Dyn.* 49, 2665–2683. doi:10.1007/s00382-016-3471-2

Cornes, R. C., Jones, P. D., and Qian, C. (2017). Twentieth-Century trends in the annual cycle of temperature across the northern Hemisphere. *J. Clim.* 30, 5755–5773. doi:10.1175/JCLI-D-16-0315.1

Dickinson, W., and Cheremisinoff, P. (1980). *Solar energy technology handbook*. London: Butterworths.

Dommenget, D., and Latif, M. (2002). A cautionary note on the interpretation of EOFs. *J. Clim.* 15 (2), 216–225. doi:10.1175/1520-0442(2002)015<0216:acnoti>2.0.co;2

Fan, L., Liu, Z., and Liu, Q. (2011). Robust GEFA assessment of climate feedback to SST EOF modes. *Adv. Atmos. Sci.* 28, 907–912. doi:10.1007/s00376-010-0081-5

Franzke, C. (2010). Long-range dependence and climate noise characteristics of antarctic temperature data. *J. Clim.* 23, 6074–6081. doi:10.1175/2010JCLI3654.1

Gao, L. H., Yan, Z. W., and Quan, X. W. (2015). Observed and sst-forced multidecadal variability in global land surface air temperature. *Clim. Dyn.* 44 (12), 359–369. doi:10.1007/s00382-014-2121-9

Guan, J., Liang, C., Zhao, L., Cui, N., Wang, C., and Jiang, S. (2018). Characteristics of temporal-spatial solar radiation distribution in northwest China based on cloud model. *Trans. Chin. Soc. Agric. Mach.* 49 (12), 233–242. (in Chinese). doi:10.6041/j.issn.100-1298.2018.12.028

He, H., Yu, G., and Niu, D. (2003). Method of global solar radiation calculation on complex territories. *Resour. Sci.* 25 (1), 78–85. (in Chinese).

Hersbach, H., Bell, B., Berrisford, P., Hirahara, S., Horanyi, A., Munoz-Sabater, J., et al. (2020). The ERA5 global reanalysis. *Q. J. R. Meteorol. Soc.* 146 (730), 1999–2049. doi:10.1002/qj.3803

Huang, P., Zhao, W., and Li, A. (2017). Estimation of solar radiation and its spatio-temporal distribution characteristics in the mountainous area of western sichuan. *Mt. Res.* 35 (3), 420–428. (in Chinese). doi:10.16089/j.cnki.1008-2786.000238

Jin, C., Wang, B., Liu, J., Ning, L., and Yan, M. (2019). Decadal variability of northern Asian winter monsoon shaped by the 11-year solar cycle. *Clim. Dyn.* 53, 6559–6568. doi:10.1007/s00382-019-04945-4

Li, D., Xie, J., and Wang, W. (1997). A study of summer precipitation features and anomaly in northwest China. *Sci. Atmos. Sin.* 21 (3), 331–340. (in Chinese).

Li, G., and Xie, S. (2014). Tropical biases in CMIP5 multimodel ensemble: the excessive equatorial pacific cold tongue and double ITCZ problems. *J. Clim.* 27 (4), 1765–1780. doi:10.1175/jcli-d-13-00337.1

Meza, F., and Varas, E. (2000). Estimation of mean monthly solar global radiation as a function of temperature. *Agric. For. Meteorology* 100 (2), 231–241. doi:10.1016/s0168-1923(99)00090-8

Qi, Y., Fang, S., and Zhou, W. (2015). Correlative analysis between the changes of surface solar radiation and its relationship with air pollution, as well as meteorological factor in East and West China in recent 50 years. *Acta Phys. Sin.* 64 (8), 10. (in Chinese). doi:10.7498/aps.64.089201

Qi, Y., Fang, S., and Zhou, W. (2014). Variation and spatial distribution of surface solar radiation in China over recent 50 years. *Acta Ecol. Sin.* 34 (24), 7444–7453. (in Chinese). doi:10.5846/stxb201303130409

Qian, C., Fu, C., and Wu, Z. (2011). Changes in the amplitude of the temperature annual cycle in China and their implication for climate change research. *J. Clim.* 24, 5292–5302. doi:10.1175/JCLI-D-11-00006.1

Qian, C., Yan, Z. W., and Fu, C. B. (2012). Climatic changes in the twenty-four solar terms during 1960–2008. *Chin. Sci. Bull.* 57, 276–286. doi:10.1007/s11434-011-4724-4

Qiao, L., Zuo, Z., Xiao, D., Bu, L., and Zhang, K. (2022). Variations in Eurasian surface air temperature over multiple timescales and their possible causes. *Int. J. Climatol.* 1, 4788–4807. doi:10.1002/joc.7504

Shen, Y., and Wang, B. (2011). Effect of surface solar radiation variations on temperature in south—east China during recent 50 years. *Chin. J. Geophys.* 54 (6), 1457–1465. (in Chinese). doi:10.3969/j.issn.0001-5733.2011.06.005

Tao, S., Qi, Y., Shen, S., Li, Y., and Zhou, Y. (2016). The spatial and temporal variation of solar radiation over China from 1981 to 2014. *J. Arid Land Resour. Environ.* 30 (11), 143–147. (in Chinese). doi:10.13448/j.cnki.jalre.2016.362

Thomas, P., Rudy, C., Euphrasie, C., and France, N. (2020). Investigation of local correlations between particulate matter (PM10) and air temperature in the Caribbean basin using Ensemble Empirical Mode Decomposition. *Atmos. Pllution Reserach* 11 (10), 1692–1704. doi:10.1016/j.apr.2020.06.031

Wang, L. (2015). *Regional variations of atmosphere radiation and its quantitative effects on the terrestrial ecosystem productivity*. Wuhan: Wuhan University. (in Chinese).

Wen, X., Shang, K., Wang, S., Yang, D., and Fan, W. (2008). Primary study on regional characteristics of solar radiation in China during 1961-2000. *J. Desert Res.* 28 (3), 554–561. (in Chinese).

Winslow, J., Hunt, E., and Pipe, R. (2001). A globally applicable model of daily solar irradiance estimated from air temperature and precipitation data. *Ecol. Model.* 143 (3), 227–243. doi:10.1016/s0304-3800(01)00341-6

Wu, Y., Zhang, H., Tian, G., and Zhao, Y. (2009). Spatial and temporal distributions of potential solar radiation of complex terrain over shanxi plateau. *Meteorol. Mon.* 35 (5). (in Chinese).

Wu, Z., and Huang, N. (2009). Ensemble empirical mode decomposition: a noise-assisted data analysis method. *Adv. Adapt. Data Anal.* 1, 1–41. doi:10.1142/s1793536909000047

Xu, J., He, J., and Yan, F. (2010). Research on secular variation of solar radiation over northwest China from 1961 to 2007. *Environ. Res.* 15 (1), 89–96. (in Chinese). doi:10.3878/j.issn.1006-9585.2010.01.10

Yan, J., Zhang, D., An, W., Liu, Y., Wu, J., and Yang, P. (2014). Distribution characteristics and assessment of solar energy resource in shanxi. *J. Arid Meteorology* 32 (5), 712–718. (in Chinese). doi:10.11755/j.issn.1006-7639(2014)-05-0712

Yang, S., Wang, K., and Lv, S. (2007). Regional characteristics of global solar radiation evolution in China over recent 40 years. *Acta Energiae Solaris Sin.* 28 (3), 227–232. (in Chinese).

You, Q., Arturo, S., Martin, W., Doris, F., Klaus, F., Ren, G., et al. (2013). Decadal variation of surface solar radiation in the Tibetan Plateau from observations, reanalysis and model simulations. *Clim. Dyn.* 40, 2073–2086. doi:10.1007/s00382-012-1383-3

Zhang, H., Zhang, Q., Yue, P., Zhang, L., Liu, Q., Qiao, S., et al. (2016). Aridity over a semiarid zone in northern China and responses to the East Asian summer monsoon. *J. Geophys. Res. Atmos.* 121 (13), 13 901–913 918. doi:10.1002/2016JD025261

Zhang, J., Shen, R., Shi, C., Bai, L., Liu, J., and Sun, S. (2021). Evaluation and comparison of downward solar radiation from new generation atmospheric reanalysis ERA5 across mainland China. *J. Geo-information Sci.* 23 (12), 2261–2274. doi:10.12082/dqxxkx.2021.180357

Zhang, M., Wu, Z., and Qiao, F. (2018). Deep atlantic ocean warming facilitated by the deep western boundary current and equatorial kelvin waves. *J. Clim.* 31, 8541–8555. doi:10.1175/JCLI-D-18-0255.1

Zhang, Y., Tian, Y., Lin, J., Zhang, Q., and Tao, J. (2020). Temporal-spatial dynamic change characteristics of solar radiation in Beibu Gulf coastal zone during 1961-2017. *Ecol. Sci.* 39 (4), 145–155. (in Chinese). doi:10.14108/j.cnki.1008-8873.2020.04.019

Zhou, B., Yan, L., and Xiao, R. (2012). Temporal and spatial distribution in solar radiation and sunshine in the "Three-River-Source" region. *Resour. Sci.* 34 (11), 2074–2079. (in Chinese).

Zuo, Z., Yang, S., Xu, K., Zhang, R., He, Q., Zhao, T., et al. (2018). Land surface air temperature variations over Eurasia and possible causes in the past century. *Int. J. Climatol.* 38 (10), 1925–1937. doi:10.1002/joc.5306

frontiers | Frontiers in Environmental Science

TYPE Correction
PUBLISHED 17 October 2022
DOI 10.3389/fenvs.2022.1056177



OPEN ACCESS

APPROVED BY
Frontiers Editorial Office,
Frontiers Media SA, Switzerland

*CORRESPONDENCE
Liang Qiao,
19113020001@fudan.edu.cn

SPECIALTY SECTION
This article was submitted to Land Use Dynamics, a section of the journal Frontiers in Environmental Science

RECEIVED 28 September 2022
ACCEPTED 30 September 2022
PUBLISHED 17 October 2022

CITATION
Jin H, Wang S, Yan P, Qiao L, Sun L and Zhang L (2022), Corrigendum: Spatial and temporal characteristics of surface solar radiation in China and its influencing factors.
*Front. Environ. Sci.* 10:1056177.
doi: 10.3389/fenvs.2022.1056177



# Corrigendum: Spatial and temporal characteristics of surface solar radiation in China and its influencing factors

Hongmei Jin[1,2], Suichan Wang[1], Pengcheng Yan[3], Liang Qiao[4]*, Linhua Sun[2] and Ling Zhang[1]

[1]Gansu Meteorological Information and Technical Equip Safeguard Center, Gansu Meteorological Bureau, Lanzhou, China, [2]Lanzhou Resources & Environment Voc-Tech University, Key Laboratory of Climate Resources Utilization and Disaster Prevention and Mitigation of Gansu Province, Lanzhou, China, [3]Institute of Arid Meteorology of CMA, Key Open Laboratory of Arid Climatic Change and Disaster Reduction of CMA, Key Laboratory of Arid Climatic Change and Reducing Disaster of Gansu Province, Lanzhou, China, [4]Department of Atmospheric and Oceanic Sciences/Institute of Atmospheric Sciences, Fudan University, Shanghai, China

KEYWORDS

**solar radiation, China, temporal and spatial characteristics, influence factor, EEMD decomposition**

A Corrigendum on
Spatial and temporal characteristics of surface solar radiation in China and its influencing factors

by Jin H, Wang S, Yan P, Qiao L, Sun L and Zhang L (2022). Front. Environ. Sci. 10:916748. doi: 10.3389/fenvs.2022.916748

## INCORRECT FUNDING

In the original article, there was an error in the Funding statement. "This work was supported by the National Natural Science Foundation of China (Grant Nos. 42005056, 42005058), the Industry Support Project of University in Gansu Province (Grant Nos. 2020C-34) and the Meteorological scientific research project of Gansu Meteorological Bureau (grant no. ZcZd2022-25)". The correct Funding statement appears below.

## FUNDING

"This work was supported by the Industry Support Project of University in Gansu Province (Grant Nos. 2020C-34), the National Natural Science Foundation of China (Grant Nos. 42005056, 42005058), and the Meteorological scientific research project of Gansu Meteorological Bureau (grant no. ZcZd2022-25)."

The authors apologize for this error and state that this does not change the scientific conclusions of the article in any way. The original article has been updated.

## Publisher's note

All claims expressed in this article are solely those of the authors and do not necessarily represent those of their affiliated organizations, or those of the publisher, the editors and the reviewers. Any product that may be evaluated in this article, or claim that may be made by its manufacturer, is not guaranteed or endorsed by the publisher.

frontiers | Frontiers in Environmental Science

TYPE Original Research
PUBLISHED 15 September 2022
DOI 10.3389/fenvs.2022.949250



OPEN ACCESS

EDITED BY
Merja H. Tölle,
University of Kassel, Germany

REVIEWED BY
Patrick Laux,
Karlsruhe Institute of Technology (KIT), Germany
Rene Orth,
Max Planck Institute for Biogeochemistry, Germany
Anna Merrifield,
ETH Zürich, Switzerland

*CORRESPONDENCE
Paul A. Dirmeyer,
pdirmeye@gmu.edu

SPECIALTY SECTION
This article was submitted to Interdisciplinary Climate Studies, a section of the journal Frontiers in Environmental Science

RECEIVED 20 May 2022
ACCEPTED 22 August 2022
PUBLISHED 15 September 2022

CITATION
Dirmeyer PA, Sridhar Mantripragada RS, Gay BA and Klein DKD (2022), Evolution of land surface feedbacks on extreme heat: Adapting existing coupling metrics to a changing climate.
*Front. Environ. Sci.* 10:949250.
doi: 10.3389/fenvs.2022.949250



# Evolution of land surface feedbacks on extreme heat: Adapting existing coupling metrics to a changing climate

Paul A. Dirmeyer [1*†], Rama Sesha Sridhar Mantripragada [1†], Bradley A. Gay [2†] and David K. D. Klein [1†]

[1]Department of Atmospheric, Oceanic, and Earth Sciences, George Mason University, Virginia, VA, United States, [2]Department of Geography and Geoinformation Science, George Mason University, Virginia, VA, United States

Episodes of extreme heat are increasing globally, and dry land surface states have been implicated as an amplifying factor in several recent heat waves. Metrics used to quantify land-heat coupling in the current climate, relating sensible heat fluxes to near-surface air temperature, are applied to multimodel simulations of the past, present, and future climate to investigate the evolving role of land–atmosphere feedbacks in cases of extreme heat. Two related metrics are used: one that describes the climatological state of land-heat coupling and one that gives an episodic estimate of land feedbacks, here defined as the metric's value at the 90th percentile of monthly mean temperatures. To provide robust statistics, seasonal multimodel medians are calculated, with the significance of changes determined by the degree of model consensus on the sign of the change. The climatological land-heat coupling mirrors other metrics of land–atmosphere interaction, peaking in transition regions between arid and humid climates. Changes from preindustrial to recent historical conditions are dominated by decreased land surface controls on extreme heat, mainly over the broad areas that have experienced expanded or intensified agriculture over the last 150 years. Future projections for increased atmospheric $CO_2$ concentrations show a waning of areas of weakened land-heat feedbacks, while areas of increasing feedbacks expand over monsoon regions and much of the midlatitudes. The episodic land-heat metric is based on anomalies, which creates a quandary: how should anomalies be defined in a nonstationary climate? When the episodic coupling is defined relative to the means and variances for each period, a broadly similar evolution to the climatological metric is found, with historically dominant decreases giving way to widespread moderate increases in future climate scenarios. Basing all statistics on preindustrial norms results in huge increases in the coupling metric, showing its sensitivity to the definition of anomalies. When the metric is reformulated to isolate the impact of changing land and temperature variability, the tropics and Western Europe emerge as regions with enhanced land feedbacks on heatwaves, while desert areas and much of the remainder of the midlatitudes show reduced land-heat coupling.

KEYWORDS

CMIP6, extreme heat, climate change, coupling metrics, near-surface air temperature, sensible heat, model consensus, land surface

# 1 Introduction

Episodes of extreme heat are a growing concern as recent heat waves continue to display unusual intensity across more locations (Albergel et al., 2019; Petch et al., 2020; Yiou et al., 2020; Neal et al., 2022). There is growing evidence of the key role that land surface conditions play in exacerbating and prolonging heatwaves (Fischer et al., 2007; Hauser et al., 2016; Hirsch et al., 2019; Schumacher et al., 2019; Wehrli et al., 2020; Benson and Dirmeyer, 2021; Dirmeyer et al., 2021). Extreme heatwave periods with distinct soil moisture deficit signatures and climatological anomalies are often characterized by reductions in terrestrial evaporative cooling and increasing air temperature in parallel with elevated soil moisture deficits and atmospheric demand for water. Such perturbations in soil moisture contribute to dramatic variability in land–atmosphere interactions and seasonality disruption, thereby affecting surface heat and moisture fluxes and atmospheric conditions. Thus, they are also critically linked to hydrologic extremes (Zscheischler et al., 2018; Bevacqua et al., 2022; O et al., 2022). These relationships present an opportunity to interpret the mechanisms driving heatwave patterns in changing climate regimes (Seneviratne et al., 2010; Lau and Nath, 2014; Ukkola et al., 2018; Miralles et al., 2019).

Land–atmosphere interactions and their associated feedback sensitivities are acknowledged as vital components of the Earth system that affect extremes such as droughts and heatwaves (Santanello et al., 2018). Miralles et al. (2012) developed a relatively simple and straightforward pair of metrics to quantify the role of land surface anomalies in extreme heat, ostensibly in the form of soil moisture, but expressed through variations in surface heat fluxes between land and atmosphere. They put forward two metrics, one to quantify the climatology of land-heat feedbacks in any location and the other to identify whether specific heatwave episodes are augmented by land–atmosphere feedbacks. Their study applied the metrics to recent climate data from observationally based sources.

In this study, we adapt the metrics of Miralles et al. (2012) to apply to a host of climate model simulations of past, recent, and future climates. Given the constraints of those metrics, we ask several questions. What patterns exist for extreme heat anomalies under preindustrial conditions? How has heatwave intensity changed since the preindustrial period? How might heatwave susceptibility change with a doubling and/or quadrupling of anthropogenic-induced greenhouse gas emissions ($CO_2$)? What conclusions may be drawn from the spatiotemporal variability of heatwave anomalies with the introduction of warming relative to preindustrial conditions? A major point that emerges from this study is the quandary of finding meaningful definitions of extreme heat in a warming climate and the role of the land surface therein. Section 2 describes the data sets, the metrics, and how they are applied to climate model output. Results are presented in Section 3, first for the climatological metric and then for the episodic one applied to the 90th percentile of extreme heat in climate model simulations. The conclusion is presented in Section 4.

TABLE 1 CMIP6 experiments and the periods utilized for each experiment.

| Experiment | Period | Description |
|---|---|---|
| piControl | All years[a] | Preindustrial control; *no external forcings* |
| Historical | Last 50 years | Late 20th century/early 21st century |
| 1pct$CO_2$ | Years 21–70 | Up to a doubling of $CO_2$ |
| 1pct$CO_2$ | Years 91–140 | Up to a quadrupling of $CO_2$ |

[a]See Supplementary Table 1 for the number of years for each model.

# 2 Materials and methods

To quantify land surface feedback in the manner of Miralles et al. (2012), particularly their episodic coupling metric $\pi$ described in the following, daily data are customarily used. In this study, temporal sampling was upscaled to be consistent with the available multimodel global data. We utilize the monthly mean model output from the Coupled Model Intercomparison Project Phase 6 (CMIP6; Eyring et al., 2016). We use a single ensemble member from each of the 30 models (see Supplementary Table S1 for a complete list), as model ensemble sizes vary greatly; choosing ensemble means or including all ensemble members would give unequal treatment to different models. The advantage of examining a large multimodel ensemble is the improved skill over single-model simulations and forecasts (Krishnamurti et al., 1999; Palmer et al., 2004; Tebaldi and Knutti, 2007), but ensembles of opportunity like CMIP6 do not inherently optimize this improvement, and harvesting potential skill beyond what is attainable by an equal weighting of each model provides many challenges (Knutti et al., 2010; Leduc et al., 2016; Abramowitz et al., 2019). The simple approach used here is that multimodel medians are calculated among all models, which minimizes the impact from unreasonable outliers that can skew the multimodel mean (Tebaldi and Knutti, 2007; Samaniego et al., 2018; Schwingshackl et al., 2018; Chen and Dirmeyer, 2019) and may offset somewhat the lack of spread among models with similar ancestry.

The analysis is performed on three CMIP6 Diagnostic, Evaluation, and Characterization of Klima (DECK) simulations, which are the most numerous: 1) preindustrial control simulations (piControl), 2) historical simulations, and 3) emission-driven simulations, that is, 1% per year $CO_2$ increase (1pctCO2). Table 1 lists the experiments and periods used. piControl simulations provide the baseline climatology for all comparisons. Historical simulations include multiple climate-forcing factors beyond $CO_2$, including time-varying land cover and aerosols. 1pctCO2 runs are idealized simulations in which atmospheric $CO_2$ is increased by 1% per year, beginning from piControl conditions, with no other changes. The 1pctCO2 runs were chosen for future simulations as they are available from many models and represent transience in the major climate forcing. The comparison between these historical and emission-forcing experiments to the piControl baseline provides an indication of how land surface feedbacks may have changed and contributed to extreme heatwave patterns since preindustrial conditions. For the 1pctCO2 simulation, two periods are considered from each model: 1) years 21–70, during which atmospheric $CO_2$ concentrations double from ~23% above preindustrial levels and 2) years 91–140 wherein atmospheric $CO_2$ concentrations ultimately quadruple beyond preindustrial levels.

The strength of land surface coupling in relation to extreme heat is quantified using the soil moisture and near-surface temperature coupling metric described by Miralles et al. (2012):

$$\Pi = r\left(H,T\right) - r\left(H_p,T\right) \tag{1}$$

where $r$ is Pearson's correlation coefficient, $H$ is the monthly surface sensible heat flux, $T$ is the monthly-averaged near-surface air temperature at 2 m above the surface, and $H_p$ is defined as the potential sensible heat flux given by:

$$H_p = H + L - \lambda E_p \tag{2}$$

where $L$ is the latent heat flux, $\lambda$ is the latent heat of vaporization, and $E_p$ is potential evapotranspiration based on the Priestley–Taylor formulation (Priestley and Taylor, 1972) expressed as:

$$\lambda E_p = \alpha m\left(\frac{H+L}{m+\gamma}\right) \tag{3}$$

whereby the sum of model sensible and latent heat represents net radiation, the P–T coefficient is $\alpha = 1.26$, $m$ is the slope of saturation vapor pressure with temperature calculated from the monthly mean near-surface air temperature, and $\gamma$ is the psychrometric constant. We found differences in patterns of $\Pi$ to be largely indiscernible if Spearman's rank correlation coefficient is used instead of Pearson's correlation coefficient, although the magnitudes are usually slightly smaller.

It should be noted that despite the title of the Miralles et al. (2012) article, the role of soil moisture is only inferred as a potential control on $H$ and $H_p$. In fact, the atmosphere does not "feel" soil moisture directly but instead feels the fluxes from the land surface that may be modulated by soil moisture. Given the variations among soil moisture parameterizations and reporting among CMIP6 models, it makes sense to focus on the more consistently reported heat fluxes as a linkage to land state impacts on climate.

In addition to the climatological metric ($\Pi$), Miralles et al. (2012) defined and applied a land-heat metric at a specific time $t$:

$$\pi(t) = \left(\frac{H(t)-\bar{H}}{\sigma_H} - \frac{H_p(t)-\overline{H_p}}{\sigma_{H_p}}\right)\left(\frac{T(t)-\bar{T}}{\sigma_T}\right) \tag{4}$$

The overbars indicate a temporal mean (in this case, a climatological mean for each month of the year), while $\sigma$ is the standard deviation over time (with the seasonal cycle removed). This $\pi$ metric identifies heat wave anomalies with a terrestrial driver component. The terrestrial component is characterized by the connection between sensible heat flux ($H$) and in particular potential sensible heat flux ($H_p$), the latter of which is small when potential evapotranspiration is large, thus contributing to large positive values of $\pi$. Furthermore, temperature anomalies act as an amplification factor.

While the climatological and land-heat metrics in Miralles et al. (2012) were derived using daily data, monthly means were extracted from CMIP6 climate model simulations in this study. The main impact of this approach is that a different timescale of extreme heat is sampled to compare temperature anomalies and associated land feedbacks over monthly periods; in this case, variations shorter than 1 month are *not* considered. Consequently, due to the highly nonlinear nature of moist thermodynamics, these calculations performed on monthly mean data will not be identical to computing monthly means based on daily observations. However, to investigate climate change, it is important to apply consistent formulation to all models in all cases, such that taking differences between experiments may ameliorate any systematic biases introduced by the application of these metrics to longer time scales.

The extreme heat coupling metrics are calculated separately for each month based on the respective experimental period wherein monthly values are seasonally averaged. For each model, metrics are calculated on its native grid, and then data from each model are regridded with nearest neighbor interpolation to a common, high-resolution global grid (2560 × 1280, roughly 0.14° × 0.14° grid cells) to preserve the spatial structure contribution from each model (Dirmeyer et al., 2013a; Dirmeyer et al., 2013b and several subsequent studies). Nearest neighbor interpolation, combined with the use of each model's land–sea mask, removes the risk of introducing data from adjacent water-covered grid cells. Effectively, for the central latitude and longitude of each grid cell of the 2560 × 1280 grid, we find the value in each model's unique grid cell that contains that

coordinate, combine the data from all models for that location, and take the median. Only ice-free land grid cells common to at least 90% of the models on the high-resolution grid are populated with the data.

To compute the monthly mean metrics, surface sensible heat flux information is extracted directly from 30 CMIP6 models, whereas in Miralles et al. (2012), net radiation and surface latent heat flux were used to estimate surface sensible heat flux. However, most of these models do not provide net radiation or ground heat flux data; thus, surface potential sensible heat flux is estimated with the application of the P–T equation. Despite the integration of CMIP-derived monthly mean data as opposed to daily datasets, this approach does have a successful precedent for climate change investigations (e.g., Dirmeyer et al., 2013a; Dirmeyer et al., 2013b). Finally, monthly means are averaged to produce seasonal means. Field significance is tested using the approach outlined by Dirmeyer et al. (2013a) and Dirmeyer et al. (2013b).

We calculate for each model the 90th percentile value of $\pi$ for each month, take the average across the 3 months in each season, and then select the median value among models as a representation of this land-heatwave coupling metric. However, each of the terms comprising Eq. 4 is sensitive to how means and variances are defined, and thus the anomalies that are at the heart of these heat metrics and many climate statistics. What is the proper climatology to use in a changing climate? Anomalies relative to the piControl mean emphasize the climate change signal, violating the implied assumption of climate stationarity in the formulation of Eq. 4. Anomalies relative to each simulation's mean tend to exaggerate anomalies in early and late years in simulations with a trend, implying a false normality around the middle of the period. Alternatively, anomalies relative to a detrended time series (e.g., running mean) emphasize the interannual variations over the climate trend. Each distinction provides a fundamentally different meaning than simply using piControl as the baseline climatology for all statistics.

Defining the standard deviations of temperature and the two sensible heating variables also presents choices, and these choices depend directly on how the means are defined. For example, if $\sigma$ is not defined relative to the same mean as the anomalies, this value will be inconsistent. However, such an approach may still be useful when examining the climatology of variability independently from the external forcings; after detrending, a growing $\sigma$ over time suggests increased variability in a warming climate, which is conducive to stronger extremes and greater societal impacts.

For comparisons, the 90th percentile value of $\pi$ is computed for each model at each grid cell for each month, representative of subseasonal periods of extreme heat. For the piControl baseline simulation, all available data are used (see Supplementary Table S1). For the other experiments, a trailing 30-year mean (unweighted–for year $t$, the climatology is defined as the average of years $t-30$ through $t-1$) is applied to define a moving climatology consistent with the period commonly used (Arguez and Vose, 2011). Moreover, this technique was compared to a linear detrending approach over a 50-year period, and the results are very similar. However, in real time, under a changing climate, future data are not available; therefore, the practicable trailing 30-year mean is used here. During the first 10 years of the period, encompassing years 21–70 of the 1pct$CO_2$ experiment, the trailing 30-year period extends before the initialization of the experiment. Under these circumstances, the last decade of the piControl simulation from the same model is used as a source of data to complete the 30-year mean calculations.

Finally, the significance of change is defined by the level of agreement among models, inasmuch as this can be considered an indicator of certainty (Pirtle et al., 2010; Parker, 2013; Brunner et al., 2020). Specifically, under the null hypothesis that each model will return a random sign of the difference between two cases with equal probability, the level of agreement among models is significant at the 99% confidence level if 22 or more models have the same sign of the change ($p = 0.008$). Such a stringent confidence level somewhat ameliorates the degree of agreement that may arise because we have included in our 30-model ensemble related models from within several modeling centers (see Supplementary Table S1). Furthermore, grid cells are masked white in difference plots when this confidence level is not met. As we are examining metrics related to extreme heat, we also do not consider grid cells at any location where the seasonal mean temperature in the warmest case is at or below 0°C.

# 3 Results

## 3.1 Climatological coupling

Figure 1 shows the multimodel median value of the climatological soil moisture–temperature coupling metric $\Pi$ for each season from the piControl simulations. First, the seasonal mean is calculated for each model, and then the multimodel median is estimated for the 30 models. The JJA and DJF panels can be compared with Figures 1A,B from Miralles et al. (2012), which were calculated with observationally constrained data from ERA-Interim (Dee et al., 2011) and GLEAM (Martens et al., 2017). Supplementary Figure S1 shows the results from the historical simulations, which are very similar but more temporally consistent with Figures 1A,B from Miralles et al. (2012). The strongest coupling between surface heat fluxes, presumably controlled by soil moisture and near-surface air temperature, tends to be highest in warm, semiarid regions, including regions on the fringes of monsoons. The index $\Pi$ is around zero in locations where surface evaporation is substantially energy limited, where extreme heat is rare, and in hot dry regions where there is no

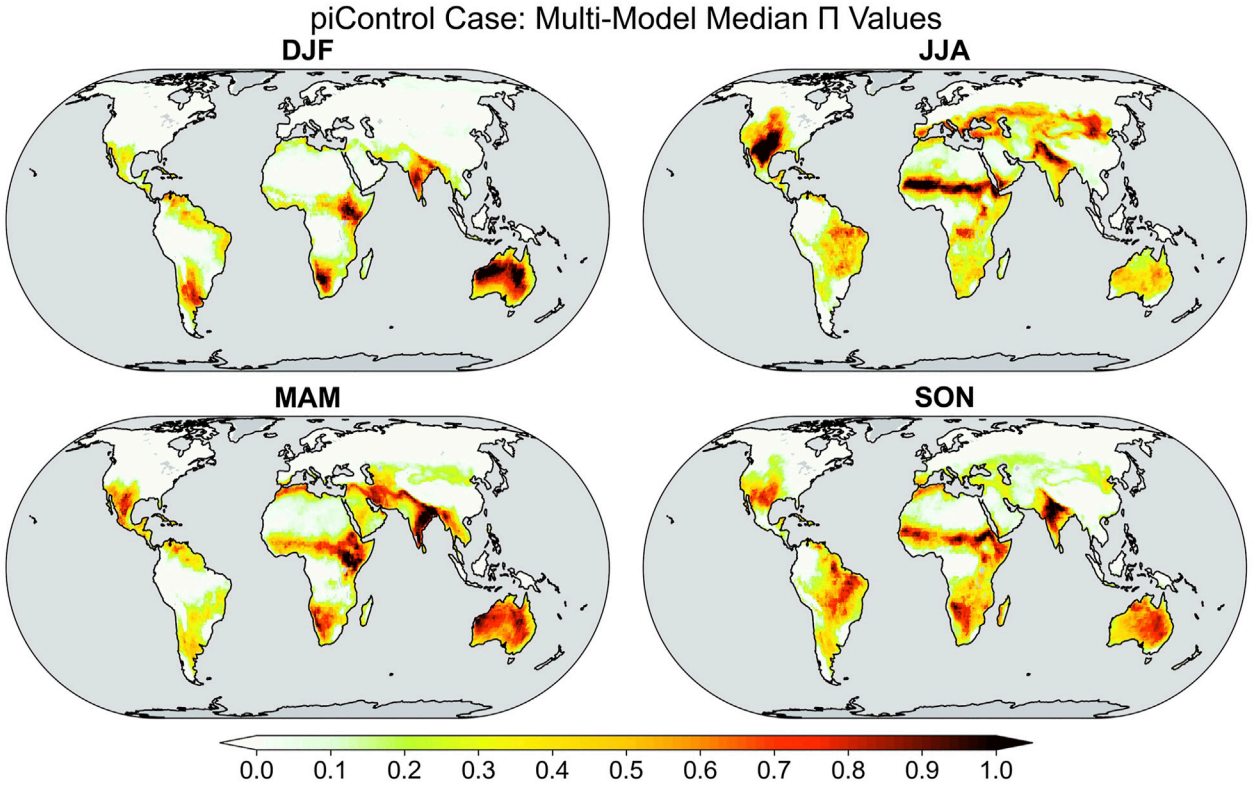


FIGURE 1
Multimodel median values of soil moisture–temperature coupling ($\Pi$; dimensionless) for each season from preindustrial control (piControl) simulations from CMIP6. Values are calculated over ice-free land areas only.

evaporation. As noted by Miralles et al. (2012), areas exhibiting large $\Pi$ values correspond well with multimodel derived hot spots of soil moisture–temperature coupling derived by other techniques (Koster et al., 2006; Dirmeyer, 2011). The agreement between $\Pi$ calculated from the CMIP6 models and the original Miralles et al. (2012) results is the greatest in the Southern Hemisphere during DJF, particularly over Africa and Australia, although the CMIP6 models also show stronger extreme heat coupling over Australia during JJA than does Miralles et al. (2012).

When comparing the coupling metric $\Pi$ from the late historical period relative to the piControl baseline (Figure 2), the median change is dominated by decreased soil moisture–temperature coupling across every season, with 99% confidence in the 30-model level of consensus. These areas of change largely correspond to regions of land cover change during the same interval, namely, the expansion of agriculture (North America, eastern Europe into central Asia, Northern China, and Northeast Brazil). Such differential effects of vegetation on extreme heat demonstrate the importance of biophysical indicators (Teuling et al., 2010). While some of the widespread areas of reduction over Africa appear to correspond to agricultural expansion, it is not indicated to be as widespread in the Hurtt et al. (2020) dataset as appears in Figure 2. Moreover, areas with indications of increasing $\Pi$ are small, scattered, and not greater than random chance in terms of field significance. Additionally, nearly one-third of the global land area displays increase in $\Pi$ across each season; however, when screening for significant model consensus, almost none of these areas pass the testing criterion.

As climate would be projected to approach the doubled $CO_2$ level with no other changes from piControl conditions (Figure 3), decreases in $\Pi$ again dominate in every season. Globally, two regions show most of this negative trend, one in Africa (mainly East Africa) and one in India. Both CMIP5 and CMIP6 models project wetter conditions over these regions (Zhao and Dai, 2015; Wang et al., 2020; Dosio et al., 2021; Zhao and Dai, 2022), and CMIP5 models had indicated reduced sensible heat flux over these areas (Dirmeyer et al., 2013b). A few contiguous areas show consensus seasonal increases in $\Pi$: the Western Mediterranean, Northern Indus and Ganges basins, the Southern Great Plains and northern Mexico during boreal winter, the South-central U.S., parts of Europe and central Australia during MAM, much of Europe and southern Arabia in SON, and just scattered and

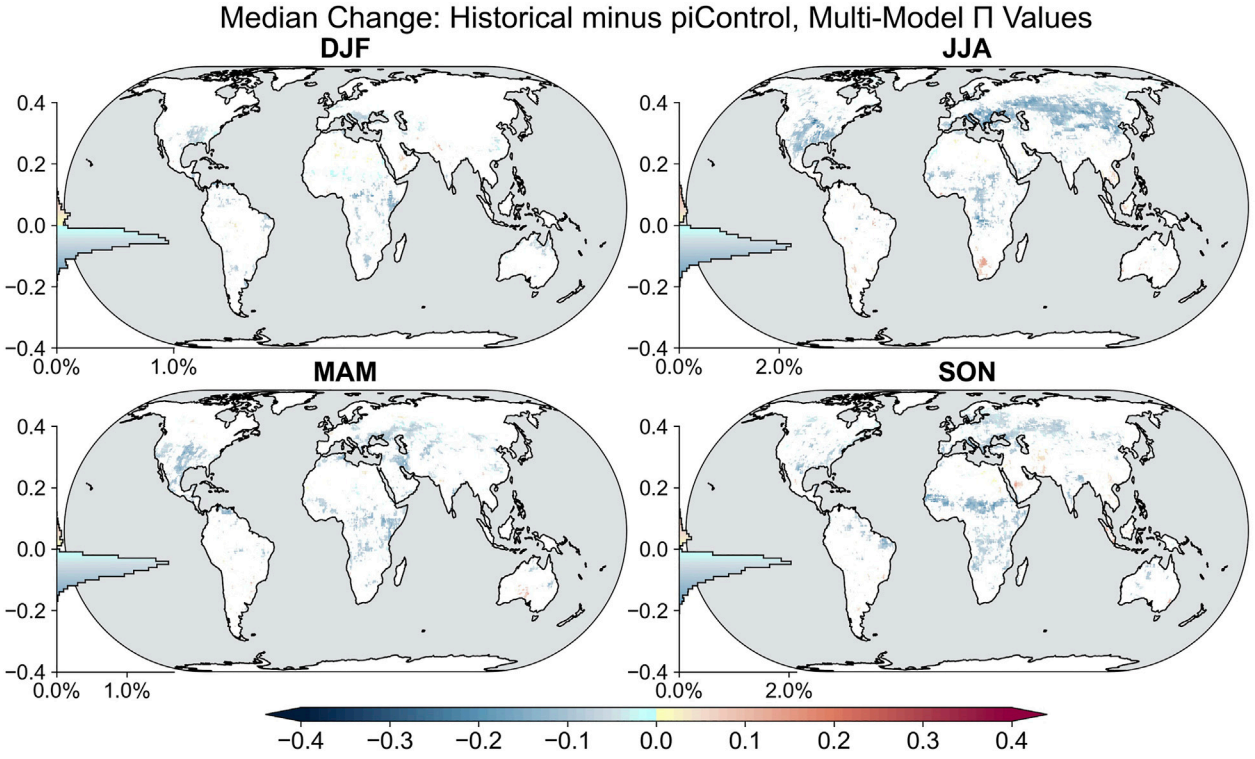


FIGURE 2
Multimodel median change in $\Pi$ (dimensionless) for each season from piControl to the last 50 years of the historical simulations in CMIP6. Areas are masked where the agreement among models on the sign of the change is below the 99% confidence level, or where the median of seasonal mean near-surface air temperature is below 0°C. Histograms show the probability distribution of significant changes as a fraction of the total land area.

diffuse locations during JJA. Note that there is no land use change specified in this experiment, but most of these models predict vegetation phenology and about half include dynamic vegetation parameterizations.

Shifting to the quadrupling $CO_2$ scenario, the strongest and most widespread signals emerge. Areas of decreased soil moisture–temperature coupling in Africa and India persist and are joined by a large area of eastern South America during the JJA and SON seasons (Figure 4). However, there is a robust appearance of increased soil moisture control on extreme heat over many parts of the world across all seasons, matching or exceeding the area of decreased coupling. Beginning with boreal spring (MAM), a band of large consensus increases exists in $\Pi$ across much of the Mediterranean region from Spain to Turkey. Additionally, many broad areas of smaller consensus increases are indicated, spanning across central Asia and North America, from the central Great Plains westward across the central Rocky Mountains. Large areas over the western Sahara exhibit small consensus increases in $\Pi$. In the tropics, large fractions of Indonesia, the Amazon, and Congo basins show increases, while Southern Hemisphere subtropics across both continents display a scattering of increased $\Pi$ distribution.

Moving into boreal summer and austral winter, widespread areas of strong increases in $\Pi$ emerge. Over North America, there is a band over the entire Northern portion of the midlatitude agricultural belt, as well as portions of the Eastern U.S. and much of the North American monsoon region. Over Eurasia, there is a similar band of large changes stretching from Southern France to the Asian Taiga in Northern Kazakhstan across to Mongolia and northward into Finland. The small magnitude consensus increases over the desert shift to the Eastern Sahara, most of Arabia, and into Southern Iran. There are also small magnitude consensus increases over parts of Southeast Asia and China. In the tropics, there are large increases in $\Pi$ over the western parts of the Congo and Amazon Basins, the latter extending Northward into the Guianas. Areas in the Southern Hemisphere with Mediterranean climates (South Africa, Western Australia, and Chile) also have large increases, while Antarctica was masked from this investigation. Concomitantly, most of the Arctic displays little visible variability among coupling regimes across experiments, baseline climatology, and external forcing, that is, little variability is indicated based on the significance criterion (i.e., no positive statistical significance in soil moisture–heat coupling.)

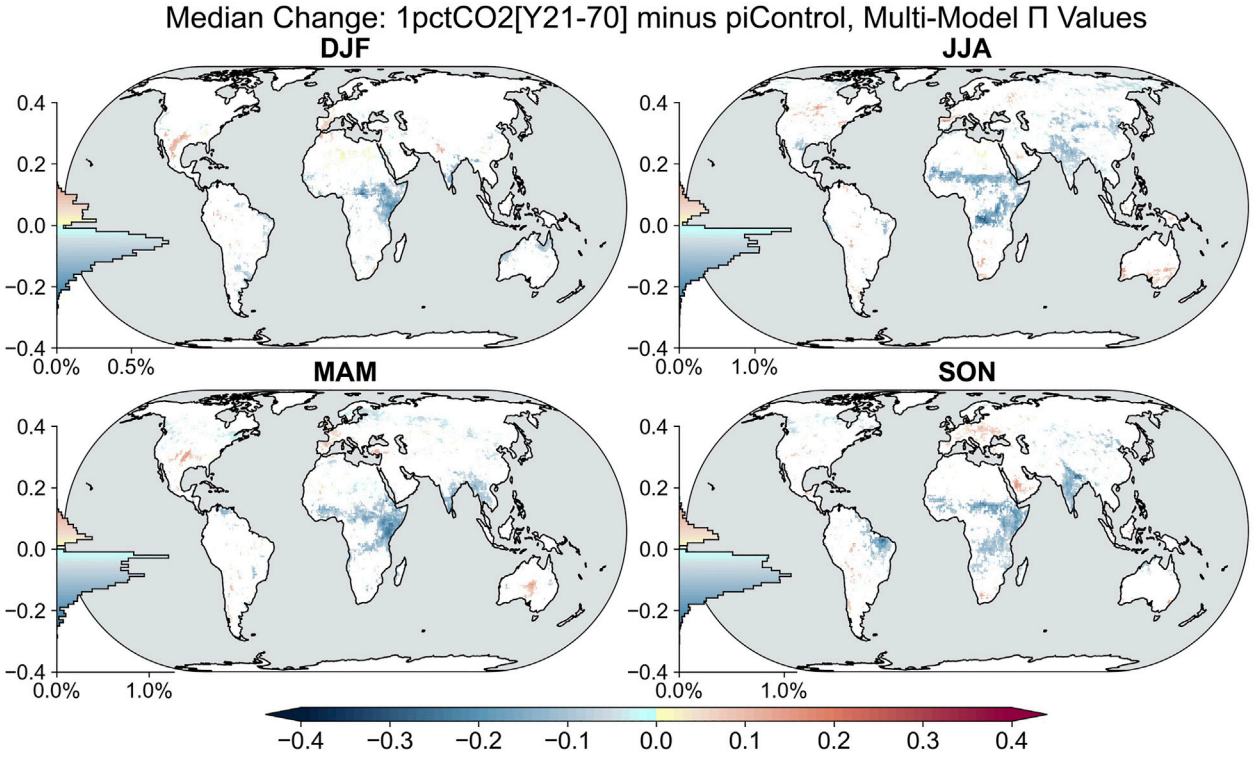


FIGURE 3
As in Figure 2 for the median change in $\Pi$ (dimensionless) from piControl to years 21–70 of the 1pctCO2 simulations (leading up to a doubling of $CO_2$).

In boreal fall and austral spring, broad areas of large increases persist in the Americas: over the central Rockies, Northern Great Plains, Northern Mexico, western Amazon, and Venezuela. Nearly all of Europe south of 55°N shows a consensus increase in $\Pi$, including the Caucasus region. There is also a band across Africa and Arabia north of 15°N and over southeastern Australia and South Africa. This season shows the greatest areal coverage of significant changes in the Arctic, mostly small decreases in land–heat coupling strength.

During boreal winter and austral summer (DJF), the most prominent feature is the broad area of a strong increase in $\Pi$ over most of Mexico and the southwestern U.S. A weaker but larger area is seen over much of South America between the equator and 20°S east of the Andes. In the Eastern Hemisphere, regions of consensus increase in $\Pi$ are patchy, with the areas of strongest increase over the Maghreb, the Levant, Tigris Basin, and upper Indus and Ganges basins. A sizeable fraction of southern Africa also shows consensus changes.

When compared to the median values of $\Pi$ from the piControl simulations, most of the consensus changes outside the low latitudes are poleward extensions of existing regions of strong soil moisture–temperature coupling, consistent with previous findings suggesting a *poleward shift* in land–atmosphere coupling regimes (Dirmeyer et al., 2013a; Dirmeyer et al., 2013b), for example, in the JJA panel of Figure 4, north of 30°N, changes where the piControl values of $\Pi$ are between 0.2 and 0.5 and average between + 0.02 and + 0.03, while above and below that range of $\Pi$, the mean changes are smaller. At low latitudes, areas of pronounced increases in $\Pi$ are also mainly an extension of higher values into regions that had low values in the piControl simulations and not an amplification of soil moisture–temperature coupling in a place where it is already strong.

## 3.2 Episodic coupling

Miralles et al. (2012) developed an instantaneous land–heat coupling metric ($\pi$) that has been applied here to the CMIP6 model simulations at monthly timescales. The $\pi$ metric indicates the degree to which a specific episode of extreme heat is driven by a feedback chain from soil moisture and surface fluxes to air temperature. As demonstrated by Eq. 4, $\pi$ is based on differences and products of normalized anomalies, that is, standard normal deviates (Koster et al., 2009). There exists a quandary for statistics of this type when applied in a

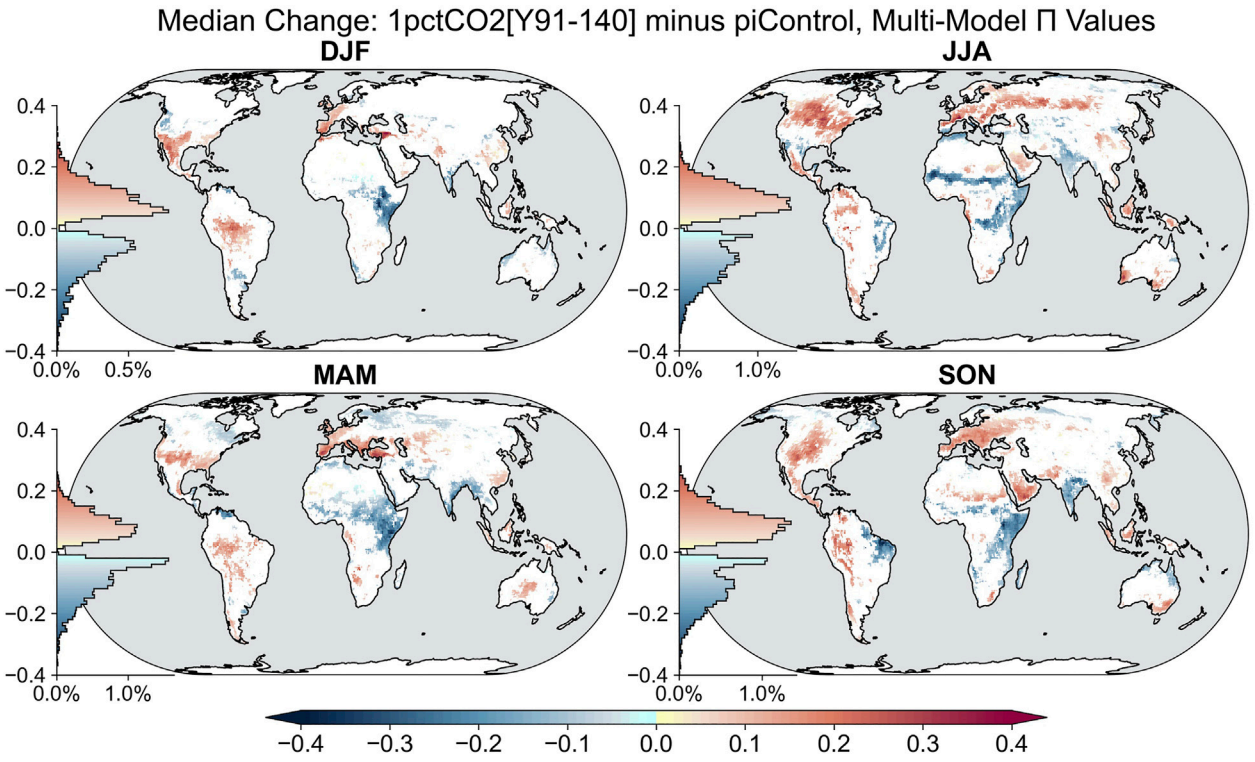


FIGURE 4
As in Figure 2 for the median change in $\Pi$ (dimensionless) from piControl to years 91–140 of the 1pctCO2 simulations (leading up to a quadrupling of $CO_2$).

nonstationary climate, as notions of "anomaly" and "variance" are dependent on the definition of the mean, a definition representative of normal conditions. What means should be used? Should one base normality on the conditions before anthropogenic climate change began, or should it be defined more proximate to the point in time under consideration?

Conventionally, climate normals are defined using a trailing 30-year (or in common practice, a complete prior 3 decade) mean (Arguez and Vose, 2011), but it has been recognized that this practice is becoming inappropriate in a changing climate as the basis of defining anomalies for predicted events (e.g., Livezey et al., 2007; Milly et al., 2008). One alternative is to fit a regression, linear or otherwise, to data to create a time-varying normal. However, we should first ask the question of the purpose of a metric like $\pi$. It was conceived to be an indicator of the strength of a physical process, namely, the contribution of the land surface to the severity of heatwaves, and that is a quantity that is worthwhile to estimate for past and future as well as present climate conditions. We examine here if it is possible to use $\pi$ for this purpose, particularly how the definitions of the means ($\bar{T}$, $\bar{H}$, $\overline{H_p}$) used to calculate the anomalies ($T'$, $H'$, $H_p^{'}$) and the mean used as a baseline to calculate the standard deviations ($\sigma_T$, $\sigma_H$, $\sigma_{H_p}$) affect $\pi$ and its interpretation.

Figure 5 shows the result for the preindustrial simulations (piControl)—it is to be noted that the scale for $\pi$ is different compared to that for $\Pi$. Large values suggest regions where there is a stronger land surface feedback on extreme heat. In austral summer (DJF), Northern Australia, inland Southern Africa, and South America, and the Amazon delta have some of the highest values. In MAM, there is a northward shift, with the strongest feedbacks indicated over a smaller portion of Northern Australia, Southeast Asia, from the Guinea coast of Africa eastward to the Ethiopian Highlands, and small areas on the continents around the Caribbean Sea and the Gulf of Mexico. By JJA, large contiguous areas of large $\pi$ emerge over much of southern North America and the Sahel region of Africa, along with scattered smaller areas, such as over Northwestern India. During SON, much of tropical and subtropical South America shows very high values, as well as several areas scattered across East Africa.

Regionally, there are some clear patterns of seasonality. North America and much of midlatitude Eurasia show a clear oscillation between summer and winter. In East Asia, there is a South-to-North progression of high $\pi$ values into summer but also an outbreak from a hotspot around Beijing and the Gobi Desert in MAM that expands across the Eurasian Steppes by JJA.

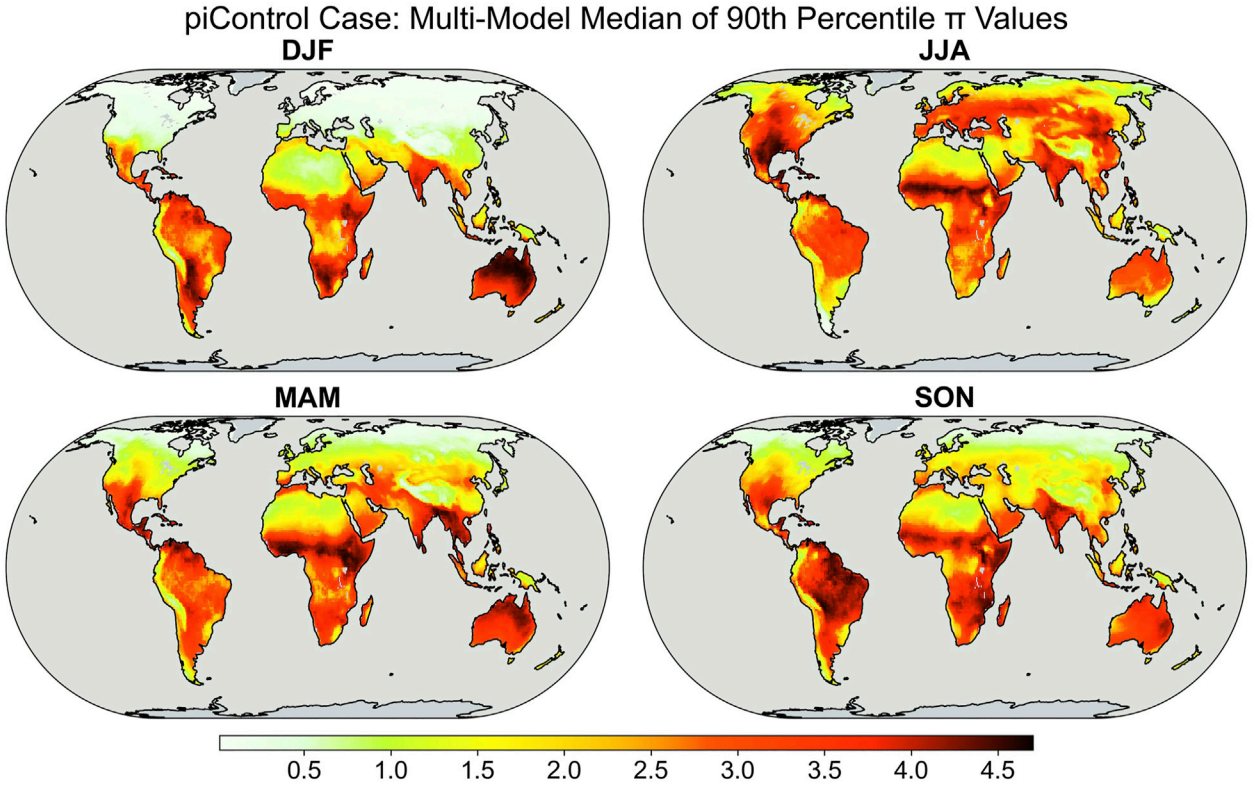


FIGURE 5
Multimodel median of the 90th percentile values of monthly scale soil moisture–temperature coupling ($\pi$; dimensionless) for each season from preindustrial control (piControl) simulations. Values are calculated over ice-free land areas only.

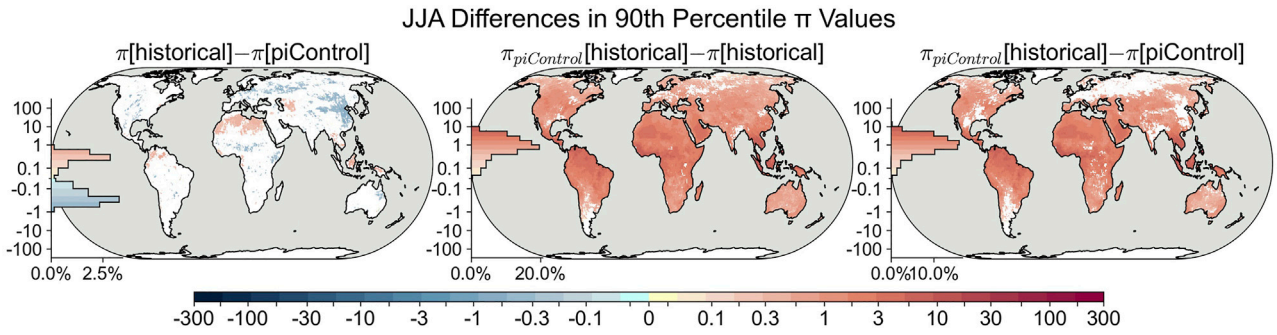


FIGURE 6
JJA multimodel median of differences in the 90th percentile values of $\pi$ (dimensionless). The left map shows differences when $\pi$ is calculated from the last 50 years' data from the historical simulations and $\pi$ from piControl. The middle map shows the difference when means and standard deviations from the piControl climatology are used to calculate $\pi$ for the late historical period versus using all climate statistics from the historical period. The right map shows the change from piControl to the late historical period when piControl climatology is used as the basis for calculating $\pi$ in both periods. Areas are masked where the agreement among models on the sign of the change is below the 99% confidence level, or where the median of seasonal mean near-surface air temperature is below 0°C. Histograms show the probability distribution of significant changes as a fraction of the total land area.

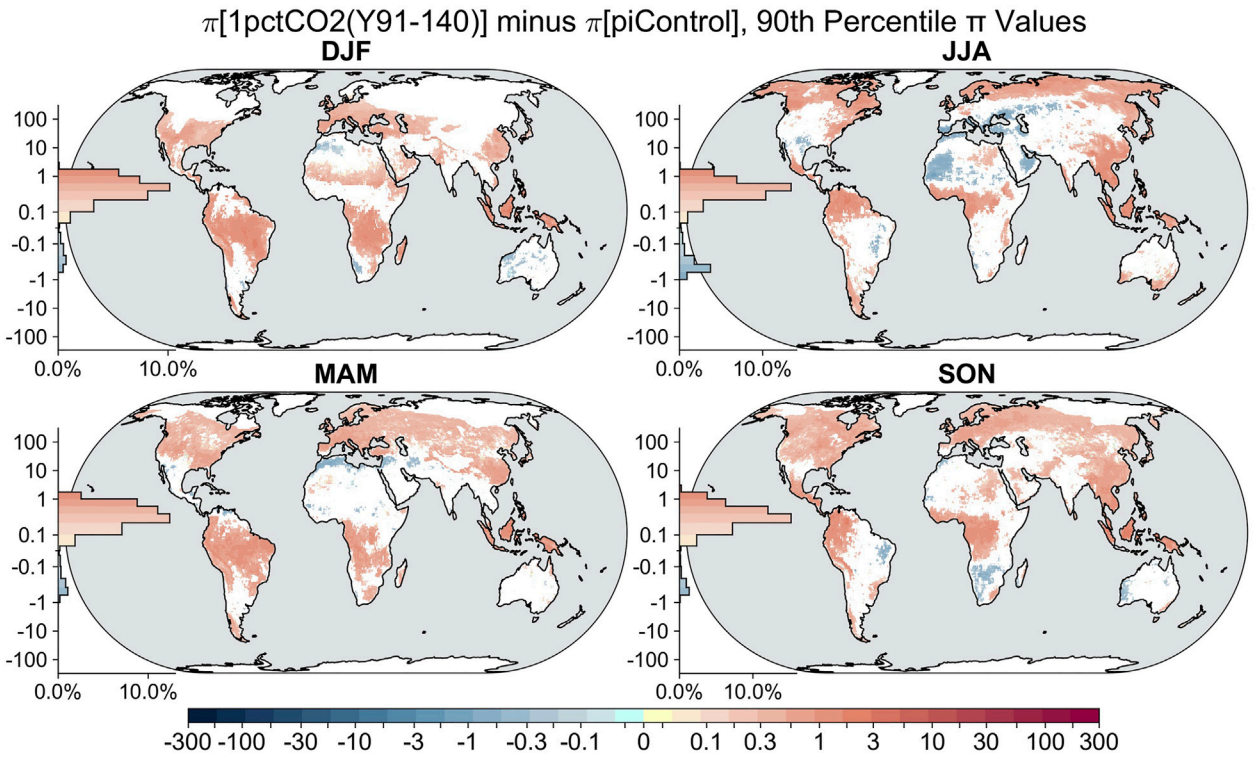


FIGURE 7
Multimodel median of differences in the 90th percentile values of $\pi$ (dimensionless) for the period of 1pctCO2 approaching quadrupled $CO_2$ minus piControl for each season. Areas are masked where the agreement among models on the sign of the change is below the 99% confidence level, or where the median of seasonal mean near-surface air temperature is below 0°C. Histograms show the probability distribution of significant changes as a fraction of the total land area.

However, regions like Mexico and India appear to maintain strong land surface feedbacks to heatwaves throughout the year, as does most of sub-Saharan Africa. Nearly all land in the Southern Hemisphere is covered in shades of red throughout the year, as shown in Figure 5.

High values of $\pi$ correspond quite well with the seasons and locations of so-called hotspots of land–atmosphere coupling (e.g., Koster et al., 2004; Dirmeyer et al., 2009). Low values of $\pi$ do not indicate a lack of heat or heatwaves but rather a lack of land surface contribution via concomitant soil drying. It is to be noted that the large deserts of Africa and Asia in Figure 5 usually have low values of the 90th percentile of $\pi$. Cool and/or moist regions also have low values for the 90th percentile of $\pi$ as they rarely, if ever, get into a state of concurrent dry soils and prolonged extreme heat.

We can see the impact of our choice of baseline for the definition of anomalies when we examine changes in the 90th percentile of $\pi$ from the preindustrial to recent historical times (Figure 6 depicts JJA; other seasons are shown in Supplementary Figure S2). When each period's anomalies and standard deviations for temperature, sensible heat, and potential sensible heat are used for each model, the left panel shows that the multimodel median of the 90th percentile value of $\pi$ shows a significant consensus change over portions of the globe. Decreases correspond largely to areas of land cover change: areas of agricultural expansion over the Americas, Northeast China, India, the Sahel, and Australia, but the correspondence between land use change and land-heat coupling has not been explicitly quantified in this study as it has been in others (e.g., Chen and Dirmeyer, 2019; Chen and Dirmeyer, 2020; Hu and Sun, 2022). Increases are largely confined to low latitudes, corresponding to areas of tropical deforestation but also in the subtropics of the Southern Hemisphere during austral summer (Figure 2) and, curiously, much of the Sahara. The multimodel median values of the time mean and standard deviations that are part of the main terms in $\pi$ (Eq. 4) are shown for all seasons in Supplementary Figures S3, S4, respectively.

This pattern of change in the 90th percentile of $\pi$ is driven by several factors. Most areas experienced warming (Supplementary Figure S5). There is an increase in the standard deviation of temperature almost everywhere (Supplementary Figure S6), which makes the denominator larger for the historical case. Notable exceptions, according to the models, include areas with large increases in cultivation: central North America, Far East Asia, the upper Ganges and Indus valleys, and much of Eastern Europe. The mean and standard deviation of sensible

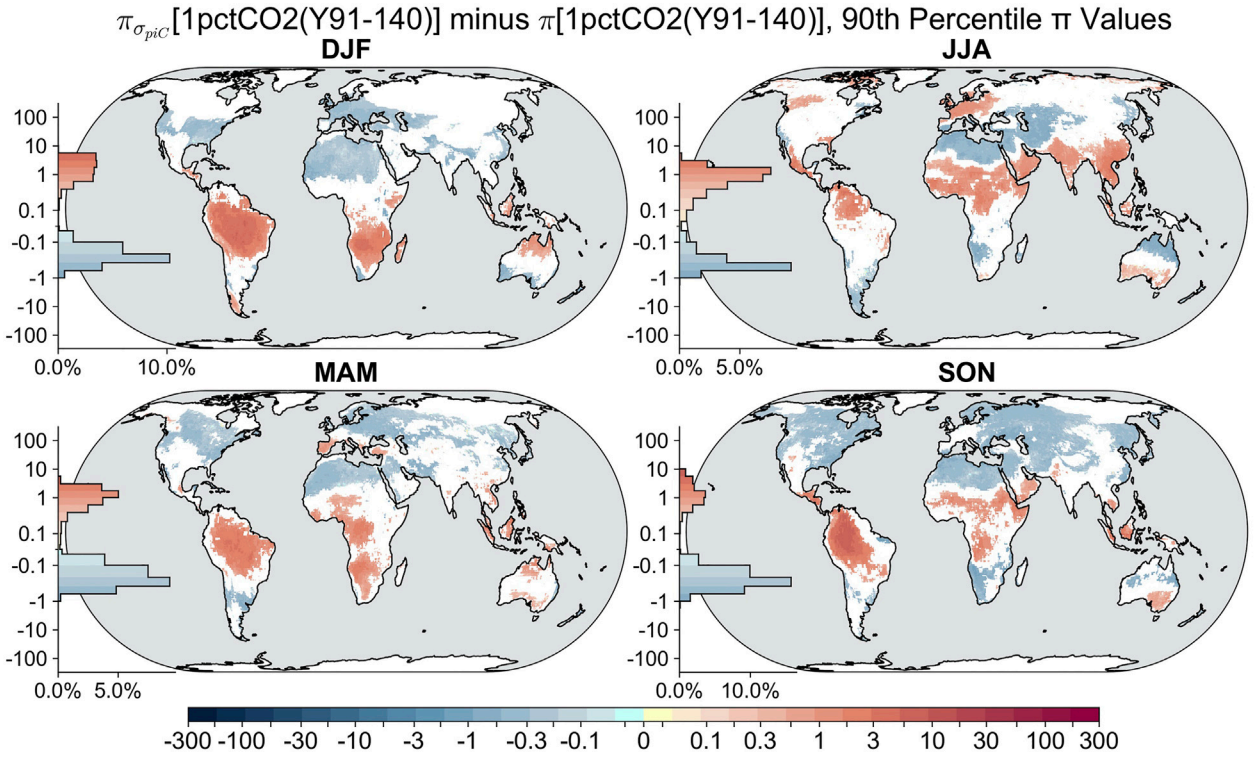


FIGURE 8
As in Figure 7 but with future values of $\pi$ (dimensionless) based on means and standard deviations from the piControl climatology.

heat flux drop over most of the same areas. The changes in potential sensible heat closely mirror temperature changes over the Western Hemisphere but not in the Eastern Hemisphere. As a global measure of the drivers of changes in $\pi$, we calculated spatial correlations of its changes in each season (from Figure 6 andSupplementary Figure S2) with the changes in each time-mean term in Eq. 4. Changes in $\sigma_T$ explain 79% of the spatial variance during MAM and JJA, 71% in SON, and 55% in DJF. $\sigma_H$ and $\sigma_{H_p}$ also explain around 50% of the variance on average and as much as 62% in MAM (note that these terms are cross-correlated; therefore, percentages for any season can sum to more than 100%). Changes in the means $\bar{T}$, $\bar{H}$, and $\overline{H_p}$ generally account for less than 30% of the variance.

Returning to Figure 6, we see a very different picture when the baseline for anomalies during the historical period is kept at piControl levels and the piControl standard deviations for the terms used to calculate $\pi$ are also used (right panel). Nearly every significant change is a substantial increase, suggesting stronger land surface coupling to extreme heat events. The middle panel of Figure 6 shows the difference that arises mainly from the differing estimates of the 90th percentile of $\pi$ during the historical period between the two baselines.

Next, we examine the doubled and quadrupled $CO_2$ periods compared with piControl. Using a trailing 30-year mean as the basis for climatology in the future projections, we see a pattern of changes for the quadrupled $CO_2$ case (Figure 7) that is very similar to but skewed more strongly to positive differences and more significant areal coverage than the doubled $CO_2$ case (Supplementary Figure S7). During all seasons, there are widespread consensus increases in the 90th percentile of $\pi$, the largest of which locally amounts to 20%–40% increases over piControl coupling strengths. Areas of consistent exception are around the Mediterranean and North Africa, as well as South Africa, indicating weaker coupling of soil moisture to extreme heat in most seasons. During boreal summer, the areas of decreased $\pi$ expand to their greatest area in several subtropical regions and some hot midlatitude locations in the Northern Hemisphere. The broad expanse of stronger land feedbacks to heat across the entire Arctic as well as across much of the tropics is striking. During SON, there are only a few areas of decrease in the Southern Hemisphere. DJF shows Australia to be exempted from increased soil moisture feedbacks on extreme heat, along with Namibia, the Maghreb, and the Pampas.

Unsurprisingly, if the preindustrial norms are used as the basis for calculating $\pi$ in future climate scenarios, the values become huge because the anomalies are huge. We have examined several variants–one of the most instructive is to calculate anomalies for future climate scenarios based on the trailing 30-year means in those cases but to retain the standard deviations from piControl

when normalizing the terms in $\pi$. This seems reasonable since there is likely to be some degree of adjustment by populations and migrating ecosystems to increasing temperatures, but changes in variability may not be easily accommodated. Figure 8 shows the difference in the 90th percentile of $\pi$ for each season in this case compared to the maps shown in Figure 7 (Supplementary Figure S8 is the equivalent for the doubled $CO_2$ case). When the three factors in $\pi$ are normalized by piControl standard deviations, rather than future standard deviations, stronger land feedbacks on extreme heat are indicated across the tropics and subtropics. The area skews toward the summer hemisphere as seasons progress, showing that the added impacts are mainly in monsoonal areas. However, arid regions and seasons in the subtropics and tropics experience less land feedback on heat in this formulation. Means and standard deviations of temperature will increase globally in all seasons in the future (Supplementary Figures S9–S12), but the areas showing a reduction in the 90th percentile of $\pi$ shown in Figure 8 correspond with regions of decreased variability in potential sensible heat flux (and thus potential evaporation), while the areas of increase align well with areas of increased sensible heat flux variability. Changes in $\sigma_T$ again explain most of the spatial variance, generally more than 80% for both future scenarios. $\sigma_H$ and $\sigma_{H_p}$ explain a comparable amount for quadrupled $CO_2$ as they did for the historical changes but slightly less for doubled $CO_2$. Changes in the mean terms account for about a quarter of the spatial variance.

## 4 Discussion and conclusion

This study estimates past, present, and future heatwave susceptibility based on surface temperature, surface sensible heat flux, and surface latent heat flux as proposed by Miralles et al. (2012). The impact of climate change on climatological coupling via land–atmosphere temperature feedbacks has been examined with the climatological metric ($\Pi$) from Miralles et al. (2012). This metric considers differing correlations between near-surface air temperature relative to potential and sensible heat flux, the former equivalent to the difference between net radiation and potential latent heat flux. Furthermore, this coupling can be robustly investigated, as it is based on temporal correlations that can well reflect changing relationships among physical climate variables such as temperature and sensible heat. This is more broadly true for correlation-based investigations of other evolving biotic indicators and land–atmosphere feedbacks in a changing climate (e.g., Notaro, 2008; Dirmeyer et al., 2013b; Berg et al., 2015; Lorenz et al., 2015; Santanello et al., 2018; Schwingshackl et al., 2018). However, the connection between these variables may not be strictly linear but can change depending on the role of soil moisture in modulating surface heat fluxes (Benson and Dirmeyer, 2021; Dirmeyer et al., 2021). It remains to be shown whether there is a better land-heat metric to use with CMIP6 model data.

Under preindustrial conditions (piControl), seasonally dependent hotspot regions of land–atmosphere coupling typically located in transitional zones between wet and dry climates in many other studies emerge once more during this analysis for $\Pi$ (Figure 1). Among CMIP6 models, historical land-use change (e.g., agriculture) corresponds spatially to areas of reduced land surface (i.e., soil moisture) controls on extreme heat (Figure 2). This relationship is consistent with crops' lack of regulation of their evapotranspiration as they have been bred to produce ample fruit rather than to survive extremes. Moreover, land surface models reflect these trade-off features via increases in gross primary productivity, high stomatal conductance, and vigorous carbon assimilation (De Kauwe et al., 2015; Franks et al., 2018).

For the future climate scenarios (Figures 3, 4), coverage of increased soil moisture–heat flux–temperature coupling (i.e., positive values of $\Pi$) emerges as doubled atmospheric $CO_2$ is approached, while regions displaying a reduction in land–atmosphere coupling early in the 1pctCO2 simulations begin to recede over time during every season. As quadrupled $CO_2$ is approached, regions of increasing land-heat coupling begin to dominate, particularly in monsoonal areas and across much of the midlatitudes where areas of seasonally high values of $\Pi$ spread northward.

Consideration of the episodic land–atmosphere heat coupling metric of Miralles et al. (2012), $\pi$, focuses on changes of its 90th percentile value in each season, including "cold" seasons that might not be considered as having heatwaves. This is done for completeness, as arbitrarily excluding months is difficult to justify. The low-temperature screening described at the end of Section 2 is our attempt to remove severely energy-limited situations from consideration. All seasons have been considered because episodes of extreme heat are not only intensifying (and projected to intensify further, cf. Perkins-Kirkpatrick and Gibson, 2017) but are also spreading in many places into seasons not historically associated with heatwaves (Shafiei Shiva et al., 2019). Changes are shown globally for each season, compared to the preindustrial baseline.

It is a much more nuanced problem to attribute the role of the land surface in the proliferation of extreme events within a changing climate as the very definition of "extreme" is by nature relative and potentially changing. This is particularly true when metrics are built with the assumption of a stationary climate as opposed to a changing one (Milly et al., 2008; Trenberth et al., 2014; Stevenson et al., 2022). The metric $\pi$ falls into this category (Figure 5), as it is based on the normalization of anomalies with temporal standard deviations, each of which can be defined from different baselines. Anomalies have been defined based on a mean climate period, a trailing 30-year mean climatology, and relative to piControl in the presence of changing climate. Relative to piControl norms, 90th percentile indices of monthly land–atmosphere coupling increase significantly over the entire globe, especially for the most recent historical period (Figure 6 and Supplementary Figure S2), and they can grow to

dozens of times more than the values when contemporaneous climate norms are used in the quadrupled $CO_2$ period (not shown). This throws into question the very meaning of such a metric.

Instead, two reasonable approaches are explored. When contemporaneous climate means and standard deviations (i.e., based on the trailing 30 years) are used to compare different periods (Figure 7 and Supplementary Figure S7), increased coupling from land to extreme heat cases becomes widespread over the moist tropics, much of the extratropics, and especially during summer in high-latitude regions. Decreased coupling appears over some of the more arid regions. However, one may assume that gradually increasing mean temperatures are not as much a factor for assessing land–atmosphere feedbacks as the changes in variability. When piControl standard deviations of temperature, sensible heat flux, and normalized sensible heat flux are used in all time periods, but anomalies are calculated based on recent climate norms, a different picture emerges (Figure 8 and Supplementary Figure S8). Increases in the 90th percentile of $\pi$ become quite large across the tropics and monsoon regions as well as northern Europe during the boreal summer, reflecting an increase in surface heat flux variability across the region in tandem with increasing temperature variability (Supplementary Figures S10, S12). Other regions mostly indicate a reduction in heat flux variability relative to piControl norms, suggesting that the land surface is less involved in the development of temperature extremes.

These conclusions should be considered provisional and serve mainly as an indicator of the difficulty surrounding the construction of an interdisciplinary, widely applicable metric, that is, navigating through the uncertainty presented by a changing climate and the Earth system processes fostering these extreme events. For modeling studies, it is rather difficult to isolate and deduce *a posteriori* the role of land surface feedbacks on extremes (e.g., heatwaves and drought) from experiments that were not specifically designed to isolate the possible role of the land via specifically constructed sensitivity analyses. This discontinuity points to the merit and necessity of targeted multimodel climate change experiments (Seneviratne et al., 2013; Hurk et al., 2016; Lawrence et al., 2016). However, with an abundance of subfield-specific model intercomparison projects (MIPs; over 20 in CMIP6), such specialized sensitivity studies become undersubscribed and model uncertainty is amplified.

Projects like GSWP-2 (Dirmeyer et al., 2006), GLACE (Koster et al., 2004; Koster et al., 2006), GLACE-2 (Koster et al., 2011), and LUCID (Pitman et al., 2009) established a model count of about one dozen as an adequate minimum for global climate studies–a mark that has been difficult to match with recent specialized MIPs. However, these innovative strategies must progress beyond the monthly scale analyses presented here in addition to investigating changes in actual heatwave events that would require daily model output. Such data are available for a few CMIP6 models, but the sample distribution is not large enough to assuage concerns over model-dependent results. Furthermore, the relatively low resolution of climate change models may obscure processes and localized features that could alter these results. Perhaps for the next round of climate model intercomparisons, MIPs can be organized that target phenomena of looming societal concern such as heatwaves and droughts.

## Data availability statement

The original contributions presented in the study are included in the article/Supplementary Material; further inquiries can be directed to the corresponding author.

## Author contributions

PD conceived of the original research project and led the analysis and writing. RM and PD conducted data processing and computations. BG organized the discussion of the analysis and drafted the manuscript. DK, BG, RM, and PD contributed to the analysis of results and the manuscript.

## Funding

PD's participation was supported by National Oceanographic and Atmospheric Administration grant NA20OAR4310422. RM's participation was supported by National Oceanographic and Atmospheric Administration grant NA20OAR4590316. BG's participation was supported by the Department of Geography and Geoinformation Science at George Mason University. Data processing and preliminary analyses for this study were performed by the coauthors as part of a graduate class project in land–climate interactions in the Climate Dynamics Program of George Mason University, Fairfax, Virginia, United States. The lead author's synthesis of the student material was supported by the Center for Ocean Land Atmosphere Studies (COLA).

## Acknowledgments

The authors acknowledge Zahra Ghodsi Zadeh and Geoffrey Rath for their early participation in this work. Additionally, the authors thank Dr. René Orth and two reviewers for their constructive comments that have substantially improved the study and the effort of one reviewer to provide the collated list of specific atmosphere and land model component information in Supplementary Table S1, which saved us a great deal of effort.

## Conflict of interest

The authors declare that the research was conducted in the absence of any commercial or financial relationships that could be construed as a potential conflict of interest.

## Publisher's note

All claims expressed in this article are solely those of the authors and do not necessarily represent those of their affiliated organizations, or those of the publisher, the editors, and the reviewers. Any product that may be evaluated in this article, or claim that may be made by its manufacturer, is not guaranteed or endorsed by the publisher.

## Supplementary material

The Supplementary Material for this article can be found online at: https://www.frontiersin.org/articles/10.3389/fenvs.2022.949250/full#supplementary-material

## References


Abramowitz, G., Herger, N., Gutmann, E., Hammerling, D., Knutti, R., Leduc, M., et al. (2019). ESD reviews: Model dependence in multi-model climate ensembles: Weighting, sub-selection and out-of-sample testing. *Earth Syst. Dyn.* 10, 91–105. doi:10.5194/esd-10-91-2019

Albergel, C., Dutra, E., Bonan, B., Zheng, Y., Munier, S., Balsamo, G., et al. (2019). Monitoring and forecasting the impact of the 2018 summer heatwave on vegetation. *Remote Sens.* 11, 520. doi:10.3390/rs11050520

Arguez, A., and Vose, R. S. (2011). The definition of the standard WMO climate normal: The key to deriving alternative climate normals. *Bull. Am. Meteorol. Soc.* 92, 699–704. doi:10.1175/2010BAMS2955.1

Benson, D. O., and Dirmeyer, P. A. (2021). Characterizing the relationship between temperature and soil moisture extremes and their role in the exacerbation of heat waves over the contiguous United States. *J. Clim.* 34, 2175–2187. doi:10.1175/JCLI-D-20-0440.1

Berg, A., Lintner, B. R., Findell, K., Seneviratne, S. I., Hurk, B., Ducharne, A., et al. (2015). Interannual coupling between summertime surface temperature and precipitation over land: Processes and implications for climate change. *J. Clim.* 28, 1308–1328. doi:10.1175/JCLI-D-14-00324.1

Bevacqua, E., Zappa, G., Lehner, F., and Zscheischler, J. (2022). Precipitation trends determine future occurrences of compound hot–dry events. *Nat. Clim. Chang.* 12, 350–355. doi:10.1038/s41558-022-01309-5

Brunner, L., Pendergrass, A. G., Lehner, F., Merrifield, A. L., Lorenz, R., and Knutti, R. (2020). Reduced global warming from CMIP6 projections when weighting models by performance and independence. *Earth Syst. Dyn.* 11, 995–1012. doi:10.5194/esd-11-995-2020

Chen, L., and Dirmeyer, P. A. (2019). The relative importance among anthropogenic forcings of land use/land cover change in affecting temperature extremes. *Clim. Dyn.* 52, 2269–2285. doi:10.1007/s00382-018-4250-z

Chen, L., and Dirmeyer, P. A. (2020). Distinct impacts of land use and land management on summer temperatures. *Front. Earth Sci. (Lausanne).* 8, 245. doi:10.3389/feart.2020.00245

De Kauwe, M. G., Kala, J., Lin, Y.-S., Pitman, A. J., Medlyn, B. E., Duursma, R. A., et al. (2015). A test of an optimal stomatal conductance scheme within the CABLE land surface model. *Geosci. Model Dev.* 8, 431–452. doi:10.5194/gmd-8-431-2015

Dee, D. P., Uppala, S. M., Simmons, A. J., Berrisford, P., Poli, P., Kobayashi, S., et al. (2011). The ERA-interim reanalysis: Configuration and performance of the data assimilation system. *Q. J. R. Meteorol. Soc.* 137, 553–597. doi:10.1002/qj.828

Dirmeyer, P. A., Balsamo, G., Blyth, E. M., Morrison, R., and Cooper, H. M. (2021). Land-atmosphere interactions exacerbated the drought and heatwave over northern Europe during summer 2018. *AGU Adv.* 2, e2020AV000283. doi:10.1029/2020AV000283

Dirmeyer, P. A., Gao, X., Zhao, M., Guo, Z., Oki, T., and Hanasaki, N. (2006). GSWP-2: Multimodel analysis and implications for our perception of the land surface. *Bull. Am. Meteorol. Soc.* 87, 1381–1398. doi:10.1175/BAMS-87-10-1381

Dirmeyer, P. A., Jin, Y., Singh, B., and Yan, X. (2013a). Evolving land–atmosphere interactions over north America from CMIP5 simulations. *J. Clim.* 26, 7313–7327. doi:10.1175/JCLI-D-12-00454.1

Dirmeyer, P. A., Jin, Y., Singh, B., and Yan, X. (2013b). Trends in land–atmosphere interactions from CMIP5 simulations. *J. Hydrometeorol.* 14, 829–849. doi:10.1175/JHM-D-12-0107.1

Dirmeyer, P. A., Schlosser, C. A., and Brubaker, K. L. (2009). Precipitation, recycling, and land memory: An integrated analysis. *J. Hydrometeorol.* 10, 278–288. doi:10.1175/2008JHM1016.1

Dirmeyer, P. A. (2011). The terrestrial segment of soil moisture-climate coupling. *Geophys. Res. Lett.* 38, L16702. doi:10.1029/2011GL048268

Dosio, A., Jury, M. W., Almazroui, M., Ashfaq, M., Diallo, I., Engelbrecht, F. A., et al. (2021). Projected future daily characteristics of African precipitation based on global (CMIP5, CMIP6) and regional (CORDEX, CORDEX-CORE) climate models. *Clim. Dyn.* 57, 3135–3158. doi:10.1007/s00382-021-05859-w

Eyring, V., Bony, S., Meehl, G. A., Senior, C. A., Stevens, B., Stouffer, R. J., et al. (2016). Overview of the coupled model intercomparison project Phase 6 (CMIP6) experimental design and organization. *Geosci. Model Dev.* 9, 1937–1958. doi:10.5194/gmd-9-1937-2016

Fischer, E. M., Seneviratne, S. I., Lüthi, D., and Schär, C. (2007). Contribution of land-atmosphere coupling to recent European summer heat waves. *Geophys. Res. Lett.* 34, L06707. doi:10.1029/2006GL029068

Franks, P. J., Bonan, G. B., Berry, J. A., Lombardozzi, D. L., Holbrook, N. M., Herold, N., et al. (2018). Comparing optimal and empirical stomatal conductance models for application in Earth system models. *Glob. Chang. Biol.* 24, 5708–5723. doi:10.1111/gcb.14445

Hauser, M., Orth, R., and Seneviratne, S. I. (2016). Role of soil moisture versus recent climate change for the 2010 heat wave in Western Russia. *Geophys. Res. Lett.* 43, 2819–2826. doi:10.1002/2016GL068036

Hirsch, A. L., Evans, J. P., Virgilio, G. D., Perkins-Kirkpatrick, S. E., Argüeso, D., Pitman, A. J., et al. (2019). Amplification of Australian heatwaves via local land-atmosphere coupling. *J. Geophys. Res. Atmos.* 124, 13625–13647. doi:10.1029/2019JD030665

Hu, T., and Sun, Y. (2022). Anthropogenic influence on extreme temperatures in China based on CMIP6 models. *Int. J. Climatol.* 42, 2981–2995. doi:10.1002/joc.7402

Hurk, B., Kim, H., Krinner, G., Seneviratne, S. I., Derksen, C., Oki, T., et al. (2016). LS3MIP (v1.0) contribution to CMIP6: The land surface, snow and soil moisture model intercomparison project – aims, setup and expected outcome. *Geosci. Model Dev.* 9, 2809–2832. doi:10.5194/gmd-9-2809-2016

Hurtt, G. C., Chini, L., Sahajpal, R., Frolking, S., Bodirsky, B. L., Calvin, K., et al. (2020). Harmonization of global land use change and management for the period 850–2100 (LUH2) for CMIP6. *Geosci. Model Dev.* 13, 5425–5464. doi:10.5194/gmd-13-5425-2020

Knutti, R., Furrer, R., Tebaldi, C., Cermak, J., and Meehl, G. A. (2010). Challenges in combining projections from multiple climate models. *J. Clim.* 23, 2739–2758. doi:10.1175/2009JCLI3361.1

Koster, R. D., Dirmeyer, P. A., Guo, Z., Bonan, G., Chan, E., Cox, P., et al. (2004). Regions of strong coupling between soil moisture and precipitation. *Science* 305, 1138–1140. doi:10.1126/science.1100217

Koster, R. D., Sud, Y. C., Guo, Z., Dirmeyer, P. A., Bonan, G., Oleson, K. W., et al. (2006). Glace: The global land–atmosphere coupling experiment. Part I: Overview. *J. Hydrometeorol.* 7, 590–610. doi:10.1175/JHM510.1

Koster, R. D., Guo, Z., Yang, R., Dirmeyer, P. A., Mitchell, K., and Puma, M. J. (2009). On the nature of soil moisture in land surface models. *J. Clim.* 22, 4322–4335. doi:10.1175/2009JCLI2832.1

Koster, R. D., Mahanama, S. P. P., Yamada, T. J., Balsamo, G., Berg, A. A., Boisserie, M., et al. (2011). The second Phase of the global land–atmosphere coupling experiment: Soil moisture contributions to subseasonal forecast skill. *J. Hydrometeorol.* 12, 805–822. doi:10.1175/2011JHM1365.1

Krishnamurti, T. N., Kishtawal, C. M., LaRow, T. E., Bachiochi, D. R., Zhang, Z., Williford, C. E., et al. (1999). Improved weather and seasonal climate forecasts from multimodel superensemble. *Science* 285, 1548–1550. doi:10.1126/science.285.5433.1548

Lau, N.-C., and Nath, M. J. (2014). Model simulation and projection of European heat waves in present-day and future climates. *J. Clim.* 27, 3713–3730. doi:10.1175/JCLI-D-13-00284.1

Lawrence, D. M., Hurtt, G. C., Arneth, A., Brovkin, V., Calvin, K. V., Jones, A. D., et al. (2016). The land use model intercomparison project (LUMIP) contribution to CMIP6: Rationale and experimental design. *Geosci. Model Dev.* 9, 2973–2998. doi:10.5194/gmd-9-2973-2016

Leduc, M., Laprise, R., Elía, R., and Šeparović, L. (2016). Is institutional democracy a good proxy for model independence? *J. Clim.* 29, 8301–8316. doi:10.1175/JCLI-D-15-0761.1

Livezey, R. E., Vinnikov, K. Y., Timofeyeva, M. M., Tinker, R., and Dool, H. M. (2007). Estimation and extrapolation of climate normals and climatic trends. *J. Appl. Meteorol. Climatol.* 46, 1759–1776. doi:10.1175/2007JAMC1666.1

Lorenz, R., Pitman, A. J., Hirsch, A. L., and Srbinovsky, J. (2015). Intraseasonal versus interannual measures of land–atmosphere coupling strength in a global climate model: GLACE-1 versus GLACE-CMIP5 experiments in ACCESS1.3b. *J. Hydrometeorol.* 16, 2276–2295. doi:10.1175/JHM-D-14-0206.1

Martens, B., Miralles, D. G., Lievens, H., van der Schalie, R., de Jeu, R. A. M., Fernández-Prieto, D., et al. (2017). GLEAM v3: Satellite-based land evaporation and root-zone soil moisture. *Geosci. Model Dev.* 10, 1903–1925. doi:10.5194/gmd-10-1903-2017

Milly, P. C. D., Betancourt, J., Falkenmark, M., Hirsch, R. M., Kundzewicz, Z. W., Lettenmaier, D. P., et al. (2008). Stationarity is dead: Whither water management? *Science* 319, 573–574. doi:10.1126/science.1151915

Miralles, D. G., Gentine, P., Seneviratne, S. I., and Teuling, A. J. (2019). Land–atmospheric feedbacks during droughts and heatwaves: State of the science and current challenges. *Ann. N. Y. Acad. Sci.* 1436, 19–35. doi:10.1111/nyas.13912

Miralles, D. G., van den Berg, M. J., Teuling, A. J., and de Jeu, R. A. M. (2012). Soil moisture-temperature coupling: A multiscale observational analysis. *Geophys. Res. Lett.* 39, L21707. doi:10.1029/2012GL053703

Neal, E., Huang, C. S. Y., and Nakamura, N. (2022). The 2021 pacific northwest heat wave and associated blocking: Meteorology and the role of an upstream cyclone as a diabatic source of wave activity. *Geophys. Res. Lett.* 49, e2021GL097699. doi:10.1029/2021GL097699

Notaro, M. (2008). Statistical identification of global hot spots in soil moisture feedbacks among IPCC AR4 models. *J. Geophys. Res.* 113, D09101. doi:10.1029/2007JD009199

O, S., Bastos, A., Reichstein, M., Li, W., Denissen, J., Graefen, H., et al. (2022). The role of climate and vegetation in regulating drought-heat extremes. *J. Clim.* 1, 5677–5685. doi:10.1175/JCLI-D-21-0675.1

Palmer, T. N., Alessandri, A., Andersen, U., Cantelaube, P., Davey, M., Délécluse, P., et al. (2004). Development of a EUROPEAN multimodel ensemble system for seasonal-to-interannual prediction (demeter). *Bull. Am. Meteorol. Soc.* 85, 853–872. doi:10.1175/BAMS-85-6-853

Parker, W. S. (2013). Ensemble modeling, uncertainty and robust predictions. *WIREs Clim. Change* 4, 213–223. doi:10.1002/wcc.220

Perkins-Kirkpatrick, S. E., and Gibson, P. B. (2017). Changes in regional heatwave characteristics as a function of increasing global temperature. *Sci. Rep.* 7, 12256. doi:10.1038/s41598-017-12520-2

Petch, J. C., Short, C. J., Best, M. J., McCarthy, M., Lewis, H. W., Vosper, S. B., et al. (2020). Sensitivity of the 2018 UK summer heatwave to local sea temperatures and soil moisture. *Atmos. Sci. Lett.* 21, e948. doi:10.1002/asl.948

Pirtle, Z., Meyer, R., and Hamilton, A. (2010). What does it mean when climate models agree? A case for assessing independence among general circulation models. *Environ. Sci. Policy* 13, 351–361. doi:10.1016/j.envsci.2010.04.004

Pitman, A. J., de Noblet-Ducoudré, N., Cruz, F. T., Davin, E. L., Bonan, G. B., Brovkin, V., et al. (2009). Uncertainties in climate responses to past land cover change: First results from the LUCID intercomparison study. *Geophys. Res. Lett.* 36, L14814. doi:10.1029/2009GL039076

Priestley, C. H. B., and Taylor, R. J. (1972). On the assessment of surface heat flux and evaporation using large-scale parameters. *Mon. Wea. Rev.* 100, 81–92. doi:10.1175/1520-0493(1972)100<0081:OTAOSH>2.3.CO;2

Samaniego, L., Thober, S., Kumar, R., Wanders, N., Rakovec, O., Pan, M., et al. (2018). Anthropogenic warming exacerbates European soil moisture droughts. *Nat. Clim. Chang.* 8, 421–426. doi:10.1038/s41558-018-0138-5

Santanello, J. A., Dirmeyer, P. A., Ferguson, C. R., Findell, K. L., Tawfik, A. B., Berg, A., et al. (2018). Land-atmosphere interactions: The LoCo perspective. *Bull. Am. Meteorol. Soc.* 99, 1253–1272. doi:10.1175/BAMS-D-17-0001.1

Schumacher, D. L., Keune, J., Heerwaarden, C. C., Arellano, J. V.-G., Teuling, A. J., and Miralles, D. G. (2019). Amplification of mega-heatwaves through heat torrents fuelled by upwind drought. *Nat. Geosci.* 12, 712–717. doi:10.1038/s41561-019-0431-6

Schwingshackl, C., Hirschi, M., and Seneviratne, S. I. (2018). A theoretical approach to assess soil moisture–climate coupling across CMIP5 and GLACE-CMIP5 experiments. *Earth Syst. Dyn.* 9, 1217–1234. doi:10.5194/esd-9-1217-2018

Seneviratne, S. I., Corti, T., Davin, E. L., Hirschi, M., Jaeger, E. B., Lehner, I., et al. (2010). Investigating soil moisture–climate interactions in a changing climate: A review. *Earth-Science Rev.* 99, 125–161. doi:10.1016/j.earscirev.2010.02.004

Seneviratne, S. I., Wilhelm, M., Stanelle, T., Hurk, B., Hagemann, S., Berg, A., et al. (2013). Impact of soil moisture-climate feedbacks on CMIP5 projections: First results from the GLACE-CMIP5 experiment. *Geophys. Res. Lett.* 40, 5212–5217. doi:10.1002/grl.50956

Shafiei Shiva, J., Chandler, D. G., and Kunkel, K. E. (2019). Localized changes in heat wave properties across the United States. *Earth's. Future* 7, 300–319. doi:10.1029/2018EF001085

Stevenson, S., Coats, S., Touma, D., Cole, J., Lehner, F., Fasullo, J., et al. (2022). Twenty-first century hydroclimate: A continually changing baseline, with more frequent extremes. *Proc. Natl. Acad. Sci. U. S. A.* 119, e2108124119. doi:10.1073/pnas.2108124119

Tebaldi, C., and Knutti, R. (2007). The use of the multi-model ensemble in probabilistic climate projections. *Phil. Trans. R. Soc. A* 365, 2053–2075. doi:10.1098/rsta.2007.2076

Teuling, A. J., Seneviratne, S. I., Stöckli, R., Reichstein, M., Moors, E., Ciais, P., et al. (2010). Contrasting response of European forest and grassland energy exchange to heatwaves. *Nat. Geosci.* 3, 722–727. doi:10.1038/ngeo950

Trenberth, K. E., Dai, A., van der Schrier, G., Jones, P. D., Barichivich, J., Briffa, K. R., et al. (2014). Global warming and changes in drought. *Nat. Clim. Chang.* 4, 17–22. doi:10.1038/nclimate2067

Ukkola, A. M., Pitman, A. J., Donat, M. G., Kauwe, M. G. D., and Angélil, O. (2018). Evaluating the contribution of land-atmosphere coupling to heat extremes in CMIP5 models. *Geophys. Res. Lett.* 0, 9003–9012. (early view). doi:10.1029/2018GL079102

Wang, B., Jin, C., and Liu, J. (2020). Understanding future change of global monsoons projected by CMIP6 models. *J. Clim.* 33, 6471–6489. doi:10.1175/JCLI-D-19-0993.1

Wehrli, K., Hauser, M., and Seneviratne, S. I. (2020). Storylines of the 2018 Northern Hemisphere heat wave at pre-industrial and higher global warming levels. *Earth Syst. Dyn.* 11, 855–873. doi:10.5194/esd-11-855-2020

Yiou, P., Cattiaux, J., Faranda, D., Kadygrov, N., Jézéquel, A., Naveau, P., et al. (2020). Analyses of the northern European summer heatwave of 2018. *Bull. Am. Meteorol. Soc.* 101, S35–S40. doi:10.1175/BAMS-D-19-0170.1

Zhao, T., and Dai, A. (2015). The magnitude and causes of global drought changes in the twenty-first century under a low–moderate emissions scenario. *J. Clim.* 28, 4490–4512. doi:10.1175/JCLI-D-14-00363.1

Zhao, T., and Dai, A. (2022). CMIP6 model-projected hydroclimatic and drought changes and their causes in the twenty-first century. *J. Clim.* 35, 897–921. doi:10.1175/JCLI-D-21-0442.1

Zscheischler, J., Westra, S., Hurk, B. J. J. M., Seneviratne, S. I., Ward, P. J., Pitman, A., et al. (2018). Future climate risk from compound events. *Nat. Clim. Chang.* 8, 469–477. doi:10.1038/s41558-018-0156-3

frontiers | Frontiers in Environmental Science

TYPE Original Research
PUBLISHED 06 December 2022
DOI 10.3389/fenvs.2022.970266



OPEN ACCESS

EDITED BY
Yan Li,
Beijing Normal University, China

REVIEWED BY
Joseph Berry,
Carnegie Institution for Science (CIS), United States
Manon Sabot,
University of New South Wales, Australia
Linnia Hawkins,
Oregon State University, United States

*CORRESPONDENCE
Simon Jones,
s.r.g.jones@exeter.ac.uk

SPECIALTY SECTION
This article was submitted to Land Use Dynamics, a section of the journal Frontiers in Environmental Science

RECEIVED 15 June 2022
ACCEPTED 17 October 2022
PUBLISHED 06 December 2022

CITATION
Jones S, Eller CB and Cox PM (2022), Application of feedback control to stomatal optimisation in a global land surface model.
*Front. Environ. Sci.* 10:970266.
doi: 10.3389/fenvs.2022.970266



# Application of feedback control to stomatal optimisation in a global land surface model

Simon Jones[1]*, Cleiton B. Eller[2] and Peter M. Cox[1]

[1]Department of Mathematics and Statistics, Faculty of Environment, Science and Economy, University of Exeter, Exeter, United Kingdom, [2]Department of Biology, Federal University of Ceará, Fortaleza, Brazil

Accurate representations of stomatal conductance are required to predict the effects of climate change on terrestrial ecosystems. Stomatal optimisation theory, the idea that plants have evolved to maximise carbon gain under certain constraints, such as minimising water loss or preventing hydraulic damage, is a powerful approach to representing stomatal behaviour that bypasses the need to represent complex physiological processes. However, while their ability to replicate observed stomatal responses is promising, optimisation models often present practical problems for those trying to simulate the land surface. In particular, when realistic models of photosynthesis and more complex cost functions are used, closed-form solutions for the optimal stomatal conductance are often very difficult to find. As a result, implementing stomatal optimisation in land surface models currently relies either on simplifying approximations, that allow closed-form solutions to be found, or on numerical iteration which can be computationally expensive. Here we propose an alternative approach, using a method motivated by control theory that is computationally efficient and does not require simplifying approximations to be made to the underlying optimisation. Stomatal conductance is treated as the control variable in a simple closed-loop system and we use the Newton-Raphson method to track the time-varying maximum of the objective function. We compare the method to both numerical iteration and a semi-analytical approach by applying the methods to the SOX stomatal optimisation model at multiple sites across the Amazon rainforest. The feedback approach is able to more accurately replicate the results found by numerical iteration than the semi-analytical approach while maintaining improved computational efficiency.

KEYWORDS

**stomatal conductance, stomatal optimisation, feedback optimisation, control theory, Amazon rainforest, JULES**

# 1 Introduction

Stomata regulate gas exchange between leaf and atmosphere, balancing carbon gain required for growth, reproduction, and respiration, against the cost of losing excessive water through transpiration and the associated consequences for the plant hydraulic tissues (Cowan and Farquhar, 1977; Sperry et al., 2017). The dynamic behaviour of stomata has a strong influence over both the terrestrial carbon and water cycles (Sellers et al., 1996; Cox et al., 1999; Gedney et al., 2006). Combined with non-linear feedbacks between the land surface and atmosphere, small changes in stomatal responses to environmental change can cause large changes to future projections of the climate (Betts et al., 2004). As the frequency and severity of drought events increase across large parts of the globe (Hartmann et al., 2013; Marengo et al., 2018), the role that stomata play in regulating local and global climate is becoming ever more prominent, as plant water use strategies determine the survival of the vegetation in vulnerable ecosystems (Cox et al., 2000; Allen et al., 2010; Ponce-Campos et al., 2013; Anderegg et al., 2015; Hochberg et al., 2018). Despite this role, however, current land surface models (LSMs) often fail to accurately capture the response of vegetation to drought (Sitch et al., 2008; Powell et al., 2013; Ukkola et al., 2016; Restrepo-Coupe et al., 2017; Martínez-de la Torre et al., 2019). This reduces their ability to predict both short and long term changes to the land surface and interactions with the climate. Significant improvement to the representation of stomatal behaviour in LSMs is required to improve projections of future climate change and its impacts.Stomatal optimisation theory, the idea that plants are able to optimise carbon gain under certain physiological constraints, such as minimising water loss (Cowan and Farquhar, 1977) or preventing hydraulic damage (Sperry et al., 2017), is a powerful approach to representing stomatal behaviour that has seen renewed interest over recent years. Optimisation approaches offer encouraging results relative to observations (Anderegg et al., 2018; Eller et al., 2018, 2020; Venturas et al., 2018; Wang et al., 2019; Sabot et al., 2020; 2022a) while bypassing the need to represent complex and poorly understood physiological processes. The central concept is that stomata act to maximise carbon dioxide uptake for photosynthesis while simultaneously minimising the costs associated with excessive stomatal opening. These costs are typically expressed in terms of water loss, but may also be associated with non-hydrological processes such as in Prentice et al. (2014), where the optimisation model aims to minimise the carbon costs of transpiration and photosynthetic capacity. In optimisation models, an objective function, typically given by the difference between instantaneous carbon uptake and a cost function associated with water loss is maximised either instantaneously or over a finite period, resulting in an optimal stomatal conductance (Cowan and Farquhar, 1977; Wolf et al., 2016; Wang et al., 2020). Many of the observed behaviours of stomata to changes in climatic or edaphic conditions have been replicated by this approach (Buckley et al., 2017), making it an attractive option for those attempting to model plant behaviour. However, despite this promising ability to replicate observed stomatal responses, many global LSMs still use empirical representations of stomatal conductance such as the Leuning (1995) and Ball et al. (1987) models. The use of optimisation models, in particular for large scale and long term simulations is currently limited, in part due to the practical difficulties involved in solving for the optimal stomatal conductance (Buckley, 2017). Generally, closed-form analytical solutions are difficult or even impossible to find, in particular when sophisticated leaf photosynthesis models are used (e.g., Farquhar et al., 1980; Collatz et al., 1991). As a result, stomatal optimisation models are typically solved through numerical iteration. Unfortunately this can be impractical for large scale simulations of the climate where computational efficiency is desirable. Simplifying assumptions can sometimes be made about the functional form of either photosynthesis or the water loss cost equation that reduce the complexity of the problem, such that analytical solutions can be found (e.g., Medlyn et al., 2011; Eller et al., 2020). However, these simplifications are not always possible and can often misrepresent some of the fundamental assumptions in the model (Buckley et al., 2017; Sabot et al., 2022b). There is therefore a need for an alternative method to solve stomatal optimisation models that avoids the need for numerical iteration yet can still produce accurate solutions of the analytically optimal $g_s$.An area of promise that has yet to be extensively explored in the context of stomatal modelling is feedback control. A basic control problem consists of a system with an input and an output. The objective is to feed an input into the system that causes it to track some desired reference signal. In feedback control, measurements of the system output are compared against the reference signal through time, and the difference between them is used to design an input that is fed back into the system, guiding it is subsequent evolution through time (Figure 1). A simple example is the regulation of room temperature by a household boiler and thermostat (Franklin et al., 2011). Measurements of room temperature relative to the desired room temperature, which acts as the reference signal, provide information to the thermostat that allows the boiler to be turned on or off, maintaining the temperature of the house at, or near, the desired reference temperature. Feedback control methods have many applications across various fields of science and engineering, including, in particular, biological sciences (Cosentino and Bates, 2011) and generic optimisation problems (Hauswirth et al., 2021). Since the maximum of a function corresponds to a first derivative of zero, by setting the system output to be the first derivative of an objective function, and the reference signal to zero, we can reformulate the basic feedback control problem into an optimisation problem. This type of feedback optimisation is commonly applied in fields of engineering (e.g., Krishnamoorthy and Skogestad, 2022).

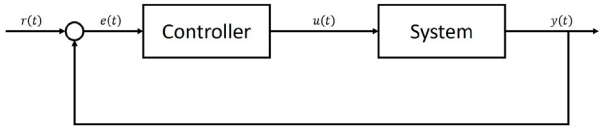


FIGURE 1
A basic feedback control system.

Applying it to stomatal optimisation we can use the same methods to find a governing equation for the rate of change of stomatal conductance that causes the objective function to track the optimum through time. Such an effort could significantly increase the viability of stomatal optimisation models in LSMs, which in turn would improve our ability to capture responses of vegetation to changing water availability in the future.In this study we apply feedback optimisation techniques to the Stomatal Optimisation based on Xylem hydraulics (SOX) model (Eller et al., 2018, 2020). We implement SOX within the Joint United Kingdom Land Environment Simulator (JULES: Best et al., 2011; Clark et al., 2011) and use three different methods: numerical iteration; an approximate analytical solution; and feedback optimisation. We run JULES-SOX using these three approaches at four sites across the Amazon.

# 2 Methods

## 2.1 SOX

The Stomatal Optimisation based on Xylem hydraulics (SOX) model is a stomatal optimisation model designed to run within the JULES LSM (Best et al., 2011; Clark et al., 2011). Below we provide a brief introduction to the model, however, a full description and detailed evaluations of the model can be found in Eller et al. (2018) and Eller et al. (2020).SOX assumes that stomata act to maximise the instantaneous product of leaf photosynthesis (A) and the normalised xylem hydraulic conductance (K). The optimal stomatal conductance ($g_{s,opt}$) is found as the solution to the following equation:

$$\frac{\partial (A \cdot K)}{\partial g_s}\left(g_{s,opt}\right) = 0 \tag{1}$$

The normalised xylem hydraulic conductance ($K$) is a function of leaf water potential ($\Psi_l$), which itself is a function of stomatal conductance. This $K$ is given by the vulnerability curve (Eller et al., 2020):

$$K(\Psi) = \frac{1}{\left[1 + \left(\frac{\Psi}{\Psi_{50}}\right)^a\right]} \tag{2}$$

where $\Psi_{50}$ is $\Psi$ when $K = 0.5$ and the parameter $a$ gives the shape of the vulnerability curve.Due to the complexity of the photosynthesis model used in JULES, and the functional form of the hydraulic conductivity equation used, a closed-form solution for $g_s$ has not been found, and the model can only be solved by numerical iteration (Eller et al., 2018) or by simplifying some of its premises to produce a semi-analytical approximation (Eller et al., 2020).

## 2.2 Numerical iteration

The default method for solving the SOX model is by numerical iteration. An array of leaf internal carbon dioxide partial pressure ($c_i$) values is used to calculate the objective function, ($J = A \cdot K$). The value of $c_i$ that gives the greatest value of the objective function is then used to calculate the optimum stomatal conductance using the equilibrium diffusion equation:

$$g_{s,opt} = \frac{A\left(c_{i,opt}\right)}{\left(c_a - c_{i,opt}\right)} \tag{3}$$

where $c_a$ is atmospheric carbon dioxide partial pressure.The difference between the solution found by numerical iteration and the "true" solution depends on the number of different $c_i$ values, or iterations used. For a sufficiently large number of iterations we can neglect differences between the numerical solution and the true analytical solution, and so for the remainder of this study we consider the solution found by numerical iteration to represent the true solution of the model. When SOX has been run using this method we refer to it as the "numerical version of SOX".

## 2.3 Semi-analytical approximation

Eller et al. (2020) also present a semi-analytical approximation to SOX:

$$g_{s,opt} = 0.5\frac{\partial A}{\partial c_i}\left(\sqrt{\frac{4\xi}{\frac{\partial A}{\partial c_i}} + 1} - 1\right) \tag{4}$$

with

$$\xi = \frac{2}{\frac{1}{K}\frac{\partial K}{\partial \psi} r_p 1.6D}$$

where $\psi$ is leaf water potential; $r_p$ is plant hydraulic resistance; and $D$ is vapur pressure deficit.This is referred to as "semi-analytical" since it is not a true closed-form solution. For most realistic models of photosynthesis, including those typically used in JULES (Farquhar et al., 1980; Collatz et al., 1991), $\frac{\partial A}{\partial c_i}$ is not independent of $g_s$. Similarly, the cost function ($K$) in SOX

depends on leaf water potential and therefore also on $g_s$. As a result the expression requires simplifying assumptions to be used. Eller et al. (2020) estimate both $\frac{\partial A}{\partial c_i}$ and $\frac{1}{K}\frac{\partial K}{\partial \psi}$ numerically, assuming both terms are constant with respect to $g_s$ and within a model time-step. For the remainder of this study we refer to the combination of this semi-analytical expression and the approximations of the gradients of photosynthesis and the cost function as the "semi-analytical version of SOX".

## 2.4 Applying feedback control to stomatal optimisation

A basic negative feedback control system consists of a system which takes a control input $(u(t))$ and produces an output $(y(t))$ (Figure 1). In the simplest case this output is given by a function of the input:

$$y = F(u(t)) \tag{5}$$

The objective of feedback control is to design a governing equation for the input such that the output of the system tracks a reference signal $(r(t))$. This is achieved by measuring the error between the system output and the reference signal, $e(t) = r(t) - y(t)$, and designing a controller that minimises this error through time, often with the additional objectives of minimising convergence time and overshoot, while maintaining stability.The aim of stomatal optimisation models is to maximise an instantaneous objective function ($J$). We want to control this objective function by varying stomatal conductance through time and hence stomatal conductance is our control variable:

$$u(t) = g_s(t) \tag{6}$$

Setting the system output function ($F$) of our feedback problem to be the first derivative of the objective function:

$$F(u(t)) = \frac{\partial J}{\partial g_s}(g_s(t)) \tag{7}$$

and setting the reference signal to zero:

$$r(t) = 0 \tag{8}$$

we now have a feedback optimisation problem. The aim is to design a governing equation for the rate of change of stomatal conductance that guides our objective function towards its maximum, and can use methods from feedback control to do so.

### 2.4.1 Applying feedback control to SOX

To apply feedback control to SOX it is first convenient to non-dimensionalise the objective function by defining a maximum value for photosynthesis ($A_{max}$). The non-dimensional objective function is given by:

$$\hat{J} = \hat{A} \cdot K \tag{9}$$

where

$$\hat{A} = \frac{A}{A_{max}} \tag{10}$$

We define $A_{max}$ as the rate of photosynthesis when intercellular leaf $CO_2$ concentration is equal to atmospheric $CO_2$:

$$A_{max} = A(c_i = c_a) \tag{11}$$

The cost function, K, in SOX is already normalised with respect to a maximum hydraulic conductance and so this is left unchanged.In order to apply the principle of feedback control, the objective function must be evaluated by the control variable. However, due to the co-limitation part of the photosynthesis model used in JULES it is not possible to rearrange $A$ in terms of $g_s$. We therefore, re-formulate the control problem in terms of $c_i$ using Fick's Law (Eq. 3). In order to maintain non-dimensionality when differentiating the objective function, we differentiate with respect to the ratio intercellular leaf, to atmospheric $CO_2$ concentration:

$$f_i = \frac{c_i}{c_a} \tag{12}$$

SOX (Eq. 1) is subsequently rewritten as:

$$\frac{\partial(\hat{A} \cdot K)}{\partial f_i}(f_{i,opt}) = 0 \tag{13}$$

The control variable is now $f_i$ and its optimum value is tracked by the feedback system. The optimum $c_i$ is found using Equation 12. As with the numerical iteration solution to SOX, the optimal stomatal conductance can be found from the optimal $c_i$ value using the equilibrium diffusion equation (Eq. 3). Non-dimensionalising and reformulating SOX in this way does not alter the biological assumptions and has no effect on the optimum $g_s$, but they are implemented here to ensure that the objective function (Eq. 9) and the optimised variable ($f_i$) both occupy the range from zero to unity.We define the rate of change of $f_i$ using a control equation analogous to the Newton-Raphson root finding algorithm:

$$\frac{df_i}{dt} = -\left(\frac{\partial^2 \hat{J}}{\partial f_i^2}\right)^{-1}\left(\frac{\partial \hat{J}}{\partial f_i}\right)\left(1 - exp\left\{-\frac{\Delta t}{\tau}\right\}\right) \tag{14}$$

where $\tau$ is a tunable time-scale parameter representing the response time of the stomata (set to $\tau$ = 900 s by default), and the $1 - exp\left\{-\frac{\Delta t}{\tau}\right\}$ term accounts for model timesteps ($\Delta t$) which are non-negligible compared to $\tau$.The derivatives for the Newton-Raphson increment are found by first expressing them in terms of $\hat{A}$ and $K$:

$$\frac{\partial \hat{J}}{\partial f_i} = \hat{A}\frac{\partial K}{\partial f_i} + K\frac{\partial \hat{A}}{\partial f_i} \tag{15}$$

$$\frac{\partial^2 \hat{J}}{\partial f_i^2} = \hat{A}\frac{\partial^2 K}{\partial f_i^2} + 2\frac{\partial \hat{A}}{\partial f_i}\frac{\partial K}{\partial f_i} + K\frac{\partial^2 \hat{A}}{\partial f_i^2} \tag{16}$$

The derivatives of $\hat{A}$ and $K$ are found numerically. It is possible to derive analytical derivatives for both $\hat{A}$ and $K$ which would allow an analytical calculation of the Newton-Raphson increment, however by using numerical derivatives we maintain greater generality as the photosynthesis model and cost function can be readily changed without requiring them to have analytical derivatives.

$$\frac{\partial X}{\partial f_i} = \frac{X(f_i + h) - X(f_i - h)}{2h} \tag{17}$$

$$\frac{\partial^2 X}{\partial f_i^2} = \frac{X(f_i + h) - 2X(f_i) + X(f_i - h)}{h^2} \tag{18}$$

where $h$ is the numerical step-size in $f_i$ (set equal to 0.0002), and variable $X$ is either $\hat{A}$ or $K$.

### 2.4.2 Additional constraints

The Newton-Raphson control equation is not sufficient by itself to track the optimum $c_i$. In addition to the above rate equation we implement three additional constraints.

The first is to limit the value of the second derivative of the objective function. The Newton-Raphson algorithm is not robust when the second derivative of the function being optimised changes sign anywhere within the optimisation domain (i.e. the function is not strictly convex or concave). In the case of attempting to maximise an objective function, this means that the method will break down if the second derivative becomes positive (the function is not concave). Unfortunately, the objective function in SOX is not strictly concave with respect to $f_i$ for all environmental conditions, and the second derivative can become positive. To solve this, we set a maximum value for the second derivative that prevents it both approaching zero and becoming positive. We relate this limit to a maximum allowed rate of change in $f_i$:

$$\left(\frac{\partial^2 \hat{J}}{\partial f_i^2}\right)_{max} = -\left|\frac{\hat{J}'}{\left(\frac{df_i}{dt}\right)_{max} dt}\right| \tag{19}$$

where $\hat{J}' = \frac{\partial \hat{J}}{\partial f_i}$, and $(\frac{df_i}{dt})_{max}$ is a plant functional type (PFT) dependent parameter with default values of $1.67 \times 10^{-4}\,s^{-1}$ for C3 and $1.67 \times 10^{-5}\,s^{-1}$ for C4 respectively. These equate to a maximum allowed change in $f_i$ of 0.15 and 0.015 per 15 minute time-step, for C3 and C4 plants respectively.The second is to set a condition for when leaf photosynthesis is limited by light and equal to zero. In this case the objective function is equal to zero for all values of $f_i$, resulting in a zero first derivative and rate of change of $f_i$. When photosynthesis is completely limited by light, there is no benefit for a plant to keep it is stomata open and so we implement the condition that when absorbed photosynthetically active radiation (APAR) is zero the rate of change of $f_i$ is given by:

$$\frac{df_i}{dt} = -\left(\frac{df_i}{dt}\right)_{max}\left(1 - exp\left\{-\frac{\Delta t}{\tau}\right\}\right) \tag{20}$$

Finally, the control variable, $f_i$, is kept within the range (0,1) i.e. intercellular leaf $CO_2$ concentration cannot drop below 0, and cannot exceed atmospheric $CO_2$ concentration.

## 2.5 An improved big leaf model within JULES

There are currently two options for canopy photosynthesis in JULES, both described fully in Clark et al. (2011). The first option is a big leaf approach, in which top of the canopy leaf photosynthesis is scaled to total canopy photosynthesis, using the assumption that both irradiance ($I_{par}$) and photosynthetic capacity ($V_{cmax}$) decline exponentially through the canopy, with the same rate of decay.The second approach is a multi-layer approach where gross photosynthesis is calculated for a number of equal increments of leaf area index (LAI) through the canopy, assuming again that both irradiance and photosynthetic capacity decay exponentially through the canopy, although with the option for these decay rates to differ. Mercado et al. (2007), along with discussion in Clark et al. (2011), demonstrate the superior performance of the multi-layer approach compared to the big-leaf approach, in particular it is ability to capture observed photosynthetic light responses, and diurnal cycles of GPP.For computational efficiency, it is beneficial for the feedback optimisation to be implemented as part of a big leaf approach, with just a single prognostic variable for the whole canopy. For this reason we present below a modified version of the big leaf approach that more accurately captures the light response and diurnal cycle of canopy photosynthesis.Photosynthesis in JULES uses the biochemistry of $C_3$ and $C_4$ photosynthesis from Collatz et al. (1991) and Collatz et al. (1992). Leaf photosynthesis is determined by three potentially-limiting rates:

1. Rubisco-limited rate ($W_c$)

$$W_c = \begin{cases} V_{cmax}\left(\dfrac{c_i - \Gamma}{c_i + K_c(1 + O_a/K_o)}\right) & \text{for } C_3 \text{ plants} \\ V_{cmax} & \text{for } C_4 \text{ plants} \end{cases} \tag{21}$$

where $V_{cmax}$ (mol $CO_2 m^{-2} s^{-1}$) is the maximum rate of carboxylation of Rubisco, $c_i$ (Pa) is the leaf internal carbon dioxide partial pressure, $\Gamma$ (Pa) is the $CO_2$ compensation point in the ansence of mitochondrial respiration, $O_a$ (Pa) is the partial pressure of atmospheric oxygen, and $K_c$ and $K_o$ (Pa) are the Michaelis-Menten parameters for $CO_2$ and $O_2$, respectively.

2. Light-limited rate ($W_l$)

$$W_l = \begin{cases} \alpha(1 - \omega) I_{par}\left(\dfrac{c_i - \Gamma}{c_i + 2\Gamma}\right) & \text{for } C_3 \text{ plants} \\ \alpha(1 - \omega) I_{par} & \text{for } C_4 \text{ plants} \end{cases} \tag{22}$$

where $\alpha$ is the quantum efficiency of photosynthesis (mol $CO_2$mol$^{-1}$PAR), $\omega$ is the leaf scattering coefficient for PAR and $I_{par}$ is the incident photosynthetically active radiation (PAR, mol m$^{-2}$s$^{-1}$).

3. Rate of transport of photosynthetic products (in the case of $C_3$ plants) and PEPCarboxylase limitation (in the case of $C_4$ plants) ($W_e$)

$$W_e = \begin{cases} 0.5V_{cmax} & \text{for } C_3 \text{ plants} \\ 2 \times 10^4 V_{cmax}\frac{c_i}{P_*} & \text{for } C_4 \text{ plants} \end{cases} \quad (23)$$

As in the original approach used in JULES and described in Clark et al. (2011), incident radiation attenuation through the canopy is assumed to follow Beer's law:

$$I_{par}(L) = I_0 e^{-k_{PAR}L} \quad (24)$$

where $I_0$ is irradiance at the top of the canopy, $k_{PAR}$ is a light extinction coefficient and $L$ is the leaf area index through the canopy.Similarly, it is also assumed that photosynthetic capacity ($V_{cmax}$) varies through the canopy. Unlike the old big leaf approach, however, we assume a distinct extinction coefficient associated with the decline of Nitrogen through the canopy, similar to that used in the multi-layer canopy scheme also present in JULES:

$$V_{cmax} = V_{cmax_0} e^{-k_n L} \quad (25)$$

where $k_n$ is the decay coefficient of Nitrogen through the canopy with the default value of 0.2.We also introduce a decay of the quantum efficiency of photosynthesis ($\alpha$) through the canopy to account for the decline of chlorophyll content through the canopy. The decay rate of $\alpha$ is assumed equal to that of $V_{cmax}$, since both depend on canopy Nitrogen.

$$\alpha(L) = \alpha_0 e^{-k_N L} \quad (26)$$

where $\alpha_0$ is the quantum efficiency of photosynthesis at the top of the canopy with the default value of 0.035.To scale to canopy photosynthesis, the three potentially-limiting rates are integrated over the canopy to find their respective canopy average values (denoted with a bar):

$$\overline{W_c} = \frac{1}{L_c}\int_0^{L_c} W_c dL = W_{c_0}\frac{1 - e^{-k_n L_c}}{k_n L_c} \quad (27)$$

$$\overline{W_l} = \frac{1}{L_c}\int_0^{L_c} W_l dL = W_{l_0}\frac{1 - e^{-(k_n + k_{PAR})L_c}}{(k_n + k_{PAR})L_c} \quad (28)$$

$$\overline{W_e} = \frac{1}{L_c}\int_0^{L_c} W_e dL = W_{e_0}\frac{1 - e^{-k_n L_c}}{k_n L_c} \quad (29)$$

Where $W_{c_0}$, $W_{l_0}$, and $W_{e_0}$ are the values of $W_c$, $W_l$ and $W_e$ at the top of the canopy respectively.Average gross canopy photosynthesis ($\overline{W}$) is then calculated as the smoothed minimum of these canopy average limiting rates. These are found as the smallest root of the following set of equations:

$$\beta_1 \overline{W_p}^2 - \overline{W_p}\left(\overline{W_c} + \overline{W_l}\right) + \overline{W_c}\ \overline{W_l} = 0 \quad (30)$$

$$\beta_2 \overline{W}^2 - \overline{W}\left(\overline{W_p} + \overline{W_e}\right) + \overline{W_p}\ \overline{W_e} = 0 \quad (31)$$

where $\overline{W_p}$ is the smoothed minimum of $\overline{W_c}$ and $\overline{W_l}$, and $\beta_1$ = 0.83 and $\beta_2$ = 0.93 are "co-limitation" coefficients.Finally total canopy gross photosynthesis is calculated by multiplying the average canopy photosynthesis by canopy LAI, with the same method also being used to calculate canopy respiration and stomatal conductance:

$$W = \overline{W} L_c \quad (32)$$

In addition to the introduction of a vertical distribution in the quantum efficiency of photosynthesis ($\alpha$), the new approach here differs from the original big-leaf approach in the order in which the co-limitation (Eq. 30 and Eq. 31) of the three potentially limiting rates is calculated, and the scaling of leaf to canopy photosynthesis. The original big leaf first calculates the co-limitation of the three rates at the top of the canopy leaf before scaling up to total canopy photosynthesis. Canopy photosynthesis is therefore rarely light-limited as top of the canopy leaves, which have the highest light conditions, determine the total canopy rate. The new approach instead performs co-limitation after each of the rates has been effectively scaled to the canopy. This better accounts for the contribution of lower canopy leaves that are typically shaded and therefore limited by incoming light.

## 2.6 JULES-SOX simulations

All three versions of SOX (numerical, feedback control and semi-analytical) were implemented into version 5.1 of the JULES LSM, along with the updated canopy photosynthesis scheme. The code for the feedback control version of JULES-SOX used in this study can be found at code. metoffice.gov.uk/svn/jules/main/branches/dev/simonjones/vn5.1_jules_SOX_feedback_control/. The revision at time of publication is 23887. Each version of JULES-SOX was then used to simulate plant function at four sites across the Amazon rainforest from the LBA network (Saleska et al., 2013). These sites include LBA-K34 Reserva Cueiras, Manaus Brazil; LBA-K83 Tapajos National forest, Santarem Brazil; LBA-RJA Reserva Jaru; and LBA-K67 Tapajos National forest, Santarem Brazil. A summary of the environmental conditions at each site is given in the supplementary material (Supplementary Figure S1, S2). The simulations were spun up for 25 years and run on a 15 minute time-step. Driving data is provided from each site on an hourly basis and is linearly interpolated to 15 min by JULES. The simulation period for each site is as follows: K34–2003-01-01 04:00:00 to 2006-01-01 03:00:00; K83–2001-01-01 04:00:00 to 2004-01-01 03:00:00; RJA - 2000-01-01 04:00:00 to 2002-12-31 23:00:00; and K67–2002-01-01 02:00:00 to 2005-01-01 03:00:00. The parameters fitted in Eller

et al. (2020) were used for SOX and are given in Supplementary Table S1.

## 2.7 Model evaluation

The aim of the study is to test the ability of feedback control to track the optimum solution of SOX found by numerical iteration. To do this we examine both predicted daily (24-h mean) grid-box gross primary productivity (GPP) and predicted daily stomatal transpiration from the feedback control approach and compare it against the same predictions from the numerical approach across all sites. We also compare predicted GPP and transpiration from the semi-analytical approximation against the numerical version of SOX, and present root mean square error (RMSE) values for both sets of comparisons. This allows us to then compare the ability of the feedback optimisation and semi-analytical versions to replicate the predictions made by the numerical version.We also compare the average diurnal cycle of predicted grid-box GPP, predicted grid-box transpiration, and predicted leaf water potential for each version of SOX at each site, in order investigate the ability of both the feedback control and semi-analytical approaches to represent the sub-daily behaviour of stomata predicted by SOX. We also assess the ability of JULES-SOX to capture observed sub-daily fluxes at each site and compare the average diurnal cycle of GPP predicted by each model to the equivalent cycle of observed GPP at each site, and across the same time period. We also compare the average diurnal cycle of transpiration to observations, although due to data availability this comparison is only made at site K67. Observations are taken from Saleska et al. (2013) and GPP and transpiration are taken as the "GEP_model" and "Fh20" variables respectively.Finally, an important part of the motivation behind the feedback control approach is that while the numerical version accurately represents the assumptions made within SOX it is computationally inefficient. So as well as evaluating each models ability to capture the assumptions made in SOX we also assess the computational efficiency of each method. We do this by presenting the total aggregate time taken to run all four sites, which provides a metric of the efficiency of each version.

# 3 Results

In general the feedback control approach was able to replicate the results from the numerical iteration approach more closely than the semi-analytical version of SOX (Figure 2 and Figure 3). With respect to predicted daily grid box GPP, the difference between the two approaches was relatively small, and both were able to replicate the result from the numerical version with reasonable accuracy (Figure 2). Non-etheless the root mean square error (RMSE) between predicted daily grid box GPP from the numerical version of SOX and the feedback control version of SOX (RMSE = 0.106) was lower than the RMSE between the numerical and semi-analytical versions (RMSE = 0.140) across all simulations (Figure 2). In contrast, there were more significant differences between the two approaches in terms of predicted daily grid-box stomatal transpiration (Figure 3) and canopy water potential (Figure 6). The feedback control version more closely matched the numerical solution, with a significantly lower RMSE value (RMSE = 29.4) for predicted transpiration compared to the semi-analytical version (RMSE = 264.4) (Figure 3). The semi-analytical version of SOX generally predicted larger values of transpiration compared with the numerical version (Figure 3). This was due to greater daily maxima in stomatal conductance, and therefore greater maxima in daily transpiration compared to the numerical and feedback control versions of SOX (Figure 5). The feedback control method generally predicted similar values of daily GPP relative to the numerical version, but there was a small bias towards lower values of daily GPP relative to the numerical version (Figure 2). This was mostly due to a lag in stomatal opening at dawn in the feedback control approach relative to the numerical version, resulting in overall lower average daily values (Figure 4).

All three approaches accurately captured the average diurnal cycle of observed GPP at each site, with the exception of the K34 site where the peak in daily GPP was underestimated by all three versions of the models (Figure 4). The similarity of the three versions of the model here is due to the weak dependence of the light-limited rate of photosynthesis ($W_l$, Eq. 22) on $c_i$ and therefore $g_s$, which is most commonly the limiting rate in our new big leaf scheme. All three versions of JULES-SOX underestimated the amplitude of the average diurnal cycle of transpiration at the K67 site, but the semi-analytical version predicted greater daily maxima than the numerical and feedback control versions and was therefore closest to the observed values. The greater difference between the approaches in terms of predicted transpiration relative to predicted GPP is due to the greater dependence of transpiration on stomatal conductance than that of photosynthesis in the light-limited regime.

As expected, the numerical version of SOX was the least computationally efficient method. To run all four sites it took a combined time of 52 min and 52 s (3,172 s). The speed of the numerical version depends on the number of iterations used and the time taken of course reduces when fewer iterations are used, although at the cost of reduced accuracy. Both the semi-analytical and feedback control approaches were significantly faster, with total run times of 38 min and 4 s, and 25 min and 26 s respectively. The efficiency of the feedback control version could be improved further if instead of using the chain rule to calculate the derivatives of the Newton-Raphson increment, the derivatives are estimated directly using:

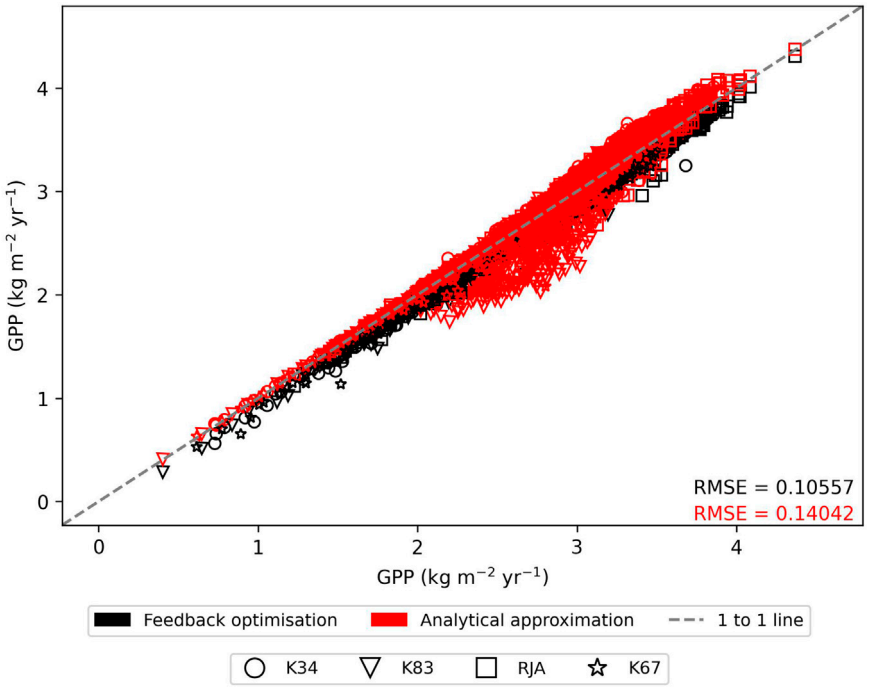


FIGURE 2
The comparison of predicted daily grid-box gross primary production (GPP, kg C m$^{-2}$ yr$^{-1}$) from the numerically solved version of JULES-SOX along the x axis against 1) feedback control version of JULES-SOX (black) and 2) the semi-analytical approximation of JULES-SOX (red) along the y-axis, across simulations from four sites in the Amazon rainforest. The sites are LBA-K34: Reserva Cuieiras, Manaus Brazil; LBA-K83: Tapajos National forest, Santarem Brazil; LBA-RJA: Reserva Jaru; LBA-K67: Tapajos National forest, Santarem Brazil. Root mean square error (RMSE) values between values predicted by the numerical version and the two other versions across all simulations are presented.

$$\frac{\partial \hat{J}}{\partial f_i} = \frac{\hat{J}(f_i + h) - \hat{J}(f_i - h)}{2h} \tag{33}$$

$$\frac{\partial^2 \hat{J}}{\partial f_i^2} = \frac{\hat{J}(f_i + h) - 2\hat{J}(f_i) + \hat{J}(f_i - h)}{h^2} \tag{34}$$

This reduces the number of calculations required but results in a slightly less accurate estimate of the derivatives and so lowers the performance of the approach with respect to replicating the results of the numerical version.

## 4 Discussion

Accurately simulating stomatal behaviour is an important part of predicting climate change and its impacts in the future. Stomatal optimisation theory has shown promise as a relatively simple way to replicate observed stomatal responses, without the need for complex understanding of physiological processes. However, it is use in large scale simulations of the land surface has been limited due to the difficulties involved in solving for optimal stomatal conductance, with methods often compromising either on scientific accuracy, or on computational efficiency. Applying methods based in feedback control, we have demonstrated an alternative approach to solving stomatal optimisation models that may allow optimisation theory to be effectively implemented in LSMs and used in large scale modelling studies. Our approach significantly increases computational efficiency relative to numerical iteration while maintaining a close representation of the underlying assumptions made in the optimisation model.

One of the largest challenges facing stomatal optimisation models is defining the cost function associated with water loss (Wang et al., 2020). Plants may experience multiple different penalties for transpiring excessive water, including loss of hydraulic conductance through xylem cavitation (Tyree and Sperry, 1989; Martínez-Vilalta et al., 2014; Sperry and Love, 2015) and reduced cell turgor required for tissue expansion and growth (Hsiao, 1973; Cosgrove, 2014; Fricke, 2017). How to aggregate these potential costs into a single function is not currently clear (Wang et al., 2020). The ability to implement new assumptions into optimisation models and test them within the context of an LSM is therefore crucial to advancing stomatal optimisation models and improving predictions of stomatal behaviour in the future. Unlike the semi-analytical solution of

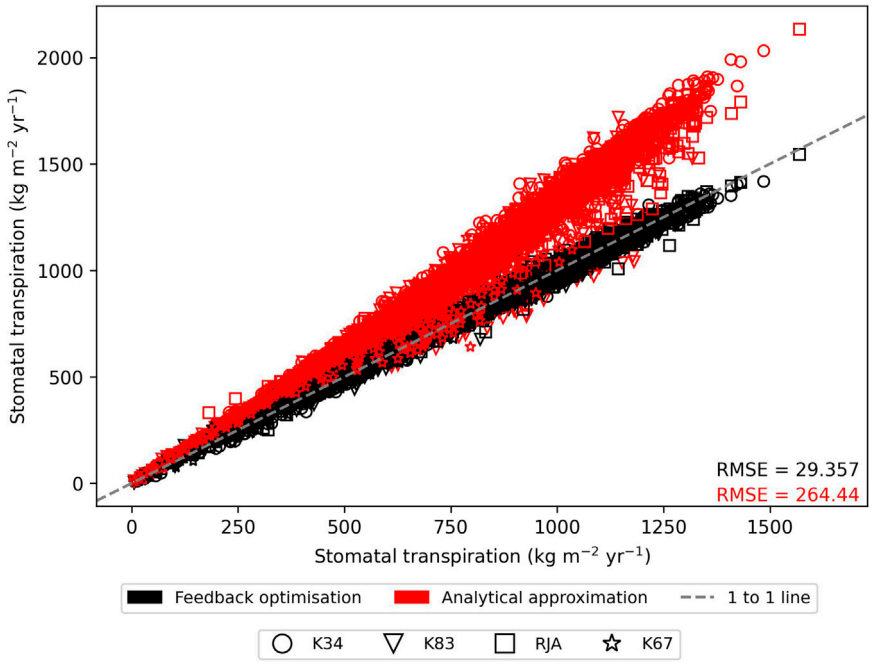


FIGURE 3
The comparison of predicted daily grid-box stomatal transpiration (kg $H_2O$ $m^{-2}yr^{-1}$) from the numerically solved version of JULES-SOX along the x axis against 1) feedback control version of JULES-SOX (black) and 2) the semi-analytical approximation of JULES-SOX (red) along the y-axis, across simulations from four sites in the Amazon rainforest. The sites are LBA-K34: Reserva Cuieiras, Manaus Brazil; LBA-K83: Tapajos National forest, Santarem Brazil; LBA-RJA: Reserva Jaru; LBA-K67: Tapajos National forest, Santarem Brazil. Root mean square error (RMSE) values between values predicted by the numerical version and the two other versions across all simulations are presented.

SOX, the feedback control approach can in theory be applied to any realistic objective function, allowing new cost functions to be readily implemented into LSMs.

Plants in JULES have been reported to have a high sensitivity to drought events (Harper et al., 2016; Williams et al., 2018), due in part to the empirical '$\beta$-factor' approach used to represent the effect of changes in soil moisture on canopy level photosynthesis (Cox et al., 1998; Clark et al., 2011). This sensitivity represents a significant component of simulating the response of vegetated ecosystems to drought and is a key source of error between model predictions and observations (Powell et al., 2013). Similarly, the response of stomata to changes in vapour pressure deficit (VPD) is traditionally controlled by the empirically derived relationship between intercellular leaf $CO_2$ and VPD from Jacobs (1994), as described in Best et al. (2011). Increases in VPD can reduce stomatal conductance and photosynthesis as the increased evaporative demand results in greater water loss through transpiration (Grossiord et al., 2020). Capturing this response is crucial for predicting the future of ecosystems across the globe as increasing VPD is a significant driver of tree mortality (Park Williams et al., 2013). The SOX model provides a theoretical basis that allows improved predictions of stomatal regulation during drought and periods of high VPD (Eller et al., 2018) that are more robust to changes in climate than the empirically derived responses. The semi-analytical approximation for SOX Eller et al. (2020) provides a means to implement stomatal optimisation into JULES that is computationally efficient and maintains some of the improved predictions of carbon and water fluxes. However, as we have shown here this approximation does not fully represent the assumptions made in SOX. In particular, the semi-analytical version often mischaracterises the sensitivity of stomata to VPD due to the linearisation of the vulnerability curve (Sabot et al., 2022b). Applying feedback control will allow SOX to be accurately and efficiently implemented into JULES while preserving the fundamental assumptions made in the model, and facilitate the implementation of alternative cost functions that may improve the capability of SOX to predict forest responses to extreme climate events such as drought, and increasing global VPD.

The feedback control approach is a promising alternative method for solving stomatal optimisation models. However, as can be seen in Figure 2–6, the method does not track the optimal solution perfectly. There are many potential reasons for this, including for example, numerical errors in the estimation of the objective function derivatives (indeed the tracking improves when analytical derivatives are

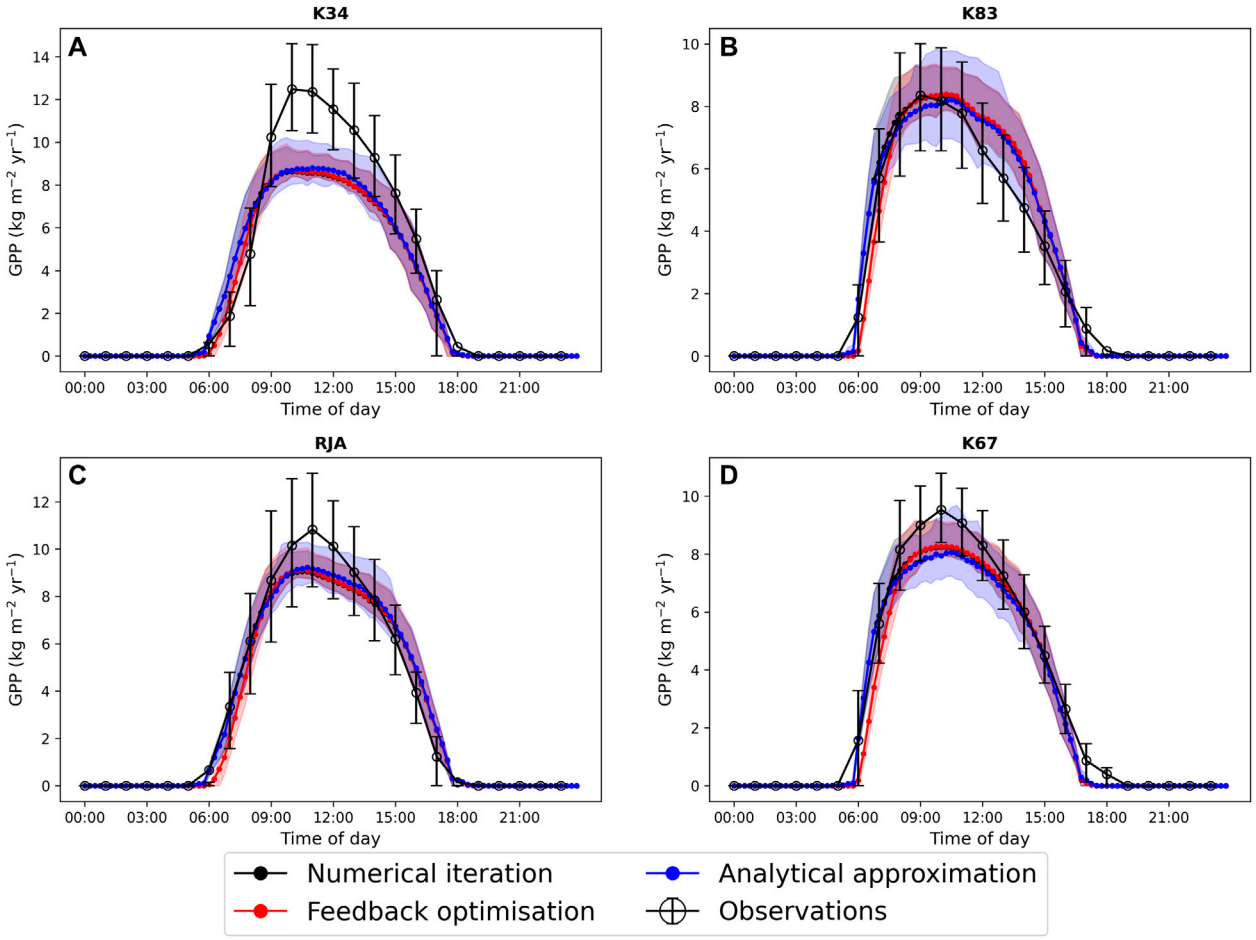


FIGURE 4
A comparison of the average diurnal cycle of predicted gross primary production (GPP, kg C m$^{-2}$yr$^{-1}$) from JULES-SOX solved using three different methods (1. Numerical iteration (black), 2. Feedback control (red), 3. A semi-analytical approximation (blue))) and observed GPP at four sites in the Amazon rainforest. **(A)** LBA-K34 Reserva Cuieiras, Manaus Brazil; **(B)** LBA-K83 Tapajos National forest, Santarem Brazil; **(C)** LBA-RJA Reserva Jaru; **(D)** LBA-K67 Tapajos National forest, Santarem Brazil. Observed data is from Saleska et al. (2013). Error bars and shaded areas represent the 25% and 75% uncertainty percentiles.

used). A more scientifically interesting difference between the feedback control approach and the numerical solution can be seen when looking in particular at the average diurnal cycle of transpiration and leaf water potential at each of the four simulated sites (Figure 5). In particular, while the feedback method closely tracks the numerical solution throughout the middle of the day, there is a clear distinction between the two approaches at dawn when the stomata first open, as in general the feedback control approach tends to lag behind the optimal solution. This is because stomatal conductance (or more accurately $f_i$ in this case) is now determined by a differential equation (Eq. 14), which introduces a time-scale into the rate of stomatal opening. The exact mechanisms that control the regulation of stomata are not well understood (Buckley, 2019). However, it is clear that physiological constraints related to the size, density and structure of stomata have a significant effect on the rate at which stomata can respond to changing environmental conditions (Lawson and Vialet-Chabrand, 2019). Observations show that these response times can be an order of magnitude or more slower than the response of photosynthesis (Lawson and Blatt, 2014; Lawson and Vialet-Chabrand, 2019), which decouples photosynthesis from stomatal conductance over short time-scales and can have important consequences for plant water use efficiency (Lawson and Blatt, 2014; Vialet-Chabrand et al., 2017; Eyland et al., 2021). Stomatal optimisation models do not intrinsically account for these physiological constraints and so implicitly assume that the rate of change of stomata is unbounded, although time-scales can be introduced using, for example, the "prognostic stomatal conductance" approach described by Sellers et al.

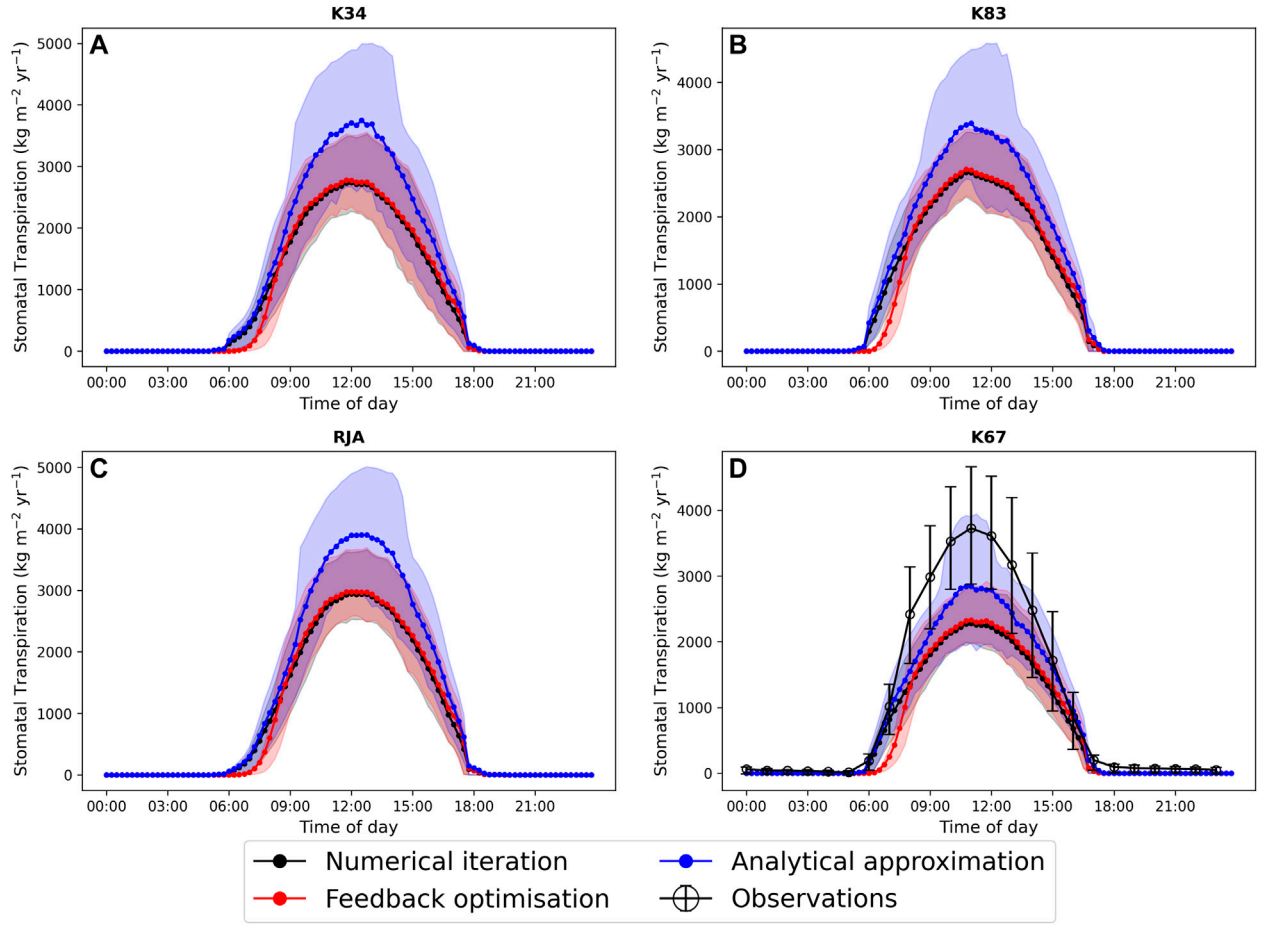


FIGURE 5
A comparison of the average diurnal cycle of predicted stomatal transpiration (kg $H_2O$ $m^{-2}yr^{-1}$) from JULES-SOX solved using three different methods (1. Numerical iteration (black), 2. Feedback control (red), 3. A semi-analytical approximation (blue))) and observed transpiration at four sites in the Amazon rainforest. **(A)** LBA-K34 Reserva Cuieiras, Manaus Brazil; **(B)** LBA-K83 Tapajos National forest, Santarem Brazil; **(C)** LBA-RJA Reserva Jaru; **(D)** LBA-K67 Tapajos National forest, Santarem Brazil. Observed data is from Saleska et al. (2013). Error bars and shaded areas represent the 25% and 75% uncertainty percentiles.

(1996). In the absence of detailed understanding of the physiological mechanisms behind lagged stomatal regulation, the feedback approach presented here presents an efficient method for physiological constraints on stomatal opening to be accounted for, at least implicitly, and may help to bridge the gap between optimisation and mechanistic approaches, allowing more accurate predictions of sub-daily stomatal behaviour.

Feedback control has strong parallels with numerical optimisation (Hauswirth et al., 2021). These algorithms allow complex equations to be solved numerically and have been applied to stomatal optimisation models previously. For example, Anderegg et al. (2018) use the Newton-Raphson algorithm to solve their stomatal optimisation model for optimal stomatal conductance at each time-step. The difference between using a numerical solver in this way, and the feedback control approach we present here is that we do not use multiple iterations per time-step. Instead the Newton-Raphson algorithm determines the rate of change of $f_i$ which is then solved through integration. It should be noted that this limits the feedback approach to simulations with relatively short time-steps, such as the 15 min time-step used here. The choice of the Newton-Raphson algorithm here was justified by our aim of replicating the numerical solution of SOX as closely as possible, as the Newton-Raphson algorithm typically has faster convergence than first order methods. However, despite the fast convergence of the Newton-Raphson algorithm and the relatively close tracking of the optimal solution by our implementation, its use requires additional constraints to be added to the model code that prevent the algorithm becoming unstable and producing unrealistic results. In particular, the algorithm is not robust when the objective function is not concave and the second derivative changes sign within the optimisation domain. This is

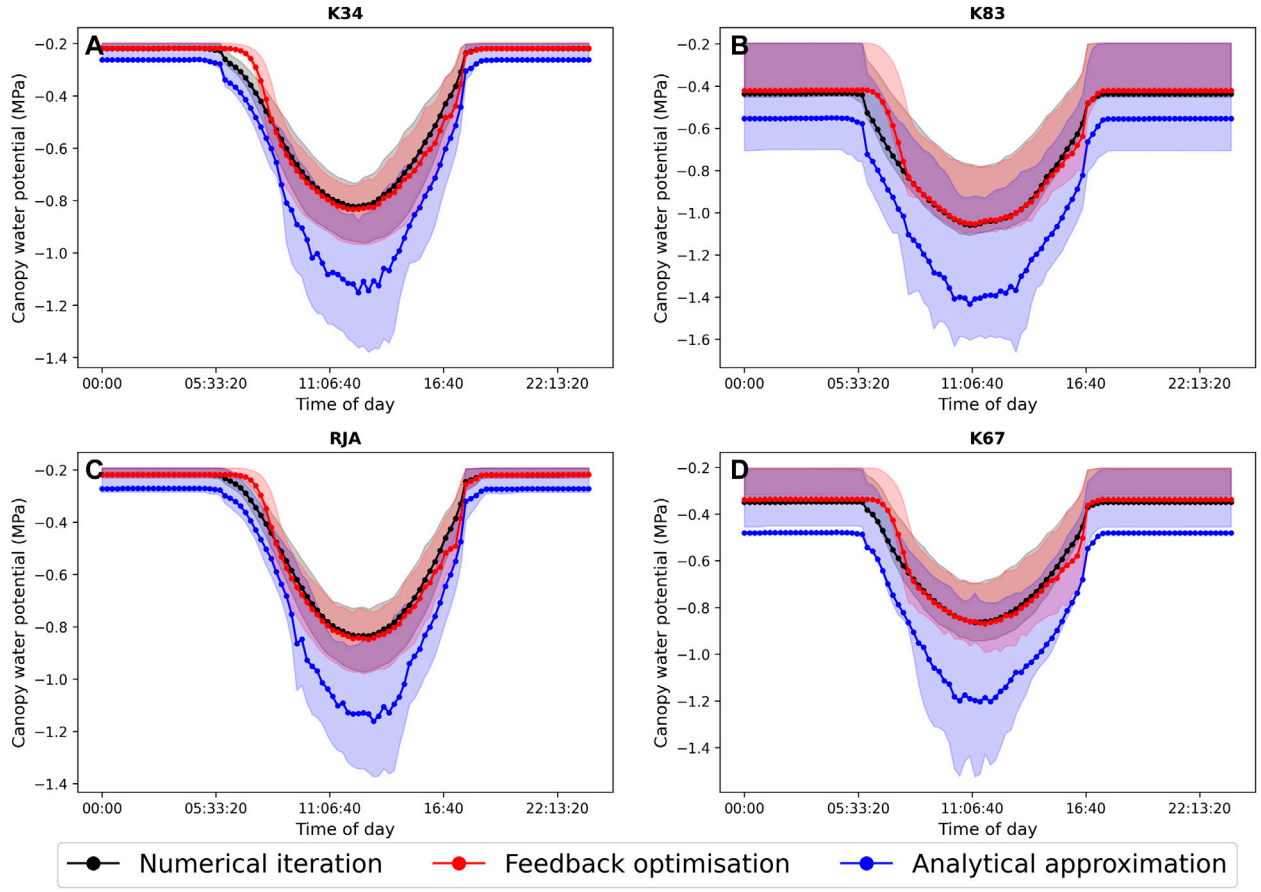


FIGURE 6
The average diurnal cycle of predicted canopy water potential (MPa) from JULES-SOX solved using three different methods (1. Numerical iteration (black), 2. Feedback control (red), 3. A semi-analytical approximation (blue)) at four sites in the Amazon rainforest. **(A)** LBA-K34 Reserva Cuieiras, Manaus Brazil; **(B)** LBA-K83 Tapajos National forest, Santarem Brazil; **(C)** LBA-RJA Reserva Jaru; **(D)** LBA-K67 Tapajos National forest, Santarem Brazil. Shaded areas represent the 25% and 75% uncertainty percentiles.

the case in SOX where under certain environmental conditions the second derivative of the objective function can become positive. Our solution of artificially preventing the second derivative from approaching zero and ultimately changing sign, by giving it a maximum value appears to have been relatively successful here. However, we currently have no clear method for determining what this maximum value should be besides the tuning we have done. This may mean that our method is not robust for all sets of environmental conditions and future applications of feedback control to stomatal optimisation may use more robust methods such as the commonly used gradient ascent method. Feedback optimisation of non-concave/non-convex functions, in particular those that change through time, is an emerging field (Häberle et al., 2020; Ding et al., 2021) and further work is required to understand how these methods may be applicable to stomatal optimisation.

## 5 Conclusion

We present a feedback control based approach for tracking the optimum stomatal conductance predicted by stomatal optimisation models through time. We apply the approach to the SOX stomatal optimisation model, where it is able to accurately replicate predicted GPP, stomatal transpiration and leaf water potential found by numerical iteration. Feedback control represents a promising avenue for stomatal optimisation models that may allow them to be efficiently implemented into LSMs, improving the representation of stomatal behaviour in projections of global climate in the future.

## Data availability statement

Publicly available datasets were analyzed in this study. This data can be found here: https://daac.ornl.gov/cgi-bin/dsviewer.pl?ds_id=1174.

## Author contributions

PC suggested the feedback control approach. CE advised on implementing the approach in SOX. All authors contributed to the design of the study. SJ conducted the simulations and analysis. SJ wrote the first draft of the manuscript. All authors contributed to manuscript revision, read and approved the submitted version.

## Funding

The authors acknowledge funding from: CSSP Brazil project P109647 ("Brazilian ecosystem resilience in net-generation vegetation dynamics scheme")—SJ; Human Frontier Science Program project RGP0016/2020 ("How plant heat stress will influence global warming this century")—CE; European Research Council ECCLES project, grant agreement number 742472 ("Emergent constraints on climate-land feedbacks in the Earth System")—PC.

## Conflict of interest

The authors declare that the research was conducted in the absence of any commercial or financial relationships that could be construed as a potential conflict of interest.

## Publisher's note

All claims expressed in this article are solely those of the authors and do not necessarily represent those of their affiliated organizations, or those of the publisher, the editors and the reviewers. Any product that may be evaluated in this article, or claim that may be made by its manufacturer, is not guaranteed or endorsed by the publisher.

## Supplementary material

The Supplementary Material for this article can be found online at: https://www.frontiersin.org/articles/10.3389/fenvs.2022.970266/full#supplementary-material

## References

Allen, C. D., Macalady, A. K., Chenchouni, H., Bachelet, D., McDowell, N., Vennetier, M., et al. (2010). A global overview of drought and heat-induced tree mortality reveals emerging climate change risks for forests. *For. Ecol. Manag.* 259, 660–684. Adaptation of Forests and Forest Management to Changing Climate. doi:10.1016/j.foreco.2009.09.001

Anderegg, W. R. L., Flint, A., Huang, C.-y., Flint, L., Berry, J. A., Davis, F., et al. (2015). Tree mortality predicted from drought-induced vascular damage. *Nat. Geosci.* 8, 367–371. doi:10.1038/ngeo2400

Anderegg, W. R. L., Wolf, A., Arango-Velez, A., Choat, B., Chmura, D. J., Jansen, S., et al. (2018). Woody plants optimise stomatal behaviour relative to hydraulic risk. *Ecol. Lett.* 21, 968–977. doi:10.1111/ele.12962

Ball, J. T., Woodrow, I. E., and Berry, J. A. (1987). *A model predicting stomatal conductance and its contribution to the control of photosynthesis under different environmental conditions*. Dordrecht: Springer Netherlands, 221. doi:10.1007/978-94-017-0519-6_48

Best, M. J., Pryor, M., Clark, D. B., Rooney, G. G., Essery, R. L. H., Ménard, C. B., et al. (2011). The joint UK land environment simulator (jules), model description - part 1: Energy and water fluxes. *Geosci. Model Dev.* 4, 677–699. doi:10.5194/gmd-4-677-2011

Betts, R. A., Cox, P. M., Collins, M., Harris, P. P., Huntingford, C., and Jones, C. D. (2004). The role of ecosystem-atmosphere interactions in simulated amazonian precipitation decrease and forest dieback under global climate warming. *Theor. Appl. Climatol.* 78, 157–175. doi:10.1007/s00704-004-0050-y

Buckley, T. N. (2019). How do stomata respond to water status? *New Phytol.* 224, 21–36. doi:10.1111/nph.15899

Buckley, T. N. (2017). Modeling stomatal conductance. *Plant Physiol.* 174, 572–582. doi:10.1104/pp.16.01772

Buckley, T. N., Sack, L., and Farquhar, G. D. (2017). Optimal plant water economy. *Plant, Cell & Environ.* 40, 881–896. doi:10.1111/pce.12823

Clark, D. B., Mercado, L. M., Sitch, S., Jones, C. D., Gedney, N., Best, M. J., et al. (2011). The joint UK land environment simulator (jules), model description - part 2: Carbon fluxes and vegetation dynamics. *Geosci. Model Dev.* 4, 701–722. doi:10.5194/gmd-4-701-2011

Collatz, G. J., Ball, J. T., Grivet, C., and Berry, J. A. (1991). Physiological and environmental regulation of stomatal conductance, photosynthesis and transpiration: A model that includes a laminar boundary layer. *Agric. For. Meteorology* 54, 107–136. doi:10.1016/0168-1923(91)90002-8

Collatz, G. J., Ribas-Carbo, M., and Berry, J. A. (1992). Coupled photosynthesis-stomatal conductance model for leaves of c4 plants. *Funct. Plant Biol.* 19, 519–538. doi:10.1071/PP9920519

Cosentino, C., and Bates, D. (2011). *Feedback control in systems biology*. Florida, United States: CRC Press.

Cosgrove, D. J. (2014). *Plant cell growth and elongation*. United States: American Cancer Society. doi:10.1002/9780470015902.a0001688.pub2

Cowan, I. R., and Farquhar, G. D. (1977). Stomatal function in relation to leaf metabolism and environment. *Symp. Soc. Exp. Biol.* 31, 471–505.

Cox, P., Betts, R. A., Jones, C., Spall, S. A., and Totterdell, I. J. (2000). Acceleration of global warming due to carbon-cycle feedbacks in a coupled climate model. *Nature* 408, 184–187. doi:10.1038/35041539

Cox, P., Huntingford, C., and Harding, R. (1998). A canopy conductance and photosynthesis model for use in a gcm land surface scheme. *J. Hydrology* 212-213, 79–94. doi:10.1016/S0022-1694(98)00203-0

Cox, P. M., Betts, R. A., Bunton, C. B., Essery, R. L. H., Rowntree, P. R., and Smith, J. (1999). The impact of new land surface physics on the gcm simulation of climate and climate sensitivity. *Clim. Dyn.* 15, 183–203. doi:10.1007/s003820050276

Ding, Y., Lavaei, J., and Arcak, M. (2021). Time-variation in online nonconvex optimization enables escaping from spurious local minima. *IEEE Trans. Autom. Contr.* 1, 1. doi:10.1109/TAC.2021.3135361

Eller, C. B., Rowland, L., Mencuccini, M., Rosas, T., Williams, K., Harper, A., et al. (2020). Stomatal optimization based on xylem hydraulics (sox) improves land surface model simulation of vegetation responses to climate. *New Phytol.* 226, 1622–1637. doi:10.1111/nph.16419

Eller, C. B., Rowland, L., Oliveira, R. S., Bittencourt, P. R. L., Barros, F. V., da Costa, A. C. L., et al. (2018). Modelling tropical forest responses to drought and el niño with a stomatal optimization model based on xylem hydraulics. *Phil. Trans. R. Soc. B* 373, 20170315. doi:10.1098/rstb.2017.0315

Eyland, D., van Wesemael, J., Lawson, T., and Carpentier, S. (2021). The impact of slow stomatal kinetics on photosynthesis and water use efficiency under fluctuating light. *Plant Physiol.* 186, 998–1012. doi:10.1093/plphys/kiab114

Farquhar, G. D., von Caemmerer, S., and Berry, J. A. (1980). A biochemical model of photosynthetic co2 assimilation in leaves of c3 species. *Planta* 149, 78–90. doi:10.1007/BF00386231

Franklin, G., Powell, J., and Emami-Naeini, A. (2011). *Feedback control of dynamic systems*. London, United Kingdom: Pearson Education.

Fricke, W. (2017). *Turgor pressure*. United States: American Cancer Society, 1–6. doi:10.1002/9780470015902.a0001687.pub2

Gedney, N., Cox, P. M., Betts, R. A., Boucher, O., Huntingford, C., and Stott, P. A. (2006). Detection of a direct carbon dioxide effect in continental river runoff records. *Nature* 439, 835–838. doi:10.1038/nature04504

Grossiord, C., Buckley, T. N., Cernusak, L. A., Novick, K. A., Poulter, B., Siegwolf, R. T. W., et al. (2020). Plant responses to rising vapor pressure deficit. *New Phytol.* 226, 1550–1566. doi:10.1111/nph.16485

Häberle, V., Hauswirth, A., Ortmann, L., Bolognani, S., and Dörfler, F. (2020). Non-convex feedback optimization with input and output constraints. *IEEE Control Syst. Lett.* 1, 1. doi:10.1109/lcsys.2020.3002152

Harper, A. B., Cox, P. M., Friedlingstein, P., Wiltshire, A. J., Jones, C. D., Sitch, S., et al. (2016). Improved representation of plant functional types and physiology in the joint UK land environment simulator (jules v4.2) using plant trait information. *Geosci. Model Dev.* 9, 2415–2440. doi:10.5194/gmd-9-2415-2016

Hartmann, D., Klein Tank, A., Rusticucci, M., Alexander, L., Broönnimann, S., Charabi, Y., et al. (2013). *Observations: Atmosphere and surface*. Cambridge, United Kingdom and New York, NY, USA: Cambridge University Press. book section 2. 159–254. doi:10.1017/CBO9781107415324.008

Hauswirth, A., Bolognani, S., Hug, G., and Dörfler, F. (2021). Optimization algorithms as robust feedback controllers. arXiv. doi:10.48550/ARXIV.2103.11329

Hochberg, U., Rockwell, F. E., Holbrook, N. M., and Cochard, H. (2018). Iso/anisohydry: A plant–environment interaction rather than a simple hydraulic trait. *Trends Plant Sci.* 23, 112–120. doi:10.1016/j.tplants.2017.11.002

Hsiao, T. C. (1973). Plant responses to water stress. *Annu. Rev. Plant Physiol.* 24, 519–570. doi:10.1146/annurev.pp.24.060173.002511

Jacobs, C. M. J. (1994). "Direct impact of atmospheric CO2 enrichment on regional transpiration," (Netherlands: Wageningen Agricultural University). Ph.D. thesis.

Krishnamoorthy, D., and Skogestad, S. (2022). Real-time optimization as a feedback control problem – A review. *Comput. Chem. Eng.* 161, 107723. doi:10.1016/j.compchemeng.2022.107723

Lawson, T., and Blatt, M. R. (2014). Stomatal size, speed, and responsiveness impact on photosynthesis and water use efficiency. *Plant Physiol.* 164, 1556–1570. doi:10.1104/pp.114.237107

Lawson, T., and Vialet-Chabrand, S. (2019). Speedy stomata, photosynthesis and plant water use efficiency. *New Phytol.* 221, 93–98. doi:10.1111/nph.15330

Leuning, R. (1995). A critical appraisal of a combined stomatal-photosynthesis model for c3 plants. *Plant Cell Environ.* 18, 339–355. doi:10.1111/j.1365-3040.1995.tb00370.x

Marengo, J. A., Souza, C. M., Thonicke, K., Burton, C., Halladay, K., Betts, R. A., et al. (2018). Changes in climate and land use over the amazon region: Current and future variability and trends. *Front. Earth Sci. (Lausanne).* 6, 228. doi:10.3389/feart.2018.00228

Martínez-de la Torre, A., Blyth, E. M., and Robinson, E. L. (2019). Evaluation of drydown processes in global land surface and hydrological models using flux tower evapotranspiration. *Water* 11, 356. doi:10.3390/w11020356

Martínez-Vilalta, J., Poyatos, R., Aguadé, D., Retana, J., and Mencuccini, M. (2014). A new look at water transport regulation in plants. *New Phytol.* 204, 105–115. doi:10.1111/nph.12912

Medlyn, B. E., Duursma, R. A., Eamus, D., Ellsworth, D. S., Prentice, I. C., Barton, C. V. M., et al. (2011). Reconciling the optimal and empirical approaches to modelling stomatal conductance. *Glob. Chang. Biol.* 17, 2134–2144. doi:10.1111/j.1365-2486.2010.02375.x

Mercado, L. M., Huntingford, C., Gash, J. H. C., Cox, P. M., and Jogireddy, V. (2007). Improving the representation of radiation interception and photosynthesis for climate model applications. *Tellus B Chem. Phys. Meteorology* 59, 553–565. doi:10.1111/j.1600-0889.2007.00256.x

Park Williams, A., Allen, C. D., Macalady, A. K., Griffin, D., Woodhouse, C. A., Meko, D. M., et al. (2013). Temperature as a potent driver of regional forest drought stress and tree mortality. *Nat. Clim. Chang.* 3, 292–297. doi:10.1038/nclimate1693

Ponce-Campos, G. E., Moran, M. S., Huete, A., Zhang, Y., Bresloff, C., Huxman, T. E., et al. (2013). Ecosystem resilience despite large-scale altered hydroclimatic conditions. *Nature* 494, 349–352. doi:10.1038/nature11836

Powell, T. L., Galbraith, D. R., Christoffersen, B. O., Harper, A., Imbuzeiro, H. M. A., Rowland, L., et al. (2013). Confronting model predictions of carbon fluxes with measurements of amazon forests subjected to experimental drought. *New Phytol.* 200, 350–365. doi:10.1111/nph.12390

Prentice, I. C., Dong, N., Gleason, S. M., Maire, V., and Wright, I. J. (2014). Balancing the costs of carbon gain and water transport: Testing a new theoretical framework for plant functional ecology. *Ecol. Lett.* 17, 82–91. doi:10.1111/ele.12211

Restrepo-Coupe, N., Levine, N. M., Christoffersen, B. O., Albert, L. P., Wu, J., Costa, M. H., et al. (2017). Do dynamic global vegetation models capture the seasonality of carbon fluxes in the amazon basin? A data-model intercomparison. *Glob. Chang. Biol.* 23, 191–208. doi:10.1111/gcb.13442

Sabot, M. E. B., De Kauwe, M. G., Pitman, A. J., Ellsworth, D. S., Medlyn, B. E., Caldararu, S., et al. (2022a). Predicting resilience through the lens of competing adjustments to vegetation function. *Plant, Cell & Environ.* 45, 2744–2761. doi:10.1111/pce.14376

Sabot, M. E. B., De Kauwe, M. G., Pitman, A. J., Medlyn, B. E., Ellsworth, D. S., Martin-StPaul, N. K., et al. (2022b). One stomatal model to rule them all? Toward improved representation of carbon and water exchange in global models. *J. Adv. Model. Earth Syst.* 14, e2021MS002761. doi:10.1029/2021ms002761

Sabot, M. E. B., De Kauwe, M. G., Pitman, A. J., Medlyn, B. E., Verhoef, A., Ukkola, A. M., et al. (2020). Plant profit maximization improves predictions of European forest responses to drought. *New Phytol.* 226, 1638–1655. doi:10.1111/nph.16376

Saleska, S., Da Rocha, H., Huete, A., Nobre, A., Artaxo, P., and Shimabukuro, Y. (2013). Lba-eco cd-32 flux tower network data compilation, brazilian amazon. Version 1. 1999–2006. doi:10.3334/ORNLDAAC/1174

Sellers, P. J., Bounoua, L., Collatz, G. J., Randall, D. A., Dazlich, D. A., Los, S. O., et al. (1996). Comparison of radiative and physiological effects of doubled atmospheric $co_2$ on climate. *Science* 271, 1402–1406. doi:10.1126/science.271.5254.1402

Sitch, S., Huntingford, C., Gedney, N., Levy, P. E., Lomas, M., Piao, S. L., et al. (2008). Evaluation of the terrestrial carbon cycle, future plant geography and climate-carbon cycle feedbacks using five dynamic global vegetation models (dgvms). *Glob. Chang. Biol.* 14, 2015–2039. doi:10.1111/j.1365-2486.2008.01626.x

Sperry, J. S., and Love, D. M. (2015). What plant hydraulics can tell us about responses to climate-change droughts. *New Phytol.* 207, 14–27. doi:10.1111/nph.13354

Sperry, J. S., Venturas, M. D., Anderegg, W. R. L., Mencuccini, M., Mackay, D. S., Wang, Y., et al. (2017). Predicting stomatal responses to the environment from the optimization of photosynthetic gain and hydraulic cost. *Plant, Cell & Environ.* 40, 816–830. doi:10.1111/pce.12852

Tyree, M. T., and Sperry, J. S. (1989). Vulnerability of xylem to cavitation and embolism. *Annu. Rev. Plant Physiol. Plant Mol. Biol.* 40, 19–36. doi:10.1146/annurev.pp.40.060189.000315

Ukkola, A. M., Kauwe, M. G. D., Pitman, A. J., Best, M. J., Abramowitz, G., Haverd, V., et al. (2016). Land surface models systematically overestimate the intensity, duration and magnitude of seasonal-scale evaporative droughts. *Environ. Res. Lett.* 11, 104012. doi:10.1088/1748-9326/11/10/104012

Venturas, M. D., Sperry, J. S., Love, D. M., Frehner, E. H., Allred, M. G., Wang, Y., et al. (2018). A stomatal control model based on optimization of carbon gain versus hydraulic risk predicts aspen sapling responses to drought. *New Phytol.* 220, 836–850. doi:10.1111/nph.15333

Vialet-Chabrand, S. R., Matthews, J. S., McAusland, L., Blatt, M. R., Griffiths, H., and Lawson, T. (2017). Temporal dynamics of stomatal behavior: Modeling and implications for photosynthesis and water use. *Plant Physiol.* 174, 603–613. doi:10.1104/pp.17.00125

Wang, Y., Sperry, J. S., Anderegg, W. R. L., Venturas, M. D., and Trugman, A. T. (2020). A theoretical and empirical assessment of stomatal optimization modeling. *New Phytol.* 227, 311–325. doi:10.1111/nph.16572

Wang, Y., Sperry, J. S., Venturas, M. D., Trugman, A. T., Love, D. M., and Anderegg, W. R. L. (2019). The stomatal response to rising co2 concentration and drought is predicted by a hydraulic trait-based optimization model. *Tree Physiol.* 39, 1416–1427. doi:10.1093/treephys/tpz038

Williams, K. E., Harper, A. B., Huntingford, C., Mercado, L. M., Mathison, C. T., Falloon, P. D., et al. (2018). Revisiting the first islscp field experiment to evaluate water stress in julesv5.0. *Geosci. Model Dev. Discuss.* 1. doi:10.5194/gmd-2018-210

Wolf, A., Anderegg, W. R. L., and Pacala, S. W. (2016). Optimal stomatal behavior with competition for water and risk of hydraulic impairment. *Proc. Natl. Acad. Sci. U. S. A.* 113, E7222–E7230. doi:10.1073/pnas.1615144113

frontiers | Frontiers in Earth Science

TYPE Original Research
PUBLISHED 24 January 2023
DOI 10.3389/feart.2023.1084892



OPEN ACCESS

EDITED BY
Yan Li,
Beijing Normal University, China

REVIEWED BY
Liang Chen,
University of Nebraska-Lincoln, United States
Ying Xu,
National Climate Center, China

*CORRESPONDENCE
Xing Li,
lx_cuit@163.com

SPECIALTY SECTION
This article was submitted to Interdisciplinary Climate Studies, a section of the journal Frontiers in Earth Science

RECEIVED 31 October 2022
ACCEPTED 09 January 2023
PUBLISHED 24 January 2023

CITATION
Li X, Li X, Hua W, Ma H, Zhou J and Pang X (2023), Modeling the effects of present-day irrigation on temperature extremes over China.
*Front. Earth Sci.* 11:1084892.
doi: 10.3389/feart.2023.1084892



# Modeling the effects of present-day irrigation on temperature extremes over China

Xiao Li[1,2], Xing Li[1]*, Wenjian Hua[2], Hedi Ma[3], Juan Zhou[1] and Xueqi Pang[4]

[1]Plateau Atmosphere and Environment Key Laboratory of Sichuan Province, College of Atmospheric Science, Chengdu University of Information Technology, Chengdu, China, [2]Key Laboratory of Meteorological Disaster, Ministry of Education (KLME)/Joint International Research Laboratory of Climate and Environment Change (ILCEC)/Collaborative Innovation Center on Forecast and Evaluation of Meteorological Disasters (CIC-FEMD), Nanjing University of Information Science and Technology, Nanjing, China, [3]Hubei Key Laboratory for Heavy Rain Monitoring and Warning Research, Institute of Heavy Rain, Wuhan, China, [4]Department of Atmospheric and Oceanic Sciences, Fudan University, Shanghai, China

Irrigation activities have been recognized as one of the most potentially sustainable land management practices to tackle climate change. In this study, we investigated the impacts of present-day irrigation activities on regional temperature extremes changes in China using the state-of-the-art regional climate model RegCM-4.8.2, through two sets of long-term numerical experiments (i.e., with and without irrigation). The key findings are as follows. Firstly, by comparing the observations, RegCM4 has a good ability to reproduce both the spatial distribution and the volume of irrigation for provincial irrigation activities in China. In this context, by comparing the results of numerical experiments, we found that irrigation led to significant reductions (slightly changes) in the extreme indices associated with the warm (cold) tails of the maximum and minimum temperatures distributions, e.g., hot days, tropical nights (cold nights, frost days), particularly in the regions with intense irrigation (e.g., the North China Plain). Furthermore, these extreme indices were dominated by irrigation-induced shifts in mean temperatures, but the impacts of changes in temperature variability on extreme hot events were also non-negligible for the strongly irrigated regions. In addition, through attributing irrigation-induced changes in mean state temperatures, we revealed that the irrigation-induced repartitioning of the surface turbulent heat fluxes (i.e., sensible and latent heat) dominated the variations of temperatures and the associated extremes. However, region-specific land-atmosphere coupling features also led to differences in the irrigation-induced responses of surface energy components. We highlight the possible effects and mechanisms of irrigation on multiple types of extreme temperature indices, particularly the extreme hot events, which provide scientific clues for mitigating and adapting regional climate change.

KEYWORDS

**irrigation, RegCM, numerical modeling, temperature extremes, China**

## 1 Introduction

Human activities have unequivocally caused climate change in every region across the globe (IPCC, 2021). According to the Special Report on Climate Change and Land (SRCCL) from the Intergovernmental Panel on Climate Change (IPCC) sixth assessment cycle, more than 70% of the global ice-free land surface, particularly most of the highly productive land area, has been directly exploited by humans (IPCC, 2019). Such intensive anthropogenic land use has led to extensive alteration of natural ecosystems - known as land use and cover change (LUCC). On

the one hand, LUCC could influence local-regional-global climate through biogeophysical and biogeochemical mechanisms (e.g., Mahmood et al., 2014; Ward et al., 2014; Bright, 2015; Li et al., 2017; Winckler et al., 2017; Li et al., 2018; Xu et al., 2022). On the other hand, over-exploitation of land resources would also negatively affect ecosystems (e.g., land degradation) and the services they provide (e.g., Arneth et al., 2019). Hence, in a context of finite Earth's land area, the sustainable use of land resources (i.e., sustainable land management, SLM) is a crucial pathway to addressing complex land use-derived issues (e.g., United Nations General Assembly, 2015).

A variety of SLM approaches are available to mitigate climate change, including forest management (e.g., extending rotation cycles), cropland management (e.g., irrigation), grazing land management (e.g., deep rooting grasses), etc (Smith et al., 2014). Conducting SLM to counter the negative effects of intensive land use activities is only one side of the coin; it is also necessary to consider whether these actions will in turn have impacts on climate change through land-atmosphere interactions. A growing number of studies have focused on the climate effects of the potential land management changes (LMC; Davin et al., 2014; Erb et al., 2017; Hirsch et al., 2017; Thiery et al., 2017; Seneviratne et al., 2018). These studies have largely come to the similar conclusion that several types of LMC (e.g., irrigation) can cause impacts on climate comparable to LUCC (e.g., Luyssaert et al., 2014; Singh et al., 2018; Chen and Dirmeyer, 2020; De Hertog et al., 2022). Of these LMC practices, irrigation is probably the one that could have the greatest impact on climate due to its direct influence on surface hydrology through water withdrawals (e.g., Sacks et al., 2009; Thiery et al., 2017; Chen and Dirmeyer, 2019; Mishra et al., 2020; Thiery et al., 2020; Gormley-Gallagher et al., 2022). Irrigation activities are mainly concentrated in regions with a high density of cropland, such as China, India and North America. Previous observational and modeling studies have shown that irrigation could exert significant influences on multiscale local-regional-global climate, mainly by affecting the repartition of surface turbulent heat fluxes, soil moisture and the coupling strength of land-atmosphere interactions (e.g., Guimberteau et al., 2012; Alter et al., 2015; de Vrese et al., 2016; Lu et al., 2017; Nocco et al., 2019; Yang et al., 2020). For example, Alter et al. (2015) highlighted that irrigation caused inhibitions (enhancements) to local (remote) precipitation over East Africa, which was probably due to its influence on surface thermal conditions and hence changes in atmospheric circulation. Guimberteau et al. (2012) modeled the impact of irrigation on climate and demonstrated that irrigation could significantly delay the onset of the Indian summer monsoon by 6 days with a corresponding decrease in precipitation during May-July. Sacks et al. (2009) modeled the global climate effects of irrigation and found that irrigation had a negligible effect on the global mean near-surface temperature, but at regional scales its effects were comparable to the magnitude of the LUCC forcing. Furthermore, the Land Use Model Comparison Project (LUMIP), a sub-project of the Coupled Model Comparison Project Phase 6 (CMIP6), also included irrigation as one of the important forcing factors for multi-model comparisons and simulations (Lawrence et al., 2016). However, compared to the coarse-resolution global-scale numerical simulations, it is more informative to explore the irrigation effects on regional climate using finer regional weather and climate models since irrigation activity is primarily a regional-scale forcing. And yet, there are many other aspects of irrigation impacts and mechanisms on regional climate that are largely uncertain (e.g., de Vrese and Hagemann, 2018).

China is one of the largest agricultural countries in the world. According to the National Bureau of Statistics of China, the irrigated area of cropland in China was ~69,600 thousand hectares at the end of 2021. Focusing on irrigation effects in China, in addition to irrigation activities affecting the mean climate state such as temperature and precipitation, their impacts on extreme weather and climate events, especially heat wave events, have received much attention in recent years (e.g., Kang and Eltahir, 2018; Wu et al., 2021). For instance, Kang and Eltahir (2018) highlighted that while irrigation activities could cool the surface, the concurrent increase in air moisture made the risk of deadly heat waves associated with wet-bulb temperatures significantly higher, especially under the high-emission scenario (i.e., RCP 8.5). Yet, for such a massive volume of irrigation activities in China, its impact on climate, especially on climate extremes, as well as the related mechanisms were often explained in terms of mean-state shifts alone (e.g., Chen and Dirmeyer, 2019). According to the IPCC special report, changes in extreme temperatures can be linked not only to the temperature mean-state shifts, but also to changes in the shape of probability distributions (i.e., changes in temperature higher order moments, e.g., variance; IPCC, 2012). However, whether the effects of irrigation on temperature extremes are dominated by the mean-state shifts or changes in higher moments of temperature, as well as what the relevant mechanisms are, remain largely unclear and require detailed explorations for further understandings. Meanwhile, a realistic irrigation scheme in the model is also critical to improve the confidence in simulating the effects of irrigation on climate extremes. In contrast to some previous regional modeling studies that used idealized forced saturation soil (e.g., Kang and Eltahir, 2018), selecting a more realistic representation of irrigation in the model is also necessary. Based on these considerations, this paper used state-of-the-art regional climate model with the realistic irrigation scheme to explore the impacts and mechanisms of present-day irrigation on temperature extremes in China, focusing on two main aspects: 1) How significant is the impact of irrigation on multiple types (e.g., absolute changes, persistent features changes, and thresholds-related changes) of temperature extremes 2) What are the main causes (i.e., is the mean-state shift or temperature variability change dominant?) and physical mechanisms underlying the irrigation effects on temperature extremes?

# 2 Methodology

## 2.1 Model and experimental design

### 2.1.1 Regional climate model

We use version 4.8.2 of the Regional Climate Model (RegCM) developed by the International Centre for Theoretical Physics (ICTP), one of the world's most popular limited area models for studying regional climate change (Giorgi et al., 2012). First developed by Dickinson et al. (1989) and Giorgi and Bates (1989), the RegCM model has been evolved over decades and the state-of-the-art RegCM4 has been widely used in refined regional climate simulations in the world. For East Asia in particular, the RegCM4 model has been broadly used for climate predictions (e.g., Gu et al., 2012), projections (e.g., Xie et al., 2021) and studying land cover changes effects (e.g., Chen et al., 2015; Li et al., 2022), aerosol impacts (e.g., Sun et al., 2012), etc., due to its good ability to reproduce regional weather and climate (e.g., Ji and Kang, 2015).

Studying the effects of irrigation on climate requires a detailed description and consideration of irrigation in the land surface parameterization of the regional model. Previous numerical simulation studies have generally taken two approaches to conduct irrigation activities. One is the idealized maximum irrigation scenario, which directly sets soil moisture to field capacity and saturated conditions (e.g., Kueppers and Snyder, 2012). The other is an observed or realistic irrigation scenario, i.e., applying observed irrigation amounts into the model (e.g., Sacks et al., 2009; Zeng et al., 2017b), or irrigating using soil moisture deficits as irrigation intensity based on the daily meteorological conditions (Ozdogan et al., 2010; Yang et al., 2016; Wu et al., 2018; Liu et al., 2021). Clearly, it is more appropriate and informative to select a more realistic irrigation approach in the model to assess the realistic impacts of irrigation on extreme events than the former (i.e., the idealized maximum irrigation approach). For this reason, the Community Land Model version 4.5 (CLM4.5) was chosen as the land surface component of RegCM4 (Oleson et al., 2013). The CLM4.5 model is the land surface component of the National Center for Atmospheric Research (NCAR) Community Earth System Model (CESM) and is one of the most advanced land surface models. In the CLM4.5 model, there are two main considerations when addressing irrigation: on the one hand, when irrigation is enabled, the default plant function types (PFT) of cropland is refined into eight extra rainfed and irrigated crops, and irrigation is valid only for the soil beneath irrigated crops; on the other hand, for the intensity of irrigation, the CLM4.5 irrigation algorithm can determine the amount of irrigation per day based on the soil moisture deficits that takes into account the current atmospheric conditions. The separation of rainfed and irrigated crop are based on a dataset of areas equipped for irrigation (AEI; Portmann et al., 2010). The soil moisture deficits ($w_{deficit}$) are calculated as follows:

$$\begin{cases} w_{target,i} = (1-0.7)\cdot w_{o,i} + 0.7 w_{sat,i} \\ w_{deficit} = \sum_i \max\left(w_{target,i} - w_{liq,i}, 0\right) \end{cases} \quad (1)$$

Where $w_{target,i}$ is the target soil moisture content in each soil layer $i$, $w_{o,i}$ is the minimum soil moisture content that results in no water stress in soil layer $i$, $w_{sat,i}$ is the soil moisture content at saturation in soil layer $i$ and $w_{liq,i}$ is the current soil water content of layer $i$. Ultimately, the amount of irrigation water withdraw is then equal to $w_{deficit}$. The advantage of this algorithm for processing irrigation is that it can determine whether and how much to irrigate depending on atmospheric conditions, i.e., it considers the irrigation-atmosphere interactions. The full descriptions of the irrigation scheme can be found on the technique notes of CLM4.5 (Chapter 20.3; Oleson et al., 2013) and will not be detailed here. Thus, by coupling CLM4.5 with RegCM4, the advantages of CLM4.5 in terms of fine-scale descriptions of land surface processes can be fully integrated, making it possible to study the effects of irrigation on climate extremes using the high-resolution regional climate model.

### 2.1.2 Experimental design

The RegCM4 is configured at a 25 km resolution and the simulated domain is set with reference to the East Asia domain of the Coordinated Regional Downscaling Experiment (CORDEX) Phase II. The domain center of the simulations is located at (35°N, 116°E) with a total of 280 (north-south) × 428 (east-west) grid points, described by the rotated Mercator projection. The simulated domain and the AEI over China can be found on Figure 1A. The atmospheric boundary conditions were selected from the European Center for Medium-Range Weather Forecasts (ECMWF) interim 6-hourly atmospheric reanalysis (Dee et al., 2011) and the ocean boundary conditions were selected from the Hadley Centre HadISST monthly sea surface temperature data. We selected MM5 hydrostatic dynamic core with a 23 level-$\sigma$ coordinate (top at 50 hPa) as the dynamical configuration. The parameterization schemes were chosen as follows: convective parameterization scheme - MIT-Emanuel (Emanuel and Živković-Rothman, 1999), planetary boundary layer scheme - Modified Holtslag (Holtslag et al., 1990), explicit moisture scheme - SUBEX (Pal et al., 2000), radiation scheme - Modified CCM3 (Kiehl et al., 1996), ocean flux scheme - Zeng et al. (1998) and land surface scheme - CLM4.5 (Oleson et al., 2013). The above parameterization schemes have been chosen because they have been proven in numerous studies to be the "best" combination of parameterization schemes for modeling the East Asian climate (e.g., Han et al., 2015; Gao et al., 2016). Based on the above configurations, two sets of experiments were conducted: one with irrigation activated (IRR) and the other without irrigation (CTL). Note that in the IRR experiments, only irrigation activity within China was turned on, irrigation activity in other areas within the simulated boundary outside China (e.g., India) remained closed (i.e., the same as CTL).

In order to turn on irrigation in RegCM4, the fully interactive crop management model (CROP) with carbon-nitrogen (CN) interactions in CLM4.5 required to be activated. As the biogeochemical cycle also turned on with CN, we first need to generate the initial conditions of the land surface biochemical equilibrium state for the RegCM4. We therefore performed an offline cold start of CLM4.5 with CROP and CN on, following the procedure in the CLM4.5 User's Guide regarding spinning up the CLM4.5 biogeochemistry, details can be found on https://www2.cesm.ucar.edu/models/cesm1.2/clm/models/lnd/clm/doc/UsersGuide/x12544.html. We integrated the CLM4.5 spinup simulation for a total of 1,200 years, including 1,000 years of accelerated decomposition spinup and 200 years of normal spinup, which driven by CRUNCEP data cycled in a loop, at a resolution of 0.5° × 0.5° (Viovy, 2018). Finally, we used the "interpinic" tool of CLM4.5 to interpolate the restart file of the last year of the CLM4.5 spinup to the RegCM4 resolution as the equilibrium state initial condition of the land surface for driving the RegCM4. To further minimize the uncertainty arising from errors in the interpolation of the initial fields generated by the offline CLM4.5 to the RegCM4 resolution, we also carried out an additional 4 years of spinup when conducting irrigation experiments (i.e., IRR and CTL). Specifically, both IRR and CTL were integrated from 1 January 1980 to 31 December 2013. The years 1980–1983 were the RegCM4 spinup phase and were not involved in the subsequent analyses. In addition, for the IRR experiment, three additional ensemble simulations (noted as IRR1, IRR2 and IRR3, respectively) with random perturbations (i.e., add or remove up to 1/10,000th of the boundary conditions) in the atmospheric boundary conditions (i.e., perturb atmospheric temperature, relative humidity and specific humidity, respectively) were carried out with reference to O'Brien et al. (2011). All results shown in the subsequent sections are ensemble averages of the four IRR realizations compared to the CTL experiment; Figure 1B shows the simulation results for the ensemble-averaged climate-state total irrigation amounts (TIAs). It is clear that irrigation in China is concentrated in three regions, namely the North China Plain (NCP), the Yangtze River Basin (YRB) as well as the western

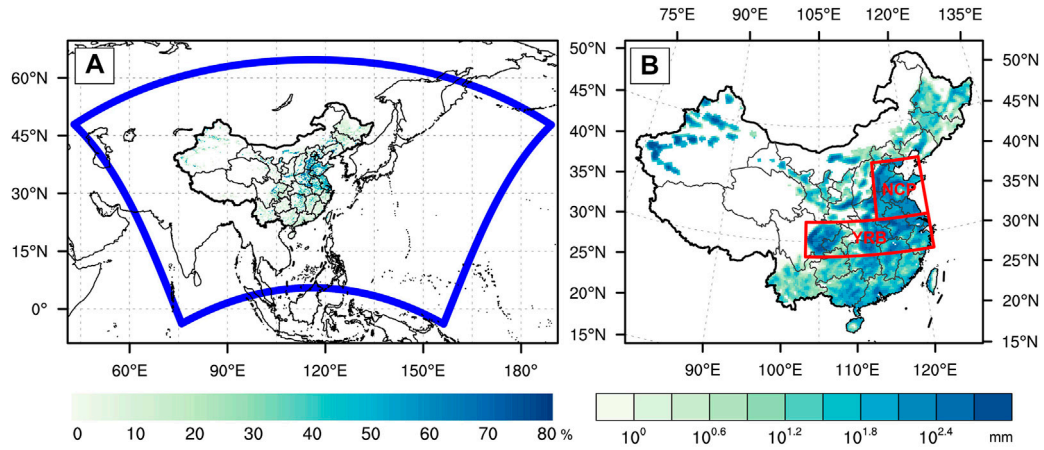


FIGURE 1
The simulation domain of the RegCM and the inputdata of areas equipped for irrigation over China, units: % **(A)** and the simulated ensemble mean of annual total irrigation amounts over China, units: mm **(B)**. Note that the thick blue lines in **(A)** are the boundaries of the domain, the red boxes in **(B)** represent areas of interest with intense irrigation activities. "NCP" for the North China Plain (32.5–40 °N, 114–122 °E) and "YRB" for the Yangtze River Basin (28–32.5 °N, 103–122 °E).

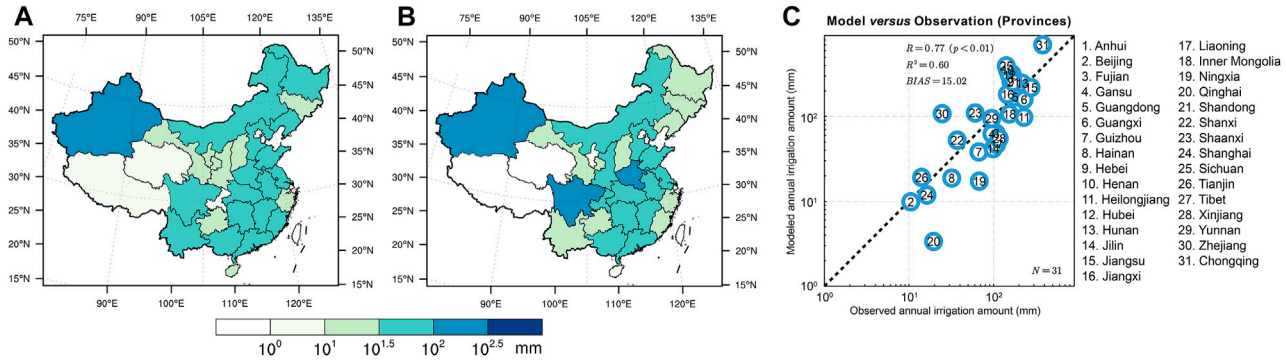


FIGURE 2
Comparison of observed and modeled multi-year average annual irrigation amount (units: mm) at the provincial scale: **(A)** observed values; **(B)** modeled values; **(C)** scatter plot of observed *versus* modeled irrigation. Note that the *R*, $R^2$, *BIAS* and *N* in **(C)** represent the correlation, R-Squared, absolute error and the number of data involved, respectively. The numbers in the hollow points in **(C)** represent the different provinces (see the list on the right side of (c)).

part of Xinjiang province, with the annual TIAs varying from $10^2$~$10^3$ mm (Figure 1B). Note that while the western irrigated regions (i.e., Xinjiang province) have comparable irrigation intensity compared to the eastern ones (i.e., NCP and YRB), the extent of western irrigation activities is sporadic, implying that irrigation effects in the west may reflect more of a local response. Therefore, in the following sections, we will mainly focus on the NCP and YRB regions as examples for more detailed analyses.

## 2.2 Validation of the simulated irrigation

The ability of the model to accurately simulate TIAs is an important basis for the confidence of modeling results for temperature extremes changes. Although CLM4.5 provides a more realistic treatment of irrigation, it is also necessary to validate that whether the TIAs simulated by the model match the observed magnitudes. Hence, we first compare the TIAs simulated by RegCM4 *versus* the observations. Note that the most reliable irrigation data for China is only available at the provincial scale. We obtained the TIAs from 1997 to 2013 by multiplying the total irrigated area from the China Statistical Yearbook (http://www.stats.gov.cn/tjsj/ndsj/) and the water use per mu of irrigated farmland (i.e., irrigation water use intensity) from the China Water Resources Bulletin (http://www.mwr.gov.cn/sj/tjgb/szygb/). A comparison between observed and simulated multiyear average TIAs is shown in Figure 2. Overall, the RegCM4 model well reproduces the observed spatial distribution of provincial TIAs (Figures 2A,B). In terms of TIAs at the provincial level, the observed annual TIAs are widely distributed across the eastern China, with magnitudes mainly in the range of $10^1$–$10^2$ mm. For western China, irrigation is mostly concentrated in Xinjiang province, where annual TIAs can reach $10^2$–$10^{2.5}$ mm. The simulated annual TIAs generally reproduce the observed distribution reasonably well, with widespread (concentrated) irrigation activities in eastern (western) China. Specifically, the modeled TIAs are slightly overestimated (underestimated) in Sichuan and Henan provinces

(northeastern China), and generally match the observed magnitudes in the other provinces (Figure 2B). Moreover, we also calculated the regression of simulated TIAs *versus* observed TIAs for the provinces of China, as shown in Figure 2C. For the 31 Chinese provinces, the provincial-level comparisons generally show relatively high correlations ($R = 0.77$) and $R$-squares ($R^2 = 0.60$), but also non-negligible biases ($BIAS = 15.02\,mm$; Figure 2C). It should be noted that the default AEI data of the model (i.e., from Portmann et al., 2010) and the observed total irrigated area (i.e., from the China Water Resources Bulletin) used to calculate the TIAs are two different data sources, so the biases in the modeled TIAs may also originate from the inconsistencies between the different AEI data. In summary, it is clear from the above results that RegCM4-CLM4.5 has a reasonable and good ability to reproduce the observed climatological patterns of annual TIAs, which provides a good basis for exploring the climatic impacts of irrigation with the model.

## 2.3 Temperature extremes indices

In order to fully quantify the impact of irrigation on temperature extremes, multiple types (e.g., intensity and duration) of extreme indices need to be selected. Following the recommendations of the World Meteorological Organization, 15 extreme temperature indices were selected from the CCl/WCRP/JCOMM Joint Expert Group on Climate Change Detection and Indices (ETCCDI), as shown in Table 1. These extreme temperature indices cover the characteristics of extreme temperatures in absolute values, thresholds, persistent events and percentiles, which is the most widely used set of extreme indices in the study of extreme climate change (e.g.; Zhang et al., 2011; Donat et al., 2013; Dunn et al., 2020). The definitions of these indices can be found on http://etccdi.pacificclimate.org/list_27_indices.shtml or Table 1.

## 2.4 The decomposed temperature metric

The surface energy budget (SEB)-based decomposed temperature metric (DTM) was introduced to investigate the mechanisms by which irrigation affects temperature extremes. The DTM has been widely used in attributing land surface processes-induced changes in temperatures (e.g., Juang et al., 2007; Luyssaert et al., 2014; Chen and Dirmeyer, 2016; Li et al., 2017). This method begins with the surface energy balance equation:

$$SR_{net} + LR_{down} - LR_{up} = SH + LH + G \tag{2}$$

where $SR_{net}$, $LR_{down}$, $LR_{up}$, $SH$, $LH$ and $G$ denote net shortwave radiation, downward longwave radiation, upward longwave radiation, sensible heat flux, latent heat flux and ground heat flux into the soil, respectively. The $SR_{net}$ can be further divided into upward ($SR_{up}$) and downward shortwave radiation ($SR_{down}$), respectively (i.e., $SR_{net} = SR_{down} - SR_{up}$). By introducing the Taylor expansion and Stefan Boltzmann's law, and retaining only the first order approximation, Equation 2 can be transformed into:

$$\Delta T_{rs} = \frac{1}{4}\sigma^{-1/4} \cdot \overline{LR_{up}}^{3/4} \cdot (\Delta SR_{net} + \Delta LR_{down} - \Delta SH - \Delta LH - \Delta G) + \varepsilon \tag{3}$$

$T_{rs}$ is the surface radiative temperature, $\sigma$ is the Stefan Boltzmann constant (i.e., $\sigma = 5.6704 \times 10^{-8}\,W/m^2 \cdot K$) and the symbols associated with radiation and turbulence fluxes are consistent with the previous ones. "Δ" indicates the difference between the IRR and the CTL experiments (i.e., the effect of irrigation), and "overbar" indicates the climate mean state of the variables in the CTL experiments. $\varepsilon$ denotes the error of DTM (i.e., the difference between the simulated $\Delta T_s$ and the calculated $\Delta T_{rs}$). Thus, by using Equation 3, we can attribute the effect of irrigation on temperature to the individual SEB components (i.e., $SR_{net}$, $LR_{down}$, $SH$, $LH$ and $G$) and thus uncover the mechanism by which irrigation affects temperatures. The detailed derivation process of DTM can be found in Juang et al. (2007) and in the appendix of Li et al. (2017).

## 2.5 Other methods

In addition to the above methods, some regular statistical methods (e.g., probability density functions and linear regression) are not repeated here. We chose the modified Student's $t$-test (Zwiers and von Storch, 1995) to determine whether the differences between IRR and CTL experiments were statistically significant (at the 90% confidence level). For the ensemble mean results, we first determine whether the difference between each paired simulation (e.g., IRR1 *versus* CTL) is significant (at the 90% confidence level). Then, we define the robustness of the ensemble mean results in terms of inter-sample consistency as follows. For the ensemble mean results at any grid point, we define the consistency as "significant" when all four realizations are statistically significant at the 90% confidence level and the responses have the same sign. We define consistency as "strong" ("moderate") when three (two) of the four realizations are statistically significant at the 90% confidence level and the responses have the same sign. We define consistency as "weak" ("insignificant") when only one (none) of the four realizations are statistically significant at the 90% confidence level. In addition, we introduced the two legged land-atmosphere coupling metrics (i.e., terrestrial leg—the coupling between soil moisture and latent heat and atmospheric leg—the coupling between sensible heat and planetary boundary layer height) to measure the coupling strength, details can be found in Dirmeyer (2011).

# 3 Results

## 3.1 Irrigation-induced changes in mean temperatures

Before exploring the effect of irrigation on the extreme temperature indices, we first examine the response of mean maximum and minimum temperatures to irrigation, which are closely related to changes in extreme temperature events, as shown in Figure 3. In terms of land surface temperatures, irrigation causes significant decreases in the annual mean maximum land surface temperature (*Tsmax*) mostly over the NCP, the YRB and parts of Xinjiang province, ranging from −0.6°C to more than −1.2°C (Figure 3A). For the minimum land surface temperature (*Tsmin*), irrigation also causes a significant reduction in annual mean *Tsmin*, but the magnitude is much weaker (approximately −0.2 to −0.6°C) in comparison to the cooling of *Tsmax* (Figure 3B). Moreover, comparing *Tsmax* and *Tsmin* we can observe that their responses have more distinct regional features, in addition to their different

**TABLE 1 Definitions of 15 ETCCDI temperature extremes.**

| Index | Descriptive name | Definition | Unit |
|---|---|---|---|
| | | Absolute indices | |
| TXx | Hottest day | Annual maximum value of daily maximum temperature | ˚C |
| TXn | Coolest day | Annual minimum value of daily maximum temperature | ˚C |
| TNx | Warmest night | Annual maximum value of daily minimum temperature | ˚C |
| TNn | Coldest night | Annual minimum value of daily minimum temperature | ˚C |
| | | Percentile-based indices | |
| TX90p | Hot days | Percentage of days in a year when daily maximum temperature >90th percentile | % |
| TX10p | Cool days | Percentage of days in a year when daily maximum temperature <10th percentile | % |
| TN90p | Warm nights | Percentage of days in a year when daily minimum temperature >90th percentile | % |
| TN10p | Cold nights | Percentage of days in a year when daily minimum temperature <10th percentile | % |
| | | Threshold-based indices | |
| SU | Summer days | Annual count of days when daily maximum temperature >25 ˚C | Days |
| TR | Tropical nights | Annual count of days when daily minimum temperature >20 ˚C | Days |
| FD | Frost days | Annual count of days when daily minimum temperature <0 ˚C | Days |
| ID | Ice days | Annual count of days when daily maximum temperature <0 ˚C | Days |
| | | Duration indices | |
| CSDI | Cold spell duration | Annual count of days with at least 6 consecutive days when daily minimum temperature <10th percentile | Days |
| WSDI | Warm spell duration | Annual count of days with at least 6 consecutive days when daily maximum temperature >90th percentile | Days |
| GSL | Growing season length | Annual count between first span of at least 6 days with daily mean temperature >5 ˚C and first span after July 1st of 6 days with daily mean temperature <5 ˚C | Days |





10.3389/feart.2023.1084892

10.3389/feart.2023.1084892

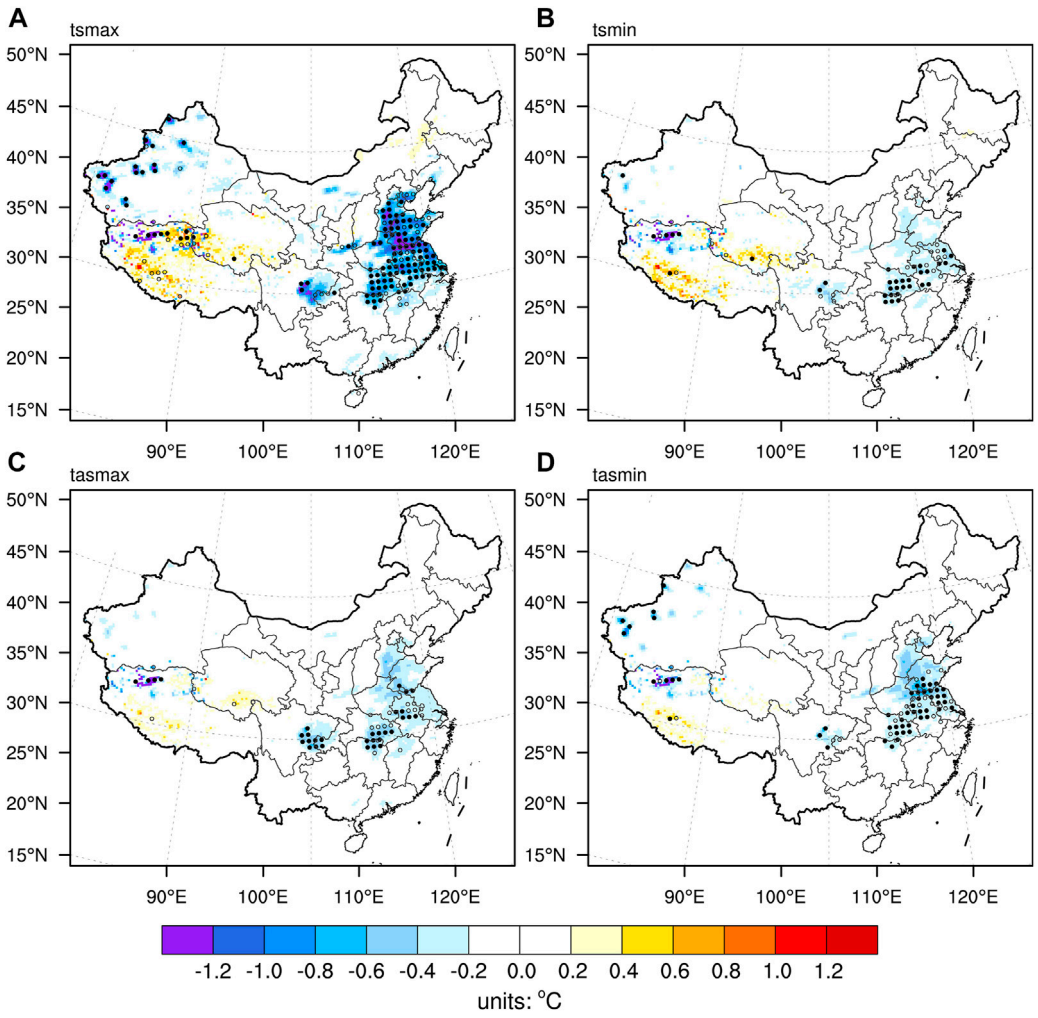


FIGURE 3
Irrigation-induced changes in annual mean surface temperature variables (units: °C): **(A)** maximum land surface temperature (*Tsmax*), **(B)** minimum land surface temperature (*Tsmin*), **(C)** maximum 2 m air temperature (*Tmax*) and **(D)** minimum 2 m air temperature (*Tmin*). Note that the solid (hollow) black dots in the figures indicate a greater than "strong" ("moderate") degree of consistency among the results of the ensemble members (i.e., statistically significant changes at the 90% confidence level are observed for 3 (2) out of four simulation pairs).

magnitudes of coolings. For example, irrigation-induced *Tsmax* cools more strongly in the NCP than in the YRB, but the opposite is true for *Tsmin* (i.e., the response of *Tsmin* is stronger in the YRB than in the NCP; Figure 3A *versus* Figure 3B). This implies that the effect of irrigation on temperatures are likely to be region-specific. For air temperatures, irrigation generally has much smaller effects on them than on the land surface temperatures (Figures 3C, D). In detail, both maximum and minimum air temperatures show cooling responses to irrigation of no more than −0.6°C, with significant cooling detected only in parts of the YRB (Figures 3C, D). Additionally, unlike the irrigation-induced distinct responses of *Tsmax* and *Tsmin*, the coolings of maximum and minimum air temperatures (refer to *Tmax* and *Tmin*, respectively) to the irrigation exhibited almost identical (Figures 3A, B *versus* Figures 3C, D). Overall, irrigation causes the surface temperature variables to be cooled and the areas of significant coolings closely correspond to those of intense irrigations (Figure 1B), suggesting that the effects of irrigation on temperatures are mainly exhibited by the local cooling responses.

## 3.2 Irrigation-induced changes in absolute indices

With the above brief impression of the mean temperatures changes, we start to investigate the changes in the extreme temperature indices caused by irrigation. Firstly, we show the changes in the annual maximum (minimum) values of the multiyear average daily maximum (minimum) temperature (short for TXx, TXn, TNx and TNn, respectively) due to irrigation, as shown in Figure 4. It is clear that the irrigation-induced changes in TXx resemble very closely to those of the mean maximum temperatures (i.e., *Tsmax* and *Tmax*; Figures 4A *versus* 3A, C). In detail, irrigation also causes strong and significant coolings in the NCP and YRB regions (−0.9 ~ −1.8°C), which are much stronger than the coolings in both *Tsmax* (no more than −1.2°C) and *Tmax* (no more than −0.6°C; Figure 4A). The changes of TNx induced by irrigation are similar to that of TXx, but the coolings are weaker (−0.6 ~ −1.2°C; Figure 4C), which also matches the above-mentioned changes in mean minimum

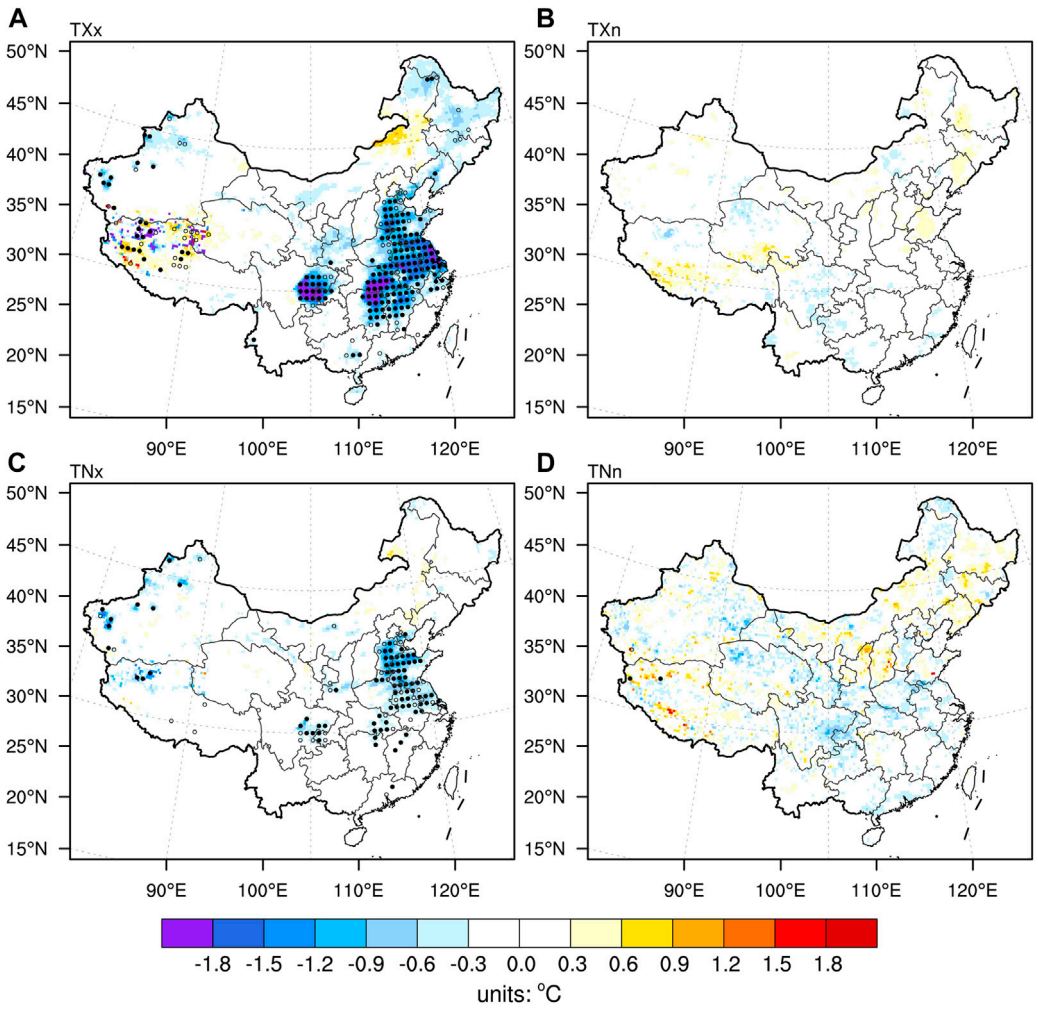


FIGURE 4
Irrigation-induced changes in multiyear mean absolute indices (units: °C): **(A)** annual maximum value of daily maximum temperature (TXx), **(B)** annual minimum value of daily maximum temperature (TXn), **(C)** annual maximum value of daily minimum temperature (TNx) and **(D)** annual minimum value of daily minimum temperature (TNn). The meanings of solid and hollow dots are the same as Figure 3.

temperatures (Figures 3C, D). In addition, for TXn and TNn, irrigation causes very little changes nationally, both in the magnitudes (no more than ±0.6 °C) and the significances (Figures 4B, D). It is also worth noting that there are much stronger coolings in maximum values (i.e., TXx and TNx) than in minimum values (i.e., TXn and TNn) of temperatures. This also implies that irrigation not only affected changes in the temperatures mean state, but may also have caused obvious changes in the higher order moments of temperatures (e.g., variance). Similar findings regarding the non-negligible role of changes in high order moments of temperatures have also been highlighted in other studies (e.g., Li et al., 2017; Li et al., 2018).

## 3.3 Irrigation-induced changes in percentile-based indices

Figure 5 shows the irrigation-induced changes in percentile-based extreme temperature indices (i.e., hot days, cool days, warm nights and cold nights; show for TX90p, TX10p, TN90p and TN10p, respectively). Obviously, dominated by the changes in mean maximum and minimum temperatures, the four percentile-based extreme indices in response to irrigation also show similar patterns as the above-mentioned absolute indices changes (Figures 5 *versus* Figure 4). Specifically, for extreme warm events, changes in hot days (i.e., TX90p) and warm nights (i.e., TN90p) are very consistent with the corresponding mean temperatures changes, namely significant reductions in warm events ranging from −2.4% to −4.8% for the NCP, YRB and parts of Xinjiang province (Figures 5A, C). For extreme cold events, cool days (i.e., TX10p) and cold nights (i.e., TN10p) respond differently to irrigation. In detail, TX10p overall exhibits almost no changes to irrigation nationally, with slight and insignificant changes over parts of the Tibet, which probably due to the internal noise of the model (Figure 5B). The TN10p, on the other hand, shows a moderate increase (~1.6%–3.2%) over the NCP region, but with a weak significance. Theoretically, if irrigation only causes a shift of the mean temperature, the changes in extreme cold and warm events should be exactly opposite (i.e., increases (decreases) in cold events

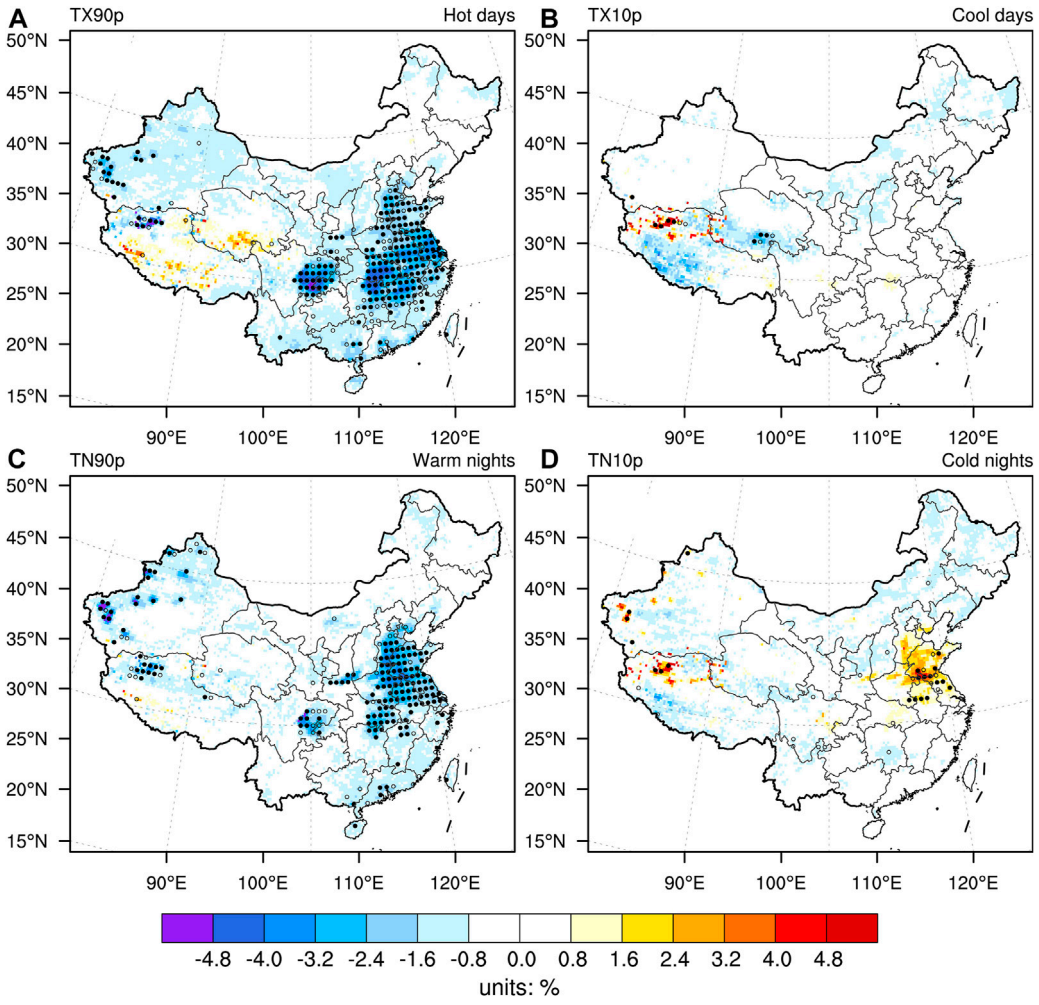


FIGURE 5
Same as Figure 4, but for percentile-based indices (units: %): **(A)** hot days (TX90p), **(B)** cool days (TX10p), **(C)** warm nights (TN90p) and **(D)** cold nights (TN10p). The meanings of solid and hollow dots are the same as Figure 3.

corresponds to decreases (increases) in warm events). Therefore, it can be inferred from the above results that for the maximum temperature-related extremes the indices (e.g., TXx, TXn, TX90p and TX10p) were probably influenced by both mean state and variability changes, while the minimum temperature-related extremes (i.e., TNx, TNn, TN90p and TN10p) show more of a mean temperature-dominated feature.

## 3.4 Irrigation-induced changes in other extreme temperature indices

In addition to changes in absolute indices and percentile-based indices of temperature extremes, we also investigate irrigation-induced changes in threshold-based indices (Figure S1) and duration indices (Figure S2). As expected, the threshold-based extreme temperature indices and the duration indices also show variations primarily corresponding to shifts in the mean-state maximum and minimum temperatures over the irrigated areas (Figures S1-S2 *versus* Figure 3). These can be briefly summarized in three points: 1) During the daytime, irrigation caused robust coolings (reductions) of surface temperatures (the warm tail-related extreme indices; e.g., TXx and TX90p) at the local-to-regional scale; 2) During the nighttime, the effects of irrigation on surface temperatures and the associated changes in extreme indices were relatively weak; 3) Synthetically, the variations in maximum and minimum temperatures and their associated extreme indices were largely influenced by the mean state shifts, but the irrigation-induced changes in the temperature variability (i.e., moments of temperature other than mean changes) may be equally important to temperature extremes for some regions (e.g., NCP and YRB).

To further confirm the role of irrigation-induced changes in temperature variability over the NCP and YRB regions, we calculated the probability density function (PDF) of the regional average land surface temperatures (i.e., *Tsmax* and *Tsmin*) in each simulation, as shown in Figure 6. Note that the we used daily temperatures anomalies to calculate PDFs in each experiment, which means the climatological annual cycle (based on the CTL experiment) was removed. Overall, the PDFs of *Tsmax* for both NCP and YRB regions indeed show not only robust left shifts of the distribution positions, but also the concurrent narrows of the distribution shapes (Figures 6A, B). This implies significant coolings of the mean state of *Tsmax* (i.e., −0.890°C for NCP and −0.572°C for

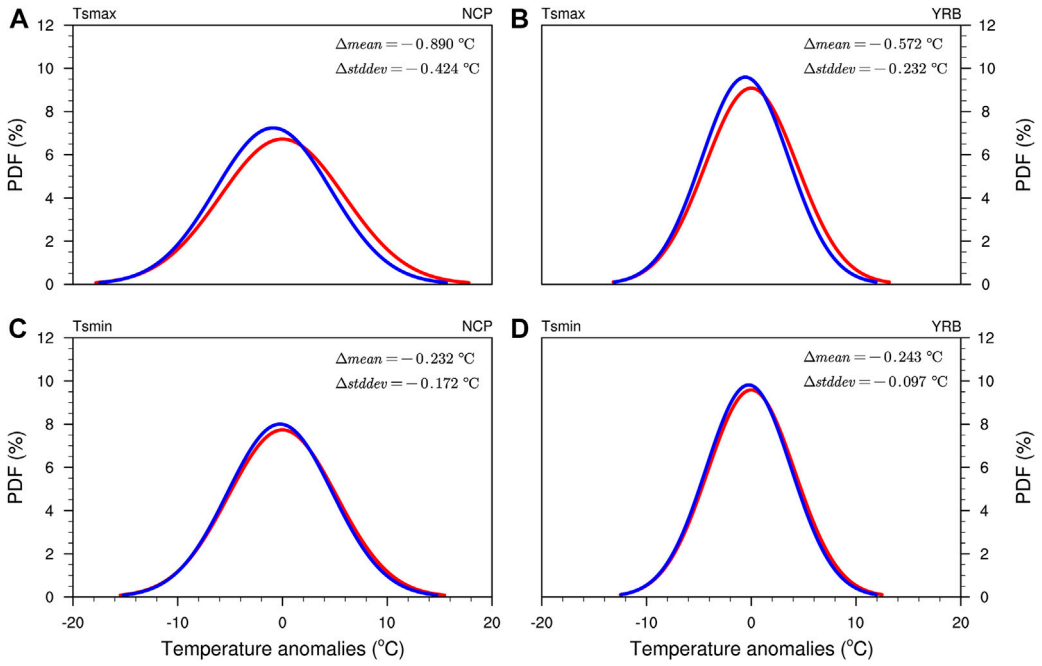


FIGURE 6
The Gaussian fitted probability density function (PDF) of land surface temperatures for CTL (red) and IRR (blue) experiments: **(A)** *Tsmax* in NCP; **(B)** *Tsmax* in YRB; **(C)** *Tsmin* in NCP and **(D)** *Tsmin* in YRB. Note that the Δ*mean* and Δ*stddev* denote the irrigation-induced changes in the mean state and standard deviation of temperatures.

YRB) and considerable reductions in its variability (e.g., the standard deviations of *Tsmax* reduce −0.424 and −0.232°C for NCP and YRB, respectively). The results of PDFs of *Tsmax* are fully consistent with the previous results (i.e., Figures 3–5, Supplementary Figures S1, S2). Consequently, we can clearly observe that for both the YRB and NCP regions, the cold tail of *Tsmax* remains almost unchanged, but the warm tail undergoes a more robust cooling than the mean state cooling. For the PDFs of *Tsmin*, there are distinct responses detected for both NCP and YRB compared to *Tsmax* (Figures 6C, D *versus* 6A, B). Specifically, we can only observe very slight leftward shifts and narrowings in the PDFs of *Tsmin* for the two regions, which also corresponds to their spatially weak performances (i.e., −0.232°C mean state cooling for NCP and −0.243°C for YRB). In summary, the modeled irrigation primarily resulted in coolings in the mean state of *Tsmax* and *Tsmin* as well as the changes of the related temperature extremes indices. However, specifically for *Tsmax*, the modeled irrigation also had non-negligible effects on the asymmetric responses of the cold and warm tails of the temperature PDFs in the NCP and YRB regions.

## 3.5 Possible mechanisms of irrigation-induced extreme temperatures changes

From the previous modeling results, we found that irrigation caused robust reductions of the warm tail-related extreme indices (e.g., TXx and TX90p), which mainly related to the mean *Tsmax* and *Tsmin* coolings. Why did irrigation cause such changes in temperatures and associated extreme indices? We next attempt to interpret the changes in extreme indices by diagnosing the mechanisms of changes in mean *Tsmax* and *Tsmin*. Previous studies have demonstrated that irrigation, as a climate-efficient form of land management, could have significant impacts on regional climate by modulating the surface energy budget and the land-atmosphere interactions (e.g., Douglas et al., 2009; Qian et al., 2013). We therefore introduced the widely used decomposed temperature metric (DTM) to explore and quantify the biogeophysical mechanisms of irrigation on *Tsmax*/*Tsmin* and associated extreme indices. Figures 7, 8 show the contributions of changes in each irrigation-induced SEB component to the variation of mean *Tsmax* and *Tsmin*. Note that we select the values of the SEB components at 06 (18) UTC for the inputs of Eq. 3 to match the time at which *Tsmax* (*Tsmin*) generally occurs. We start with the DTM diagnostic results for *Tsmax*.

Firstly, we focus on the contributions of changes in the radiation components (i.e., $SR_{down}$, $SR_{up}$ and $LR_{down}$) due to irrigation to the *Tsmax* (i.e., Figures 7A–C). It is clear that irrigation generally caused no significant changes in the three radiation components (i.e., $SR_{down}$, $SR_{up}$ and $LR_{down}$). In particular, irrigation induces very weak changes in the $SR_{down}$ and $LR_{down}$, which in turn leads to little change in temperature (within ±0.3°C). The $SR_{down}$ and $LR_{down}$ changes due to irrigation generally correlate with changes in cloudiness, which also suggests that the effect of irrigation on cloudiness may not be robust at the annual mean scale in our modeling results. In addition, we can observe that $SR_{up}$ are reduced in a few parts of both the NCP and YRB, which would further increase the net solar radiation received at the surface (Figure 7B). The net increase in shortwave radiation may be due to a slight decrease in surface albedo, which is caused by irrigation-induced wet soils being darker than dry soils. As a result, moderate (~0.6°C) but less significant warmings induced by $SR_{up}$ are detected

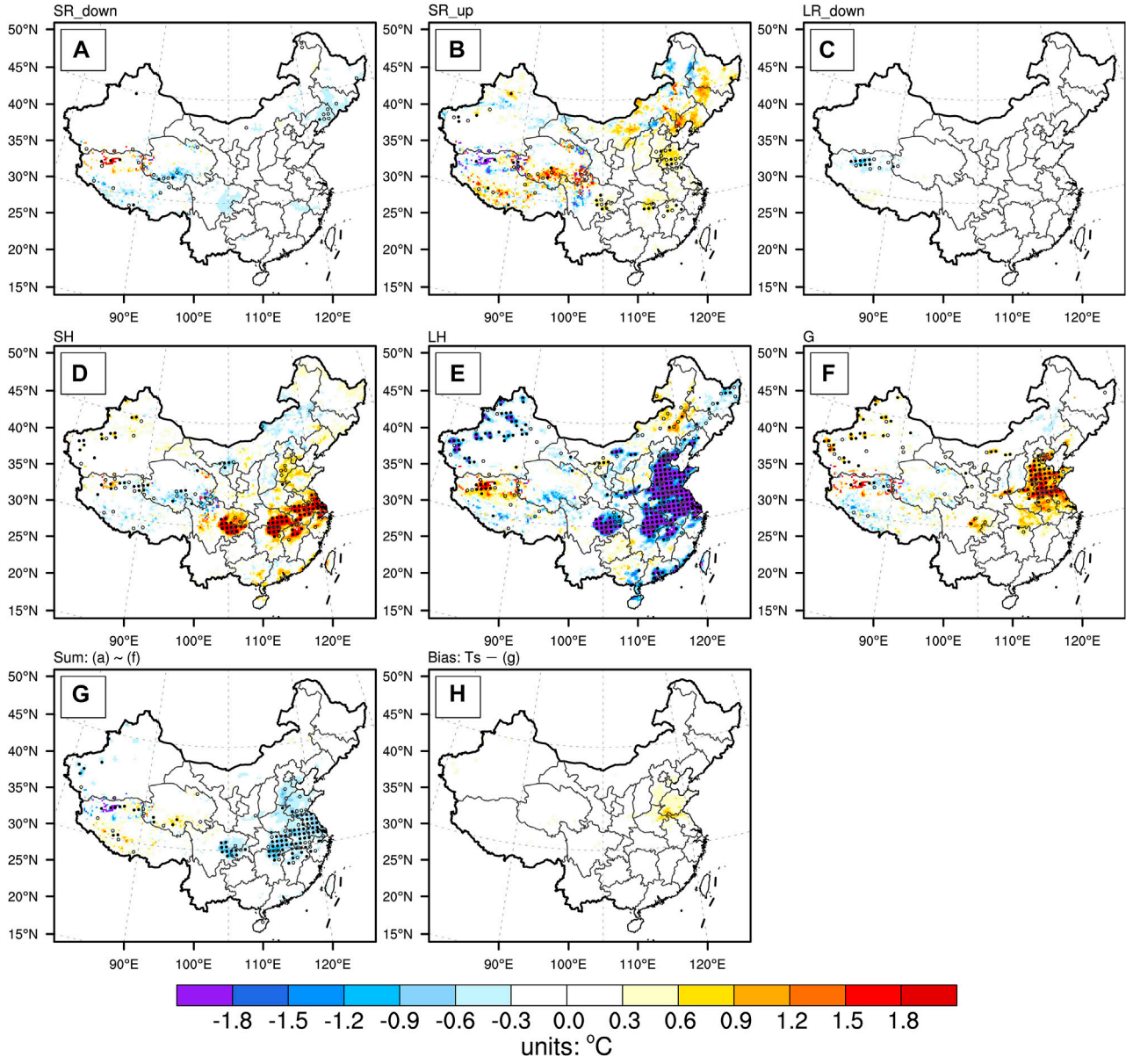


FIGURE 7
Ensemble mean results of the irrigation-induced multiyear mean changes in daytime (06 UTC) surface temperature due to changes in the surface energy budget components: **(A)** downward shortwave radiation, **(B)** upward shortwave radiation, **(C)** downward longwave radiation, **(D)** sensible heat flux, **(E)** latent heat flux, **(F)** ground heat flux, **(G)** sum of **(A–F)** and **(H)** errors of the decomposed temperature metric (i.e., simulated land surface temperature minus **(G)**), units: °C. The meanings of solid and hollow dots are the same as Figure 3.

over few parts of the YRB and NCP (Figure 7B). The effect of irrigation on the non-radiative components (i.e., *SH*, *LH* and *G*) is much stronger than the variation in the radiative components, which results in a significant repartition of non-radiative heat fluxes (Figures 7D–F). In general, the responses of all three non-radiative components (i.e., *SH*, *LH* and *G*) to irrigation are strong and significant over the irrigated areas (e.g., NCP and YRB), but significant regional differences in their patterns are also detected. Specifically, irrigation mainly leads to robust reductions (increases) in sensible and ground heat fluxes (latent heat flux) locally in the irrigated areas, which in turn leads to evident warmings (coolings) of more than 1.8°C (−1.8°C) of the land surface. However, focusing on the main irrigated areas, a comparison of the NCP and YRB reveals a clear difference in irrigation-induced non-radiative heat repartition between these two regions. More specifically, as irrigation tends to increase surface moisture, turbulent heat fluxes show a greater partitioning towards *LH* in both YRB and NCP regions. What's different is that, in the YRB region, the warming caused by the significant reduction in *SH* partly counterbalances the cooling effect of the significant increase in *LH*, and the turbulent repartition caused by irrigation is mainly reflected in a combined variation of the two. In contrast, for the NCP region, the irrigation-induced increases in *LH* are not accompanied by corresponding decreases in *SH*, but ultimately manifests as increases in the ground heat flux into the soil (i.e., downward) to balance the changes in the other SEB components. Consequently, this leads to

10.3389/feart.2023.1084892

significant *G*-induced warmings that partially offsets the coolings of *LH* (Figures 7E, F). Combining the changes in the radiative and non-radiative components, the accumulated results ultimately show an irrigation-induced *LH*-dominated locally significant cooling effect (Figure 7G). In addition, we calculated the bias of the SEB-based land surface temperature changes (i.e., Figure 7G) from the simulated daytime land surface temperature changes (i.e., Figure 3A), as shown in Figure 7H. It is clear that the bias of the SEB method is very small, showing a warm bias of around 0.3 °C only in parts of the NCP, and around 0 in all other regions (Figure 7H). This indicates that SEB can well decompose the variation in irrigation-induced *Tsmax*.

At night, the effect of irrigation on the SEB components is much weaker than during the day, which is probably related to the fact that CLM4.5 describes the moment when irrigation activity takes place as being in the morning (Oleson et al., 2013). Specifically, irrigation barely changes the nighttime radiation components (i.e., $SR_{down}$, $SR_{up}$ and $LR_{down}$) and thus the magnitudes of its effect on nighttime surface temperature through radiative effects are generally zero (Figures 8A–C). For the changes of the non-radiative components, the change in *LH* is almost zero probably because there is no irrigation activity at night (Figure 8E). However, for the NCP region, the anomalous *G* stored in the soil during the day could probably be released into the air at night with the diurnal cycle. This may lead to a significant enhancement of nighttime *G*-induced air warming accompanied by surface cooling (Figure 8F). In addition, the enhanced diurnal cycle of *G* caused by irrigation may simultaneously weaken the ground-air temperature difference (Supplementary Figures S3) at night, thus tending to reduce the

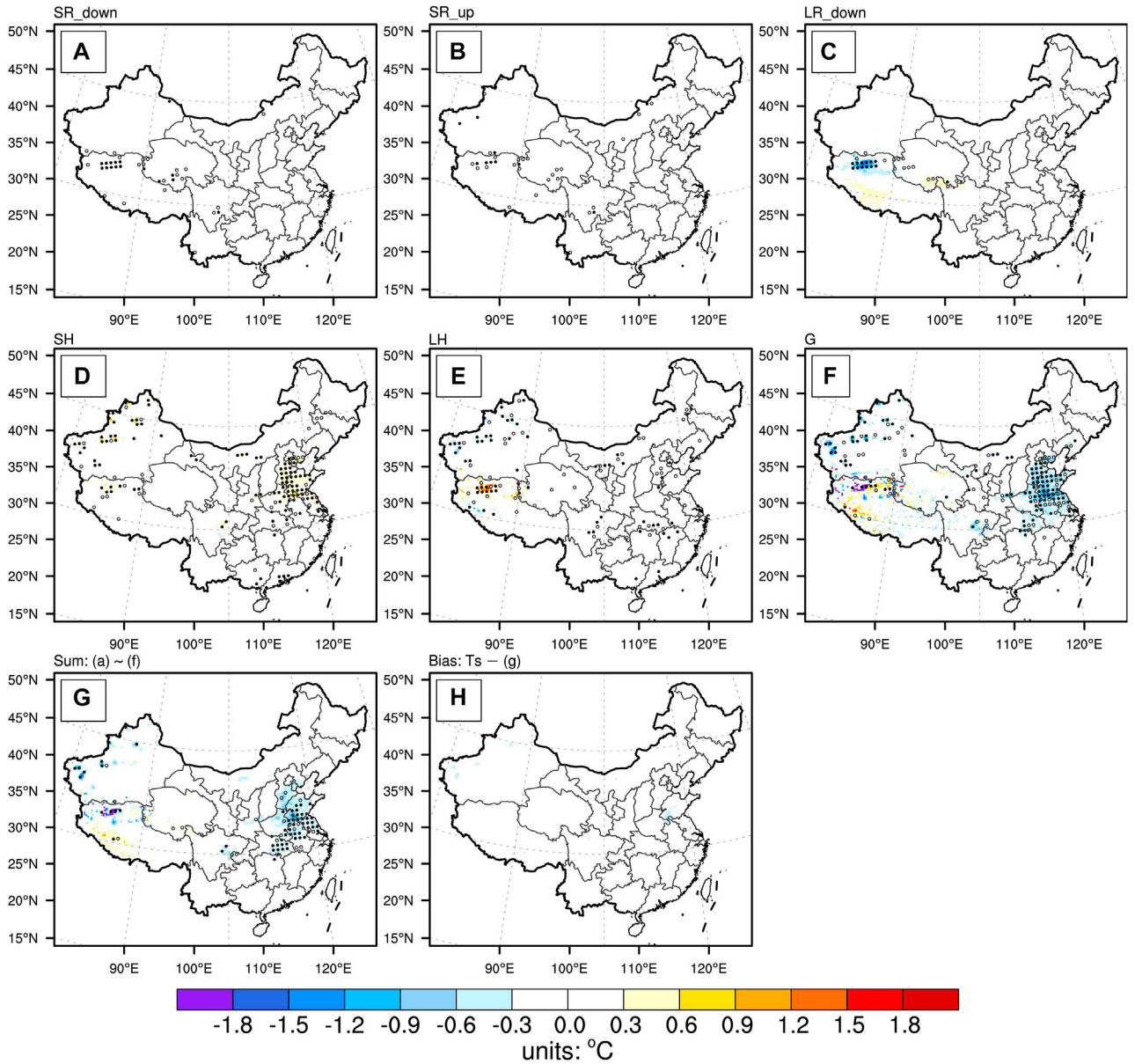


FIGURE 8
Ensemble mean results of the irrigation-induced multiyear mean changes in nighttime (18 UTC) surface temperature due to changes in the surface energy budget components: **(A)** downward shortwave radiation, **(B)** upward shortwave radiation, **(C)** downward longwave radiation, **(D)** sensible heat flux, **(E)** latent heat flux, **(F)** ground heat flux, **(G)** sum of **(A–F)** and **(H)** errors of the decomposed temperature metric [i.e., simulated land surface temperature minus **(G)**], units: °C. The meanings of solid and hollow dots are the same as Figure 3.

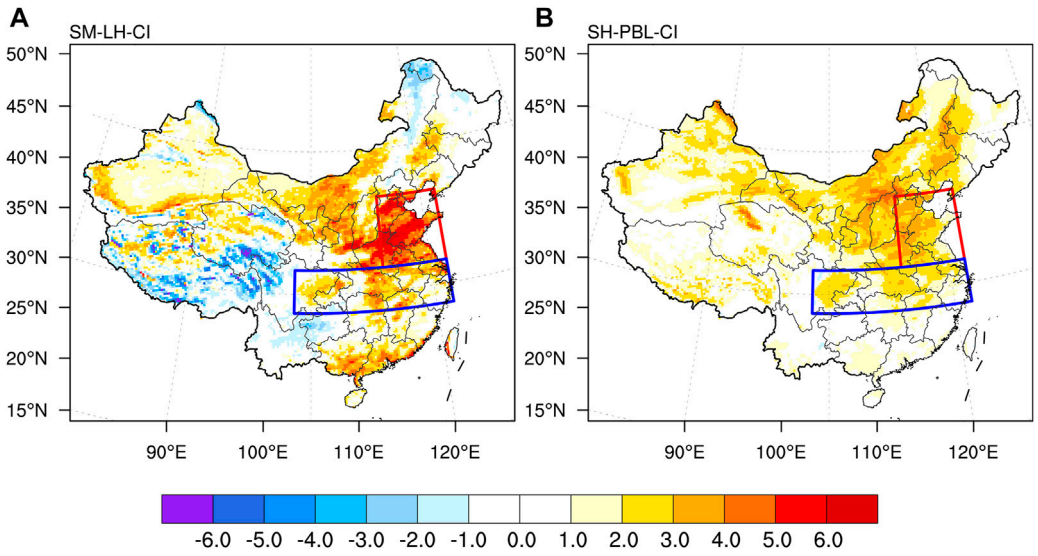


FIGURE 9
The climatology features of land-atmosphere coupling strength in the CTL experiment calculated using the "two legged" land-atmosphere coupling metric: **(A)** terrestrial coupling indices (i.e., the coupling between soil moisture and latent heat), units: W $m^{-2}$ and **(B)** atmospheric coupling indices (i.e., the coupling between sensible heat and planetary boundary layer height), units: $10^1$ W $m^{-2}$. Note that the red and blue boxes in the figure represent NCP (32.5–40 °N, 114–122 °E) and YRB (28–32.5 °N, 103–122 °E) regions, respectively.

nighttime sensible heat, which may also cause surface warmings (Figure 8D). In contrast, for the YRB region, all non-radiative heat fluxes respond weakly to irrigation and therefore the change in *Tsmin* is slight (Figures 8D–F). From these results we can conclude that the weak cooling at night induced by irrigation is probably caused by the persistence of daytime *G* anomalies through the diurnal cycle into the night. The regional differences of SEB responses at night are also closely related to the specific irrigation-induced repartitioning effects during the day. In addition, the role of *G* in the diurnal cycle of temperatures as well as the corresponding temperature extremes changes has been highlighted in other studies of land surface processes (e.g., Li et al., 2017).

# 4 Discussions

In the previous section we modeled the effects and possible mechanisms of present-day irrigation on a wide range of extreme indices. We found significant decreases (almost no change) in the extreme indices associated with the warm (cold) tail of the probability density function of temperatures, e.g., TXx, TX90p (TNn, TX10p). In addition to the above results, there are several caveats and uncertainties that need to be specifically stated.

## 4.1 Possible causes of the region-specific differences in SEB responses

Why did these two areas (i.e., NCP and YRB) have similar irrigation intensities (Figures 1, 2) and temperatures responses (Figure 3), but responded so differently regarding SEB components? We can interpret this in terms of region-specific land-atmosphere coupling features. According to Budyko's classical hydrological framework, we can distinguish the geographically dependent evapotranspiration regimes by the soil moisture-limited or energy-limited regimes (e.g., Seneviratne et al., 2010). The different regimes and their transition zones are all subject to very different land-atmosphere interactions. For instance, Koster et al. (2004) and Seneviratne et al. (2006) highlighted the critical role of soil moisture on evapotranspiration variability in the wet-dry transitional zone than in the too wet or too dry climate regimes. Take the YRB (i.e., a humid region) for example, soil moisture is generally at a high level because of more adequate precipitation. While irrigation activities over YRB, although adding additional water to the soil, would probably result in a much lower rate of soil moisture variations than those caused by precipitation. It is also suggested that moist terrestrial surface is not sensitive to the changes in soil moisture. Thus, the repartition effect caused by irrigation in the YRB region reflects both increases in *LH* and decreases in *SH*. Conversely, for the NCP region, which is a wet-dry transition zone in terms of climatological states, it exhibits a soil moisture-limited regime. As a result, changes in evapotranspiration in the NCP region are very sensitive to soil moisture. What this causes is that the irrigation-induced reparation effect of turbulent heat in the NCP region is absolutely dominated by strong increases in *LH* alone. The above-mentioned possible mechanisms are probably the main reason why similar irrigation activities produced different SEB responses in the two regions. To confirm the above speculations, we have also calculated the land-atmosphere coupling strength (LACS) in the CTL experiment using the "two legged" coupling metric, as shown in Figure 9. As we suspected, the LACS (shown in both terrestrial and atmospheric legs) in the NCP region are indeed significantly stronger than in the YRB region. This suggests that region-specific land-atmosphere coupling features can modulate the effects of irrigation, which in turn leads to different responses in SEB components and temperatures. In addition, although the differences in the repartition

effects of *LH* and *SH* between the two regions (i.e., NCP and YRB) were substantial, it was *G* that ultimately served as the counterbalance to the combined effects of the two turbulent heat fluxes (i.e., *SH* and *LH*). Due to the counterbalance of *G*, there is ultimately little difference between NCP and YRB regarding temperature responses. In conclusion, we can infer from our results that the different responses of the SEB in the YRB and NCP regions are probably due to different climatic states (i.e., land-atmosphere coupling) in specific regions.

## 4.2 Uncertainties

We have modeled present-day irrigation activities affecting temperature extremes *via* numerical simulations, which means that all of our results for irrigation impacts are entirely dependent on the ability of the model itself to describe weather, climate and their complex interactions. Although the outstanding modeling capabilities of the RegCM4 have been demonstrated from the previous validation results (i.e., Section 2.2) and previous studies (e.g., Ji and Kang, 2015), some uncertainties remain.

First, these uncertainties arise mainly from the data driving the model, the single-model simulations and the combination of the selected physical processes of the model. Each of the above points could affect not only the irrigation itself, but also key physical processes (e.g., land-atmosphere coupling strength) that may be directly or indirectly related to climate and extremes changes. (e.g., Bonan et al., 2011; Du et al., 2016; Jach et al., 2022). For instance, the default AEI data (i.e., Portmann et al., 2010) reflected monthly irrigated and rainfed crop areas around the year 2000, which was relatively out-of-date and would introduce uncertainties when assessing the present-day irrigation effects. In future studies, it is necessary to use more accurate and up-to-date data to conduct multi-model ensemble simulations with various combinations of initial and boundary conditions, parameterization schemes in order to better assess irrigation-induced climate extremes changes.

Second, the simulated irrigation activity is entirely dependent on the CLM4.5 parameterization scheme - the irrigation it describes may differ significantly from the actual irrigation activity. Overall, the representations of irrigation activities have several shortcomings in the model. The first is the source of the water withdraw for irrigation, which can come from either the surface or the underground. However, the irrigation parameterization scheme of RegCM4-CLM4.5 did not account for groundwater and surface water-groundwater interactions. It has been highlighted that irrigation activities based on different water sources have completely opposite effects on the regional hydrological changes caused by climate change (e.g., Leng et al., 2015). Therefore, irrigation water sources may be critical for regional climate extremes changes and need to be considered in future studies. The second consideration is the method of irrigation. In CLM 4.5, irrigation was done through surface irrigation only, with water withdrawal applied directly to the land surface (bypassing canopy interception). With the development of technology, in addition to the common method of surface irrigation, there are sprinkler irrigation, drip irrigation and compound irrigation systems. Each type of irrigation has considerable differences in the treatments of eco-hydrology processes, which could in turn potentially lead to distinct impacts on regional climate, water and food supplies (e.g., Wang et al., 2020; Fu et al., 2022). As a result, this may introduce uncertainties into the corresponding simulated changes in temperature extremes, which should also be involved in the future modeling studies. In addition to the above, the timing of irrigation, the control of irrigation amounts and the interaction between irrigation and vegetation are also of great importance for the regional climate change (e.g., Lobell et al., 2009; Sacks et al., 2009; Wu et al., 2018). These are key processes that are not (or fixed) in the simulations, but should be refined and represented.

In addition, we have only investigated the effect of irrigation on annual-scale temperature extremes based on the modeling results, which only reflects a small aspect of the irrigation effects on extreme weather and climate events. In fact, the impacts of irrigation on extreme events are much broader and more complex. Other studies have highlighted that the irrigation could also significantly affect precipitation extremes, compound temperature-humidity extremes and compound hydrological extremes (e.g., Kang and Eltahir, 2018; de Vrese and Stacke, 2020; Ambika and Mishra, 2021). And the human socio-ecological-economic consequences of changes in these compound extreme events are often catastrophic and therefore should require more attentions. Moreover, Zeng et al. (2017a) revealed that irrigation had distinct influences on turbulent and carbon fluxes over the northwestern China. Hence, the irrigation-induced changes seasonal-scale or monthly-scale climate extremes should be further investigated. In conclusion, in addition to the current study, further attention needs to be paid to the impact and mechanisms of irrigation on a broader range of extreme events (e.g., compound extreme events) and regions (e.g., Xinjiang province).

# 5 Conclusion

In this study, the modeling effects and mechanisms of present-day irrigation activities on temperature extremes in China are investigated using the state-of-the-art regional climate model (i.e., RegCM4-CLM4.5) coupled with a dynamic and realistic irrigation parameterization scheme. By analyzing two groups of comparative experiments, namely with and without irrigation, regarding changes in multiple extreme temperature indices, we obtained the following conclusions:

The RegCM4 coupled CLM4.5 model could reproduce the annual mean TIAs well. By comparing the provincial-scale observations, RegCM4 could generally simulate the primary regions and magnitudes of irrigation activities in China. That is, irrigation in China mainly occurred in the NCP, YRB and parts of Xinjiang province, and the annual averaged TIAs are ranging from $10^2$ to $10^3$ mm.

By comparing the results of comparative experiments with and without irrigation, it was found that the irrigation activities in China could significantly reduce the extreme temperature indices associated with the PDFs warm tails of the maximum and minimum temperatures (e.g., TXx, TN90p, TR and WSDI) in the NCP and YRB regions. However, for the cold tails, the extreme temperature indices associated with the cold tails of the maximum temperature (e.g., TX10p) remained largely unchanged, while the cold-tail extreme indices associated with the minimum temperature (e.g., TNn) were relatively similar to the changes in their warm-tail indices. Further investigations revealed that the responses of extreme indices associated with maximum and minimum temperatures to irrigation were largely dominated by mean-state changes, but the changes in temperature variability (e.g., variance) were also non-negligible in areas of intense irrigation activities (i.e., NCP and YRB).

The decomposition of the mean changes in daytime temperature (i.e., *Tsmax*) showed that irrigation caused a significant decrease (cooling) in the relevant extreme temperature indices mainly through the repartitioning of turbulent heat fluxes (i.e., *SH* and *LH*). However, there were also specific regional differences in the repartitioning of *SH* and *LH*, which either showed an absolute dominance of *LH* enhancement due to irrigation-induced moisture increases (e.g., in the NCP region) or comparable redistribution of *SH* and *LH* (e.g., in the YRB region). Ultimately, the changes (i.e., repartitioning of *SH* and *LH*) were counterbalanced in the form of *G*, making coolings similar in both regions. At night, the *G* stored in the soil during the day continued to influence nighttime surface and air temperature changes as the diurnal cycle progresses, but the magnitudes of the changes of surface energy components, temperatures and extreme indices were all slight. In addition, region-specific differences may be dominated by different land-atmosphere coupling processes (i.e., the water-limited regime or the energy-limited regime) dominating.

Overall, irrigation activities, as one of the most important SLM approaches, also require the use of multi-regional/earth system models and experiments to increase confidence in relevant assessments and mechanisms, and provide more informed scientific clues for policymakers.

## Data availability statement

The ERA-interim and HadISST data used for running the model can be obtained from https://apps.ecmwf.int/datasets/data/interim-fulldaily/levtype=pl/ and https://www.metoffice.gov.uk/hadobs/hadisst/data/download.html, respectively. The source code of the latest release of RegCM can be obtained from https://github.com/ICTP/RegCM/. The raw data supporting the conclusions of this article will be made available by the authors, without undue reservation.

## Author contributions

All authors contributed to the study conception and design. Material preparation, data collection and analysis were performed by XoL, XP, and JZ. The first draft of the manuscript was written by XoL and XgL. WH, HM, XoL and XgL wrote sections of the manuscript. All authors contributed to manuscript revision, read and approved the submitted version.

## Funding

This study was jointly supported by the National Natural Science Foundation of China (41905080, 41905065 and 42075022), the Scientific Research Foundation of CUIT (KYTZ202124, KYTZ202123, KYQN202201), the Joint Open Project of KLME and CIC-FEMD, NUIST (KLME202002, KLME20220001) and the National Natural Science Foundation of Jiangsu Province (BK20200096).

## Acknowledgments

We acknowledge all the innovation platforms at Chengdu University of Information Technology for providing the necessary research conditions for this study. We also acknowledge the Climpact software (see www.climpact-sci.org) for calculating climate indices used in this study.

## Conflict of interest

The authors declare that the research was conducted in the absence of any commercial or financial relationships that could be construed as a potential conflict of interest.

## Publisher's note



## Supplementary material

The Supplementary Material for this article can be found online at: https://www.frontiersin.org/articles/10.3389/feart.2023.1084892/full#supplementary-material

## References

Alter, R. E., Im, E.-S., and Eltahir, E. A. B. (2015). Rainfall consistently enhanced around the Gezira Scheme in East Africa due to irrigation. *Nat. Geosci.* 8, 763–767. doi:10.1038/ngeo2514

Ambika, A. K., and Mishra, V. (2021). Modulation of compound extremes of low soil moisture and high vapor pressure deficit by irrigation in India. *J. Geophys. Res. Atmos.* 126, e2021JD034529. doi:10.1029/2021JD034529

Arneth, A., Denton, F., Agus, F., Elbehri, A., Erb, K., Osman Elasha, B., et al. (2019). "Framing and context," in *Climate change and land: An IPCC special report on climate change, desertification, land degradation, sustainable land management, food security, and greenhouse gas fluxes in terrestrial ecosystems*. Editors P. R. Shukla, J. Skea, E. Calvo Buendia, V. Masson-Delmotte, H.-O. Pörtner, D. C. Roberts, et al. In press. Available at: https://www.ipcc.ch/site/assets/uploads/sites/4/2019/12/04_Chapter-1.pdf (Accessed Oct 17, 2022).

Bonan, G. B., Lawrence, P. J., Oleson, K. W., Levis, S., Jung, M., Reichstein, M., et al. (2011). Improving canopy processes in the Community Land Model version 4 (CLM4) using global flux fields empirically inferred from FLUXNET data. *J. Geophys. Res. Biogeosciences* 116, G02014. doi:10.1029/2010JG001593

Bright, R. M. (2015). Metrics for biogeophysical climate forcings from land use and land cover changes and their inclusion in life cycle assessment: A critical review. *Environ. Sci. Technol.* 49, 3291–3303. doi:10.1021/es505465t

Chen, H., Li, X., and Hua, W. (2015). Numerical simulation of the impact of land use/land cover change over China on regional climates during the last 20 years. *Chin. J. Atmos. Sci.* 39, 357–369. (in Chinese). doi:10.3878/j.issn.1006-9895.1404.14114

Chen, L., and Dirmeyer, P. A. (2016). Adapting observationally based metrics of biogeophysical feedbacks from land cover/land use change to climate modeling. *Environ. Res. Lett.* 11, 034002. doi:10.1088/1748-9326/11/3/034002

Chen, L., and Dirmeyer, P. A. (2020). Distinct impacts of land use and land management on summer temperatures. *Front. Earth Sci.* 8, 245. doi:10.3389/feart.2020.00245

Chen, L., and Dirmeyer, P. A. (2019). Global observed and modelled impacts of irrigation on surface temperature. *Int. J. Climatol.* 39, 2587–2600. doi:10.1002/joc.5973

Davin, E. L., Seneviratne, S. I., Ciais, P., Olioso, A., and Wang, T. (2014). Preferential cooling of hot extremes from cropland albedo management. *Proc. Natl. Acad. Sci.* 111, 9757–9761. doi:10.1073/pnas.1317323111

De Hertog, S. J., Havermann, F., Vanderkelen, I., Guo, S., Luo, F., Manola, I., et al. (2022). The biogeophysical effects of idealized land cover and land management changes in Earth system models. *Earth Syst. Dyn.* 13, 1305–1350. doi:10.5194/esd-13-1305-2022

De Vrese, P., Hagemann, S., and Claussen, M. (2016). Asian irrigation, African rain: Remote impacts of irrigation. *Geophys. Res. Lett.* 43, 3737–3745. doi:10.1002/2016GL068146

De Vrese, P., and Hagemann, S. (2018). Uncertainties in modelling the climate impact of irrigation. *Clim. Dyn.* 51, 2023–2038. doi:10.1007/s00382-017-3996-z

De Vrese, P., and Stacke, T. (2020). Irrigation and hydrometeorological extremes. *Clim. Dyn.* 55, 1521–1537. doi:10.1007/s00382-020-05337-9

Dee, D. P., Uppala, S. M., Simmons, A. J., Berrisford, P., Poli, P., Kobayashi, S., et al. (2011). The ERA-interim reanalysis: Configuration and performance of the data assimilation system. *Q. J. R. Meteorological Soc.* 137, 553–597. doi:10.1002/qj.828

Dickinson, R. E., Errico, R. M., Giorgi, F., and Bates, G. T. (1989). A regional climate model for the Western United States. *Clim. Change* 15, 383–422. doi:10.1007/BF00240465

Dirmeyer, P. A. (2011). The terrestrial segment of soil moisture–climate coupling. *Geophys. Res. Lett.* 38, L16702. doi:10.1029/2011GL048268

Donat, M. G., Alexander, L. V., Yang, H., Durre, I., Vose, R., Dunn, R. J. H., et al. (2013). Updated analyses of temperature and precipitation extreme indices since the beginning of the twentieth century: The HadEX2 dataset. *J. Geophys. Res. Atmos.* 118, 2098–2118. doi:10.1002/jgrd.50150

Douglas, E. M., Beltrán-Przekurat, A., Niyogi, D., Pielke, R. A., and Vörösmarty, C. J. (2009). The impact of agricultural intensification and irrigation on land–atmosphere interactions and Indian monsoon precipitation — a mesoscale modeling perspective. *Glob. Planet. Change* 67, 117–128. doi:10.1016/j.gloplacha.2008.12.007

Du, E., Vittorio, A. D., and Collins, W. D. (2016). Evaluation of hydrologic components of community land Model 4 and bias identification. *Int. J. Appl. Earth Observation Geoinformation* 48, 5–16. doi:10.1016/j.jag.2015.03.013

Dunn, R. J. H., Alexander, L. V., Donat, M. G., Zhang, X., Bador, M., Herold, N., et al. (2020). Development of an updated global land in situ-based data set of temperature and precipitation extremes: HadEX3. *J. Geophys. Res. Atmos.* 125, e2019JD032263. doi:10.1029/2019JD032263

Emanuel, K. A., and Živković-Rothman, M. (1999). Development and evaluation of a convection scheme for use in climate models. *J. Atmos. Sci.* 56, 1766–1782. doi:10.1175/1520-0469(1999)056<1766:DAEOAC>2.0.CO;2

Erb, K.-H., Luyssaert, S., Meyfroidt, P., Pongratz, J., Don, A., Kloster, S., et al. (2017). Land management: Data availability and process understanding for global change studies. *Glob. Change Biol.* 23, 512–533. doi:10.1111/gcb.13443

IPCC (2012). "Summary for policymakers," in *Managing the risks of extreme events and disasters to advance climate change adaptation*. Editors C. B. Field, V. Barros, T. F. Stocker, D. Qin, D. J. Dokken, K. L. Ebi, et al. (Cambridge, UK, and New York, NY, USA: Cambridge University Press), 1–19. A Special Report of Working Groups I and II of the Intergovernmental Panel on Climate Change.

Fu, J., Kang, S., Zhang, L., Li, X., Gentine, P., and Niu, J. (2022). Amplified warming induced by large-scale application of water-saving techniques. *Environ. Res. Lett.* 17, 034018. doi:10.1088/1748-9326/ac4b52

Gao, X., Shi, Y., and Giorgi, F. (2016). Comparison of convective parameterizations in RegCM4 experiments over China with CLM as the land surface model. *Atmos. Ocean. Sci. Lett.* 9, 246–254. doi:10.1080/16742834.2016.1172938

Giorgi, F., and Bates, G. T. (1989). The climatological skill of a regional model over complex terrain. *Mon. Weather Rev.* 117, 2325–2347. doi:10.1175/1520-0493(1989)117<2325:TCSOAR>2.0.CO;2

Giorgi, F., Coppola, E., Solmon, F., Mariotti, L., Sylla, M. B., Bi, X., et al. (2012). RegCM4: Model description and preliminary tests over multiple CORDEX domains. *Clim. Res.* 52, 7–29. doi:10.3354/cr01018

Gormley-Gallagher, A. M., Sterl, S., Hirsch, A. L., Seneviratne, S. I., Davin, E. L., and Thiery, W. (2022). Agricultural management effects on mean and extreme temperature trends. *Earth Syst. Dyn.* 13, 419–438. doi:10.5194/esd-13-419-2022

Gu, H., Wang, G., Yu, Z., and Mei, R. (2012). Assessing future climate changes and extreme indicators in east and south Asia using the RegCM4 regional climate model. *Clim. Change* 114, 301–317. doi:10.1007/s10584-012-0411-y

Guimberteau, M., Laval, K., Perrier, A., and Polcher, J. (2012). Global effect of irrigation and its impact on the onset of the Indian summer monsoon. *Clim. Dyn.* 39, 1329–1348. doi:10.1007/s00382-011-1252-5

Han, Z., Gao, X., Shi, Y., Wu, J., Wang, M., and Giorgi, F. (2015). Development of Chinese high resolution land cover data for the RegCM4/CLM and its impact on regional climate simulation. *J. Glaciol. Geocryol. (in Chinese)* 37, 857–866. doi:10.7522/j.issn.1000-0240.2015.0095

Hirsch, A. L., Wilhelm, M., Davin, E. L., Thiery, W., and Seneviratne, S. I. (2017). Can climate-effective land management reduce regional warming? *Journal of Geophysical Research Atmospheres* 122, 2269–2288. doi:10.1002/2016JD026125

Holtslag, A. a. M., De Bruijn, E. I. F., and Pan, H. L. (1990). A high resolution air mass transformation model for short-range weather forecasting. *Monthly Weather Review* 118, 1561–1575. doi:10.1175/1520-0493(1990)118<1561:AHRAMT>2.0.CO;2

Jach, L., Schwitalla, T., Branch, O., Warrach-Sagi, K., and Wulfmeyer, V. (2022). Sensitivity of land–atmosphere coupling strength to changing atmospheric temperature and moisture over Europe. *Earth System Dynamics* 13, 109–132. doi:10.5194/esd-13-109-2022

Ji, Z., and Kang, S. (2015). Evaluation of extreme climate events using a regional climate model for China. *International Journal of Climatology* 35, 888–902. doi:10.1002/joc.4024

Juang, J.-Y., Katul, G., Siqueira, M., Stoy, P., and Novick, K. (2007). Separating the effects of albedo from eco-physiological changes on surface temperature along a successional chronosequence in the southeastern United States. *Geophysical Research Letters* 34, L21408. doi:10.1029/2007GL031296

Kang, S., and Eltahir, E. A. B. (2018). North China Plain threatened by deadly heatwaves due to climate change and irrigation. *Nature Communications* 9, 2894. doi:10.1038/s41467-018-05252-y

Kiehl, J. T., Hack, J. J., Bonan, G. B., Boville, B. A., Briegleb, B. P., Williamson, D. L., et al. (1996). *Description of the NCAR community climate model (CCM3). Technical note*. Boulder, CO: NCAR.

Koster, R. D., Dirmeyer, P. A., Guo, Z., Bonan, G., Chan, E., Cox, P., et al. (2004). Regions of strong coupling between soil moisture and precipitation. *Science* 305, 1138–1140. doi:10.1126/science.1100217

Kueppers, L. M., and Snyder, M. A. (2012). Influence of irrigated agriculture on diurnal surface energy and water fluxes, surface climate, and atmospheric circulation in California. *Climate Dynamics* 38, 1017–1029. doi:10.1007/s00382-011-1123-0

Lawrence, D. M., Hurtt, G. C., Arneth, A., Brovkin, V., Calvin, K. V., Jones, A. D., et al. (2016). The land use model intercomparison project (LUMIP) contribution to CMIP6: Rationale and experimental design. *Geoscientific Model Development* 9, 2973–2998. doi:10.5194/gmd-9-2973-2016

Li, X., Chen, H., Liao, H., Hua, W., Sun, S., Ma, H., et al. (2017). Potential effects of land cover change on temperature extremes over eurasia: Current versus historical experiments. *International Journal of Climatology* 37, 59–74. doi:10.1002/joc.4976

Li, X., Chen, H., Wei, J., Hua, W., Sun, S., Ma, H., et al. (2018). Inconsistent responses of hot extremes to historical land use and cover change among the selected CMIP5 models. *Journal of Geophysical Research Atmospheres* 123, 3497–3512. doi:10.1002/2017JD028161

Li, X., Li, X., Ma, H., Hua, W., Chen, H., Wen, X., et al. (2022). Reforestation in Southern China enhances the convective afternoon rainfall during the post-flood season. *Front. Environ. Sci.* 10, 942974. doi:10.3389/fenvs.2022.942974

Liu, J., Jin, J., and Niu, G.-Y. (2021). Effects of irrigation on seasonal and annual temperature and precipitation over China simulated by the WRF model. *Journal of Geophysical Research Atmospheres* 126, e2020JD034222. doi:10.1029/2020JD034222

Lobell, D., Bala, G., Mirin, A., Phillips, T., Maxwell, R., and Rotman, D. (2009). Regional differences in the influence of irrigation on climate. *Journal of Climate* 22, 2248–2255. doi:10.1175/2008JCLI2703.1

Lu, Y., Harding, K., and Kueppers, L. (2017). Irrigation effects on land–atmosphere coupling strength in the United States. *Journal of Climate* 30, 3671–3685. doi:10.1175/JCLI-D-15-0706.1

Luyssaert, S., Jammet, M., Stoy, P. C., Estel, S., Pongratz, J., Ceschia, E., et al. (2014). Land management and land-cover change have impacts of similar magnitude on surface temperature. *Nature Climate Change* 4, 389–393. doi:10.1038/nclimate2196

Mahmood, R., Pielke Sr, R. A., Hubbard, K. G., Niyogi, D., Dirmeyer, P. A., Mcalpine, C., et al. (2014). Land cover changes and their biogeophysical effects on climate. *International Journal of Climatology* 34, 929–953. doi:10.1002/joc.3736

IPCC (2021). "Summary for policymakers," in *Climate change 2021: The physical science basis. Contribution of working group I to the sixth assessment report of the intergovernmental Panel on climate change*. Editors V. MassonDelmotte, P. Zhai, A. Pirani, S. L. Connors, C. Péan, S. Berger, et al. (Cambridge, United Kingdom and New York, NY, USA: Cambridge University Press), 3–32. doi:10.1017/9781009157896.001

Mishra, V., Ambika, A. K., Asoka, A., Aadhar, S., Buzan, J., Kumar, R., et al. (2020). Moist heat stress extremes in India enhanced by irrigation. *Nature Geoscience* 13, 722–728. doi:10.1038/s41561-020-00650-8

Nocco, M. A., Smail, R. A., and Kucharik, C. J. (2019). Observation of irrigation-induced climate change in the Midwest United States. *Global Change Biology* 25, 3472–3484. doi:10.1111/gcb.14725

O'brien, T. A., Sloan, L. C., and Snyder, M. A. (2011). Can ensembles of regional climate model simulations improve results from sensitivity studies? *Climate Dynamics* 37, 1111–1118. doi:10.1007/s00382-010-0900-5

Oleson, K., Lawrence, D., Bonan, G., Drewniak, B., Huang, M., Koven, C., et al. (2013). *Technical description of version 4.5 of the community land model (CLM)*. Boulder, CO: NCAR.

Ozdogan, M., Rodell, M., Beaudoing, H. K., and Toll, D. L. (2010). Simulating the effects of irrigation over the United States in a land surface model based on satellite-derived agricultural data. *Journal of Hydrometeorology* 11, 171–184. doi:10.1175/2009JHM1116.1

Pal, J. S., Small, E. E., and Eltahir, E. A. B. (2000). Simulation of regional-scale water and energy budgets: Representation of subgrid cloud and precipitation processes within RegCM. *Journal of Geophysical Research Atmospheres* 105, 29579–29594. doi:10.1029/2000JD900415

Portmann, F. T., Siebert, S., and Döll, P. (2010). MIRCA2000—global monthly irrigated and rainfed crop areas around the year 2000: A new high-resolution data set for agricultural and hydrological modeling. *Global Biogeochemical Cycles* 24, GB1011. doi:10.1029/2008GB003435

Qian, Y., Huang, M., Yang, B., and Berg, L. K. (2013). A modeling study of irrigation effects on surface fluxes and land–air–cloud interactions in the Southern Great Plains. *Journal of Hydrometeorology* 14, 700–721. doi:10.1175/JHM-D-12-0134.1

Sacks, W. J., Cook, B. I., Buenning, N., Levis, S., and Helkowski, J. H. (2009). Effects of global irrigation on the near-surface climate. *Climate Dynamics* 33, 159–175. doi:10.1007/s00382-008-0445-z

Seneviratne, S. I., Corti, T., Davin, E. L., Hirschi, M., Jaeger, E. B., Lehner, I., et al. (2010). Investigating soil moisture–climate interactions in a changing climate: A review. *Earth-Science Reviews* 99, 125–161. doi:10.1016/j.earscirev.2010.02.004

Seneviratne, S. I., Lüthi, D., Litschi, M., and Schär, C. (2006). Land–atmosphere coupling and climate change in Europe. *Nature* 443, 205–209. doi:10.1038/nature05095

Seneviratne, S. I., Phipps, S. J., Pitman, A. J., Hirsch, A. L., Davin, E. L., Donat, M. G., et al. (2018). Land radiative management as contributor to regional-scale climate adaptation and mitigation. *Nature Geoscience* 11, 88–96. doi:10.1038/s41561-017-0057-5

IPCC (2019). "Summary for policymakers," in *Climate change and land: An IPCC special report on climate change, desertification, land degradation, sustainable land management, food security, and greenhouse gas fluxes in terrestrial ecosystems*. Editors P. R. Shukla, J. Skea, E. Calvo Buendia, V. Masson-Delmotte, H. O. Pörtner, D. C. Roberts, et al. In press. Available at: https://www.ipcc.ch/site/assets/uploads/sites/4/2020/02/SPM_Updated-Jan20.pdf (Accessed Oct 17, 2022).

Singh, D., Mcdermid, S. P., Cook, B. I., Puma, M. J., Nazarenko, L., and Kelley, M. (2018). Distinct influences of land cover and land management on seasonal climate. *Journal of Geophysical Research Atmospheres* 123 (12), 12017–12039. doi:10.1029/2018JD028874

Smith, P., Bustamante, M., Ahammad, H., Clark, H., Dong, H., Elsiddig, E. A., et al. (2014). "Agriculture, forestry and other land use (AFOLU)," in *Climate change 2014: Mitigation of climate change. Contribution of working group III to the fifth assessment report of the intergovernmental Panel on climate change*. Editors O. Edenhofer, R. Pichs-Madruga, Y. Sokona, E. Farahani, S. Kadner, K. Seyboth, et al. (Cambridge, United Kingdom and New York, NY, USA: Cambridge University Press). doi:10.1017/CBO9781107415416.017

Sun, H., Pan, Z., and Liu, X. (2012). Numerical simulation of spatial-temporal distribution of dust aerosol and its direct radiative effects on East Asian climate. *Journal of Geophysical Research Atmospheres* 117, D13206. doi:10.1029/2011JD017219

Thiery, W., Davin, E. L., Lawrence, D. M., Hirsch, A. L., Hauser, M., and Seneviratne, S. I. (2017). Present-day irrigation mitigates heat extremes. *Journal of Geophysical Research Atmospheres* 122, 1403–1422. doi:10.1002/2016JD025740

Thiery, W., Visser, A. J., Fischer, E. M., Hauser, M., Hirsch, A. L., Lawrence, D. M., et al. (2020). Warming of hot extremes alleviated by expanding irrigation. *Nature Communications* 11, 290. doi:10.1038/s41467-019-14075-4

United Nations General Assembly (2015). *Transforming our world: the 2030 agenda for sustainable development*. New York, NY, USA: United Nations. Available at: https://sdgs.un.org/sites/default/files/publications/21252030%20Agenda%20for%20Sustainable%20Development%20web.pdf (Accessed Oct 17, 2022).

Viovy, N. (2018). *CRUNCEP version 7 - atmospheric forcing data for the community land model*. Boulder, CO: Research Data Archive at the National Center for Atmospheric Research, Computational and Information Systems Laboratory. 10.5065/PZ8F-F017 (Accessed Oct 17, 2022).

Wang, Y., Li, S., Qin, S., Guo, H., Yang, D., and Lam, H.-M. (2020). How can drip irrigation save water and reduce evapotranspiration compared to border irrigation in arid regions in northwest China. *Agricultural Water Management* 239, 106256. doi:10.1016/j.agwat.2020.106256

Ward, D. S., Mahowald, N. M., and Kloster, S. (2014). Potential climate forcing of land use and land cover change. *Atmospheric Chemistry and Physics* 14, 12701–12724. doi:10.5194/acp-14-12701-2014

Winckler, J., Reick, C. H., and Pongratz, J. (2017). Robust identification of local biogeophysical effects of land-cover change in a global climate model. *Journal of Climate* 30, 1159–1176. doi:10.1175/JCLI-D-16-0067.1

Wu, L., Feng, J., and Miao, W. (2018). Simulating the impacts of irrigation and dynamic vegetation over the North China Plain on regional climate. *Journal of Geophysical Research Atmospheres* 123, 8017–8034. doi:10.1029/2017JD027784

Wu, X., Wang, L., Yao, R., Luo, M., and Li, X. (2021). Identifying the dominant driving factors of heat waves in the North China Plain. *Atmospheric Research* 252, 105458. doi:10.1016/j.atmosres.2021.105458

Xie, W., Zhou, B., Han, Z., and Xu, Y. (2021). Projected changes in heat waves over China: Ensemble result from RegCM4 downscaling simulations. *International Journal of Climatology* 41, 3865–3880. doi:10.1002/joc.7047

Xu, R., Li, Y., Teuling, A. J., Zhao, L., Spracklen, D. V., Garcia-Carreras, L., et al. (2022). Contrasting impacts of forests on cloud cover based on satellite observations. *Nature Communications* 13, 670. doi:10.1038/s41467-022-28161-7

Yang, B., Zhang, Y., Qian, Y., Tang, J., and Liu, D. (2016). Climatic effects of irrigation over the Huang-Huai-Hai Plain in China simulated by the weather research and forecasting model. *Journal of Geophysical Research Atmospheres* 121, 2246–2264. doi:10.1002/2015JD023736

Yang, Q., Huang, X., and Tang, Q. (2020). Irrigation cooling effect on land surface temperature across China based on satellite observations. *Science of The Total Environment* 705, 135984. doi:10.1016/j.scitotenv.2019.135984

Zeng, X., Zhao, M., and Dickinson, R. E. (1998). Intercomparison of bulk aerodynamic algorithms for the computation of sea surface fluxes using TOGA COARE and TAO Data. *Journal of Climate* 11, 2628–2644. doi:10.1175/1520-0442(1998)011<2628:IOBAAF>2.0.CO;2

Zeng, Y., Xie, Z., and Liu, S. (2017a). Seasonal effects of irrigation on land–atmosphere latent heat, sensible heat, and carbon fluxes in semiarid basin. *Earth System Dynamics* 8, 113–127. doi:10.5194/esd-8-113-2017

Zeng, Y., Xie, Z., and Zou, J. (2017b). Hydrologic and climatic responses to global anthropogenic groundwater extraction. *Journal of Climate* 30, 71–90. doi:10.1175/JCLI-D-16-0209.1

Zhang, X., Alexander, L., Hegerl, G. C., Jones, P., Tank, A. K., Peterson, T. C., et al. (2011). Indices for monitoring changes in extremes based on daily temperature and precipitation data. *WIREs Climate Change* 2, 851–870. doi:10.1002/wcc.147

Zwiers, F. W., and Von Storch, H. (1995). Taking serial correlation into account in tests of the mean. *Journal of Climate* 8, 336–351. doi:10.1175/1520-0442(1995)008<0336:TSCIAI>2.0.CO;2

frontiers | Frontiers in Ecology and Evolution

TYPE Original Research
PUBLISHED 09 February 2023
DOI 10.3389/fevo.2023.1067209



OPEN ACCESS

EDITED BY
Merja H. Tölle,
University of Kassel,
Germany

REVIEWED BY
Tsegaye Gemechu Legesse,
Chinese Academy of Agricultural Sciences (CAAS), China
Juanle Wang,
Institute of Geographic Sciences and Natural Resources Research (CAS), China

*CORRESPONDENCE
Tingxiang Liu
✉ liutingxiang@ccsfu.edu.cn

SPECIALTY SECTION
This article was submitted to Environmental Informatics and Remote Sensing, a section of the journal Frontiers in Ecology and Evolution

RECEIVED 11 October 2022
ACCEPTED 17 January 2023
PUBLISHED 09 February 2023

CITATION
Li G, Yu L, Liu T, Bao Y, Yu J, Xin B, Bao L, Li X, Chang X and Zhang S (2023) Spatial and temporal variations of grassland vegetation on the Mongolian Plateau and its response to climate change.
*Front. Ecol. Evol.* 11:1067209.
doi: 10.3389/fevo.2023.1067209



# Spatial and temporal variations of grassland vegetation on the Mongolian Plateau and its response to climate change

Guangshuai Li[1,2], Lingxue Yu[2], Tingxiang Liu[1]*, Yulong Bao[3], Jiaxin Yu[1,2], Bingxia Xin[2], Lun Bao[2], Xuan Li[2], Xinyue Chang[2] and Shuwen Zhang[2]

[1]College of Geography Science, Changchun Normal University, Changchun, China, [2]Remote Sensing and Geographic Information Research Center, Northeast Institute of Geography and Agroecology, Chinese Academy of Sciences, Changchun, China, [3]School of Geography Science, Inner Mongolia Normal University, Hohhot, China

The Mongolian Plateau is an arid and semi-arid region with grassland as its main vegetation. It has a fragile ecosystem and is a sensitive area for global warming. The study is based on MODIS NDVI data and growth season meteorological data from 2000 to 2018, this study examined the spatial and temporal variation characteristics of grassland vegetation on the Mongolian Plateau during the growing season using trend analysis, partial correlation analysis, and residual analysis, and it explores the dual response of NDVI changes to climate and human activities. The study's findings demonstrated that the growing season average NDVI of grassland vegetation on the plateau gradually increased from southwest to northeast during the growing season; the growing season average NDVI demonstrated a significant overall increase of 0.023/10a ($p < 0.05$) from 2000 to 2018, with an increase rate of 0.030/10a in Inner Mongolia and 0.019/10a in Mongolia; the area showing a significant increase in NDVI during the growing season accounted for 91.36% of the entire study area. In Mongolian Plateau grasslands during the growing season of 2000–2018, precipitation and downward surface shortwave radiation grew significantly at rates of 34.83mm/10a and 0.57 W/m2/10a, respectively, while average air temperature decreased slightly at a rate of −0.018°C/10a. Changes in meteorological factors of grassland vegetation varied by region as well, with Inner Mongolia seeing higher rates of precipitation, lower rates of average air temperature, and lower rates of downward surface shortwave radiation than Mongolia. On the Mongolian Plateau, the NDVI of grassland vegetation in the growing season showed a significant positive correlation with precipitation (0.31) and a significant negative correlation with average air temperature (−0.09) and downward surface shortwave radiation (−0.19), indicating that increased in NDVI was driven by an increase in precipitation paired with a decrease in air temperature and a decrease in surface shortwave radiation. The overall increase in NDVI caused by human activity in the grasslands of the Mongolian Plateau was primarily positive, with around 18.37% of the region being beneficial. Climate change and human activity both affect NDVI variations in Mongolian Plateau grasslands, which are spatially heterogeneous. Moderate ecological engineering and agricultural production activities are crucial for vegetation recovery. This work is crucial to further understanding surface–atmosphere interactions in arid and semi-arid regions in the context of global climate change.

KEYWORDS

**Mongolian Plateau, grassland vegetation, climate change, NDVI, vegetation changes**

# 1. Introduction

One of the key scientific topics in global change research has been how terrestrial ecosystems respond to and give feedback on global climate change (Fu, 2018; Yu G. et al., 2020). The report of working group I of the sixth assessment of IPCC (Ar6) stated that the average global surface temperature rose by around 1°C during 1850–1900 and the average temperature change over the next 20 years will be 1.5°C, with average precipitation also predicted to rise (Zhou et al., 2021). Extreme weather events have become more frequent as a result of global warming, which has a negative influence on vegetation changes and the balance of the entire ecosystem (Fu et al., 2014). One of the largest and most extensively dispersed terrestrial ecosystems, grasslands contain one-third of the world's terrestrial carbon pool and served as the foundation for the development of animal husbandry (Scurlock and Hall, 1998; Du et al., 2004). However, the grassland ecosystem habitats are delicate, prone to outside perturbation, and extremely sensitive to changes in global temperature and the environment, particularly in arid and semi-arid regions where water resources are short (Scurlock and Hall, 1998). For a complete understanding of the interaction between ecosystems and climate change in the context of climate warming, it is crucial to clarify how vegetation changes in grassland ecosystems respond to climate change (Gao et al., 2017).

The arid and semi-arid Mongolian Plateau is a typical ecologically fragile area that has experienced significant desertification in the past (Kang et al., 2007). Guo (2021) examined that the characteristics of desertification evolution on the plateau from 2000 to 2019 using MODIS/MCD43A4 data in conjunction with GEE and Markov models. He came to the conclusion that the desertification area on the Mongolian Plateau region has shown a weakening decreasing trend in recent decades (Guo, 2021). However, recent studies using remote sensing observations have revealed that there are significant regional differences in the vegetation changes on the plateau: the vegetation in the larger areas of Inner Mongolia has tended to become greener as a result of ecological conservation efforts, whereas the vegetation in some areas of Mongolia still shows general overall degradation (Li et al., 2022). Numerous studies have investigated how the various vegetation varieties react to climate change. For instance, Xie et al. (2022) used the maximum synthesis method, trend analysis, and correlation analysis to analyze the spatial and temporal variation characteristics of vegetation and the mechanisms influenced by climatic factors based on MODIS normalized vegetation index, enhanced vegetation index, and meteorological data in the Yellow River basin from 2000 to 2018. They discovered that throughout the growing season, temperature and precipitation—which were both very important for grassland—were mainly positively connected with the vegetation indices, with a lag time of 1 month for temperature and 3 months for precipitation (Xie et al., 2022). In 2015, Shen et al. investigated how vegetation in the grassland region of China responded to climate change. They discovered that the region's overall vegetation cover had increased over the previous 25 years, and there was a clear spatial variation in seasonal changes (Shen et al., 2015). According to Peng et al. (2013), the NDVI of vegetation during the growing season on the Qinghai–Tibet Plateau exhibited a positive association with both the average maximum temperature and lowest temperature of the growing season (Peng et al., 2013). According to Shen et al. (2016), the NDVI of grassland vegetation on the Tibetan Plateau was strongly negatively associated with the mean maximum temperature and positively correlated with the mean minimum summer temperature (Shen et al., 2016). Currently, the long-term changes of grassland vegetation on the Mongolian plateau during the growing season and their attribution are still relatively rare, and it is still unclear how human activities affect these changes and regional differences. And basically, the relationship between NDVI and meteorological factors is revealed in a holistic manner, ignoring how different vegetation types are responding to climate change. Therefore, it is crucial to research recent trends in vegetation change and the factors that have contributed to them on the Mongolian Plateau.

In light of this, this paper uses one-dimensional linear trend analysis, partial correlation analysis, and multiple regression residual analysis based on MODIS NDVI data and meteorological data (precipitation, average air temperature and downward surface shortwave radiation) from 2000 to 2018 to characterize the spatial and temporal variation of NDVI in the growing season (May–September) of grassland vegetation on the Mongolian plateau. In order to better understand the interrelationship between vegetation, climate, and human activity, it also looked at the factors that influence NDVI changes caused by both the climate and human activity. Clarification of the characteristics of the spatial and temporal variation of grassland vegetation on the Mongolian Plateau and its response to climate change can provide a scientific basis for revealing the mechanism of the relationship between grassland vegetation and climate change. It can also aid in scientific understanding of the response and feedback relationship between vegetation change and global change in various physical and human environments.

# 2. Materials and methods

## 2.1. Study area

The Mongolian Plateau is located in the central hinterland of East Asia, between 39°41′1.40″ to 50°53′40.24″ N and 87°44′58.76″ to 120°34′27.19″ E (Figure 1A). It extends from the Great Khingan Mountains in the east to the Altai Mountains in the west, and from the Kent-Yabunov Mountains in the north to the Yinshan Mountains in the south, mainly including all of Mongolia and the whole territory of Inner Mongolia Autonomous Region, China (Liu, 1993). The Mongolian Plateau is a massive, gently sloping plateau with an average elevation of 1,580 meters. With mountains in the north and west, sizable hills in the center and east, and the huge Gobi Desert in the southwest, the landscape is high in the west and low in the east, falling gradually from the surrounding mountains to the high plains in the middle (Zhang et al., 2018). The Mongolian Plateau experiences four distinct seasons: cold and lengthy winter, dry and windy spring, hot and brief summer, and cool autumn. The climate is temperate continental with an uneven temperature distribution, with relatively low temperatures in the humid north and east caused by the influence of moisture from the Arctic Ocean to the north, and relatively high temperatures in the arid southwest. The semi-humid zone in the north and east gradually gives way to semi-arid, arid, and highly arid zones in the southwest, with an average annual precipitation on the plateau of around 200 mm and an irregular spatial and temporal distribution of precipitation (Zhang et al., 2009; Miao et al., 2014). While Inner Mongolia and Mongolia share many natural characteristics, and their populations used to lead mostly nomadic and herding lifestyles, significant socioeconomic contrasts have emerged between the two regions as a result of social and economic development. Since 1978, China has attached great attention to ecological restoration projects in the northern China to reverse the depredated environment, and as a

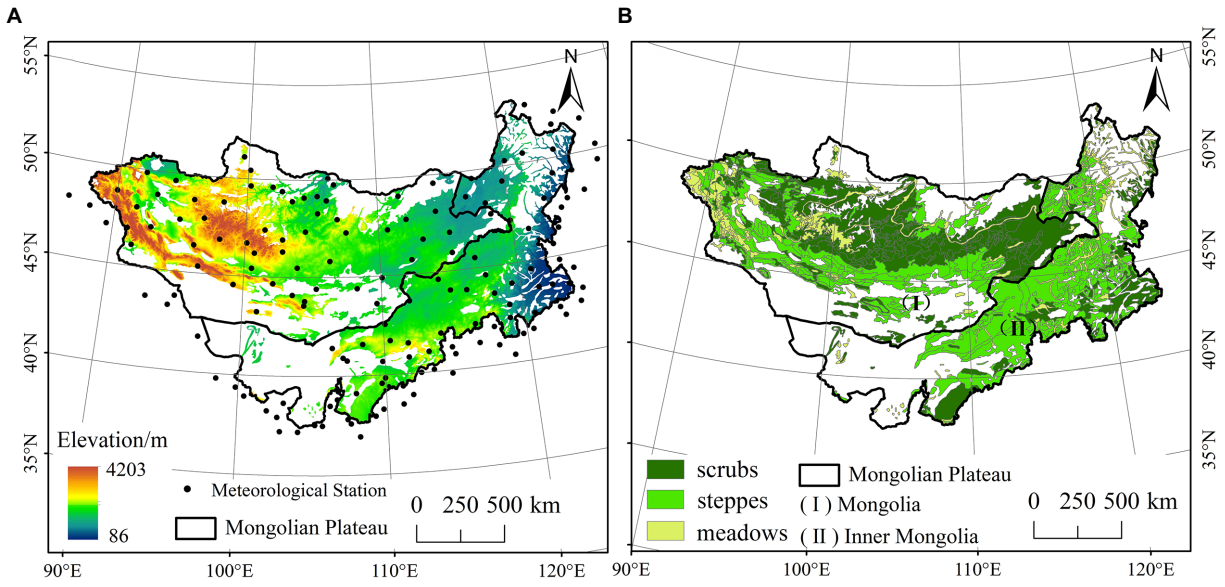


FIGURE 1
**(A)** Geographical location and meteorological stations of Mongolian Plateau and **(B)** distribution of grassland vegetation types.

result, many ecological restoration projects have been implemented in Inner Mongolia, which was in contrast for Mongolia, where human disturbances were rare. Steppes in the study area are mainly distributed in the southeast, with scrubs in the northeast and north, while meadows are mostly distributed at high altitudes on the western edge of the study area (Figure 1B).

## 2.2. Data processing and analysis

Meteorological data including precipitation, average air temperature and downward surface shortwave radiation. The meteorological data on the China side were obtained from the National Weather Science Data Center's dataset of monthly values of surface climate information[1], and the Mongolian data were taken from the National Oceanic and Atmospheric Administration's weather data.[2] A total of 86 meteorological observation sites containing valid precipitation data and 98 valid air temperature data in the Mongolian Plateau from 2000 to 2018, in addition to 58 nearby meteorological stations collected as supplementary data (Figure 1A), were interpolated and cropped using professional ANUSPLIN software to obtain 1 km resolution air temperature and precipitation raster data for the study area from 2000 to 2018. The downward surface shortwave radiation data are derived from the monthly value dataset TerraClimate provided by the Google Earth Engine[3] platform with a spatial resolution of 1/24° and resampled to 1 km.

The MOD13A2.006 product data of 2000–2018 from the Google Earth Engine platform (see footnote 3) with a spatial resolution of 1 km and a temporal resolution of 16 days, were used in this investigation to extract NDVI. In this study, the average NDVI values from May to September were used to characterize the NDVI values during the growth season, and the NDVI values of all pixels in the study region pertaining to each type of grassland were used to represent the NDVI values of this type of grassland vegetation.

The 1:4,000,000 vegetation map published by the Chinese Academy of Sciences in 1996, was used to determine the vegetation types in Inner Mongolia, and a 1:3,000,000 vegetation map provided by the Mongolian Academy of Sciences was used to determine the vegetation types in Mongolia. The accuracy of these datasets was verified utilizing a combination of ground verification, remote sensing techniques, and discriminative interactive human–computer interpretation of the data.

## 2.3. Methods

### 2.3.1. Slope trend analysis

In this study, we used the regCoef function in NCL to compute NDVI trends and examine the NDVI trends of grassland vegetation on the Mongolian Plateau in the growing seasons from 2000 to 2018. The regCoef [x, y (lat|:, lon|:, time|:)] function is mostly used to process multidimensional x- and y-arrays. To determine the multiyear trend of NDVI, linear regression coefficients (using least squares) were produced. The calculating equation is as follows:

$$NDVI_{Slope} = \frac{n\sum_{i=1}^{n}(iQ_i) - \sum_{i=1}^{n} i \sum_{i=1}^{n} Q_i}{n\sum_{i=1}^{n} i^2 - \left(\sum_{i=1}^{n} i\right)} \quad (1)$$

where $NDVI_{Slope}$ is the slope of NDVI change during the research time period, $i$ is the study year, $n$ is the time series length (19 years), and $Q_i$ is the NDVI value for the growing season in year $i$. Positive $NDVI_{Slope}$ indicating the NDVI is increasing, while negative values means the NDVI is decreasing.

1 http://data.cma.cn/
2 https://www.ncei.noaa.gov/maps-and-geospatial-products/
3 https://code.earthengine.google.com/

### 2.3.2. ANUSPLIN meteorological data interpolation

The meteorological stations on the Mongolian Plateau were interpolated using the ANUSPLIN multivariate data interpolation and analysis software package for meteorological data created by the Australian National University (Hijmans et al., 2005). It is made up of eight submodule programs that offer a comprehensive set of functions for statistical analysis, data diagnosis, and the computation of spatial distribution standard errors (Hijmans et al., 2005; Liu et al., 2008a). The SPLINA and LAPGRD modules, whose built-in thin-disk smooth spline function enables the inclusion of covariates (elevation, coastline, etc.), are the principal applications for interpolating temperature and precipitation (Liu et al., 2008b). The local thin-disk smooth spline function's theoretical statistical model is written as:

$$Z_i = f(x_i) + b^T y_i + e_i (i = 1,2,\ldots\ldots,N) \quad (2)$$

where $z_i$ is the dependent variable, located at point $i$ in the interpolation space; $x_i$ is a d-dimensional vector with respect to the sample independent variables; $f$ is an unknown smooth function with respect to $x_i$; $y_i$ is a p-dimensional independent covariate; $b^T$ is a p-dimensional coefficient with respect to the $y_i$ coefficients; $e_i$ is a random error term in the independent variable, with expectation 0; and $N$ is the number of interpolated sample points.

In this study, the optimal spatial interpolation model was used for spatial interpolation of precipitation and air temperature, that was, a three variable local thin disk smooth spline function with longitude and latitude as independent variables of precipitation and elevation as covariate of air temperature, and the number of splines was set to 2.

### 2.3.3. Partial correlation analysis

When two variables are simultaneous correlated with a third variable, partial correlation analysis is the process of removing the impact of the third variable and examining only the level of correlation between the other two variables. The calculating equation is as follows:

$$R_{xy,z} = \frac{R_{xy} - R_{xz} - R_{yz}}{\sqrt{\left(1 - R_{xz}^2\right)\left(1 - R_{yz}^2\right)}} R_{xy} = \frac{\sum_{i=1}^{n}(x_i - \bar{x})(y_i - \bar{y})}{\sqrt{\sum_{i=1}^{n}(x_i - \bar{x})^2}\sqrt{\sum_{i=1}^{n}(y_i - \bar{y})^2}} \quad (3)$$

where $R_{xy\ z}$ is the partial correlation coefficient; $R_{xy}$, $R_{xz}$, $R_{yz}$ are the simple correlation coefficients between $x$, $y$, $z$. If $R_{xy\ z}$ is greater than 0, then the two variables are positively correlated, otherwise if $R_{xy\ z}$ is less than 0, then the two variables are negatively correlated.

### 2.3.4. Residual analysis

By eliminating the effects of precipitation and air temperature on the NDVI long time series change, natural and anthropogenic factors in vegetation cover change were distinguished. The predicted value of NDVI is fitted by meteorological factors, that is, the impact of climate change. According to the residual trend method, the difference between the calculated NDVI prediction and the actual value is regarded as anthropogenic influences (Evans and Geerken, 2004).

$$NDVI_{pre} = aT + bP + c \quad (4)$$

$$\varepsilon = NDVI_{real} - NDVI_{pre} \quad (5)$$

Where $NDVI_{pre}$ is the NDVI prediction value obtained by establishing a binary linear regression model based on NDVI, precipitation, and air temperature time series data, with NDVI as the dependent variable and air temperature and precipitation as the independent variables, under the assumption that anthropogenic influences have no impact. $T$ and $P$ are growing season air temperature and precipitation; a, b, and c are model parameters.

Where $\varepsilon$ is the residual of NDVI; $NDVI_{real}$ is the NDVI value in the remote sensing image. Calculate with formula (1) $\varepsilon$ if it is positive, it means that anthropogenic influences promote NDVI, otherwise, it indicates an inhibitory effect.

## 3. Results

### 3.1. Spatial and temporal variation of NDVI in growing seasons of grassland vegetation on Mongolian Plateau

The spatial distribution of growing season average NDVI of grassland vegetation on the Mongolian Plateau from 2000 to 2018 showed that it gradually increased from southwest to northeast (Figure 2A). On the plateau, low NDVI values are primarily found in the southwest and center, and high values are primarily concentrated in the northeast Great Khingan Mountains. The multi-year growing season average of NDVI for the three different grassland vegetation in order of magnitude were: meadows (0.36) > scrubs (0.31) > steppes (0.27). The average NDVI for the growing season of grassland vegetation on the Mongolian Plateau was around 0.30, and the average NDVI for Inner Mongolia and Mongolia were 0.36 and 0.26, respectively. The average NDVI and trends of various grassland vegetation types varied greatly between Inner Mongolia and Mongolia. As can be seen from Table 1, in terms of both the multiyear average NDVI and multiyear NDVI trends, the vegetation was significantly greener in Inner Mongolia than in Mongolia. The average NDVI of various types of grassland vegetation in both regions for the growing seasons in 2000–2018 was compared. The results showed that higher values for Inner Mongolian meadows (0.49) than Mongolian meadows (0.28), inner Mongolian scrubs (0.38) than Mongolian scrubs (0.29), and inner Mongolian steppes (0.33) than Mongolian steppes (0.19).

In terms of time variation, the average NDVI of the growing seasons on the Mongolian Plateau showed a considerable increase overall from 2000 to 2018, while the NDVI values of scrubs, steppes, and meadows exhibited strong increasing trends (Figure 3). Grassland vegetation demonstrated a considerable overall rising trend (Figure 2B), with an increase of 0.023/10a, as can be seen in Figure 3. During the growing season, NDVI increased significantly for meadows, steppes, and scrubs, with the change trend varying among the vegetation types; the largest NVDI increase was found for scrubs (0.028/10a), followed by steppes (0.021/10a), and meadows (0.020/10a). On the Mongolian Plateau, the area of growing season grassland vegetation showing an increasing NVDI trend (91.36%) is significantly larger than the area showing a decreasing trend (8.64%). Additionally, when looking at the entire Mongolian Plateau spatially, the rising trend for Inner Mongolia is 0.030/10a while that for Mongolia is only 0.019/10a. The comparison of NDVI trends for various types of grassland vegetation in Inner and Outer Mongolia during

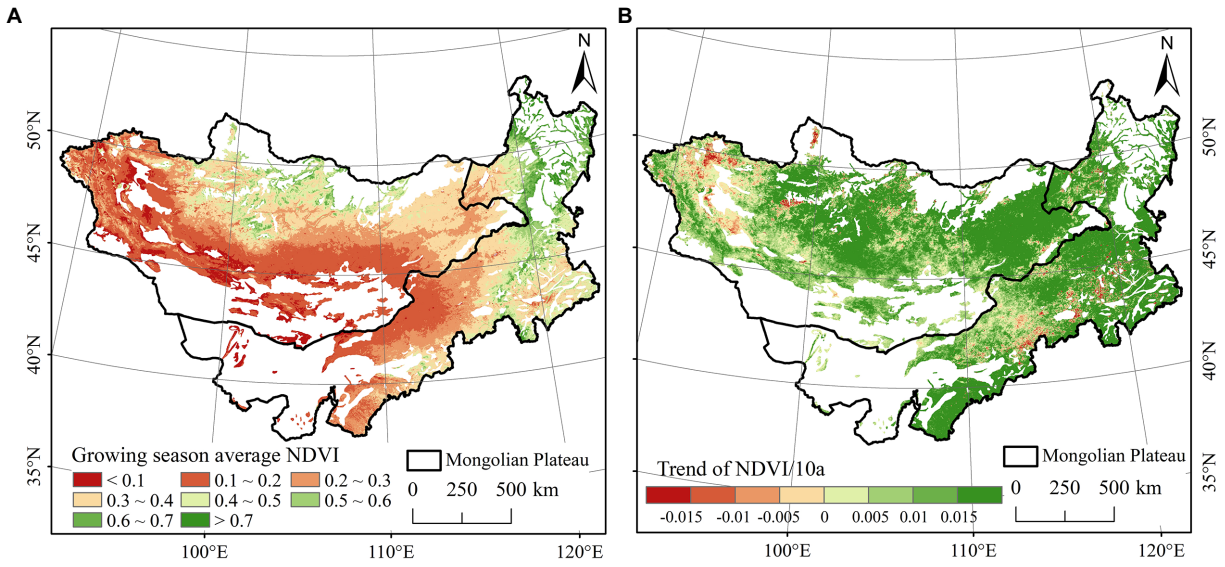


FIGURE 2
**(A)** Spatial distribution map of average NDVI **(A)** and NDVI change trend **(B)** for grassland vegetation during growing season from 2000 to 2018 across Mongolian Plateau.

TABLE 1 Comparison of growing season average NDVI and associated trend of grassland vegetation types in Inner Mongolia and Mongolia from 2000 to 2018.

| Growing season average NDVI of grassland vegetation in Inner Mongolia and Mongolia during 2000–2018 | | | NDVI change trend of grassland vegetation in Inner Mongolia and Mongolia during growing season 2000–2018 /10a | | |
|---|---|---|---|---|---|
| Vegetation type | Inner Mongolia | Mongolia | Vegetation type | Inner Mongolia | Mongolia |
| Scrubs | 0.38 | 0.30 | scrubs | 0.040 | 0.024 |
| Steppes | 0.33 | 0.19 | steppes | 0.027 | 0.013 |
| Meadows | 0.49 | 0.28 | meadows | 0.026 | 0.016 |

the growing seasons in 2000–2018 (Table 1) shows the following: Inner Mongolia scrubs (0.040) > Mongolia scrubs (0.024); Inner Mongolia steppes (0.027) > Mongolia steppes (0.013); Inner Mongolia meadows (0.026) > Mongolian meadows (0.016). Among them, NDVI increased most significantly for grasslands in eastern and southern Inner Mongolia during the growing seasons. Areas showing a decrease in NDVI for grassland vegetation were mainly found in the central and western parts of Chifeng City and the southern part of Xilin Gol League in Inner Mongolia, the northern part of Tuv Province, the border area between Tuv Province and Govisumber Province, the eastern part of Zavkhan Province, and the northern part of Khuvsgul Province (Figure 2B).

## 3.2. Climate change traits on the Mongolian Plateau

This paper uses the ANUSPLIN meteorological interpolation model to interpolate the growing season precipitation and average air temperature across the Mongolian Plateau based on the measured data from meteorological stations. Additionally chosen was the TerraClimate monthly value dataset's downward surface shortwave radiation. It also calculates the growing season average air temperature, precipitation and downward surface shortwave radiation trends in the grassland vegetation to further explain the spatial and temporal variation of NDVI in the growing season on the Mongolian Plateau. From 2000 to 2018, the growing season precipitation increased significantly by 34.83 mm/10a the downward surface shortwave radiation increased by 0.57 W/m$^2$/10a and average air temperature decreased slightly by −0.018°C/10a throughout the grassland (Table 2 and Figure 4). The growing season precipitation for each grasslands vegetation types showed a significant increasing trend for scrubs (37.55 mm/10a), steppes (31.11 mm/10a), and meadows (40.45 mm/10a), and the average air temperature trend indicated a downward trend for scrubs (−0.273°C/10a), steppes (−0.121°C/10a), and meadows (−0.089°C/10a). In the grassland vegetation, the downward surface shortwave radiation during the growing season increased for scrubs and steppes at rates of 0.27 W/m$^2$/10a and 1.09 W/m$^2$/10a, respectively, while it decreased for meadows at a rate of −0.47 W/m$^2$/10a. The trends of precipitation, average air temperature and downward surface shortwave radiation for each kind of grassland vegetation in the growing season varied by location. Each grassland vegetation in Inner Mongolia has a higher precipitation trend than the corresponding grassland vegetation in Mongolia. Similarly, Inner Mongolia has a higher average air temperature trend than Mongolia, while Inner Mongolia has a lower downward surface shortwave radiation trend than Mongolia. Following is a comparison of the change trend of meteorological factors during the growing season of grassland vegetation in Inner Mongolia and Mongolia (Table 3) specifically shows the following, the growing season precipitation trend

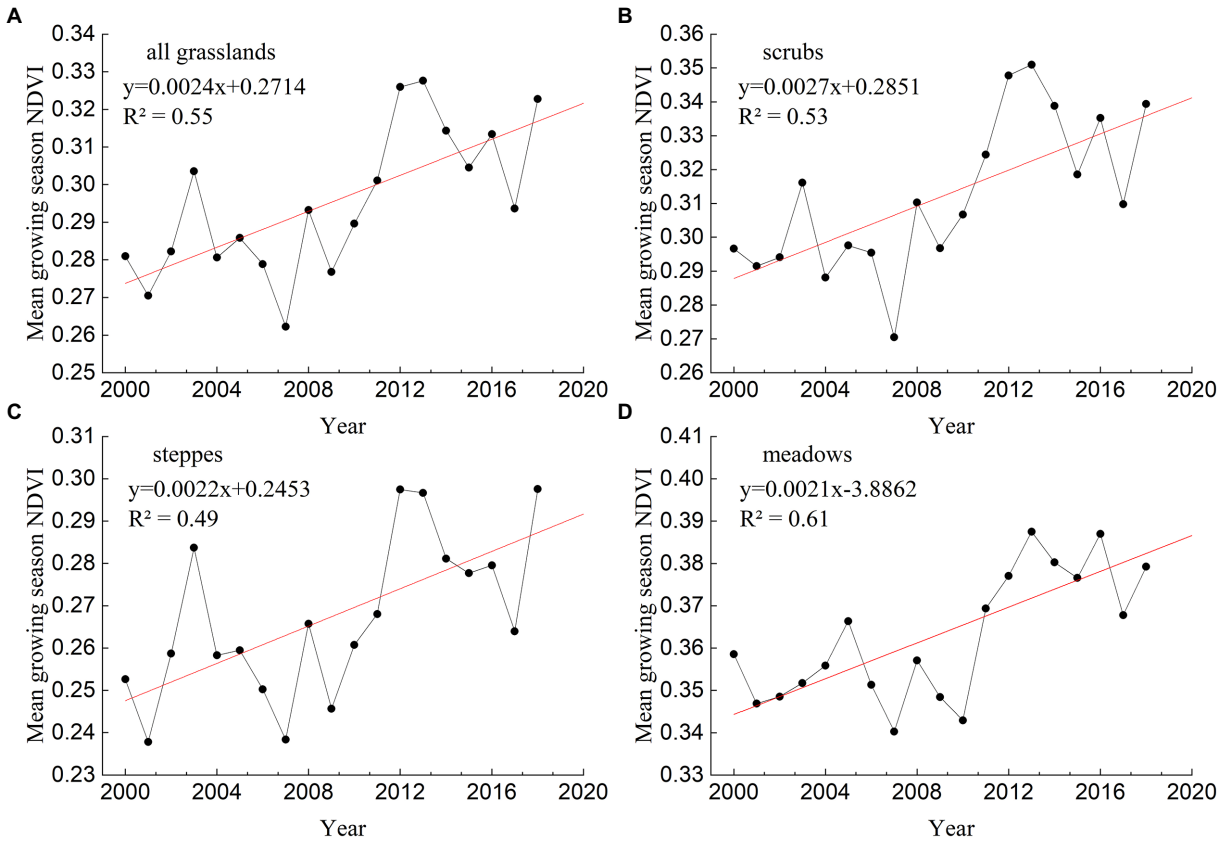


FIGURE 3
NDVI changes for different types of grassland vegetation on Mongolian Plateau during growing seasons from 2000 to 2018. **(A)** All grasslands, **(B)** scrubs, **(C)** steppes, **(D)** meadows.

TABLE 2 Change trend of growing season meteorological factors for grassland vegetation on Mongolian Plateau from 2000 to 2018.

| Grassland type | Growing season precipitation/(mm/10a) | Growing season mean air temperature/(°C/10a) | Growing season downward surface shortwave radiation/ (W/m²/10a) |
|---|---|---|---|
| The whole grassland | 34.83 | −0.180 | 0.57 |
| Scrubs | 37.55 | −0.273 | 0.27 |
| Steppes | 31.11 | −0.121 | 1.09 |
| Meadows | 40.45 | −0.089 | −0.47 |

of Inner Mongolia scrubs (60.37 mm/10a) > Mongolia scrubs (31.63 mm/10a), Inner Mongolia steppes (41.16 mm/10a) > Mongolia steppes (18.42 mm/10a), Inner Mongolia meadows (68.31 mm/10a) > Mongolia meadows (24.21 mm/10a). The growing season average air temperature trend of Inner Mongolia scrubs (−0.057°C/10a) > Mongolia scrubs (−0.330°C/10a), Inner Mongolia steppes (−0.085°C/10a) > Mongolia steppes (−0.166°C/10a), Inner Mongolia meadows (−0.042°C/10a) > Mongolia meadows (−0.117°C/10a).

## 3.3. Correlation between NDVI and meteorological factors of the grassland vegetation on Mongolian Plateau

The Mongolian Plateau is located in an arid and semi-arid region, and the amount of precipitation directly affects the change of NDVI. The average air temperature and downward surface shortwave radiation are also one of the direct causes of NDVI change in the Mongolian Plateau to explore the response of grassland vegetation to climate change, we conducted a partial correlation analysis and significance test of the NDVI of grassland vegetation with precipitation, average air temperature, and downward surface shortwave radiation during the growing season of 2000–2018. The results indicate that (Tables 4, 5 and Figure 5A), the NDVI of grassland vegetation during the growing season on the Mongolian Plateau generally showed a highly significant positive correlation with precipitation ($p < 0.05$), with a partial correlation coefficient of 0.31. In the Inner Mongolia region, the partial correlation coefficient between NDVI and precipitation was 0.37, with 0.26 for scrubs, 0.44 for steppes, and 0.20 for meadows. In Mongolia, it was 0.28, with 0.33 for the scrubs, 0.25 for steppes, and 0.14 for meadows. This suggests that the key element influencing the development of grassland vegetation on the plateau is precipitation throughout the growing season, i.e., increasing precipitation encourages increased NDVI in grassland

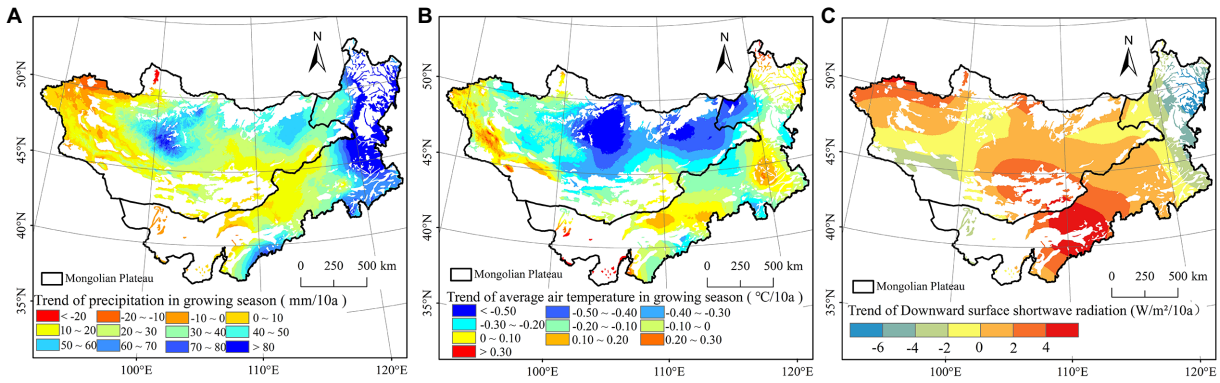


FIGURE 4
Temporal and spatial variation trend of growing season meteorological factors for grassland vegetation on Mongolian Plateau from 2000 to 2018. **(A)** Trend of precipitation in growing season (mm/10a), **(B)** Trend of air temperature in growing season (°C/10a), **(C)** Trend of downward surface shortwave in growing season (W/m$^2$/10a).

**TABLE 3** Comparison of meteorological factors change trends of grassland vegetation types in Inner Mongolia and Outer Mongolia during growing seasons from 2000 to 2018.

| Precipitation trend of grassland vegetation growing seasons in Inner Mongolia and Mongolia from 2000 to 2018 (mm/10a) | | | Trend of average air temperature of grassland vegetation growing seasons in Inner Mongolia and Mongolia from 2000 to 2018 (°C/10a) | | Trend of downward surface shortwave radiation of grassland vegetation growing seasons in Inner Mongolia and Mongolia from 2000 to 2018 (W/m$^2$/10a) | |
|---|---|---|---|---|---|---|
| Vegetation type | Inner Mongolia | Mongolia | Inner Mongolia | Mongolia | Inner Mongolia | Mongolia |
| The whole grassland | 48.35 | 26.09 | −0.074 | −0.246 | 0.54 | 0.60 |
| Scrubs | 60.37 | 31.63 | −0.057 | −0.329 | −0.46 | 0.46 |
| Steppes | 41.16 | 18.42 | −0.085 | −0.167 | 1.33 | 0.80 |
| Meadows | 68.31 | 24.21 | −0.042 | −0.117 | −2.28 | 0.58 |

vegetation. The areas with a positive correlation between NDVI and precipitation in the growing season accounted for 86.87% of the entire grassland distribution area, and only about 13.13% of the distribution area showed a negative correlation, these areas were mainly concentrated in the eastern meadows range of Zavkhan Province, the central meadows range of Khuvsgul Province and the western scrubs range in Mongolia, and some scattered areas showed negative correlations mostly in the meadows ranges of Bayan-Ulgii, Uvs and Khovd Provinces; negative correlations existed in the northern steppes of Alxa League and some steppes ranges of Great Khingan in Inner Mongolia.

It is obvious from Tables 4, 5 and Figure 5B that the average growing season air temperature showed a highly significant negative correlation ($p < 0.05$) with the NDVI of grassland vegetation, with a partial correlation coefficient of −0.09, and the partial correlation coefficients between NDVI and air average temperature in Inner Mongolia and Mongolia were − 0.04 and − 0.12, respectively, with −0.02 for scrubs, −0.08 for steppes, and 0.12 for meadows in Inner Mongolia, and − 0.16 for scrubs, −0.09 for steppes, and − 0.08 for meadows in Mongolia. Areas showing a negative correlation between NDVI and average air temperature in the growing season accounted for 63.92% of the entire grassland vegetation distribution area, and about 36.08% of the area showed a positive correlation. Positive correlation areas are primarily found in Inner Mongolia's Great Khingan Mountains meadows area, the scrubs area east of Tongliao City, the Xilin Gol League's southern scrubs area, and the Alxa League's northern scrubs and southern meadows areas. It has also been discovered in the steppes of northern Dornogovi Province and eastern Dundgovi Province, the steppes of central Govi-Altai Province, the scrubs in the north, the meadows in the south and west of Arkhangai Province, the meadows of northern Khuvsgul Province, and the meadows of northern western Bayan-Ulgii Province and western Uvs Province in Mongolia.

It is obvious from Tables 4, 5 and Figure 5C that the downward surface shortwave radiation showed a highly significant negative correlation ($p < 0.05$) with the NDVI of grassland vegetation, with a partial correlation coefficient of −0.19, and the partial correlation coefficients between NDVI and downward surface shortwave radiation in Inner Mongolia and Mongolia were − 0.15 and − 0.21, respectively, with −0.20 for scrubs, −0.15 for steppes, and 0.12 for meadows in Inner Mongolia, and − 0.16 for scrubs, −0.29 for steppes, and − 0.15 for meadows in Mongolia. Areas showing a negative correlation between NDVI and downward surface shortwave radiation in the growing season accounted for 75.06% of the entire grassland vegetation distribution area, and about 24.94% of the area showed a positive correlation. The locations with positive correlations were mostly found in the steppes distribution regions of Xilin Gol League and Ulanqab City in the center of Inner Mongolia, the scrubs regions of Sukhbaatar and Oriental Province in the east, and the scrubs region of Zavkhan Province in the west.

As shown in Table 5, the partiality correlation coefficients of average air temperature and downward surface shortwave radiation are both

TABLE 4 Partial correlation of NDVI and meteorological factors in the growing season of Mongolian Plateau.

| Partial correlation coefficient | Growing season precipitation | Growing season average air temperature | Growing season downward surface shortwave radiation |
|---|---|---|---|
| The whole grassland | 0.31** | −0.09** | −0.19** |
| NDVI of scrub steppe | 0.31** | −0.13** | −0.17** |
| NDVI of grassland | 0.36** | −0.09** | −0.21** |
| NDVI of meadow | 0.17** | −0.01** | −0.14** |

** Indicates highly significant correlation ($p < 0.05$).

TABLE 5 Partial correlation comparison between NDVI and meteorological factors in growing seasons of Inner Mongolia and Mongolia from 2000 to 2018.

| Growing season precipitation | | | Growing season average air temperature | | | Growing season downward surface shortwave radiation | |
|---|---|---|---|---|---|---|---|
| Vegetation type | Inner Mongolia | Mongolia | | Inner Mongolia | Mongolia | Inner Mongolia | Mongolia |
| The whole grassland | 0.37** | 0.28** | | −0.2998** | −0.3642** | −0.15** | −0.21** |
| Scrubs | 0.26** | 0.33** | | −0.2057** | −0.4289** | −0.20** | −0.16** |
| Steppes | 0.44** | 0.25** | | −0.3716** | −0.3234** | −0.15** | −0.29** |
| Meadows | 0.20** | 0.14** | | −0.0556** | −0.2101** | −0.12** | −0.15** |

**Indicates extremely significant correlation ($p < 0.05$).

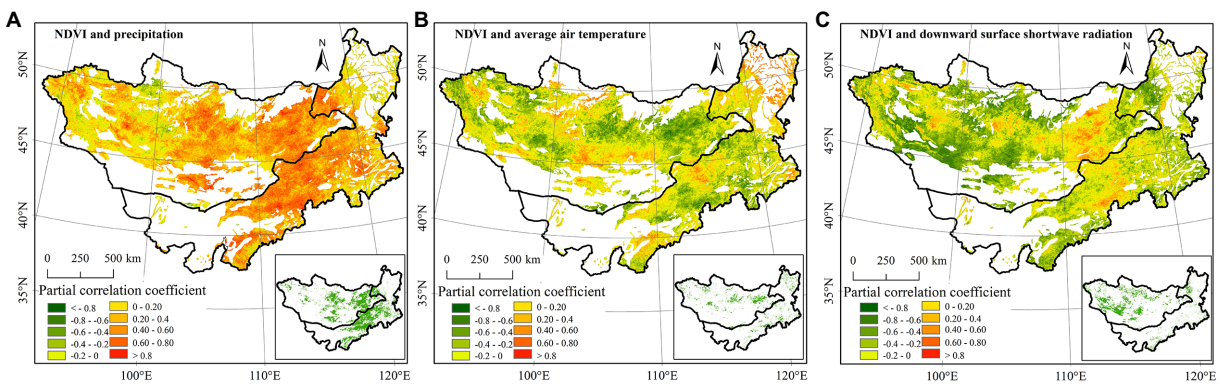


FIGURE 5
Spatial distribution of partial correlation coefficient of growing season NDVI and **(A)** precipitation, **(B)** average air temperature, and downward surface shortwave radiation **(C)** on Mongolian Plateau.

negatively correlated, and all of these correlation coefficients are significant at the 0.05 level. The growing season NDVI of each vegetation in the Mongolian plateau grassland is positively correlated with the growing season precipitation partiality correlation coefficient. This shows that precipitation, a significant factor affecting the interannual dynamics of grassland vegetation in arid and semi-arid regions, primarily controls the growing season NDVI of these three types of vegetation in Mongolian plateau grasslands.

## 3.4. Effects of human activity on the NDVI in the Mongolian Plateau

Multiple linear regression was developed to simulate the anticipated values of NDVI (NDVIpre) through model parameters and precipitation and air temperature data in order to reveal the effects of climate change on NDVI. This was done using precipitation and air temperature of the long time series as independent variables. The comparison reveals that the multi-year trends of the measured and predicted values are similar (Figure 6), but that the predicted NDVI before 2010 is marginally higher and the predicted value after 2010 is lower than the actual value. The measured NDVI is 0.0023 greater than the predicted NDVI of 0.0014, as determined by the slope of change.

In addition to natural factors like climate change, human activities also play a significant role in the change in NDVI of grassland vegetation. Positivity in the slope of the residual change trend indicates positive disturbance, and human activities support rising NDVI and vegetation recovery. Negative disturbance, caused by human activities, will result in a decrease in NDVI and have a suppressive effect on the vegetation recovery if the slope of the residual change trend is negative.

The residual trend was statistically analyzed to better understand how human activities affect the growth status of vegetation (Figure 7). We discovered that human activity had considerably impacted 18.37% of the grasslands on the Mongolian Plateau, with Inner Mongolia

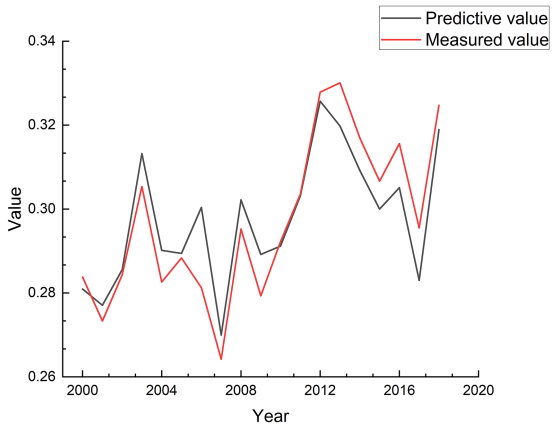


FIGURE 6
Comparison of predicted and measured NDVI values for grasslands on the Mongolian Plateau from 2000 to 2018.

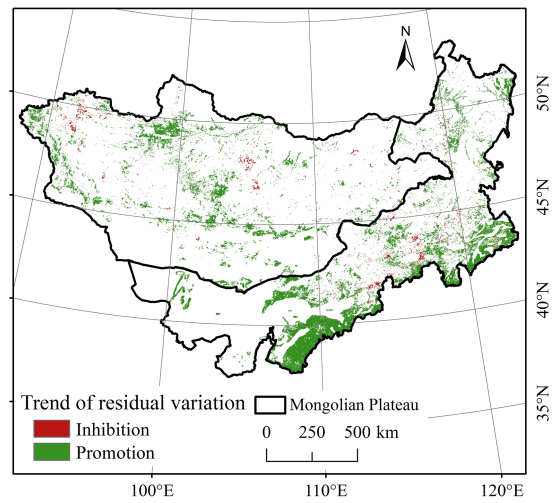


FIGURE 7
Trend distribution of NDVI residuals on the Mongolian Plateau from 2000-2018.

accounting for 11.67% of these impacts and Mongolia for 6.68%. On the Mongolian Plateau, there were 17.24% of grassland regions with positive NDVI residual trends, including 11.07% in Inner Mongolia and 6.16% in Mongolia. The overall effect of human activities on NDVI growth was primarily facilitative. These areas are primarily found in Inner Mongolia's Great Khingan Mountains, the Xilin Gol League grassland region, Tongliao City, the Erdos City region, Dundgovi Province, Ovorhangay Province, and Khuvsgul Province of Mongolia, among other places. Due to ecological engineering construction, agricultural development, grazing bans and rest periods, etc., these areas are impacted by human activities that promote vegetation. About 1.13% of the areas inhibited by human activities, including 0.60% in Inner Mongolia and 0.52% in Mongolia, are concentrated in various urban clusters, such as Ulaanbaatar, Tuv Province, Hohhot and Baotou City, etc. These areas have high population density, developed economic development, urban expansion, and a large amount of land turned into construction land. There are also inhibiting effects of human activity in the Hulunbuir steppe area, the Xilin Gol League steppe area, and the steppe area in eastern Mongolia. These effects are primarily brought on by excessive grazing and other actions that stunt the growth of vegetation.

# 4. Discussion

## 4.1. Growing season NDVI variations and its correlation with climatic factors

This study used MODIS NDVI data and meteorological data from 2000 to 2018 to analyze the spatial and temporal variation characteristics of NDVI and correlation with its meteorological factors during the growing season of grassland vegetation on the Mongolian Plateau. It was discovered that on the Mongolian Plateau, the average NDVI of grassland vegetation growing seasons showed a substantial upward trend from 2000 to 2018, with the largest increase in the Great Khingan Mountains of Inner Mongolia, followed by a larger increase in the area around Arkhangai Province in northern Mongolia, and the average growing season NDVI gradually climbed from the southwest to the northeast. Numerous studies on the spatial and temporal characteristics of NDVI changes in grasslands on the Mongolian Plateau have been conducted recently. Bai and Alatengtuya (2022) used decision tree classification to analyze the spatial and temporal changes of grassland cover in the grassland area of the Mongolian Plateau from 2001 to 2020. They discovered that the grassland area had gradually increased over the previous 20 years, while the vegetation cover had gradually decreased from the northeast to the southwest. (Bai and Alatengtuya, 2022). The Mongolian Plateau's vegetation cover reached 14.60 and 18.43% from 1986 to 1999 and 2000 to 2013, respectively, according to Zhang et al.'s analysis of NDVI data on the vegetation cover from 1982 to 2013 (Zhang et al., 2018). Dai et al. (2014) used a one-dimensional linear regression method to assess the NDVI trend on the Mongolian Plateau from 1982 to 2006, which showed that the NDVI of vegetation has improved during the preceding 25 years (Dai et al., 2014). The findings mentioned above generally agree with this study's conclusions. In this paper, in addition to the spatial and temporal variation of NDVI of grassland vegetation across the Mongolian Plateau, we also compared grassland vegetation in two regions with different land use management practices, Mongolia and Inner Mongolia, and found that both the multiyear average NDVI and NDVI variation trends in Inner Mongolia during the growing season resulted in greener vegetation than that in Mongolia. Li et al. (2021) noted that numerous ecological protection and restoration initiatives have been launched in China since 1978, with the Three Northern Protective Forests, the Key Construction Project for Soil and Water Conservation, the Beijing-Tianjin Wind and Sand Source Control Project, among 13 others, being the main ecological initiatives covering the dry zone. These initiatives have improved land degradation and increased ecosystem functions in dry regions, and they have had significant effects on vegetation, the water cycle, desertification, and ecosystem services (Ouyang et al., 2016; Bryan et al., 2018; Li et al., 2021). They have also helped to make the vegetation greener. In contrast, rather than being driven by human activity, changes in the vegetation cover in the Mongolian region are mostly caused by climatic change (John et al., 2013).

By analyzing the meteorological data for the Mongolian Plateau, we discovered that the average air temperature has been weakly dropping since 2000, while there has been a large increase in precipitation and downward surface shortwave radiation during the growing season of the entire Mongolian Plateau grassland vegetation distribution area. Among them, Inner Mongolia had more precipitation than Mongolia, whereas the

trend of average air temperature and downward surface shortwave radiation fluctuates more in Mongolia than in Inner Mongolia. This discovery is consistent with earlier research by Cao et al. (2019) and Yu et al. (2021), who used satellite observations and numerical simulations to identify a general cooling trend brought on by revegetation in semi-arid regions of northern China. However, some studies, such as those by Huang and Peng, reported that the greening of vegetation may lead to atmospheric warming effects in arid and semi-arid regions due to the effect of enhanced net radiation (Peng et al., 2014; Huang et al., 2018). Due to its significant role in changing surface characteristics, surface energy, and water balance, vegetation degradation or improvement has an impact on local and regional climate through interactions between the land surface and the atmosphere (D'Odorico et al., 2013). The effect of plant restoration on the regional water cycle is more significant and debatable in arid and semi-arid regions than temperature. According to several research reports, a coupled land–atmosphere global climate model demonstrated that the greening of vegetation in northern China boosts precipitation and reduces increased evapotranspiration (Li et al., 2018). Zhu et al. (2021) found that revegetation in a semi-arid basin led to a significant decrease in the aridity index and more precipitation was involved in the soil water–groundwater cycle (Zhu et al., 2021). However, there are also other findings; for example, Jackson et al. (2005) and Ge et al. (2020) found that extensive revegetation led to increased evapotranspiration, which in turn could lead to severe water shortage (Jackson et al., 2005; Ge et al., 2020).

## 4.2. Spatial heterogeneity of correlations between NDVI and climatic factors

The effects of average air temperature, precipitation and downward surface shortwave radiation on grassland vegetation vary widely across space. This region's grassland vegetation's NDVI shows a positive correlation with precipitation and a negative correlation with average air temperature and downward surface shortwave radiation, indicating that more precipitation and less average air temperature and downward surface shortwave radiation are favorable for vegetation growth. For instance, Lin et al. (2020) used GIMMS-MODIS data to study the spatial and temporal variation characteristics of NDVI in northern China from 1982 to 2018, and explored the primary drivers of NDVI changes using regression analysis. The findings revealed that precipitation has a positive dominant effect on NDVI in Inner Mongolia (Lin et al., 2020). According to the findings of studies by Dai and others, high temperatures cause more evaporation in arid and semi-arid regions, while a decrease in surface moisture inhibits the growth of vegetation (Dai et al., 2014). On the other hand, an increase in precipitation promotes the growth of vegetation. In their investigation on the detection of trends and attribution of vegetation greening in China over the previous 30 years, Piao et al. (2015) determined that precipitation was the primary factor driving vegetation greening in arid regions. The amount of precipitation during the growing seasons is higher in Inner Mongolia than in Mongolia, and the region has less of a decrease in average air temperature and downward surface shortwave radiation, which is consistent with a better recovery of vegetation in Inner Mongolia than in Mongolia.

## 4.3. NDVI and human activities

Overall, the grassland vegetation on the Mongolian Plateau is improving, and human activity is a significant factor in the growth of the vegetation, which can have both positive as well as negative disturbance impacts on NDVI changes. The analysis leads to the conclusion that afforestation and agricultural production have a positive influence on vegetation recovery (Xin et al., 2007). Additionally, it has been discovered that implementing ecological projects like converting farmland back to forestry (grass), conserving soil and water, and enacting policies and regulations on sensible grazing and protecting arable land will all have a positive impact on the development of regional vegetation (Li et al., 2011; Jin et al., 2020). Urbanization and economic growth inevitably have an impact on vegetation, which degrades the local natural environment. This is consistent with the paper's conclusion, which found that human activity interfered negatively in urban areas but positively in agricultural production and grassland reserves.

## 4.4. Uncertainties and future work

The current study may have some uncertainties. Frist, since Mongolia and Inner Mongolia are included in the research area, there may be differences in the classification systems used for grassland vegetation, which could affect how the vegetation distribution is determined. Furthermore, when discussing the response of vegetation to climate change, this study does not consider the feedback effect of vegetation on climate, and our previous studies show that the feedback effect of vegetation change on regional climate is strong, which may affect the results of this paper, Yu L. X. et al. (2020) determined the response of vegetation change to climate by using a high-resolution land atmosphere coupled regional climate model, and found that the northern part of northern China showed obvious cooling, including the Northeast Plain, the Loess Plateau and the eastern part of the arid and semi-arid areas in the north (Yu L. X. et al., 2020). Li et al. (2022) used a long time series multi-source satellite and a high-resolution land-air coupled regional climate model (WRF) to investigate the climate feedbacks of surface changes observed in the Mongolian Plateau from the 1990s to the 2010s. According to model simulations, vegetation greening produces a local cooling effect, while vegetation degradation produces a warming effect (Li et al., 2022). Liu et al. (2022) used multi-source satellite measurements records and a high-resolution land atmosphere coupled regional climate model (WRF) to investigate the land surface changes and their associated thermal and wet effects in three major ecosystems in the Heilong-Amur River basin from 1982 to 2018, highlighting the different surface responses and feedbacks of different ecosystems to climate change, depending on the specific vegetation variation and background climate, which may lead to warming/cooling and wetting/drying effects (Liu et al., 2022). To better understand the relationship between vegetation and climate in arid zones, future research should consider the feedback effects of vegetation on climate.

# 5. Conclusions

During the growing season from 2000 to 2018 on the Mongolian Plateau, we examined the temporal and spatial variation of grassland vegetation, as well as how it responded to climate change. We also looked at the partiality connection between precipitation, temperature, downward shortwave radiation, and NDVI. The findings indicate that the grassland vegetation index improved greatly across the plateau from 2000 to 2018, with NDVI increasing at a rate of 0.023/10a during the growing season. Only 8.64% of grassland NDVI degraded, compared

to 91.36% that significantly improved. The scrubs NDVI increased at the fastest pace (0.028/10a), followed by steppes (0.021/10a), and meadows (0.020/10a). While Mongolia's NDVI climbed at a slower rate of 0.019/10y, it increased at a faster rate of 0.030/10y in Inner Mongolia. Three species of grassland vegetation saw faster NDVI growth rates in Inner Mongolia than in Mongolia.

There is an increasing trend of precipitation and upward shortwave radiation across the Mongolian Plateau, with a significant increase at 34.83 mm/10a and 0.57 W/m$^2$/10a, respectively, variable grassland vegetation types saw different rates of precipitation and downward surface shortwave radiation throughout the growing season, with meadows receiving the greatest precipitation (40.45 mm/10a), scrubs (37.55 mm/10a), and steppes (31.11 mm/10a), and steppes having the most downward surface shortwave radiation (1.09 W/m$^2$/10a), followed by scrubs (0.27 W/m$^2$/10a) and meadows mild drop of −0.47 W/m$^2$/10a. The average air temperature decreased slightly by −0.018°C/10a, with the greatest rate of decline in scrubs (−0.273°C/10a), followed by steppes (−0.121°C/10a) and meadows with (−0.089°C/10a). The rates of meteorological factors that impact flora in Inner Mongolia and Mongolian grasslands are also varied, with Inner Mongolia seeing higher rates of precipitation and lower rates of average air temperature and downward surface shortwave radiation.

On the Mongolian Plateau, there is a correlation between NDVI variations in grassland vegetation and meteorological factors. It had a 0.31 correlation coefficient with precipitation and exhibited a highly significant positive association ($p < 0.05$). There was a negative connection between NDVI and precipitation during the growing season for only roughly 13.13% of the grassland distribution area, whereas there was a positive association for 86.87% of the whole distribution area. The sensitivity of grassland vegetation types to precipitation was in the order of steppes > scrubs > meadows. Additionally, the connection between NDVI variation and precipitation differed by area, with Inner Mongolia (0.37) having a larger correlation with precipitation than Mongolia (0.28). A highly significant negative correlation with average air temperature and downward surface shortwave radiation were shown, with a correlation coefficient of −0.09 and −0.19 ($p < 0.05$). The growing season NDVI was negatively associated with average air temperature in 63.92% of the grassland vegetation range, positive in about 36.08% of the grassland range, significantly and negatively correlated with downward surface shortwave radiation in 75.06% of the grassland vegetation range, and positive in about 24.94% of the grassland range. The sensitivity of grassland vegetation types to average air temperature and downward surface shortwave radiation were in the order of meadows > steppes > scrubs. Additionally, there were regional differences in the correlations of NDVI changes with average air temperature and downward surface shortwave radiation, with Inner Mongolia having a greater correlation with average air temperature (−0.04) than Mongolia (−0.12) and having a higher correlation with downward surface shortwave radiation (−0.15) than Mongolia (−0.21). The influence of precipitation on NDVI of grassland vegetation in this region is more pronounced than the relationships between the NDVI of grassland vegetation on the Mongolian Plateau and average air temperature and downward surface short-wave radiation, and the NDVI of grassland vegetation on the Mongolian Plateau is primarily controlled by precipitation during the growing season.

On the Mongolian Plateau, human activity has a large, primarily positive effect on NDVI variations in vegetation. Roughly 17.24% of the areas had a positive residual NDVI trend, and human activities generally facilitated NDVI growth overall, while they inhibited growth in about 1.13% of the regions. This suggests that some of the Mongolian Plateau's ecological conservation and development efforts have been successful.

## Data availability statement

The original contributions presented in the study are included in the article/supplementary material, further inquiries can be directed to the corresponding author.

## Author contributions

GL: methodology, software, writing – original draft, writing – review and editing, formal analysis, and validation. TL: methodology, software, writing – review and editing, formal analysis, and software. JY, YB, and BX: project administration, resources, and investigation. XL, XC, and LB: data curation, software, and writing – review and editing. LY: conceptualization, methodology, and funding acquisition. SZ: conceptualization and methodology. All authors contributed to the article and approved the submitted version.

## Funding

This study was supported by the National Key Research and Development Program of China (2022YFF1300601) the National Natural Science Foundation of China (42071025 and 32161143025).

## Conflict of interest

The authors declare that the research was conducted in the absence of any commercial or financial relationships that could be construed as a potential conflict of interest.

## Publisher's note



## References

Bai, Q. K., and Alatengtuya. (2022). Response of grassland cover change to drought in the Mongolian Plateau from 2001 to 2020. *Pratacult. Sci.* 39, 443–454. doi: 10.11829/j.issn.1001-0629.2021-0505

Bryan, B. A., Gao, L., Ye, Y., Sun, X., Connor, J. D., Crossman, N. D., et al. (2018). China's response to a national land-system sustainability emergency. *Nature* 559, 193–204. doi: 10.1038/s41586-018-0280-2

Cao, Q., Wu, J., Yu, D., and Wang, W. (2019). The biophysical effects of the vegetation restoration program on regional climate metrics in the Loess Plateau, China. *Agric. For. Meteorol.* 268, 169–180. doi: 10.1016/j.agrformet.2019.01.022

Dai, L., Zhang, L., Wang, K., and Wang, R. L. (2014). Vegetation Changing Trend and Its Affecting Factors in Mongolian Plateau. *Bull. Soil Water Conserv.* 34, 218–225. doi: 10.13961/j.cnki.stbctb.2014.05.047

D'Odorico, P., Bhattachan, A., Davis, K. F., Ravi, S., and Runyan, C. W. (2013). Global desertification: drivers and feedbacks. *Adv. Water Resour.* 51, 326–344. doi: 10.1016/j.advwatres.2012.01.013

Du, M. Y., Kawashima, S., Yonemura, S., Zhang, X., and Chen, S. (2004). Mutual influence between human activities and climate change in the Tibetan Plateau during recent years. *Glob. Planet. Chang.* 41, 241–249. doi: 10.1016/j.gloplacha.2004.01.010

Evans, J., and Geerken, R. (2004). Discrimination between climate and human-induced dryland degradation. *J. Arid Environ.* 57, 535–554. doi: 10.1016/S0140-1963(03)00121-6

Fu, B. (2018). Thoughts on the recent development of physical geography. *Prog. Geogr.* 37, 1–7. doi: 10.18306/dlkxjz.2018.01.001

Fu, Y. H., Piao, S., Op de Beeck, M., Cong, N., Zhao, H., Zhang, Y., et al. (2014). Recent spring phenology shifts in western Central Europe based on multiscale observations. *Glob. Ecol. Biogeogr.* 23, 1255–1263. doi: 10.1111/geb.12210

Gao, J., Jiao, K. W., Wu, S. H., Ma, D., Zhao, D., Yin, Y., et al. (2017). Past and future effects of climate change on spatially heterogeneous vegetation activity in China. *Earths Fut.* 5, 679–692. doi: 10.1002/2017EF000573

Ge, J., Pitman, A. J., Guo, W., Zan, B., and Fu, C. (2020). Impact of revegetation of the Loess Plateau of China on the regional growing season water balance. *Hydrol. Earth Syst. Sci.* 24, 515–533. doi: 10.5194/hess-24-515-2020

Guo, X. (2021). *Desertification in Mongolian Plateau in recent 20 years: evolutional trend, driving mechanism, and ecological effects*, Shanghai: East China Normal University.

Hijmans, R. J., Cameron, S. E., Parra, J. L., Jones, P. G., and Jarvis, A. (2005). Very high resolution interpolated climate surfaces for global land areas. *Int. J. Climatol.* 25, 1965–1978. doi: 10.1002/joc.1276

Huang, L., Zhai, J., Liu, J., and Sun, C. (2018). The moderating or amplifying biophysical effects of afforestation on CO2-induced cooling depend on the local background climate regimes in China. *Agric. For. Meteorol.* 260, 193–203. doi: 10.1016/j.agrformet.2018.05.020

Jackson, R. B., Jobbagy, E. G., Avissar, R., Roy, S. B., Barrett, D. J., Cook, C. W., et al. (2005). Trading water for carbon with biological carbon sequestration. *Science* 310, 1944–1947. doi: 10.1126/science.1119282

Jin, K., Wang, F., and Han, J. Q. (2020). Contribution of climatic change and human activities to vegetation NDVI change over China during 1982-2015. *Acta Geograph. Sin.* 75, 961–974. doi: 10.11821/dlxb202005006

John, R., Chen, J., Ou-Yang, Z.-T., Xiao, J., Becker, R., Samanta, A., et al. (2013). Vegetation response to extreme climate events on the Mongolian Plateau from 2000 to 2010.ENVIRONMENTAL. *Res. Lett.* 8:035033. doi: 10.1088/1748-9326/8/3/035033

Kang, L., Han, X., Zhang, Z., and Sun, O. J. (2007). Grassland ecosystems in China: review of current knowledge and research advancement. *Philos. Trans. R. Soc. B Biol. Sci.* 362, 997–1008. doi: 10.1098/rstb.2007.2029

Li, C., Fu, B., Wang, S., Stringer, L. C., Wang, Y., Li, Z., et al. (2021). Drivers and impacts of changes in China's drylands. *Nat. Rev. Earth Environ.* 2, 858–873. doi: 10.1038/s43017-021-00226-z

Li, H. X., Liu, G. H., and Fu, B. J. (2011). Response of vegetation to climate change and human activity based on NDVI in the Three-River Headwaters region. *ACTA ECOLOGICA SINICA* 31, 5495–5504.

Li, Y., Piao, S., Li, L. Z. X., Chen, A., Wang, X., Ciais, P., et al. (2018). Divergent hydrological response to large-scale afforestation and vegetation greening in China. *Sci. Adv.* 4:eaar4182. doi: 10.1126/sciadv.aar4182

Li, G. S., Yu, L. X., Liu, T. X., Jiao, Y., and Yu, J. (2022). Modeling potential impacts on regional climate due to land surface changes across Mongolia Plateau. *Remote Sens.* 14:2947. doi: 10.3390/rs14122947

Lin, X., Niu, J., Berndtsson, R., Yu, X., Zhang, L., and Chen, X. (2020). NDVI dynamics and its response to climate change and reforestation in Northern China. *Remote Sens.* 12:4138. doi: 10.3390/rs12244138

Liu, Z. (1993). Analysis of landscape ecological region in Mongolian Plateau. *J. Arid Land Resour. Environ.* Z1, 256–261.

Liu, Z. H., Li, L. T., Tim, R. M., Van Niel, T. G., Yang, Q. K., and Li, R. (2008b). Introduction of the professional interpolation software for meteorology data: ANUSPLINN. *Meteorol. Monthly* 2, 92–100.

Liu, Z. H., Tim, R. M., Li, L. T., Van Niel, T. G., Yang, Q. K., Li, R., et al. (2008a). Interpolation for time series of meteorological variables using ANUSPLIN. *J. Northwest A&F University* 10, 227–234. doi: 10.13207/j.cnki.jnwafu.2008.10.008

Liu, T. X., Yu, L. X., Bu, K., Yang, J., Yan, F., Zhang, S., et al. (2022). Thermal and moisture response to land surface changes across different ecosystems over Heilong-Amur River Basin. *Sci. Total Environ.* 818:151799. doi: 10.1016/j.scitotenv.2021.151799

Miao, L., Jiang, C., He, B., Liu, Q., Zhu, F., and Xuefeng, C. (2014). Response of vegetation coverage to climate change in Mongolian Plateau during recent 10 years. *Acta Ecol. Sin.* 34, 1295–1301. doi: 10.5846/stxb201304100659

Ouyang, Z., Zheng, H., Xiao, Y., Polasky, S., Liu, J., Xu, W., et al. (2016). Improvements in ecosystem services from investments in natural capital. *Science* 352, 1455–1459. doi: 10.1126/science.aaf2295

Peng, S., Piao, S., Ciais, P., Myneni, R. B., Chen, A., Chevallier, F., et al. (2013). Asymmetric effects of daytime and night-time warming on Northern Hemisphere vegetation. *Nature* 501:88. doi: 10.1038/nature12434

Peng, S. S., Piao, S., Zeng, Z., Ciais, P., Zhou, L., Li, L. Z. X., et al. (2014). Afforestation in China cools local land surface temperature. *Proc. Natl. Acad. Sci. U. S. A.* 111, 2915–2919. doi: 10.1073/pnas.1315126111

Piao, S., Yin, G., Tan, J., Cheng, L., Huang, M., Li, Y., et al. (2015). Detection and attribution of vegetation greening trend in China over the last 30 years. *Glob. Chang. Biol.* 21, 1601–1609. doi: 10.1111/gcb.12795

Scurlock, J. M. O., and Hall, D. O. (1998). The global carbon sink: a grassland perspective. *Glob. Chang. Biol.* 4, 229–233. doi: 10.1046/j.1365-2486.1998.00151.x

Shen, M., Piao, S., Chen, X., An, S., Fu, Y. H., Wang, S., et al. (2016). Strong impacts of daily minimum temperature on the green-up date and summer greenness of the Tibetan Plateau. *Glob. Chang. Biol.* 22, 3057–3066. doi: 10.1111/gcb.13301

Shen, X. J., Zhou, D. W., Li, F., and Zhang, H. Y. (2015). Vegetation change and its response to climate change in grassland region of chinain grassland region of China. *Sci. Geogr. Sin.* 35, 622–629. doi: 10.13249/j.cnki.sgs.2015.05.015

Xie, H., Tong, X. J., Li, J., Zhang, J. R., Liu, P. R., and Yu, P. Y. (2022). Changes of NDVI and EVI and their responses to climatic variables in the Yellow River Basin during the growing season of 2000-(2018). *Acta Ecol. Sin.* 42, 4536–4549. doi: 10.5846/stxb202104271108

Xin, Z. P., Xu, J. X., and Zheng, W. (2007). Climate change and the impact of human activities on the loess plateau vegetation change. *Sci. China Press* 11, 1504–1514.

Yu, G., Li, W., Shao, M. A., Zhang, Y., Wang, S., Niu, S., et al. (2020). Ecosystem science research and ecosystem management. *Acta Geograph. Sin.* 75, 2620–2635. doi: 10.11821/dlxb202012006

Yu, L. X., Liu, Y., Liu, T. X., and Yan, F. (2020). Impact of recent vegetation greening on temperature and precipitation over China. *Agric. For. Meteorol.* 295:108197. doi: 10.1016/j.agrformet.2020.108197

Yu, L., Xue, Y., and Diallo, I. (2021). Vegetation greening in China and its effect on summer regional climate. *Sci. Bull.* 66, 13–17. doi: 10.1016/j.scib.2020.09.003

Zhang, X., Hu, Y., Zhuang, D., and Qi, Y. (2009). The spatial pattern and differentiation of NDVI in Mongolia Plateau. *Geogr. Res.* 28, 10–19. doi: 10.11821/yj2009010003

Zhang, Y. Z., Wang, Z. Q., Yang, Y., Li, J. L., Zhang, Y., and Zhang, C. B. (2018). Research on the quantitative evaluation of grassland degradation and spatial and temporal distribution on the Mongolia Plateau. *Pratacult. Sci.* 35, 233–243. doi: 10.11829/j.issn.1001-0629.2017-0220

Zhou, T. J.., Chen, Z. M., Chen, X. L., Zuo, M., Jiang, J., and Hu, S. (2021). Interpreting IPCC AR6: future global climate based on projection under scenarios and on near-term information. *Clim. Change Res.* 17, 652–663.

Zhu, L., Liu, J.-T., Yang, M.-N., Zhang, Y.-X., and Wen, D.-P. (2021). Evolutionary trend of water cycle in Beichuan River Basin of China under the influence of vegetation restoration. *J. Groundw. Sci. Eng.* 9, 202–211. doi: 10.19637/j.cnki.2305-7068.2021.03.003

# Frontiers in
# Environmental Science

**Explores the anthropogenic impact on our natural world**

An innovative journal that advances knowledge of the natural world and its intersections with human society. It supports the formulation of policies that lead to a more inhabitable and sustainable world.

---

## Discover the latest Research Topics

See more →

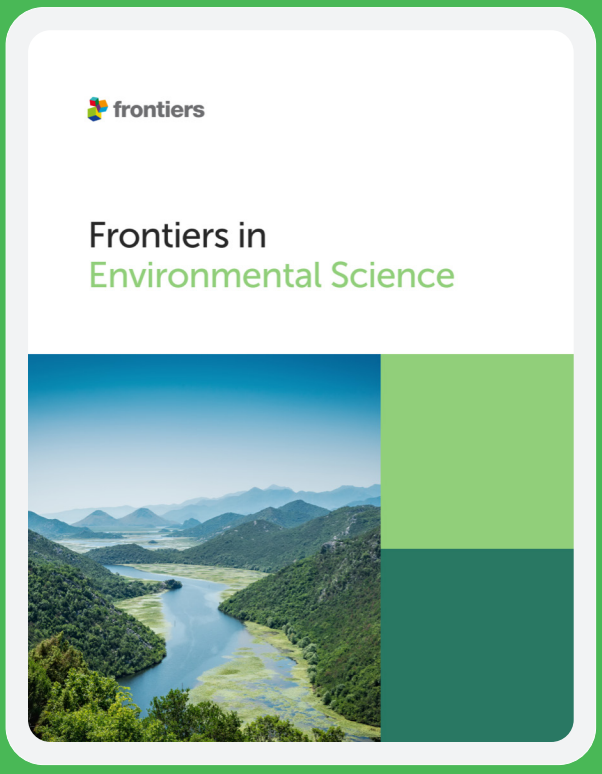


**Frontiers**

Avenue du Tribunal-Fédéral 34
1005 Lausanne, Switzerland
frontiersin.org

**Contact us**

+41 (0)21 510 17 00
frontiersin.org/about/contact